

Mads Radmer Almind

**Induction-heated catalytic  
hydrogen production  
- a magnetic investigation**

Ph.d. thesis  
Kgs. Lyngby, October 2020

Supervised by Professor Cathrine Frandsen  
Co-supervised by Professor Ib Chorkendorff

*Induction-heated catalytic hydrogen production - a magnetic investigation*

Copyright © 2020 Mads Radmer Almind. All Rights Reserved.  
Typeset using L<sup>A</sup>T<sub>E</sub>X.

Department of Physics  
Technical University of Denmark  
DTU Physics Building 307, DK-2800 Kongens Lyngby, Denmark

# Preface

This thesis contains the work performed during my ph.d. project at the Technical University of Denmark (DTU) in the period from March 15<sup>th</sup> 2017 to October 14<sup>th</sup> 2020. The work was supported by Innovation Fund Denmark, grant nr.: 5160-00004B.

I would like to thank my supervisors, Cathrine Frandsen and Ib Chorkendorff, for the opportunity to work on this project, and guidance throughout the process. I am grateful to Mikkel Fougth Hansen for instructing me in VSM, for his vast knowledge on both the technical, theoretical, and practical aspects of this field, as well as for always lending me an extra set of eyes and a pair of helping hands. I would like to thank Jakob Engbæk and Søren Vendelbo for hosting a great external stay, for all their aid, discussions, and for their assistance when I was writing my first article. Peter Mortensen has also been a great help throughout this project, offering a sharp eye in what is relevant and doable, for giving the industrial perspective, and his knowledge on process chemistry. I would like to thank my colleagues Nikolaj Langemark and Mathias Kure for sparring and an uncountable number of coffee breaks, Sebastian Wismann for discussions, especially on the chemical aspects of the project, Morten Vinum, for fruitful collaborations and insightful discussions, and Miriam Varón for help with synthesis, discussions, and ordering an endless number of gas-bottles for me over the years. My thanks to Olivia Sloth and Michelle Herlufsen, whose Python scripts were a great help in early on in my ph.d.. I would like to thank the floor managers, Brian Knudsen and Patrick Strøm-Hansen, for always, more or less willingly, finding time to assist me. I would also like to thank Jeppe Ormstrup for the talks we had throughout our respective projects, and for checking in every once in a while to see if I was doing okay during this last stretch of my project. I would also like to thank my family, for all the help and encouragement they gave me over the years.

Finally, I am endlessly grateful to my girlfriend, Alina. Without her, this thesis would never have been written. She tolerated my incessant complaining, and dragged me out of bed and poured coffee in me on a daily basis. You were always there in the good times and the bad to support me and keep my spirits up. Thank you for being so patient and kind, and for doing everything you could think of to make my life a little easier. This work is dedicated to you.





# Abstract

Due to the rising concerns on global warming, there has been an increasing focus on the necessity of converting to sustainable energies. However, efficient storage of the electricity produced from sustainable energy sources such as wind or solar is still a challenge. One proposed method of storage is to use the excess energy to produce H<sub>2</sub>. Steam methane reforming (SMR) remains the most cost-optimal technology to produce large amounts of hydrogen. The steam reforming reaction is strongly endothermic (heat consuming), and happens at high temperatures. Electrifying the heating of this process could reduce global CO<sub>2</sub> emissions, and using this greener form of technology could be implemented as a transition technology to support global demand for H<sub>2</sub> while the world transitions to relying on sustainable energy.

This project focused on exploring the possibility of electrifying the heating of the SMR process by exchanging the conventional burner technology with induction heating of magnetic materials (the *susceptor*) situated inside the steam reforming reactor. In particular, the project revolved around the characterisation of magnetic susceptor materials, focusing on the role of composition of the susceptor particle, particle size, and improving on current magnetic characterisation of the magnetic susceptor materials by controlling the atmosphere around the sample.

During this project, induction heated SMR was performed using Co<sub>x</sub>Ni<sub>(100-x)</sub> nanoparticles on an alumina support, where the nanoparticles act as both catalyst and magnetic susceptor. It was shown that, unlike in a conventional reformer, the Co<sub>x</sub>Ni<sub>(100-x)</sub>/Al<sub>2</sub>O<sub>3</sub> system was not limited by heat transfer, as the heat is delivered directly to the catalytic sites using the susceptor properties of the system. Instead, the system was shown to be limited by reaction kinetics. Moreover, it was demonstrated that this system had the ability to tune the heating and catalytic capabilities of the material by changing the nanoparticle composition, presenting an opportunity for e.g. layering a reactor with materials of different compositions to optimize reactor performance. Additionally, it was found that the operational temperature in the reactor was limited by the Curie temperature of the material, opening up for applications using the Curie temperature to act as a safety feature to avoid over-

heating endothermic reactions. This project also studied the optimal size of pure cobalt nanoparticles for maximising hysteresis loss as a function of temperature and applied magnetic field, and estimated the optimal size to be in the range of around 24-31 nm. Through studying the power losses in the induction heated bench scale reformer, the energy transfer efficiency was estimated to be  $> 80\%$  when scaling to industrial conditions. This scaling indicates that the system would be competitive with commercially available ways of producing hydrogen via electricity, when considering only energy requirements.

Vibrating sample magnetometry (VSM) was instrumental in characterizing the susceptor materials at high temperatures and screening them for which to use in high temperature applications. However, the conventional vibrating sample magnetometers do not allow for control of the atmosphere around the sample. In order to improve on this, a retrofittable in situ holder for commercial vibrating sample magnetometers was conceived of, produced, and tested during this project. This holder was shown to be able to function under temperatures of up to  $1000\text{ }^{\circ}\text{C}$ , while tolerating the vibrations of the magnetometer, and could expose the sample to a well-defined gas mixture chosen by the user.

In summary, this work has shown that induction heating of magnetic nanoparticles functions even at high temperatures, that it can heat locally inside a reactor, that these systems are highly tunable, and present unique opportunities to be exploited, e.g. using the Curie temperature to avoid overheating. The retrofittable in situ holder should prove valuable for future studies of magnetic materials at high temperatures. In this project the focus has been on SMR, but showing that induction heating of magnetic nanoparticles can function at the high temperatures, strongly endothermic, and chemically harsh conditions of SMR makes the application of induction heating for other reactions less daunting.

# Resumé

På grund af den stigende bekymring for global opvarmning har der været et stigende fokus om nødvendigheden af at konvertere til bæredygtige energier. Dog er effektiv opbevaring af elektriciteten produceret fra vedvarende energityper som vind eller sol stadig en udfordring. Et forslag er, at opbevare den overskydende energi som  $H_2$ . Dampreforming af metan (SMR) er pt. den mest omkostningsoptimale metode til at producere store mængder brint. SMR er en stærkt endoterm (varmeforbrugende) proces, og foregår ved høje temperaturer. Elektrificering af opvarmningen af denne proces kunne sænke den globale  $CO_2$  udledning, og brug af denne grønne form for teknologi kunne implementeres som en overgangsteknologi til at understøtte den globale brintproduktion mens verden går over til brug af vedvarende energi.

Dette projekt har fokuseret på elektrificering af opvarmningen af SMR processen ved at bytte den konventionelle brænder-teknologi ud med induktionsopvarmning af magnetiske materialer (*susceptorer*) placeret inde i selve reaktoren. Mere specifikt, så har projektet drejet sig om karakteriseringen af magnetiske susceptor-materialer, med fokus på rollen af den kemiske sammensætning af susceptor-partiklerne, og af partikelstørrelsen, samt at forbedre den nuværende magnetiske karakterisering af de magnetiske susceptor-materialer ved at kontrollere atmosfæren omkring prøven.

I projektet blev der udført induktionsopvarmet SMR ved brug af  $Co_xNi_{(100-x)}$  nanopartikler på et alumina support, hvor CoNi nanopartiklerne både fungerer som katalysator og som magnetisk susceptor. I projektet blev det vist, at  $Co_xNi_{(100-x)}$ -systemet ikke er begrænset af varmetransport, som er tilfældet i en konventionel reformer. I stedet viste det sig at systemet var begrænset af reaktionskinetik. Det blev også vist, at opvarmningsegenskaberne og de katalytiske egenskaber i dette system kunne justeres og optimeres ved at ændre på sammensætningen af nanopartiklen, hvilket giver mulighed for f.eks. at lagdele en reaktor med materialer med forskellige sammensætninger for at optimere reaktorpræstation. Derudover blev det set at operationstemperaturen i reaktoren var begrænset af Curie temperaturen af materialet, hvilket åbner op for brugen af Curie temperaturen som en sikkerhedsmekanisme til at undgå overophedning af endoterme processer. I dette projekt studeredes også den optimale størrelse af rene kobolt nanopartikler for optimering af

hysteresetab som funktion af temperatur og påsat magnetisk felt, og vi estimerede et optimal størrelse til at ligge omkring 24-31 nm. Ved at studere effekttabet i den induktionsopvarmede laboratorieskala reformerings-reaktor blev det estimeret at energioverførings-effektiviteten kunne komme op på  $> 80\%$  når man ekstrapolerer til industrielt relevante betingelser. Den beregnede opskalering indikerede også at systemet ville være konkurrencedygtigt med nuværende kommercielle måder at producere brint via elektricitet, når man kun tager energi-krav i betragtning.

Vibrating sample magnetometry (VSM) var centralt i karakteriseringen af susceptormaterialerne og i udvælgelsen af hvilke susceptorer der kunne bruges i anvendes ved høje temperaturer. Der er dog ikke mulighed for at kontrollere atmosfæren omkring prøven i konventionelle vibrating sample magnetometers. Derfor blev der i dette projekt udviklet, produceret, og testet en retrofittable in situ holder til disse vibrating sample magnetometers. Denne holder kan tolerere vibrationerne i magnetometeret, temperaturer op til  $1000\text{ }^{\circ}\text{C}$ , og kan udsætte en prøve for en gas-sammensætning valgt af brugeren.

Kort sagt, så har resultaterne i dette projekt vist, at induktionsopvarmning af magnetiske nanopartikler fungerer selv ved høje temperaturer, at de kan opvarmes induktivt inde i en reaktor, at disse systemer kan justeres i høj grad, og at disse systemer har unikke magnetiske egenskaber der kan udnyttes når man opvarmer en reaktion, f.eks. brug af Curie temperaturen til at undgå overophedning. Den retrofittable in situ holder forventes at vise sig brugbar i fremtidige studier af magnetiske nanopartikler ved høje temperaturer. I dette projekt har fokus været på dampreforming af metan, men ved at vise at induktiv opvarmning af magnetiske nanopartikler kan lade sig gøre under hårde kemiske forhold og høje temperaturer i stærkt endoterme processer, gør det udfordringen ved anvendelsen af dette til andre reaktioner mindre vanskelig.

# Contents

<b>Preface</b>	<b>iii</b>
<b>Abstract</b>	<b>v</b>
<b>Resumé</b>	<b>vii</b>
<b>Contents</b>	<b>ix</b>
<b>List of publications</b>	<b>xi</b>
<b>Nomenclature</b>	<b>xiii</b>
<b>1 Introduction</b>	<b>1</b>
1.1 Global warming and energy concerns . . . . .	1
1.2 Steam methane reforming . . . . .	2
1.3 Induction heating in further detail . . . . .	4
1.4 State of the art . . . . .	6
1.5 Focus of this thesis . . . . .	8
1.6 Thesis outline . . . . .	10
<b>2 Magnetometry</b>	<b>11</b>
2.1 Vibrating sample magnetometry . . . . .	11
2.2 High temperature oven option . . . . .	12
2.3 Sample holders . . . . .	12
2.4 Magnetic measurements . . . . .	15
2.5 Data treatment . . . . .	21
<b>3 Papers and results</b>	<b>23</b>
3.1 Paper I: Dual-function cobalt-nickel nanoparticles tailored for high temperature induction-heated steam methane reforming . . . . .	23
3.2 Paper II: Improving performance of induction-heated steam methane reforming . . . . .	29

---

3.3	Paper III: Tunability of CoNi Nanoparticle Composition for Optimal and Curie-temperature-controlled Induction-heated Catalysis . . . . .	42
3.4	Universal Susceptors . . . . .	67
	Cobalt-aluminium . . . . .	67
	Iron-chromium-aluminium . . . . .	69
3.5	Paper IV: Size-dependent magnetic properties of cobalt nanoparticles for high-temperature applications . . . . .	71
3.6	Paper V: Retrofittable plug-flow reactor for in situ high-temperature vibrating sample magnetometry . . . . .	90
<b>4</b>	<b>Summary and Perspectives</b>	<b>113</b>
<b>A</b>	<b>Appendix</b>	<b>119</b>
A.1	Scripts for data-analysis . . . . .	119
A.1.1	Example of base script for treating raw data . . . . .	123
A.1.2	Example of base script for slicing through data across samples	138
A.1.3	Scripts for definitions and functions used in the scripts . . . . .	157
	<b>Bibliography</b>	<b>171</b>

# List of publications

## Peer-reviewed journal papers

- Paper I. M. G. Vinum, M. R. Almind, J. S. Engbæk, S. B. Vendelbo, M. F. Hansen, C. Frandsen, J. Bendix, And P. M. Mortensen, *Dual-Function cobalt-nickel nanoparticles tailored for high-temperature induction-heated steam methane reforming*, *Angewandte Chemie* **130**, 10729-10733 (2018). Enclosed in Section [3.1](#).
- Paper II. M. R. Almind, S. B. Vendelbo, M. F. Hansen, M. G. Vinum, C. Frandsen, P. M. Mortensen, and J. S. Engbæk, *Improving performance of induction-heated steam methane reforming*, *Catalysis Today* **342**, 13-20 (2019). Enclosed in Section [3.2](#).

## Papers in preparation

- Paper III. M. R. Almind, M. G. Vinum, S. T. Wismann, M. F. Hansen, S. B. Vendelbo, J. S. Engbæk, P. M. Mortensen, I. Chorkendorff, and C. Frandsen, *Tunability of CoNi Nanoparticle Composition for Optimal and Curie-temperature-controlled Induction-heated Catalysis*, Enclosed in Section [3.3](#)
- Paper IV. M. R. Almind, M. Varón, C. Frandsen, et al., *Size-dependent magnetic properties of cobalt nanoparticles for high-temperature applications*, Enclosed in Section [3.5](#)
- Paper V. M. R. Almind, J. S. Engbæk, M. F. Hansen, S. B. Vendelbo, P. M. Mortensen, Christian D. Damsgaard, I. Chorkendorff, and C. Frandsen, *Retrofittable plug-flow reactor for in situ high-temperature vibrating sample magnetometry*, Enclosed in Section [3.6](#)

### **Contributions to papers**

- Paper I. Involved in planning of the TEM and VSM studies. Carried out TEM measurements and analysis. Carried out VSM data-analysis, and was involved in the interpretation of these results. Contributed with the TEM focused parts of the article. Contributed to the VSM parts of the paper. Contributed with figures for the TEM and VSM parts of the article. Contributed to the parts on the VSM instrumentation and the parts on magnetic measurements in SI. Contributed in internal review of the paper, especially on the microscopy and magnetic parts.
- Paper II. Planning of VSM investigations. Analysis of activity data and interpreting results. Research on, and development of, the mathematical framework. Carrying out VSM measurements. Analysis of VSM results, and interpretation of these. Writing the first draft of the complete manuscript. Development of tables and figures. Improvement through internal reviews and the improvement cycle with journal editors.
- Paper III. Planning of VSM investigations. Analysis of activity data and interpreting results. Carrying out VSM measurements. Analysis of VSM results, and interpretation of these. Writing first draft of the complete manuscript. Development of tables and figures. Improvement of the paper through internal reviews.
- Paper IV. Took part in the formulation of the study. Planning of VSM investigations. Carrying out VSM measurements. Analysis of VSM results, and interpretation of these. Writing the first draft of the complete manuscript. Development of tables and figures. Improvement through internal reviews.
- Paper V. Designed holder prototypes. Designed the experiments Planning of VSM investigations. Produced and tested holder prototypes. Analysis of data and interpreting results. Carrying out VSM measurements. Analysis of VSM results, and interpretation of these. Writing the first draft of the complete manuscript. Development of tables and figures. Improvement through internal reviews.



# Nomenclature

Abbreviation	Term
VSM	Vibrating sample magnetometer/magnetometry
SMR	Steam methane reforming
BN	Boron nitride
AC	Alternating current
DC	Direct current
D.o.R.	Degree of reduction
RT	Room temperature
hcp	Hexagonal close packed
fcc	Face centered cubic
SPM	Superparamagnetic/superparamagnetism
XRD	X-ray diffraction
TEM	Transmission electron microscopy
STEM	Scanning transmission electron microscopy
EDS	Electron dispersive x-ray spectroscopy
SEM	Scanning electron microscopy
SD	(Magnetic) single domain
MD	(Magnetic) multi domain
NP	Nanoparticle
MNP	Magnetic nanoparticle
TW	Terawatt
CFD	Computational fluid dynamics
IWI	Incipient wetness impregnation

Symbol	Description	Unit
$T$	Temperature	$^{\circ}\text{C}$
$f$	Frequency	Hz
$B$	Magnetic field	T
$H$	Magnetic field	$\frac{\text{A}}{\text{m}}$
$K$	Magnetic anisotropy constant	$\frac{\text{J}}{\text{m}^3}$
$V$	Volume	$\text{m}^3$
$k_{\text{B}}$	Boltzmann's constant	$\frac{\text{J}}{\text{K}}$
$B_{\text{app}}$	Maximal applied magnetic field	T
$W_{\text{h}}$	Hysteresis area	$\frac{\text{J}}{\text{kg}}$
$T_{\text{C}}$	Curie temperature	$^{\circ}\text{C}$
$T_{\text{B}}$	Blocking temperature	$^{\circ}\text{C}$
$\sigma$	Mass specific magnetization	$\frac{\text{Am}^2}{\text{kg}_2}$
$\sigma_{\text{R}}$	Mass specific remanent magnetization	$\frac{\text{Am}^2}{\text{kg}_2}$
$\sigma_{\text{S}}$	Mass specific saturation magnetization	$\frac{\text{Am}^2}{\text{kg}}$
$\mu_0$	Vacuum permeability	$\frac{\text{H}}{\text{m}}$
$\mu_0$	Relative permeability	Unitless
$\delta$	Resistivity	$\Omega\text{m}$
$\rho$	Density	$\frac{\text{kg}}{\text{m}^3}$
$\mu_0 H_{\text{C}}$	Coercive field	mT
$d_{\text{C}}$	Critical diameter	m
$E_{\text{d}}$	Demagnetization energy	J
$E_{\text{BW}}$	Boch wall energy	J
$d_{\text{skin}}$	Skin depth	m
$P_{\text{Eddy}}$	Eddy current power loss density	$\frac{\text{W}}{\text{m}^3}$
$P_{\text{hys}}$	Hysteresis power loss density	$\frac{\text{W}}{\text{m}^3}$

# Chapter 1

## Introduction

### 1.1 Global warming and energy concerns

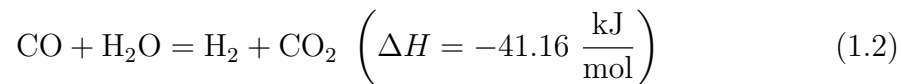
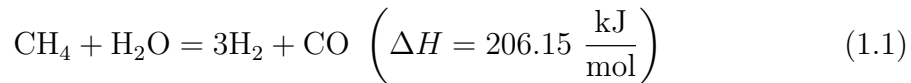
It is widely accepted that global warming is a reality, and that it is caused by the emission of greenhouse gasses, of which CO<sub>2</sub> has shown to be the largest contributor. These emissions are mainly caused by the use of fossil fuels in industry, transport, and generation of heat and electricity[1]. In the coming years, society will have to move away from relying on fossil fuels to such a large degree, and towards utilizing mainly renewable energy. Of these, solar and wind energy have the biggest potential for supplying the bulk of the needed power, at around 100 and 55 TW, respectively[2]. The global power consumption is theorized to be around 25-30 TW in the year 2050 [2], and combining solar, wind, and other renewable energy types, should be able to achieve this power-output. This, coupled with the decrease in the levelized cost of energy of wind and solar over the last decade[3], makes a good case for the achievability of a society based on renewable energy.

There are, however, many challenges tied to the transition to a society based on renewable energy. For wind and solar, kinetic energy and radiation is transformed into electricity, which goes on the power grid. Unfortunately, the wind does not always blow and the sun does not always shine. So, when the power generation is higher than the energy consumption, there is a need to store that energy, so it can be used when power consumption exceeds power generation. However, finding efficient ways of storing this energy is challenging. One suggested storage method is the use of excess power generated by these intermittent energy sources to produce hydrogen[4]. The technologies used to produce hydrogen are however all either still in R&D, or have a higher cost compared to the current benchmark technology: steam reforming[5]. Until these technologies mature, an alternative way to produce hydrogen could be to use greener versions of traditional hydrogen production methods as transition technologies to lessen some of the greenhouse-gas emissions, until

sustainable technologies can take over.

## 1.2 Steam methane reforming

Today, around 96 % of hydrogen is produced from fossil fuels, with 4% being produced through electrolysis of water[6]. Roughly half of the hydrogen produced globally is produced through steam methane reforming (SMR)[6], and SMR is also responsible for nearly 3% of global CO<sub>2</sub> emissions[7]. In SMR, a mixture of methane and water reacts at high temperatures and pressures through the highly endothermic reaction 1.1, followed by the water-gas shift reaction, reaction 1.2[8, 9, 10], to produce a mixture of unconverted methane, hydrogen, carbon monoxide, and carbon dioxide.



This is typically done at temperatures ranging from 450-650 °C in inlet temperature and 850-950 °C in outlet temperature, and steam partial pressures of up to 30 bar[8][11].

In practice, this is often done in a tubular reformer, which can have capacities up to 300.000  $\frac{\text{Nm}^3}{\text{hr}}$  H<sub>2</sub>[8]. In a tubular reformer, the reaction happens inside a series of tubes loaded with pellets (made from, for example, MgAl<sub>2</sub>O<sub>4</sub>) that are impregnated with catalyst (typically nickel). These tubes are usually 100-200 mm thick, and 10-13 m tall[8]. The tubes are externally heated by burners, where part of the methane feed is mixed with air and combusted to drive the highly endothermic reaction[8]. In these types of reactors, heat transfer is the limiting factor[12]. The thermal gradients lowers the reactor lifetime[13], and also introduces the risk of undesired secondary processes, such as carbon deposition[8], which is harmful to the operation of the reformer. Additionally, the large thermal mass of the tubes contributes to a slow start-up of the reformer, typically several days[14]. Moreover, the burner type setup only transfers around 50 % of the heat to the process gas, with the rest being recovered in the waste heat section of the reformer.

Electrifying the heating of the SMR process could help address the heat transfer challenges, shortening the start-up time, as well as minimizing production of CO<sub>2</sub>, as electrical heating could be used to locally heat the catalytic material, has short reaction times for heating, and could utilize electricity from renewable sources[12,

7, 15]. In Fig. 1.1, three methods of heating the SMR process are sketched: the conventional method using burners, a method using resistive heating, and a method using induction heating, along with their respective temperature profiles.

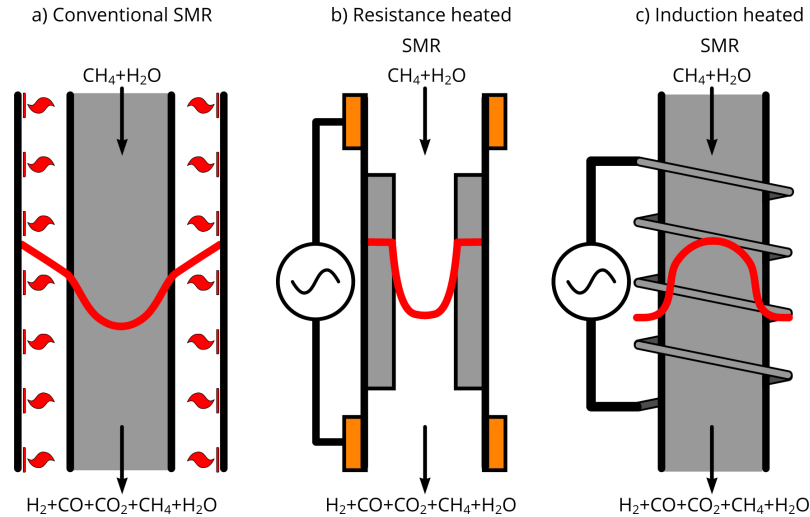


**Figure 1.1:** Sketches of: a) conventional burner technology for heating in SMR, b) resistive heating of SMR, and c) induction heating of SMR, and their temperature profiles. Red lines are sketches of the temperature profile, and the black arrows indicate the gas flow direction. Adapted from Mortensen et al.[12] and Wismann et al.[7].

As mentioned, the conventional burner technology is limited by slow start-up times and heat transfer, which the other two methods of heating can circumvent[12, 7, 15]. In resistive heating, a current is sent through a conducting material, which produces heat by Ohmic losses. This was used by Wismann et al. [7, 15] to heat a tube covered with a nickel-impregnated (i.e. catalytic) washcoat to perform resistively heated SMR. Based on these experiments, he built a CFD (Computational Fluid Dynamics) model, and found that there was a minimal thermal gradient across the washcoat (indicated by the horizontal T-profile in Fig. 1.1b, near the reactor wall), circumventing the heat transfer limitation that dominates in conventional SMR. Instead, the model predicts that diffusion of gas to the washcoat becomes the limiting factor[15]. This means that reactor tubes of small diameters would be favoured in an electrical reformer for SMR[15]. Results obtained through Wismann et al.'s CFD model also indicate that switching from conventional heating to resistive heating would allow for a significant reduction in reactor volume when compared to a conventional reformer, as well as reducing the start-up time significantly, allowing for intermittent operation[7]. Here, they estimate that these electrical reformers could be up to 100 times smaller[7]. Furthermore, Wismann et al. state that if electrification of SMR is implemented on a large scale, it could lead to a reduction

of global CO<sub>2</sub>-emissions of up to approx. 1%[7].

Induction heating (which is the heating method studied in this thesis) takes advantage of an alternating magnetic field to heat materials in contact with the field. This type of heating has been applied successfully to SMR[12], here the penetration depth of the alternating magnetic field was utilized to locally heat nanoparticles to supply heat for the steam reforming reaction (principle sketched in Fig. 1.2). Induction heating by nanoparticles distributed in the reactor essentially flips the temperature profile when compared to the conventional reformer (see Fig. 1.1a), as it supplies uniform local heating throughout the reactor. This method may, like the resistance heated reactor (see Fig. 1.1b), reduce the reactor volume significantly, as the burners would be replaced by an AC (alternating current) coil, and the waste-heat section would be minimized, as the heat is generated close to the catalyst, inside the reactor. Induction heating is a somewhat less direct type of heating when compared to resistive heating, but the penetration depth of the magnetic field has the ability to reach further into the reactor to heat susceptor material. Induction heating has also demonstrated fast on/off switching of the reaction[16], making intermittent operation possible.

Due to the reduction of CO<sub>2</sub> emission, the reductions in reactor volume, and the short start-up times, electrifying the heating of SMR could amount to a flexible and greener production of hydrogen, as it would enable intermittent production of H<sub>2</sub> from renewable sources. The smaller reactors would also make it possible to de-centralize production of H<sub>2</sub>, alleviating the risks and costs of transporting pressurized tanks of H<sub>2</sub>.

### 1.3 Induction heating in further detail

Induction heating is perhaps best known for its use in induction stoves, where an alternating magnetic field induces currents to run in the bottom of a pot, heating it through ohmic resistance. Induction heating is also used in welding, heat treatment of metals, and has more recently found a possible use in cancer treatment using magnetic hyperthermia[17, 18, 19, 20]. The materials used for induction heating we call *magnetic susceptors* or just *susceptors*.

Two main effects contribute to heating when talking about induction heating: eddy currents and magnetic hysteresis loss. Eddy currents are current loops induced in the material that heat up the material by ohmic resistance. Hysteresis loss is the energy lost as heat when cycling through a hysteresis loop. These two effects dominate at different length scales, with hysteresis loss dominating in the sub-micrometer range, and eddy currents dominating above this range[21]. This can be shown by

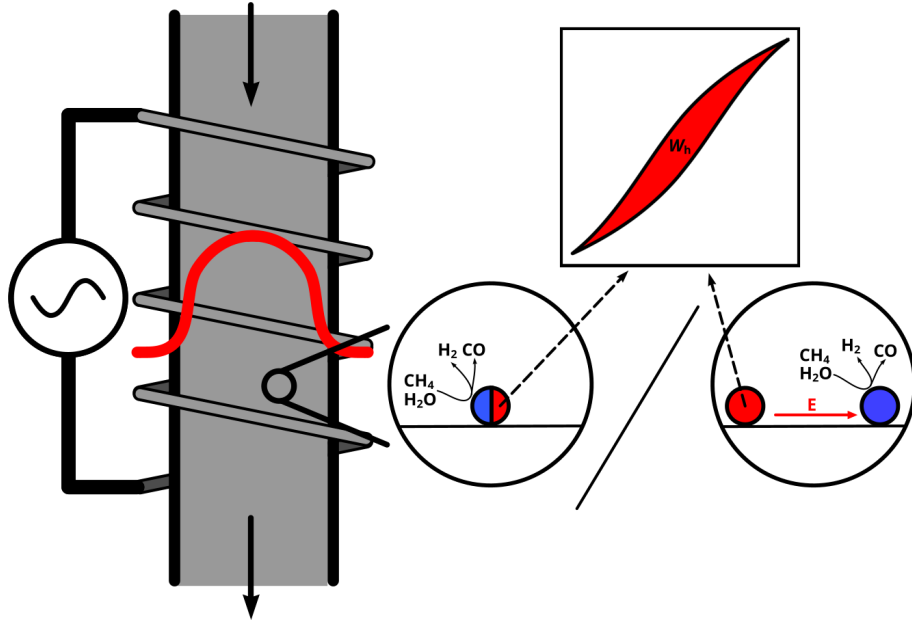


**Figure 1.2:** Sketch of induction-heated SMR using nanoparticles as susceptors. The red line represents the temperature profile, dashed line represents the symmetry axis.  $W_h$  is the amount of energy lost as heat when cycling through the hysteresis loop once, and  $E$  is the energy transferred to the catalytic particle in the form of heat. In the particles, blue represents catalytic material, and red represents magnetic susceptor material. Adapted from Mortensen et al.[12].

a few simple calculations of each of the losses in the range of 0-10  $\mu\text{m}$  for spherical cobalt particles in an oscillating magnetic field. For these calculations an applied magnetic field of 25 mT was chosen, as well as a frequency of 200 kHz. These parameters are representative of the experiments carried out during this project. In order to calculate the eddy current loss, it is necessary to calculate the skin depth. The skin depth is the depth at which the alternating magnetic field falls off by  $\frac{1}{e}$ [22]. If the object has dimensions below this depth, it can be assumed that the magnetic field is homogeneous inside of the material. In this case the calculations will be made for a sphere, which represents a particle in the powder-samples used throughout this project. The skin depth can be calculated using[22]:

$$d_{\text{skin}} = \sqrt{\frac{2\delta}{\mu_0\mu_r\omega}} \quad (1.3)$$

with  $\mu_0$  being the vacuum permeability,  $\mu_r = 250$ [23] being the maximum relative permeability of cobalt,  $\delta = 6.24 \times 10^{-8} \Omega\text{m}$  is the resistivity of cobalt[23], and  $\omega = 2\pi f$ , with  $f$  being the frequency. For the parameters used in this calculation,

the skin depth would then equal  $d_{\text{skin}} = 18 \mu\text{m}$ . As we in the following will restrict the calculations to sizes ranging from  $0 \leq D \leq 10 \mu\text{m}$ , the expression for the eddy current loss will not take the skin depth into account, and assume a uniform field inside the material. The expression for eddy current losses in the absence of a skin effect can be written as[24]:

$$P_{\text{eddy}} = \frac{(\pi R \mu_0 \mu_r f H)^2}{5\delta} \quad (1.4)$$

with  $P_{\text{eddy}}$  being the power density lost as heat in  $\frac{\text{W}}{\text{m}^3}$ ,  $R$  being the radius of a sphere, and  $H = \frac{20 \text{ mT}}{\mu_0} \approx 16 \frac{\text{kA}}{\text{m}}$ .

Assuming that the hysteresis loss scales linearly with frequency, and has a constant hysteresis loss as a function of size (which is not true, see Sec. 3.5), the hysteresis loss is estimated by:

$$P_{\text{hys}} = W_{\text{h}} \rho f \quad (1.5)$$

where  $P_{\text{hys}}$  is the power lost as heat in  $\frac{\text{J}}{\text{m}^3}$ ,  $W_{\text{h}} = 0.34 \frac{\text{J}}{\text{kg}_{\text{Co}}}$ , and  $\rho = 8790 \frac{\text{kg}}{\text{m}^3}$  is the density of cobalt[23].  $W_{\text{h}}$  was taken from the studies in Paper V (Section 3.6) on supported cobalt nanoparticles, where the hysteresis loop was measured at 200 °C and  $B_{\text{app}} = 20 \text{ mT}$ , after a reduction of the sample.

The hysteresis loss for particles with diameters,  $D = 2R$ , between 0 and 10  $\mu\text{m}$  can be seen along with the eddy current loss in Fig. 1.3. In the figure, it can be seen that with the parameters used here, the hysteresis losses and the eddy current losses would be approximately equal at a particle size of  $D = 8.5 \mu\text{m}$ . These simple calculations do however depend on the material parameters used, the shape of the particle, the applied magnetic field, etc., which might not reflect exactly what happens in reality. The takeaways from these calculations are that in the  $< 1 \mu\text{m}$  range, hysteresis losses tend to dominate, whereas in the  $> 10 \mu\text{m}$  range, eddy current losses tend to dominate. In the range of 20-50 nm (the NP sizes in Paper I-V), eddy current losses should be negligible.

## 1.4 State of the art

During the last two decades there has been a rising interest in using magnetic nanoparticles (MNPs) in everything from cancer treatment[20], to recycling of catalyst [25, 26], to combustion of volatile compounds[27], to studying the formation of cobalt-carbide in Fischer-Tropsch synthesis in situ[28]. A good review of some of the applications of magnetic materials in catalytic processes can be found in Wang et al.[16].



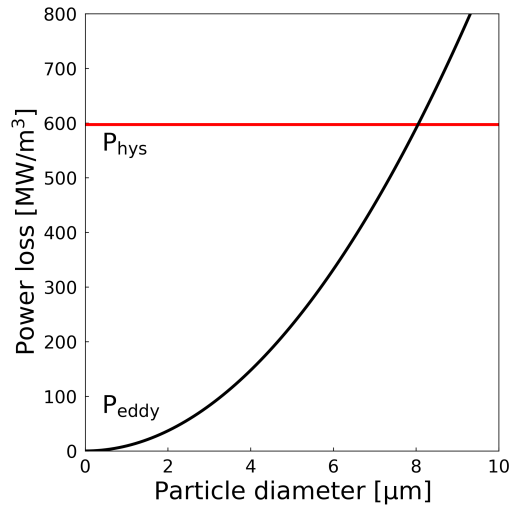


**Figure 1.3:** Comparison of the power lost as heat per cubic meter of sample for eddy currents,  $P_{\text{eddy}}$ , and hysteresis loss,  $P_{\text{hys}}$ , for a sample of spherical cobalt particles. For these calculations, the following parameters were used:  $\mu_r = 250$ ,  $f = 200$  kHz,  $H \approx 16 \frac{\text{kA}}{\text{m}}$ ,  $\delta = 6.24 \times 10^{-8} \Omega\text{m}$ ,  $W_h = 0.34 \frac{\text{J}}{\text{kgCo}}$ , and  $\rho = 8790 \frac{\text{kg}}{\text{m}^3}$ .

Most of the interest in using the heating properties of MNP's has been in the field of magnetic hyperthermia for cancer therapy [17, 18, 19, 20]. However, in the last decade there has been a rising interest in the use of heating using MNP's in various aspects of catalysis. This was initiated by Kirschings group with a study in 2008 on liquid organic chemical synthesis on silica-coated iron oxide particles that could be decorated with various catalysts[29], which was later expanded upon[30, 31]. Others started to utilize induction heating of magnetic materials as well, e.g. Chatterjee et al.[32] using induction heating for a near-isothermal micro-trickle bed reactor. Also, Meffre et al.[33] published the first paper from Chaudret's group in 2015 on nanoparticles with both magnetic and catalytic properties, used for performing Fischer-Tropsch synthesis. Chaudret's group has since then published multiple papers in this field, a select few mentioned here: two papers on driving  $\text{CO}_2$  hydrogenation using magnetic heating[34, 35], a paper on a FeC-Ni core-shell nanoparticle for improved water electrolysis[36], and one on hydrodeoxygenation using magnetic induction[37].

In the area of heating reforming reactions at high temperatures using magnetic materials, there have been some contributions in the recent years. Varsano et al.[38] published on dry reforming of methane using a micrometer-sized NiCo-powder able to heat to  $> 850$  °C, Perez-Camacho et al.[39] publishing on a perovskite-type mixed metal oxide for use in converting surplus electricity from windmills to hydrogen

through dry reforming and steam reforming of methane using induction heating, and Marbaix et al.[40] who used iron-cobalt nanoparticles for propane and methane dry reforming, among other reactions.

Our group has focused on the steam reforming reaction, kicked off by Mortensen et al. in 2017[12] with a proof-of-concept paper on a Ni-Co nanoparticle system acting both as catalyst and heating element, which was able to heat to  $> 780$  °C using only hysteresis heating. Since then, Vinum et al.[14] published on a highly tuneable CoNi dual function nanoparticle system for induction heated SMR (included in this thesis as Paper I). Afterwards, we have also looked into how to improve the performance on induction heated SMR[41] (included as Paper II in this thesis).

## 1.5 Focus of this thesis

This thesis focuses on the characterization of magnetic susceptor materials for induction heating of the SMR process (by magnetic hysteresis heating). The main topics on investigation of these susceptor materials have revolved around:

- The optimum composition of a  $\text{Co}_x\text{Ni}_{(100-x)}/\text{Al}_2\text{O}_3$  dual function system (outlined below) for induction heated SMR
- Investigation of energy transfer efficiency in a bench scale induction heated reformer with an extrapolation to industrial conditions
- Optimal nanoparticle size to maximize hysteresis losses
- How to improve control of the atmosphere around the sample when performing high-temperature VSM measurements

Other work included in this thesis relate to the development of a "universal susceptor" (see below), and improving on the heat transfer efficiency of the induction heated SMR reformer.

The susceptor systems studied are briefly described below in order to introduce the systems to the reader, and to explain why these materials were chosen as susceptor candidates. Each of the studied susceptor systems consist of magnetic (Co, CoNi or FeCr) particles supported on (denoted by putting a "/" followed by the support material after the susceptor name, e.g.  $\text{Co}_x\text{Ni}_{(100-x)}/\text{Al}_2\text{O}_3$ ) or protected by (denoted by the susceptor name followed by "-" and the protective material, e.g. FeCr- $\text{Al}_2\text{O}_3$ ) a non-magnetic oxide ( $\text{Al}_2\text{O}_3$  or  $\text{MgAl}_2\text{O}_4$ ).

The  $\text{Co}_x\text{Ni}_{(100-x)}/\text{Al}_2\text{O}_3$  system was based on the idea of mixing nickel, which is a preferred catalyst for SMR, with cobalt, which has the highest known Curie

temperature (1121 °C[23]), in order to have a heatable magnetic susceptor and catalytically active nickel-sites in one particle. The compositions of the samples were varied with  $x$ , in steps of 10 mol% (i.e.  $\text{Co}_{10}\text{Ni}_{90}$ ,  $\text{Co}_{20}\text{Ni}_{80}$ , and so on).

Two universal susceptor systems of  $\text{Co-Al}_2\text{O}_3$  and  $\text{FeCr-Al}_2\text{O}_3$  were studied during this project. In these systems the susceptor material is separated from the catalytic particles and protected by an  $\text{Al}_2\text{O}_3$  shell, such that they do not alloy with the catalytic particle or react with the gas in the reactor. Due to the separation, the magnetic properties/heating capabilities can be optimized independently of the catalyst.

A system of  $\text{Co/Al}_2\text{O}_3$  samples with different Co particle sizes were synthesized in order to investigate the effect of size on the magnetic properties of nanoparticles for high temperature applications.

## 1.6 Thesis outline

This section gives a short overview of the chapters in the rest of the thesis.

- **Chapter 2:** An introduction is given to vibrating sample magnetometry (VSM), and the setups used in this project. This chapter also contains an overview of the types of magnetic measurements that were performed using the VSM, and an explanation of the experimental profile used. A brief outline of the data treatment is also given.
- **Chapter 3:** This chapter presents the results obtained during this project. The results are given mostly in the format of "papers" (published and in preparation), and includes the following:
  - Paper I on the proof of concept of a dual function CoNi nanoparticle system ( $\text{Co}_{50}\text{Ni}_{50}/\text{Al}_2\text{O}_3$ ) for hysteresis heated SMR
  - Paper II on improving the performance on induction-heated SMR (tested on  $\text{Co}_{50}\text{Ni}_{50}/\text{Al}_2\text{O}_3$ )
  - Paper III on the tunability of the  $\text{Co}_x\text{Ni}_{(100-x)}/\text{Al}_2\text{O}_3$  system
  - Preliminary results obtained on the two universal suscepter systems ( $\text{Co}/\text{Al}_2\text{O}_3$  and  $\text{FeCr}/\text{Al}_2\text{O}_3$ )
  - Paper IV on the optimal size of cobalt nanoparticles ( $\text{Co}/\text{Al}_2\text{O}_3$ ) to maximize hysteresis losses as a function of temperature and applied magnetic field
  - Paper V on the design of a new in situ sample holder for high-temperature VSM studies with controlled gas atmospheres (tested on  $\text{Co}/\text{Al}_2\text{O}_3$ )
- **Chapter 4:** This chapter is devoted to a summation and discussion of the results obtained in during this project, as well as my perspective on what could be done in the project going forward.

# Chapter 2

## Magnetometry

### 2.1 Vibrating sample magnetometry

Vibrating sample magnetometry (VSM) has been used throughout this project to characterize the magnetic properties of various susceptor-materials. This was done in order to explain and predict performance of the susceptors when running induction-heated SMR.

Two magnetometers have been used throughout this project: a Lake Shore 7407 model VSM[42], and a Lake Shore 7404-S model VSM[43], modified with an in situ system (see Paper V). A sketch of a typical vibrating sample magnetometer (also abbreviated VSM) can be seen in Fig. 2.2. A sample sits centered in the gap of an electromagnet. The sample holder, in the case of conventional high temperature VSM, is a quartz tail (a long quartz rod that can be attached via a screw to the head drive of the VSM) with a boron-nitride cup screwed on at the end. This can handle prolonged exposure to temperatures ranging from room temperature (RT) to 1000 °C[44]. The electromagnet exposes the sample to a homogeneous magnetic field (dashed lines in Fig. 2.2a), which can reach a maximum of 1.5 T for the 7404-S model[43], and around 2 T for the Lake Shore 7407 model[42], when performing VSM with the oven mounted (not shown in the figure). All high temperature VSM measurements were performed with a Lake Shore 74034 oven option, which allowed us to study the magnetic properties of materials at temperatures ranging from RT to 950 °C.

In order to measure the magnetic moment of the sample, four pickup coils are placed symmetrically around the centre of the pole-pieces (coloured orange in Fig. 2.2). The sample is saddled to the geometric center of the coils between the pole-pieces, and vibrates vertically at 80 Hz. The vibration leads to a time-varying magnetic flux through the pickup-coils (see Fig. 2.2(b)), which induces a AC voltage

in the coils with an amplitude that is proportional to the magnetization of the sample. The four coils are hooked up in such a way that the two top coils (A and B) have the same polarity, while the two bottom coils (C and D) have the reverse polarity:  $S = (S_A + S_B) - (S_C + S_D)$ , with S being signal, and the subscripts being each of the pick-up coils. This four-coil configuration[45] quadruples the output signal, and is insensitive to the applied field from the electromagnet. The signal is then amplified via a lock-in amplifier, which is commonly used to pick out a specific oscillating signal from noise. Briefly, this amplifier mixes the signal from the pickup-coils with a reference signal of the same frequency. This mixing amplifies signals with the same frequency and phase, while signals of other frequencies (the noise) remains un-amplified. The signal is then passed through a low-pass filter, which filters out noise. The VSM is calibrated by a reference sample to convert from the induced voltage to magnetic moment. The reference sample of choice is usually nickel[46].

## 2.2 High temperature oven option

Both the Lake Shore 7404 VSM and The Lake Shore 7407 VSM is equipped with a Lake Shore 74034 oven option when performing high temperature measurements. A sketch of the oven can be seen in Fig. 2.1, along with the quartz sample holder. The oven option can be used to perform magnetic measurements at temperatures between RT and up to 1000 °C, but has not been operated over 950 °C in this project, in order to extend the oven lifetime. The sample sits in the heating zone of the oven, approx. 30 cm from the top of the oven. The oven is made of two tubes, and the space in between these is evacuated by a pump, and the vacuum functions as thermal insulation. In order to protect the sample and the inside of the oven from oxidation, Lake Shore recommends a flow of argon of around 100  $\frac{\text{mL}}{\text{min}}$  is fed to the spout in Fig. 2.1. In order to reduce our samples, we have used a flow of 2.4 vol.% H<sub>2</sub> in Ar fed to the oven option, which is not what Lake Shore recommends. The argon should pull the hydrogen down around the sample cup inside of the oven, and diffuse into the BN cup and reduce the sample. This way of reducing the sample is less than ideal, which is one of the reasons for the invention of the retrofittable in situ holder in Paper V. When measuring with the in situ holder, argon is fed to the oven option.

## 2.3 Sample holders

Two sample-holder systems have been used to contain samples for VSM: the conventional boron-nitride (BN) cup from Lake Shore[44], used in most of the studies (Paper I-II, Sections 3.1-3.5), and a novel in situ sample holder made of quartz tubes. These two systems are compared in Paper V (Section 3.6).

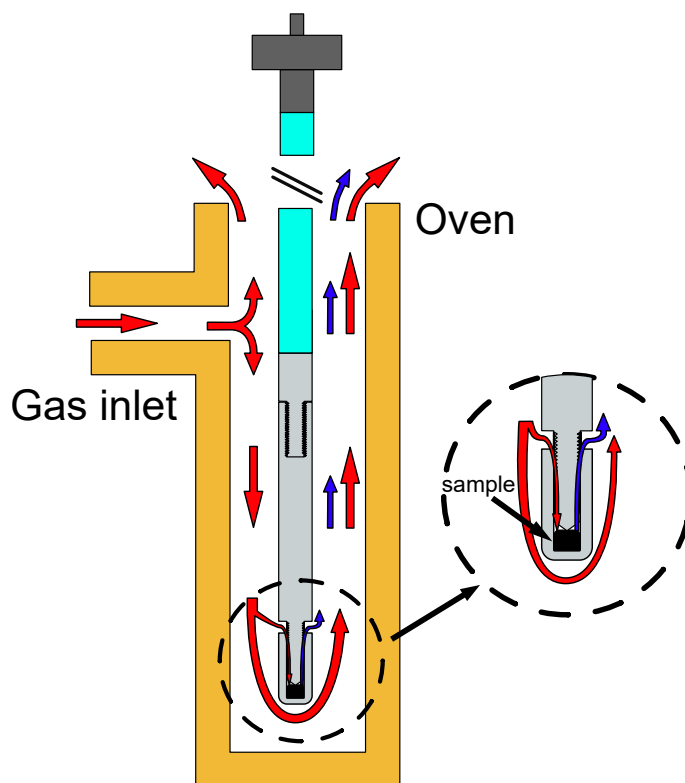


**Figure 2.1:** Sketch of the Lake Shore 74034 oven option. Red arrows represent inlet gas (Ar or 2.4 vol.% H<sub>2</sub> in Ar). Blue arrows represents gas that has diffused out of the BN sample holder. The oven option is open in the top, as seen in the figure.

#### **Boron-nitride sample cup:**

A sketch of the BN sample cup used for high temperature measurements can be seen in Fig. 2.3a. Samples measured in disposable BN cups are loaded as follows. The BN cup is weighed several times on an Ohaus PA224C balance (with a precision of 0.1 mg), and the average was calculated. Sample powder is deposited in the BN cup, and then weighed multiple times. To find mass of the sample, the average mass of the BN cup without sample is subtracted from the average mass of the BN cup with sample. Afterwards, the sample cup is opened and closed in an argon-filled bag, in order to expel as much air from the cup as possible. The BN cup is then screwed onto a quartz sample tail while still in the Ar filled bag, and transferred from the Ar bag directly to the oven option on the VSM with as little time spent in air as possible, and connected to the head drive of the VSM. The "sample tail" is a long rod of quartz, which is threaded in one end, and has a screw in the other. This screw then fits into the head drive of the VSM, which facilitates the vibration of the sample. Prior to the sample being put into the oven, a flow of around 100  $\frac{\text{mL}}{\text{min}}$

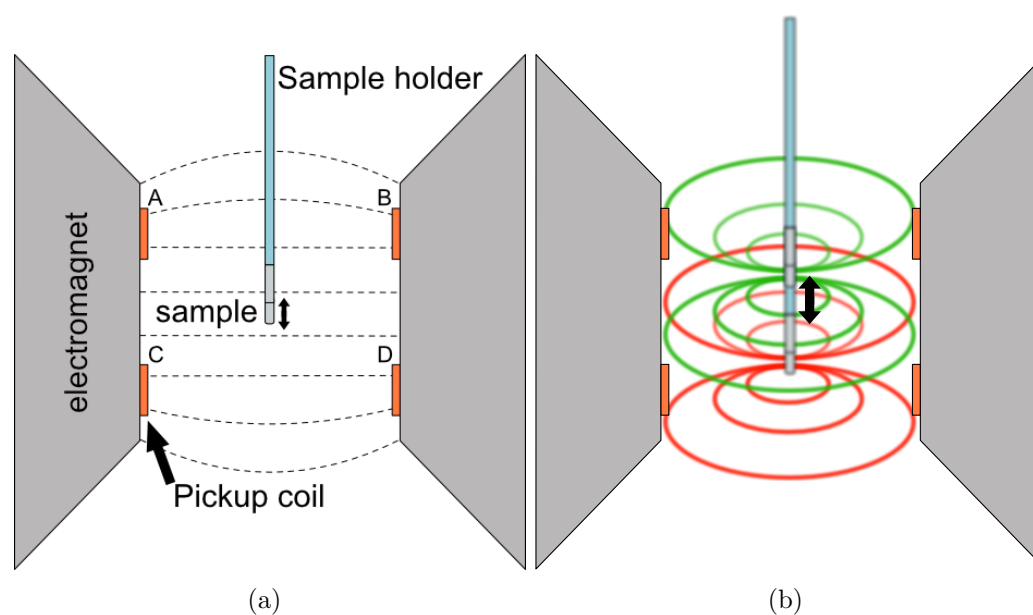


**Figure 2.2:** a) A sketch of a VSM. Electromagnet (grey) produces a homogeneous magnetic field (dashed) in the area of the sample. Pickup coils (orange) measures the change in magnetic flux. b) Sketch of how the vibration of the sample changes the magnetic flux in the pickup coils, which induces a voltage proportional to the magnetization of the sample.

of 2.4 vol.%  $H_2$  in Ar is connected to the oven-option for at least 5 min. When the sample is mounted in the oven option on the VSM, it is then saddled, and ready to be measured.

#### Quartz based in situ holder:

The prototype in situ holder developed during this project is described in Paper V (Section 3.6). This section outlines the loading-procedure of the inner quartz-tube, with more details on the holder available in Section 3.6.

The disposable inner quartz-tube is roughly 350 mm long with an inner diameter of 2 mm, as seen in Fig. 2.3b. The tube has two indents approximately 1 cm from the end of the tube to act as a shelf for the quartz wool to sit on. All of the loading of the tube was performed in a fume hood. A thin 400 mm long steel rod is used to load the quartz tube with Insulfrax LT quartz wool from Unifrax[47]. This wool is stamped thoroughly before the sample powder is poured into the tube. As powder tend to stick to the side of the tube, it is tapped against the table surface. When all of the powder has settled on top of the quartz wool, another layer of wool is stamped down on top of the sample to secure it in place. The in situ holder is then assembled inside a fume-hood, and transported to the VSM to be saddled and measured. In



the VSM it is then connected to a gas-supply (separate from the supply of gas to the oven option), so the sample can be exposed to varying gas-mixtures of Ar, H<sub>2</sub> and synthetic air, while being measured (see Paper V).

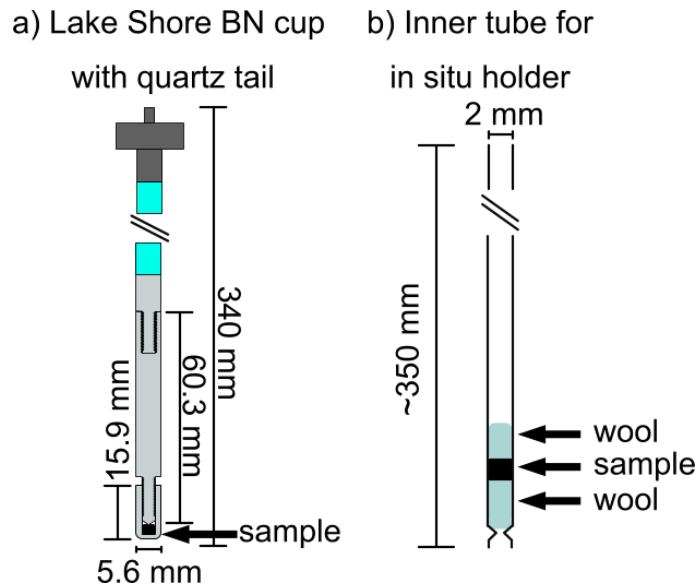


**Figure 2.3:** a) Quartz sample tail with a cross-section and dimensions of a disposable BN sample cup from Lake Shore, loaded with sample. b) sketch of the dimensions and loading of the disposable inner quartz tube in the in situ VSM holder.

## 2.4 Magnetic measurements

In this section, the types of magnetic measurements relevant to this project will be presented, and the theory behind them outlined. As magnetic properties are a complex interplay of temperature, particle size and shape, material parameters, etc., the theoretical introduction will be limited to general concepts that are relevant to the magnetic investigations in sections 3.1 to 3.6. Throughout this project we have used the *mass specific magnetization*,  $\sigma$ . Unless otherwise stated, all mentions of magnetization will refer to the mass specific magnetization.

### Curie temperature measurements:

The Curie temperature ( $T_C$ ) is the temperature at which the material loses its ferro/ferri-magnetic properties, and transitions to being paramagnetic. This can be seen schematically represented in Fig. 2.4, where a uniformly magnetized ferro-magnetic single-domain (SD) particle has ordered moments pointing in the same

direction at  $T < T_C$ , resulting in a net magnetization,  $\bar{\sigma}$ . Above  $T_C$ , the direction of the magnetic moments are fluctuating randomly, showing no net magnetization without an applied magnetic field. Applying an external magnetic field to the sample above  $T_C$  will induce a weak magnetization linearly proportional to the applied field, and inversely proportional to temperature.

$T_C$  can be estimated experimentally using what in this project we called a *Curie temperature curve*, or simply a  $T_C$  curve. In this, the mass-specific magnetization,  $\sigma$  in  $\left[\frac{\text{Am}^2}{\text{kg}}\right]$ , is measured in an applied magnetic field of 10 mT as a function of temperature for heating, or cooling, between 200 °C and 950 °C. Two examples of  $T_C$  curves can be seen in Fig. 2.5 for  $\text{Co}_{50}\text{Ni}_{50}/\text{Al}_2\text{O}_3$  (black curve), and a mixture of FeCr- $\text{Al}_2\text{O}_3$  and nickel/Mg $\text{Al}_2\text{O}_3$  (blue curve). The figure shows how, when alloyed with Ni, the  $T_C$  of cobalt is lowered from the bulk value of 1121 °C[23], to  $\sim 850$  °C. In the case of samples with multiple magnetic materials, the  $T_C$  would show several steps along the curve, at  $T_C$ 's characteristic for each magnetic material. This can be seen for the blue curve in Fig. 2.5, where the  $T_C$ 's for nickel (358 °C[23]) and iron (770 °C[23]) can be seen in the curve. The steps in the curve between those temperatures would then represent different FeCr-alloys. In this way, the  $T_C$  can be used to help determine which magnetic materials are in a sample. As the focus of this project is to use magnetic heating for high-temperature catalysis, steam-reforming in particular,  $T_C$  is very important. For steam reforming at 1 bar and a steam-carbon ratio of 1, around 800 °C is needed to reach 90% conversion of the methane[8], and even higher temperatures are needed at higher pressures. This is why only cobalt, and cobalt-containing alloys, have been studied for use in magnetically heated SMR in this project, as cobalt is the only element with a  $T_C$  high enough to be magnetic at these temperatures.

### Hysteresis measurements:

Further magnetic characterisation was performed by recording hysteresis loops at different  $B_{\text{app}}$ 's (the maximal applied magnetic field amplitude in the hysteresis loops) and temperatures. In a hysteresis loop, the sample is cycled through a magnetic field,  $B$ , from  $+B_{\text{app}}$  to  $-B_{\text{app}}$ , and back to  $+B_{\text{app}}$ , while the magnetization of the sample is measured. A sketch of a hysteresis loop can be seen in Fig. 2.6.

As the applied magnetic field increases, the measured magnetization will taper off (see Fig. 2.6). When an increase in applied magnetic field no longer induces a change in magnetization the *saturation magnetization*,  $\sigma_S$ , has been reached. The saturation magnetization is a characteristic property of a pure magnetic material. In some cases this can be used to estimate the amount of magnetic material in a sample. An example of this can be seen in Section 3.5, where  $\sigma_S$  is used to estimate if samples of cobalt nanoparticles impregnated on an alumina support had been fully reduced. When  $B$  is lowered from  $B_{\text{app}}$  to zero applied field, some magnetic ma-

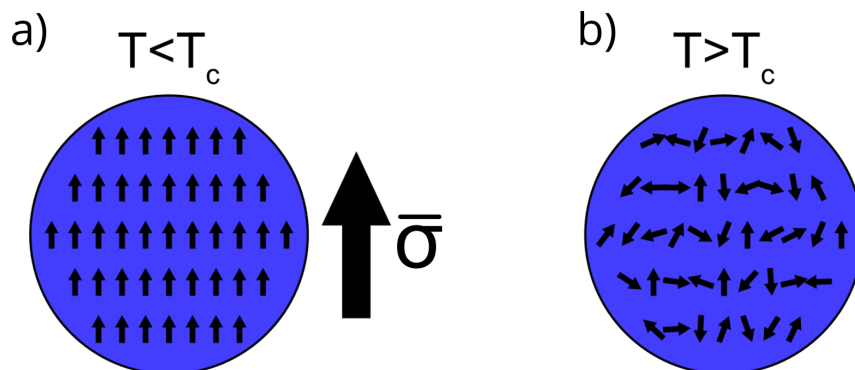


**Figure 2.4:** Sketch of a single domain particle transition from ferromagnetic to paramagnetic when passing through  $T_C$ . a) ferromagnetic SD magnetic particle under  $T_C$  with a magnetization,  $\bar{M}$ . b) the same particle at a temperature above  $T_C$  with no net magnetization.

materials retain a certain amount of magnetization, which is defined as the *remanent magnetization*,  $\sigma_R$ . The field needed to revert the magnetization of the sample to zero is called the *coercive field*,  $\mu_0 H_C$ . Both of these parameters are shown in the hysteresis loop in Fig. 2.6. The area spanned by the loop is called the *hysteresis area*, and is denoted as  $W_h$  (see Fig. 2.6).  $W_h$  is the energy lost as heat, in  $\frac{J}{kg}$ , in the material, after cycling through the loop once. Maximizing  $W_h$  at relevant temperatures and  $B_{app}$ 's was an essential aspect of this project.

These parameters,  $\sigma_R$ ,  $\sigma_S$ ,  $\mu_0 H_C$ , and  $W_h$ , are complex functions of particle size, crystal structure, temperature, and composition[48, 51, 23, 40]. In this project, the aspect of particle size has been a central point of investigation. The particle size of the samples investigated during this project have ranged from approx. 10 nm to 10  $\mu m$ . The size of the particle has a large effect on the macroscopic magnetic properties of the material when working in this size range. The effect of particle size on  $\mu_0 H_C$  can be seen in the schematic in Fig. 2.7 adapted from similar figures in Kneller and Luborsky[48], Lee et al.[49], and Li et al.[50], for the effect of particle size on the coercive field. Here it can be seen how  $\mu_0 H_C$  is zero for a superparamagnetic particle, grows to a maximum in the range of non-superparamagnetic magnetic single domain particles, and decays again when transitioning to magnetic multidomain particles. As  $\mu_0 H_C$  is half the width of a hysteresis loop,  $W_h$  is proportional to  $\mu_0 H_C$ , and the same trend is expected to apply to  $W_h$ . We investigated this for a range of particle sizes for a set of  $B_{app}$ 's and temperatures in order to estimate the most optimal size-range for Co nanoparticles for high temperature magnetic heating, which can be seen in Paper IV, Section 3.5.

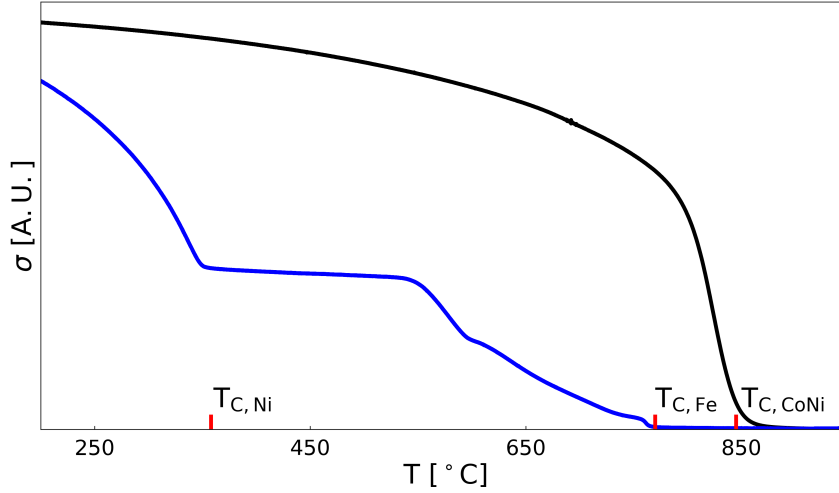


**Figure 2.5:**  $T_C$  curves for FeCr-Al<sub>2</sub>O<sub>3</sub> and nickel on a MgAl<sub>2</sub>O<sub>4</sub>-spinel (blue, see Sec. 3.4) and Co<sub>50</sub>Ni<sub>50</sub> (black, see Paper III, Sec. 3.3). The  $T_C$ 's for nickel, iron, and Co<sub>50</sub>Ni<sub>50</sub> are annotated in red on the T-axis.

As the particle size decreases, the MNP will at some point enter the *superparamagnetic* regime (see Fig. 2.7). When a MNP is superparamagnetic (SPM), the anisotropy energy of the particle is low enough that the thermal energy causes the magnetization of the particle to randomly flip direction on a shorter timescale than the measuring time. This means that the particle does not show a spontaneous magnetisation without an applied magnetic field. An applied magnetic field can then tend to align the magnetization of SPM particles. This behaviour of the is similar to that of paramagnetism of atomic moments, hence the name *superparamagnetism*. Superparamagnetism depends on both the temperature, the size of the particle, and on the measuring time. When a material becomes superparamagnetic on the timescale of a VSM measurement the hysteresis loop collapses, and will show no  $\sigma_R$ , no  $\mu_0 H_C$ , and by extension, no  $W_h$ .

For particles above the critical diameter (dashed line in Fig. 2.7) it is energetically favourable to form domains. The reversal of magnetization in the hysteresis loop would then be facilitated by domain wall movement and domain wall nucleation, which lowers the coercive field in the sample (see Fig. 2.7)[52], and by extension, the hysteresis area. Just before the particles form multiple domains, the coercive field and the hysteresis area will reach a maximum. In the simplified case of a SD particle of uniaxial anisotropy the energy cost associated with flipping the magnetization, scales with the volume of the particle[53]. Therefore, the hysteresis area will continue to grow until multiple magnetic domains start forming. As we are aiming to maximize the heating properties of the material, it is desirable to stay at the top

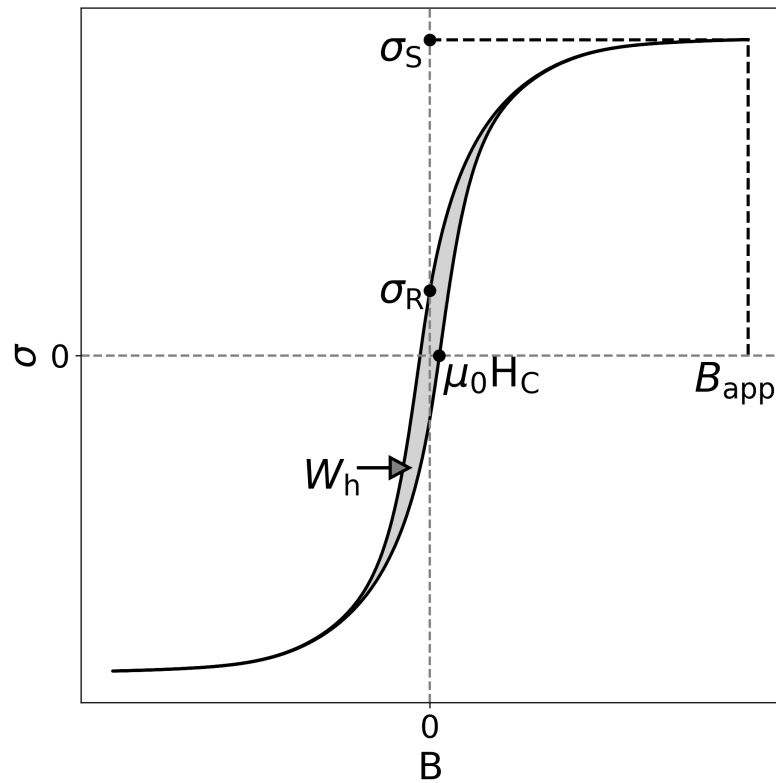


**Figure 2.6:** Overview of the parameters extracted from the hysteresis loop: hysteresis area,  $W_h$ , remanent mass-specific magnetization,  $\sigma_R$ , coercive field,  $\mu_0 H_C$ , and for sufficiently large  $B_{app}$ 's, the mass-specific saturation magnetization,  $\sigma_S$ .

of this curve (see Fig. 2.7) when utilising hysteresis heating to supply heat to a reaction.

### The experimental profile

In this project the term *experimental profile* means a series of measurements of the sample magnetization in the VSM at different temperatures and applied fields. Various experimental profiles have been used throughout this project, and they all had some common aspects. These can be seen in Fig. 2.8. An experimental profile would typically start with a measurement hysteresis loops at 200 °C, which served two purposes. The first of which was, that leaving the sample a 200 °C for a few hours would evaporate any moisture present in the sample, which would hopefully diffuse out of the BN cup or the quartz tube (see Section 2.3), as water vapour can facilitate sintering of the particles[54]. The second reason was to have a set of hysteresis loops which could be compared with later measurements to be able to track any changes in magnetic properties during the course of the measurements.

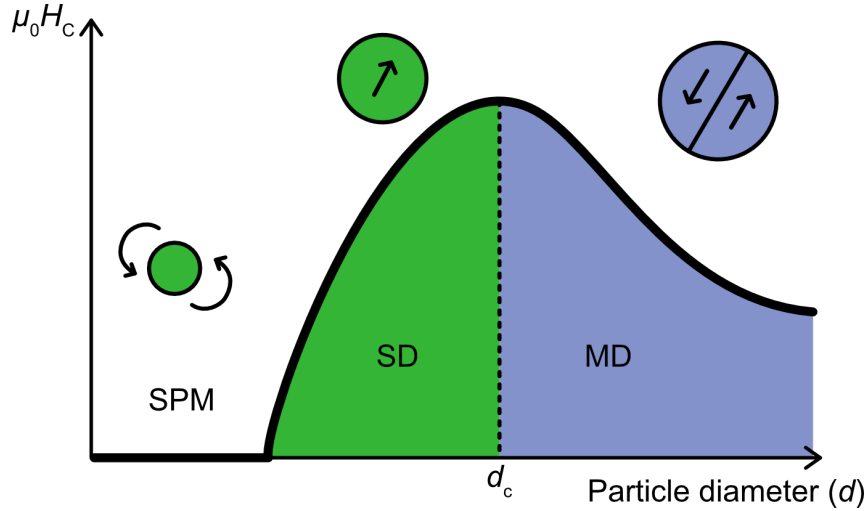


**Figure 2.7:** Sketch of the coercive field ( $\mu_0 H_C$ ) as a function of particle size ( $d$ ), with superparamagnetic (SPM) range, non-superparamagnetic single domain (SD) range, and (magnetic) multi-domain (MD) range annotated. Sketch inspired by figures in Kneller and Luborsky[48], Lee et al.[49], and Li et al.[50].

For samples such as  $\text{Co}_x\text{Ni}_{(100-x)}/\text{Al}_2\text{O}_3$ -system (Paper I-III, Sec. 3.1-3.3), and the Co nanoparticles (Section 3.5), an extra step was added to reduce the samples. In this step, the magnetization of the sample was measured in 1 T for 12 hours at high temperatures (see Fig. 2.8), 800 °C in the case of the  $\text{Co}_x\text{Ni}_{(100-x)}/\text{Al}_2\text{O}_3$ -system in Paper III, and 850 °C in the case of Co nanoparticles on alumina support in Paper V.

After the reduction step, the sample was heated to 950 °C, and a  $T_C$  measurement was performed from 950 °C to 200 °C. The following measurements were what we defined as a *run* (see Fig. 2.8): measurements of hysteresis loops were made from 200 °C to 950 °C in steps of 50 °C, followed by a  $T_C$  measurement. The hysteresis loops were measured at a  $B_{\text{app}}$  from 5 mT to 55 mT in steps of 5 mT, as well as at  $B_{\text{app}} = 100, 500, \text{ and } 1500 \text{ mT}$ . The 1500 mT measurement was performed mainly to capture the properties of the materials at saturation, while the steps from 5 to 55 mT was the range of applied fields most often used in the induction heated reformer (see Paper I-III, Sec. 3.1-3.3). The steps at 100 and 500 mT were made to get an idea about the approach to saturation. Some samples were prone to change during the first run, especially when using BN sample cups. We did not observe significant changes between runs after the second run. Therefore, the amount of runs for most samples were limited to 2.

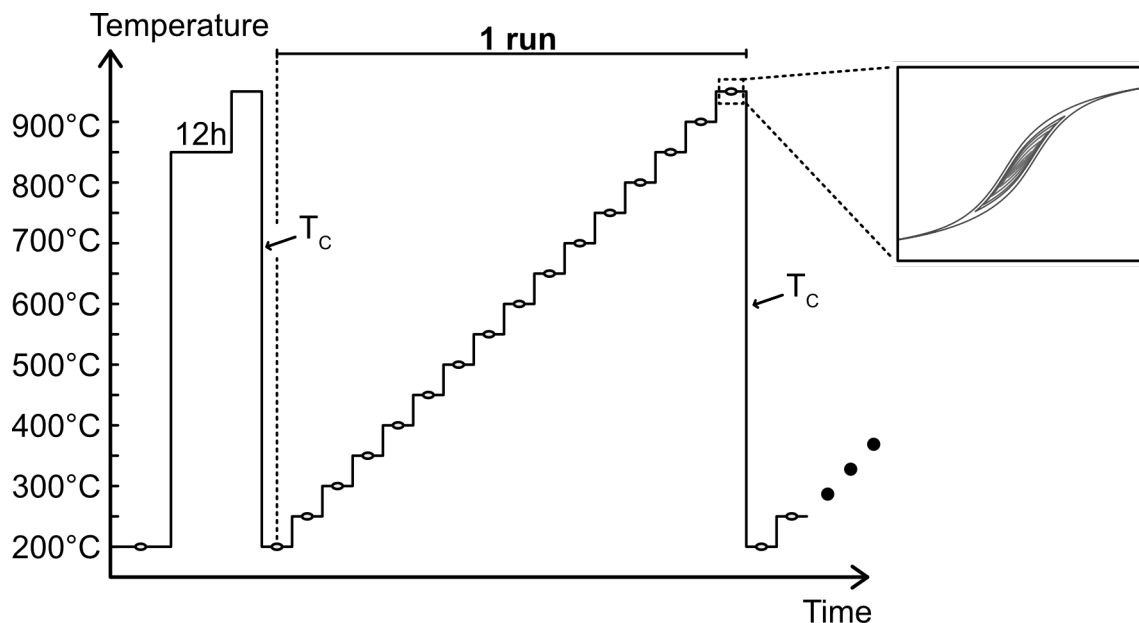


**Figure 2.8:** Diagram of the typical components of an experimental profile. Hollow ellipses represent measurements at the given temperature of a set of hysteresis loops with  $B_{\text{app}}$  ranging from 5 mT to 55 mT, as well as at 100, 500, and 1500 mT.  $T_C$  indicates where Curie temperature measurements are made.

## 2.5 Data treatment

A short overview of the data treatment of the VSM data treatment is given here. A more in-depth description of the data treatment, and the scripts used for this, is given in the appendix, Sec. A.1. In the scripts, the hysteresis loops at each temperature-step of the experimental profile in Fig. 2.8 are loaded in to a data-structure, and sorted according to its placement in the profile, its temperature, and its  $B_{\text{app}}$ . Then each hysteresis loop is analysed, and the properties seen in Fig. 2.6 are collected:  $W_h$ ,  $\sigma_R$ ,  $\mu_0 H_C$ , and  $\sigma_S$  (the latter only for hysteresis loops with  $B_{\text{app}} = 1500$  mT). The remanent magnetization is obtained by finding the data-points closest to the positive and negative y-axis and averaging:  $\frac{+\sigma_R - (-\sigma_R)}{2}$ .  $\mu_0 H_C$  is computed similarly with the datapoints closest to the x-axis. For the 1500 mT hysteresis loops  $\sigma_S$  is found by finding the maximum and minimum of the hysteresis loops and averaging.  $W_h$  is found by integration of the hysteresis loop.

$T_C$  was found by Grommé’s two tangent method[55], and a detailed explanation of the exact procedure used to estimate  $T_C$  can be found in the supporting information of Paper II. In this paper, a possible systemic error in  $T_C$  of up to 10 °C was estimated.





# Chapter 3

## Papers and results

### 3.1 Paper I: Dual-function cobalt-nickel nanoparticles tailored for high temperature induction-heated steam methane reforming

In this paper we present the synthesis of a dual-function CoNi nanoparticle system tailored for induction heated SMR. By the use of TEM techniques, we determined that the synthesis produced CoNi nanoparticles of uniform size (approx. 40 nm in diameter) and well-defined alloy composition of the NPs of  $52.9 \pm 5.8$  % cobalt. The synthesized  $\text{Co}_{50}\text{Ni}_{50}/\text{Al}_2\text{O}_3$  samples with a Co+Ni loading of 32.5 wt.% showed a hysteresis-area of approx.  $0.1 \frac{\text{J}}{\text{kg}}$  at 700 °C and  $B_{\text{app}} = 25$  mT, and a Curie temperature of approx. 890 °C. It was shown that the material could be heated to above 800 °C in reaction conditions using only induction heating with a methane to hydrogen conversion of close to 100 %. The activities were comparable to that of the Ni reference catalyst, and the system was stable in reaction conditions for >300 hours with no apparent loss in conversion of methane. The system proved not to be limited by heat transfer to the catalyst, as is the case for externally fired reactors, but by reaction kinetics. Further tuning of the catalytic properties of the particles was possible through doping with metals (e.g. Cu) in the synthesis.

This work demonstrates that the heat transfer limitation in conventional fired reactors can be circumvented by using induction heating. Furthermore, this synthesis method can be tuned to include almost whatever active metal needed for a reaction, and is therefore not limited to steam reforming.

*Published in: Angewandte Chemie in 2018, DOI: <https://doi.org/10.1002/anie.201804832>*

**Heterogeneous Catalysis**

Deutsche Ausgabe: DOI: 10.1002/ange.201804832

Internationale Ausgabe: DOI: 10.1002/anie.201804832

# Dual-Function Cobalt–Nickel Nanoparticles Tailored for High-Temperature Induction-Heated Steam Methane Reforming

Morten G. Vinum,\* Mads R. Almind, Jakob S. Engbæk, Søren B. Vendelbo, Mikkel F. Hansen, Cathrine Frandsen, Jesper Bendix,\* and Peter M. Mortensen\*

**Abstract:** The tailored chemical synthesis of binary and ternary alloy nanoparticles with a uniform elemental composition is presented. Their dual use as magnetic susceptors for induction heating and catalytic agent for steam reforming of methane to produce hydrogen at temperatures near and above 800 °C is demonstrated. The heating and catalytic performance of two chemically synthesized samples of **CoNi** and **Cu<sub>2</sub>CoNi** are compared and held against a traditional Ni-based reforming catalyst. The structural, magnetic, and catalytic properties of the samples were characterized by X-ray diffraction, elemental analysis, magnetometry, and reactivity measurements. For induction-heated catalysts, the conversion rate of methane is limited by chemical reactivity, as opposed to the case of traditional externally heated reformers where heat transport limitations are the limiting factor. Catalyst production by the synthetic route allows controlled doping with minuscule concentrations of auxiliary metals.

**D**irect heating of magnetic nanoparticles (NPs) by magnetic induction, including using magnetic hysteresis heating, holds many potential advantages over conventional heating as it allows for a vast number of new approaches to otherwise difficult tasks. The most prominent of these are drug release,<sup>[1,2]</sup> control of single-cell functions,<sup>[3]</sup> and disease treatment by hyperthermia.<sup>[4,5]</sup> While a collective feature of all these applications is the aim towards medical use, only few examples exist of industrial applications of magnetically heated NPs.<sup>[6]</sup> Herein, we present the preparation and

implementation of a novel nanostructured material for hydrogen production via endothermic steam reforming of methane (SMR) using solely induction heating as energy source.<sup>[7]</sup>

Hydrogen is by far the most produced chemical worldwide on a molar basis.<sup>[8]</sup> To accommodate an ever-growing demand, efforts have been made to generate hydrogen from biofuels, electrolysis, wind, solar, and nuclear energy. The most affordable and efficient way to generate hydrogen is still various forms of steam reforming of hydrocarbons from fossil fuels.<sup>[9]</sup> The SMR takes place according to Equations (1) and (2):



This overall endothermic reaction presents a challenge as it is only thermodynamically favored at temperatures approaching 700 °C at ambient conditions, and even higher temperatures of 950 °C are needed in industry owing to the high operational pressures used.<sup>[10]</sup>

A typical SMR plant for production of hydrogen generally consists of a pre-reformer followed by a tubular reformer, a shift converter, and final product purification (typically done by pressure swing adsorption (PSA)) in combination with expensive heat-exchange coils to minimize heat loss.<sup>[11]</sup> A long-standing challenge in hydrogen production has been the excessive heating needed in the reforming section of the current design, which, due to costly waste-heat sections, favors large-scale plants to achieve a feasible reforming economy. Usually, energy delivered to the reactor bed from the fired section is only around 50%, the rest is recovered in the flue gas.<sup>[10,12]</sup> This however dictates, that a significant amount of energy is spent outside of the actual reaction chamber. Additionally, the start-up time of such plants is often on the order of a few days to ensure controlled heating of the large tubes with minimum risk of tube rupture. In stark contrast, induction heating provides rapid and efficient heating of ferromagnetic materials, and potentially the heat can be delivered directly in the catalyst, if such a magnetic catalyst can be realized. This requires special radiofrequency transparent reactors to avoid shielding effects between the catalyst and the induction coil. In a future hydrogen economy, we therefore envision induction-heated reforming as a small-scale hydrogen production technology with a fast start-up for ad hoc on-site supply of hydrogen.

Previously, induction heating of ferromagnetic Fe-based NPs was utilized in a liquid phase organic synthesis flow


[\*] M. G. Vinum, Dr. P. M. Mortensen  
Haldor Topsøe A/S  
Nymøllevej 55, 2800 Kgs. Lyngby (Denmark)  
E-mail: morten.vinum@chem.ku.dk  
pmor@topsoe.com

M. G. Vinum, Prof. Dr. J. Bendix  
Department of Chemistry, University of Copenhagen  
2100 Copenhagen (Denmark)  
E-mail: bendix@kiku.dk

M. R. Almind, Prof. Dr. C. Frandsen  
DTU Physics, Technical University of Denmark  
2800 Kgs. Lyngby (Denmark)

Dr. J. S. Engbæk, Dr. S. B. Vendelbo  
Danish Technological Institute  
2630 Taastrup (Denmark)

Dr. M. F. Hansen  
DTU Nanotech, Technical University of Denmark  
2800 Kgs. Lyngby (Denmark)

 Supporting information and the ORCID identification number(s) for the author(s) of this article can be found under:  
<https://doi.org/10.1002/anie.201804832>

reactor in a series of pioneering studies,<sup>[13–15]</sup> although the NPs were only used for heating and did not supply a catalytic function. Others have later made research into magnetic zeolites and related systems, where NiFe-based particles may also play a catalytic role.<sup>[16,17]</sup> More recently, others reported iron-based core–shell NPs doped with precious metals as candidates for induction heated heterogeneous catalysis.<sup>[18,19]</sup> However, in case of SMR with reaction temperatures around 800 °C, iron with a Curie temperature,  $T_C$ , of 770 °C is not suitable as magnetic susceptor. The only element with a higher  $T_C$  than iron is cobalt ( $T_C = 1115$  °C)<sup>[20]</sup> and hence for induction heated SMR, the magnetic susceptor must be based on Co and alloys thereof.

Oxidation of Co readily takes place at the high temperatures and partial pressures of water relevant to the SMR process, and a significant challenge is to avoid oxidation of Co as this leads to the formation of antiferro- and paramagnetic phases.<sup>[21,22]</sup> Alloying with Ni provides a dual solution to this as Ni is an excellent catalyst for endothermic SMR, and Ni stabilizes the Co phase against oxidation while maintaining activities similar to that of pure Ni.<sup>[22]</sup> Recently, we had some success with this idea in a proof-of-concept showing that it was indeed possible to heat such alloyed NPs to temperatures approaching the desired range, and to produce hydrogen at these elevated temperatures. However, owing to the serendipity of sequential impregnation used in the previous study, control over the microscopic metal distribution had to be renounced, evidenced by the large differences found in alloy compositions in that study, leaving only a small fraction with high  $T_C$  and a very small hysteresis opening (see below) accessible for the purpose of heating.<sup>[23–25]</sup>

Herein, to take control at the molecular level, we conceptually changed the approach to catalyst manufacture, by preparing both active NPs and inert carrier by a chemical synthesis route, with the aim of producing more stable and uniform NPs, accessible in the desired temperature regime. Forming the catalyst precursor in solution and then precipitating it by addition of base, guaranteed the homogeneity of the material. Subsequently, the material was reduced, hereby directly producing catalytic nanoparticles within a porous non-active carrier material. To benchmark the activity of the formed catalyst, we also synthesized a traditional Ni catalyst on  $\text{MgAl}_2\text{O}_4$  support by the same route with a loading of 15 wt % Ni (**1**) as a reference, to mimic commercially available reforming catalyst,<sup>[10]</sup> denoted **Ni-ref** (Supporting Information, Table S1, Figure S1).

The synthetic procedure (see the Supporting Information and Figure S2 therein) uniformly gave a homogeneous compound, which could be tuned to accommodate a vast range of metals at different ratios. The initial precipitate was shown by XRD to consist of a spinel-type phase of  $\text{M}_y\text{Co}_{(1-x-y)}\text{Ni}_{(x-y)}\text{Al}_2\text{O}_4$  (where  $\text{M} = \text{Cr, Mn, Fe, Cu}$  as shown in the Supporting Information, Table S1, Figure S3). Here, we chose to focus on just two chemically synthesized samples, one un-doped sample with  $x = 0.5$  (**2a**) hereafter **CoNi**, and a Cu-doped sample with  $x = 0.5$  and  $y = 0.01$  (**2b**) hereafter **CuCoNi** (Table 1). Following reduction of both samples in hydrogen, peaks originating from *fcc*-Co/Ni (Supporting Information, Figures S4 and S5) were identified

**Table 1:** Selected properties of samples **1**, **2a**, and **2b**.

Sample (Name)	Composition	Activity <sup>[a]</sup> [ $\text{mol g}^{-1} \text{h}^{-1}$ ]	$T_C$ [°C]	Ni-TOF <sup>[a]</sup> [ $\text{s}^{-1}$ ]
<b>1 (Ni-ref)</b>	15.0 wt% Ni/ $\text{MgAl}_2\text{O}_4$	0.440	355 <sup>[b]</sup>	0.584
<b>2a (CoNi)</b>	$\text{Co}_{0.5}\text{Ni}_{0.5}\text{Al}_2\text{O}_3$	0.184	892 <sup>[b]</sup>	0.435
<b>2b (CuCoNi)</b>	0.36 wt% Cu/ $\text{CuCoNi}$	0.244	875 <sup>[b]</sup>	0.535

[a] Measured at 450 °C. [b] Estimated via the two-tangent method applied to the magnetic moment vs. temperature plots (see the Supporting Information and Figure S10 therein).

able in the XRD patterns of both **CoNi** and **CuCoNi** indicating the formation of metallic NPs, as well as  $\gamma\text{-Al}_2\text{O}_3$  (both cubic and tetragonal phases) by the degradation of the original spinel structure. No evidence of non-reduced starting material was found in the final samples.

120 kV scanning transmission electron microscopy (STEM) high-angle annular dark field (HAADF) images were used in combination with electron dispersive X-ray spectroscopy (EDS) to map and evaluate the nature and composition of the NPs of **CoNi** and **CuCoNi** formed on the surface of the alumina support by the reduction process (Figure 1). From this, an average length/width of ca. 44/ca. 36 nm and ca. 54/ca. 43 nm, were evaluated for **CoNi** and **CuCoNi**, respectively (Supporting Information, Figure S6).

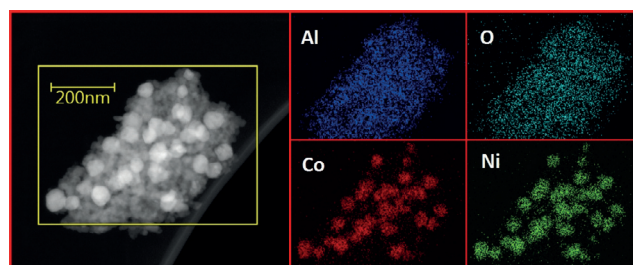


**Figure 1.** Left: STEM-HAADF image of a freshly prepared sample of **CoNi**. Right: Elemental mapping of Al (purple), O (teal), Co (red), and Ni (green) using EDS analysis of the same sample. Co wt % determined by EDS analysis for **CoNi** is presented in Figure 2.

These results are consistent with the crystallite sizes of 20–30 nm estimated from XRD analysis using the Scherrer equation, considering the uncertainties associated with this (Supporting Information, Table S1, see the Supporting Information for further comments).

The EDS analysis revealed an even distribution of Ni and Co throughout the nanoparticles (more than 40 NPs were individually addressed per sample) with an average Co content of each NP of 52.9 wt % ( $\pm 5.8$  wt %) in sample **CoNi** (Figure 2) and 52.9 wt % ( $\pm 3.0$  wt %) in sample **CuCoNi** (Supporting Information, Figures S7–S9), close to the stoichiometric ratio defined by the synthetic route.

Measurements using a traditional externally heated setup dedicated for steam reforming activity measurements revealed a steam reforming activity for **CoNi** of 40 % of that for **Ni-ref**. Chemically tuning the activity with miniscule dopings of Cu (**CuCoNi**) increased the performance significantly to reach 55 %. In terms of turn over frequency (TOF)

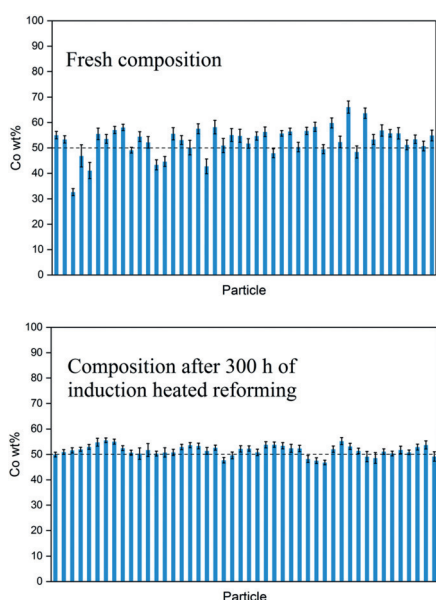


**Figure 2.** Top: Weight percentage of Co throughout individual NPs in **CoNi**. Bottom: Composition of the same sample after a 300 h induction heated steam reforming experiment (see Figure 6). The dashed line at 50 wt% represents the nominal composition.

per exposed metal site (taking the size and metal distribution into account), the TOFs of **CoNi** and **Cu<CoNi** were found to 75% and 91% of that of **Ni-ref**, respectively (Table 1). The observation that miniscule doping with Cu promotes activity of Ni catalysts in SMR concurs with previous results<sup>[26]</sup> and additional results obtained by traditional activity measurements (Supporting Information, Table S1). Any possible support related effects on the activity was not studied herein.

The magnetic moment of **CoNi** and **Cu<CoNi** was measured versus temperature in a small applied magnetic field of 10 mT to determine the effective Curie temperature of the samples as well as to check for the presence of multiple magnetic phases (Figure 3). At temperatures below 800 °C, the nanomaterial acted as a ferromagnet with a slow decrease of the magnetic moment upon heating. Above this temper-

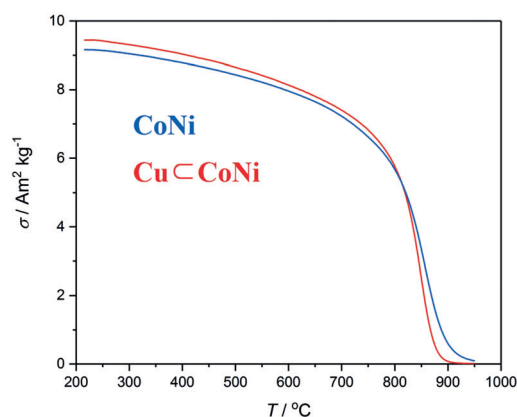


**Figure 3.** Magnetic moment versus temperature of **CoNi** and **Cu<CoNi**. The sample was measured in an applied magnetic field of  $B_{\text{app}} = 10$  mT at temperatures decreasing from 950 °C to 200 °C at 5 °C min<sup>-1</sup>. Apparent solid lines are actual data points.

ature, the moment decreased more rapidly and reached a value close to zero at the maximum measurement temperature of 950 °C. Effective Curie temperatures for **CoNi** and **Cu<CoNi** were determined to  $T_C = 892$  °C and 875 °C, respectively (see the Supporting Information). The single rapid decrease in moment around 850 °C or 825 °C indicates a homogenous material with a narrow alloy composition in both samples in agreement with EDS results. The smaller  $T_C$  for **Cu<CoNi** relative to **CoNi** despite similar composition in EDS may be due to the small content of nonmagnetic Cu which was not evaluated by EDS.

Moreover, hysteresis measurements of **CoNi** and **Cu<CoNi** in maximum applied magnetic fields  $B_{\text{max}}$  ranging from 5 mT to 55 mT were conducted isothermally between temperatures of 200 °C and 950 °C in increments of 50 °C (Supporting Information, Figures S11–S14). The area of the hysteresis loop is defined as:

$$W_{\text{H}} = \oint_{B_{\text{max}}} \sigma(B_{\text{app}}) dB_{\text{app}} \quad (3)$$

where  $\sigma$  [ $\text{Am}^2 \text{kg}^{-1}$ ] is the specific magnetization (magnetic moment per sample mass), indicates the heat generated per cycle in units of  $\text{J kg}^{-1}$  upon cycling the applied magnetic field between  $+B_{\text{max}}$  to  $-B_{\text{max}}$  and back (Figure 4). From the measurements conducted on **CoNi**, it is clear that  $W_{\text{H}}$  is still appreciably different from zero at temperatures above 800 °C at moderate values of  $B_{\text{max}}$ . This suggests the possibility of using magnetic hysteresis heating at and above this temperature.

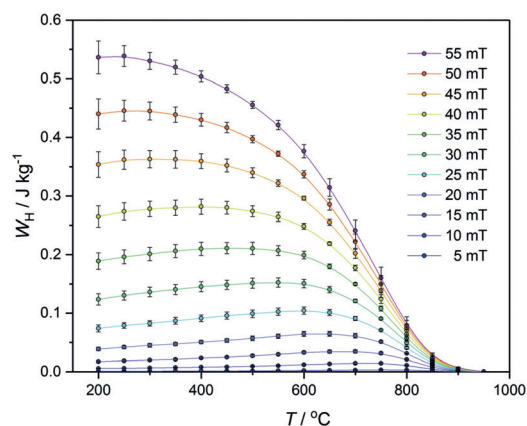


**Figure 4.** Field dependence of hysteresis heating per loop cycle for **CoNi** obtained from hysteresis measurements performed at temperatures between 200 °C and 950 °C at the indicated values of  $B_{\text{max}}$ . Error bars represent standard deviations calculated for four consecutive runs. Solid lines are guides to the eyes.

Identical measurements on **Cu<CoNi** reveal a similar hysteretic behavior, which is not surprising given the similar magnetization curves (Supporting Information, Figures S15, S16). A reactor setup dedicated for induction-heated SMR was designed and used for the testing of these catalysts under operating conditions (see the Supporting Information). A reactor made of quartz was implemented to avoid any



magnetic shielding effects. Based on the composition of the outlet gas, the SMR equilibrium temperature, energy transfer, and conversion of feed was calculated. For both **CoNi** and **CuCoNi**, the calculated energy transfer to the process gas was around 3–20 W g<sup>-1</sup>, (averaged over a sample mass of 10 g) as estimated from the change in enthalpy, depending on the flow-rate of reactants however, the actual transfer to the reactor may be higher owing to heat losses associated with the reactor insulation. In all measurements, a frequency of 69 kHz and field amplitudes of up to 42 mT was used. For simplicity, only flow rates of 51 and 152 Nl h<sup>-1</sup> are shown in Figure 5 (for a full view, see the Supporting Information, Figures S17 and S18).

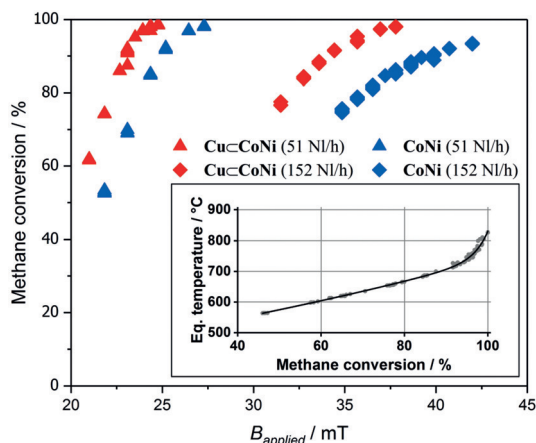


**Figure 5.** Influence of methane-flow on the conversion of CH<sub>4</sub> in the steam reforming reaction for a gas mixture treated over **CoNi** (blue) and **CuCoNi** (red) as a function of applied magnetic field. Inset: steam reforming equilibrium temperature as function of methane conversion at the experimental conditions. Inlet temperature ca. 200 °C, S/C ≈ 2, P ≈ 0 bar gauge. Gas composition is as explained in the text and the Supporting Information.

Traditionally, the limiting factor on the reaction rate in industrial type externally heated reformer tubes is not the catalyst activity but the heat transfer to the catalyst.<sup>[19]</sup> This means that effectively only 10%, or less, of the catalyst activity is utilized, the rest being lost owing to transport restrictions of the heat flux in the reactor bed.<sup>[27]</sup>

Interestingly, the data for **CoNi** and **CuCoNi** showed the CH<sub>4</sub> conversion increasing with magnetic field until a certain point where the increase in field is accompanied only by a small increase in H<sub>2</sub>. For certain gas flows, this maximum is reached at full conversion (equilibrium). The curvature observed on approaching equilibrium is caused by the catalyst operating at the kinetic limit, that is, the catalyst is limited by reaction kinetics and not by the heat transfer (Figure 5). This is an important observation, as it is in stark contrast to the externally fired case. Additionally, owing to the improved activity of **CuCoNi**, 95% conversion of methane to hydrogen was realized using roughly 15% smaller applied magnetic fields as compared to **CoNi** for flows of 152 Nl h<sup>-1</sup>.

The robustness of **CoNi** was evaluated in a prolonged experiment with a constant flow-rate of 101 Nl h<sup>-1</sup> with a feed

gas mixture of 29.7% CH<sub>4</sub>, 59.5% H<sub>2</sub>O, and 10.8% H<sub>2</sub> (mol%), an input temperature of 237 °C, at close to atmospheric pressure, under an applied magnetic field of about 32 mT and a frequency of 69 kHz. Under these conditions, the conversion of methane was 90–95%, corresponding to an equilibrium temperature of 715 °C. In the time frame of the experiment, which was more than 300 h, no significant decrease of the activity was observed as evidenced by the constant value of the methane conversion (Figure 6, red data

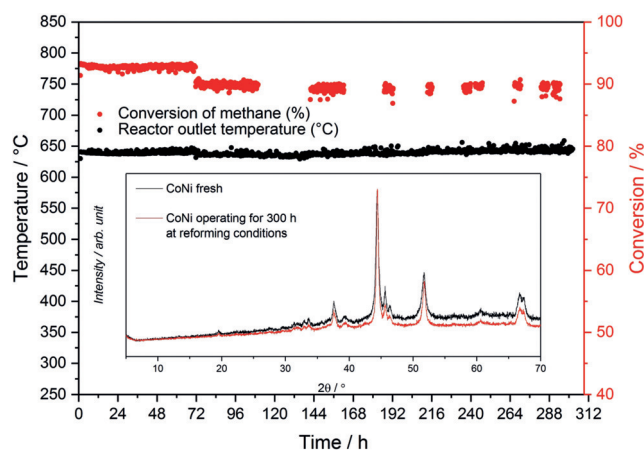


**Figure 6.** Overview of prolonged reforming experiment on **CoNi** using the induction-heated setup discussed in the text. No loss of activity is seen within the time frame of the experiment. The bump observed at  $t = 72$  h is due to instrumental instabilities (see text). Inset: the XRD diffractogram before and after the experiment. For a larger view, see the Supporting Information, Figure S19.

points). The recorded time interval (ca. 14 days) is clearly much shorter than a typical reactor lifetime (years), but on the other hand, it is the time interval where most changes to the catalyst would be expected to occur. The drop observed in CH<sub>4</sub> conversion at 72 h is a result of water contamination of the gas chromatograph (GC) caused by a short power outage and does not represent an actual loss of catalyst performance. To avoid further damage, GC measurements after this point were performed in steps, roughly 24 h apart. The reactor outlet temperature was measured constantly throughout the experiment (black data points) using a Type-K thermocouple as described in the Supporting Information. Subsequently, the catalyst was unloaded and checked for changes in composition by XRD, ICP and STEM (Figure 2; Supporting Information, Figures S19–S21). All of these results underline the remarkable stability of the NP material, as no structural changes were found in addition to no carbon formation and no change of the Co wt% ratio, which was practically unchanged at 51.8 wt% ( $\pm 2.0$  wt%; Figure 2).

In summary, the preparation of a new chemically tailored nanostructured system was presented and its use in induction heated SMR was demonstrated. The chemical synthesis of metallic NPs allowed for the controlled production of a sample with a uniform and predictable Ni-Co alloy composition. Compared to previous ideas,<sup>[25]</sup> the realization of well-defined NPs through chemical synthesis led to an

increase in both hysteresis opening and steam reforming catalytic activity, presumably caused by a larger fraction of the NPs being ferromagnetic at the elevated reaction temperature. As a result, a marked increase was found in the efficiency of the NPs in terms of energy conversion under induction-heated steam reforming using only a magnetic field generated from electrical current as a power source.

With similar or even slightly inferior magnetic properties, **CuCoNi** demonstrated significantly improved reforming properties compared to **CoNi**, opening up for the possibility of producing even better catalysts by engineering the reactivity, as this is presently the limiting factor. Finally, we show the stability of chemically synthesized NPs to be excellent, and essentially inert to degradation in the first 300 h of operating at reforming conditions. Examining the CH<sub>4</sub> conversion under such conditions revealed that kinetic effects alone and not thermodynamics hampered the catalyst, opposed to the case of externally fired SMR, highlighting the excellent heat transfer from the induction field to the magnetic susceptor and active catalyst.

Combining chemically robust NPs with induction-heated catalysis may prove useful for many other industrial reactions, as the NPs can be modified to contain whatever active metal may be needed, and the operating temperature controlled by adjusting the applied field.

The implementation of induction heating in SMR may eliminate expensive waste-heat sections used in traditional methane reforming setups, significantly reducing the complexity of the process design and has the potential to drastically lower CO<sub>2</sub> emissions from the process.<sup>[28]</sup> This, together with the possibility of fast plant startup, holds promise for these materials as competitors for classical hydrogen plants or as part of ammonia plants in a future hydrogen economy and especially for ad hoc small-scale demands.

## Acknowledgements

This work was partly funded by The University of Copenhagen, Haldor Topsøe A/S, the CoNeXT project and Innovation Fund Denmark (IFD) under File No. 5160-00004B. A PCT patent has been approved based on the results obtained.

## Conflict of interest

The authors declare no conflict of interest.

**Keywords:** heterogeneous catalysis · hysteresis · induction heating · nanoparticles · steam reforming

**How to cite:** *Angew. Chem. Int. Ed.* **2018**, *57*, 10569–10573  
*Angew. Chem.* **2018**, *130*, 10729–10733

- [1] M. S. Yavuz, Y. Cheng, J. Chen, C. M. Cobley, Q. Zhang, M. Rycenga, J. Xie, C. Kim, K. H. Song, A. G. Schwartz, et al., *Nat. Mater.* **2009**, *8*, 935–939.

- [2] B. P. Timko, K. Whitehead, W. Gao, D. S. Kohane, O. Farokhzad, D. Anderson, R. Langer, *Annu. Rev. Mater. Res.* **2011**, *41*, 3.1–3.20.
- [3] H. Huang, S. Delikanli, H. Zeng, D. M. Ferkey, A. Pralle, *Nat. Nanotechnol.* **2010**, *5*, 602–606.
- [4] N. W. Shi Kam, M. O'Connell, J. A. Wisdom, H. Dai, *Proc. Natl. Acad. Sci. USA* **2005**, *102*, 11600–11605.
- [5] P. Cherukuri, E. S. Glazer, S. A. Curley, *Adv. Drug Delivery Rev.* **2010**, *62*, 339–345.
- [6] M. N. Pérez-Camacho, J. Abu-Dahrieh, D. Rooney, K. Sun, *Catal. Today* **2015**, *242*, 129–138.
- [7] “Ferromagnetic Materials for Induction Heated Catalysis”: M. G. Vinum, P. M. Mortensen, PCT: WO 2017/186608 A1, **2017**.
- [8] M. McCoy, M. Reisch, A. H. Tullo, P. L. Short, J.-F. Tremblay, W. J. Storck, *Chem. Eng. News* **2005**, *83*, 67–76.
- [9] A. T-Raissi, D. L. Block, *IEEE Power Energy Mag.* **2004**, *2*, 40–45.
- [10] J. R. Rostrup-Nielsen, J. Sehested, J. K. Nørskov, *Adv. Catal.* **2002**, *47*, 65–139.
- [11] N. R. Udengaard, *Prepr. Pap. Am. Chem. Soc. Div. Fuel Chem.* **2004**, *49*, 906–907.
- [12] J. R. Rostrup-Nielsen, L. J. Christiansen, *Concepts in Syngas Manufacture*, Imperial College Press, London, **2011**.
- [13] S. Ceylan, C. Friese, C. Lammel, K. Mazac, A. Kirschning, *Angew. Chem. Int. Ed.* **2008**, *47*, 8950–8953; *Angew. Chem.* **2008**, *120*, 9083–9086.
- [14] J. Wegner, S. Ceylan, C. Friese, A. Kirschning, *Eur. J. Org. Chem.* **2010**, 4372–4375.
- [15] S. Ceylan, L. Coutable, J. Wegner, A. Kirschning, *Chem. Eur. J.* **2011**, *17*, 1884–1893.
- [16] J. García-Aguilar, J. Fernández-García, E. V. Rebrov, M. R. Lees, P. Gao, D. Cazorla-Amorós, Á. Berenguer-Murcia, *Chem. Commun.* **2017**, *53*, 4262–4265.
- [17] Y. Liu, N. Cherkasov, P. Gao, J. Fernández, M. R. Lees, E. V. Rebrov, *J. Catal.* **2017**, *355*, 120–130.
- [18] A. Meffre, B. Mehdaoui, V. Connord, J. Carrey, P. F. Fazzini, S. Lachaize, M. Respaud, B. Chaudret, *Nano Lett.* **2015**, *15*, 3241–3248.
- [19] A. Bordet, L. M. Lacroix, P. F. Fazzini, J. Carrey, K. Soulantica, B. Chaudret, *Angew. Chem. Int. Ed.* **2016**, *55*, 15894–15898; *Angew. Chem.* **2016**, *128*, 16126–16130.
- [20] J. M. Leger, C. Loriers-Susse, B. Vodar, *Phys. Rev. B* **1972**, *6*, 4250–4261.
- [21] I. Barin, *Thermochemical Data of Pure Substances*, VCH, Weinheim, **1989**.
- [22] J. R. Rostrup-Nielsen in *Catalysis—Science and Technology* (Eds.: J. R. Anderson, M. Boudart), Springer, Berlin, **1984**.
- [23] C. Perego, P. Villa, *Catal. Today* **1997**, *34*, 281–305.
- [24] J. A. Schwarz, C. Contescu, A. Contescu, *Chem. Rev.* **1995**, *95*, 477–510.
- [25] P. M. Mortensen, J. S. Engbæk, S. B. Vendelbo, M. F. Hansen, M. Østberg, *Ind. Eng. Chem. Res.* **2017**, *56*, 14006–14013.
- [26] J. Barcicki, A. Denis, W. Grzegorzczak, D. Nazimek, T. Borowiecki, *React. Kinet. Catal. Lett.* **1976**, *5*, 471–478.
- [27] K. Aasberg-Petersen, J. H. Bak Hansen, T. S. Christensen, I. Dybkjaer, P. S. Christensen, C. S. Nielsen, S. E. L. W. Madsen, J. R. Rostrup-Nielsen, *Appl. Catal. A* **2001**, *221*, 379–387.
- [28] N. Muradov, F. Smith, C. Huang, A. T-Raissi, *Catal. Today* **2006**, *116*, 281–288.

Manuscript received: April 26, 2018

Revised manuscript received: May 25, 2018

Accepted manuscript online: June 19, 2018

Version of record online: July 13, 2018

## 3.2 Paper II: Improving performance of induction-heated steam methane reforming

In this paper, we studied how to improve the performance of induction heated SMR, and how the energy efficiency scales when extrapolating to industrial conditions. To do this, we used a  $\text{Co}_{50}\text{Ni}_{50}/\text{Al}_2\text{O}_3$ -system prepared through the synthesis-method from Paper I, and investigated how to improve induction heated SMR by changing the applied frequency and AC coil geometry on a bench-scale induction heated SMR reactor. By increasing the frequency from 68 kHz to 201 kHz, and using a narrower coil, we increased the maximum energy transfer efficiency from 11% to 23%. Based on a simple theoretical framework to estimate the energy-losses in the system, we were able to qualitatively explain the changes in energy-losses when changing frequency and coil geometry. Through this framework, most of the power losses were found to originate in the AC coil, and the in the surrounding electronics, such as the power supply. Using this framework, we performed a simple volumetric scaling to industrially relevant conditions, predicting an increase in energy transfer efficiency to > 80 %. Through the volumetric scaling, we also found that when only considering energy requirements, the system could be competitive with commercially available electrolyzers.

*Published in: Catalysis in 2019, DOI: <https://doi.org/10.1016/j.cattod.2019.05.005>*



## Improving performance of induction-heated steam methane reforming

Mads Radmer Almind<sup>a</sup>, Søren Bastholm Vendelbo<sup>b</sup>, Mikkel Fougth Hansen<sup>c</sup>,  
Morten Gotthold Vinum<sup>d,e</sup>, Cathrine Frandsen<sup>a</sup>, Peter Mølgaard Mortensen<sup>e,\*</sup>,  
Jakob Soland Engbæk<sup>b,\*</sup>

<sup>a</sup> Department of Physics, Technical University of Denmark, Fysikvej, Building 307, DK-2800, Kongens Lyngby, Denmark

<sup>b</sup> Danish Technological Institute, Gregersensvej 1, DK-2630, Taastrup, Denmark

<sup>c</sup> Department of Health Technology, Technical University of Denmark, Ørsted Plads, Building 345C, DK-2800, Kongens Lyngby, Denmark

<sup>d</sup> Department of Chemistry, Copenhagen University, Universitetsparken 5, DK-2100, Copenhagen, Denmark

<sup>e</sup> Haldor Topsøe A/S, Haldor Topsøes Allé 1, DK-2800, Kongens Lyngby, Denmark



### ARTICLE INFO

#### Keywords:

Catalysis  
Electric heating  
Ferromagnetism  
Hysteresis  
Induction  
Steam reforming

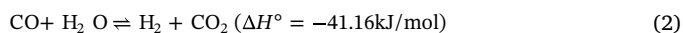
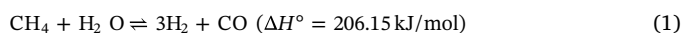
### ABSTRACT

Induction heating may be an electrical solution for heating of catalytic reactors. Recent studies have shown that CoNi nanoparticles may act as both inductors for hysteresis heating and catalyst, such that they in an alternating magnetic field are able to drive the strongly endothermic steam methane reforming reaction with > 90% gas conversion at temperatures of  $\approx 800$  °C. However, lab-scale induction-heated reactors are limited by low energy transfer efficiency and previous work did not optimize the surrounding instrumentation. Here, we focused on the optimization of an induction setup for steam methane reforming. The performance of the reactor system was investigated through experiments at varying alternating magnetic field conditions, to evaluate the effect of frequency and coil geometry. The results from these experiments were modelled by a simple theoretical framework. Increasing the frequency of the alternating magnetic field from 68 kHz to 189 kHz was found to increase the energy transfer efficiency. Moreover, the energy transfer efficiency also increased when going from a short and wide coil with height to radius ratio of 3.8 to a long and narrow coil with height to radius ratio of 10.8. Overall, the energy transfer efficiency was increased from an initial 11% in the bench scale reactor setup, to 23% in the optimized version. Moreover, combining the bench scale results with the theoretical framework we extrapolated the data to large-scale systems. The analysis indicated that the energy efficiency of induction-heated steam reforming systems scaled to larger H<sub>2</sub> capacities may be above 80%. This efficiency would allow the technology to be competitive with other electricity driven routes to hydrogen production when considering only the energy requirements.

### 1. Introduction

Today, a range of methods exists for delivering energy to endothermic chemical catalytic reactions. One such is pre-heating coupled with an adiabatic reactor, where the reactant is heated prior to entering the reactor and the temperature decreases towards the thermodynamic equilibrium temperature of the given reaction in the catalyst bed [1]. Other methods include heat-exchanging technologies, where a hot fluid is in heat exchange contact with the reaction zone of a reactor to provide energy for the reaction [2,3]. For strongly endothermic processes requiring high reaction temperatures, fired reactors are a preferred solution. In this case, burners are used to heat up the catalytic reactor to the desired reaction temperature. These are used extensively for steam methane reforming [4].

Almost half of the world's hydrogen demand is produced through the steam methane reforming reaction [5], where a mix of steam and methane is converted into carbon monoxide and hydrogen by Reaction (1) [4,6,7]. This is accompanied by the reverse water gas shift in Reaction (2) [4,6,7]:



Typically, industrial steam methane reforming reactors operate around 25 bar, which requires temperatures of 800–950 °C to obtain sufficient conversion of the natural gas feedstock. In industrial reactors, this heating is typically done in a tubular reformer configuration, which includes the reformer furnace, and a waste-heat section, in addition to

\* Corresponding authors.

E-mail addresses: [pmor@topsøe.com](mailto:pmor@topsøe.com) (P.M. Mortensen), [jae@teknologisk.dk](mailto:jae@teknologisk.dk) (J.S. Engbæk).

<https://doi.org/10.1016/j.cattod.2019.05.005>

Received 22 September 2018; Received in revised form 22 April 2019; Accepted 2 May 2019

Available online 08 May 2019

0920-5861/ © 2019 Elsevier B.V. All rights reserved.



several reformer tubes placed centrally in the furnace [4]. These tubes are usually 100–200 mm in diameter, and 10–13 m long. This geometry is used to optimize the heat transfer from the reformer burners [4]. However, only around 50% of the heat supplied by the reformer burners is transferred to the reforming reaction in the catalyst bed, the rest of the heat is recovered in the waste-heat section and used for pre-heating and steam production [4]. As a consequence, the technology relies on economy of scale to make tubular reformers energy efficient [4]. Additionally, in order to allow for controlled material expansion, the reformer tubes are heated slowly to the reaction temperature, and hence start-up times are long, often on the order of days.

Induction heating offers an alternative route to supply energy to the steam methane reforming reaction that may solve some of the challenges of tubular reformers. Induction-heated steam methane reforming will require a coil outside the catalyst bed, while an inductor material (a magnetic material) is incorporated into the reactor [8]. When passing an alternating current through the coil, it generates an alternating magnetic field, which enables local heating of the catalytic material inside the reformer, either by magnetic hysteresis heating (dominating in nanoparticles) [9] or by resistive heating due to eddy currents (dominating in macroscopic conducting materials), and efficient heat transfer to the reaction zone is possible. The direct heating would allow for high reaction rates in the catalyst material, and by extension, more compact reformer plants. Induction heating could also have the added benefit of lowering the start-up time, as induction heating, in general, provides a fast and more homogeneous heating response [10,11]. Lowering start-up times would also make the induction-heated steam methane reformers more flexible, allowing for on demand production of hydrogen.

Induction heating (by hysteresis) of nanoparticles has been studied extensively as a way to treat cancer (magnetic hyperthermia) [12], but efforts were also made to do hysteresis heated catalysis [9]. Previously, induction (hysteresis) heating of magnetic particles in chemical reactors was pioneered by Ceylan et al. [13] on liquid organic chemical synthesis using modifiable silica-coated iron oxide particles as the heatable media. Chatterjee et al. [14] applied induction heating for fast and isothermal heating of a micro-reactor to 80–100 °C, using nickel-ferrite material as susceptor, and Bordet et al. [15] demonstrated induction heating for continuous CO<sub>2</sub> hydrogenation using iron carbide nanoparticles.

Within this topic, our group has demonstrated steam methane reforming on CoNi nanoparticles [16,17], which are both catalytically active for induction-heated steam methane reforming and can be heated to above 800 °C using only induction heating. In this configuration it is desirable to maximize the hysteresis heating of the nanoparticles, while also ensuring high catalytic activity, which must be secured in the synthesis of the catalyst [17]. The previous work showed that the direct delivery of heat to the active site lead to efficient transfer of energy to the chemical reaction [17]. Consequently, the catalyst activity was identified as the limiting factor in the reaction test [17]. In contrast, industrial scale tubular reformers are typically limited by heat transfer rates [4].

To utilize induction heating for industrial scale steam methane reforming, it is important to address the energy required to make an alternating magnetic field, which is yet unaddressed, but the topic of this article. We focus on optimizing the performance of induction-heated steam methane reforming by manipulating two key parameters: the frequency of the alternating magnetic field in the coil and the coil geometry. We also establish a simple theoretical framework to explain general trends in the performance as a function of these parameters, with the aim of using the framework to study the prospective performance of induction-heated steam methane reforming at larger scale.

## 2. Material and experimental methods

The catalytic material used for this study consisted of CoNi

nanoparticles on a porous samarium aluminium oxide support (CoNi/Sm<sub>2</sub>O<sub>3</sub>-Al<sub>2</sub>O<sub>3</sub>). The nanoparticles of this system act both as catalyst for steam methane reforming (due to the Ni) and as susceptor for magnetic hysteresis heating (due to the ferromagnetic properties of the metallic CoNi nanoparticles). The sample was synthesized as described by Vinum et al. [17], and then reduced in H<sub>2</sub> at 850 °C for 4 h, followed by passivation in 1% O<sub>2</sub> in N<sub>2</sub> at 25 °C. Inductively coupled plasma mass spectroscopy (ICP-MS) analysis showed a sample composition of 29.5 wt% Al, 15.6 wt% Co, 15.5 wt% Ni, and 8.15 wt% Sm, and x-ray diffraction showed dispersed CoNi particles of ≈ 24 nm in size on the Sm<sub>2</sub>O<sub>3</sub>-Al<sub>2</sub>O<sub>3</sub> support. Samarium was intentionally included in the synthesis of the catalyst to increase the hysteresis heating of the CoNi particles [18], but analysis of the sample showed that during the synthesis Sm had oxidized and migrated to the support, leaving behind practically un-doped CoNi nanoparticles on an oxide support. Still, the catalyst was found suitable for induction-heated steam methane reforming and offered a good model system for the current investigation. The system described here is very similar to the one described by Vinum et al. [17]. This study saw no loss of activity for > 300 h of the ca. 50 nm CoNi nanoparticles in a similar setup as the one used in this paper, and under similar conditions.

The catalytic activity of the sample during induction heating was measured by an induction-heated steam methane reforming continuous plug flow bench scale laboratory setup (similar to the one used in Refs. [16] and [17]). In this setup, the sample was placed in a quartz reactor tube, concentrically surrounded by insulation material and an induction coil, as sketched in Fig. 1. The quartz tube had an inner radius,  $r_1$ , of 6.5 mm and a length of 1 m. For the reactor experiments, 11 g of the CoNi/Sm<sub>2</sub>O<sub>3</sub>-Al<sub>2</sub>O<sub>3</sub> sample was loaded in the quartz tube with quartz wool situated above and below the sample. This gave a loading height of the sample of  $h_s = 9.5$  cm and an average sample loading density of 0.87 g/cm<sup>3</sup>.

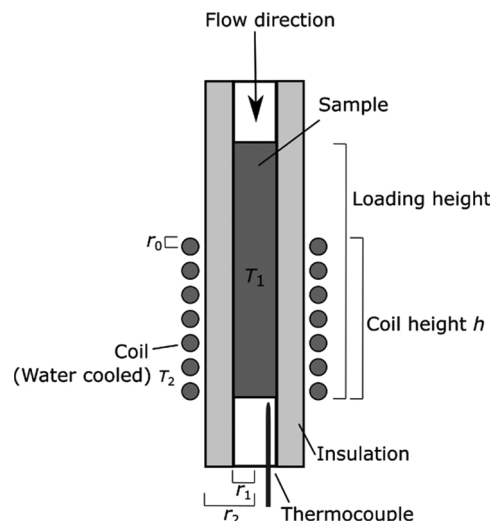


Fig. 1. Cross-sectional sketch of the reactor setup with sample, insulation and coil.

In all experiments, the sample was placed in the same relative position in the reactor and only coil dimensions (height  $h$ , and inner radius  $r_2$ ), insulation type, and frequency ( $f$ ) of the alternating magnetic field were changed. Two types of insulation were tested: Promat Promasil 1000 L (cut to shape) and Promat FreeFlow (pellets) [19,20]. Water-cooled copper coils with three different dimensions (see Table 1) were used to provide the alternating magnetic field. When the short coils ( $h = 6.0$  cm,  $h = 7.5$  cm) were used, the bottom of the coil was aligned with the bottom of the sample as illustrated in Fig. 1, whereas for the long coil ( $h = 13.5$  cm) the sample was at the centre of the coil.

**Table 1**  
Geometric specifications for the three different copper coils.

Coil	Number of windings ( <i>N</i> )	Inner radius ( <i>r</i> <sub>2</sub> ) [mm]	Height ( <i>h</i> ) [cm]	Length of copper tubing ( <i>L</i> ) [m]
Wide, short	9	20	7.5	1.23
Narrow, short	7	12.5	6.0	0.64
Narrow, long	17	12.5	13.5	1.18

Here it should be mentioned that only the susceptor material placed inside the coil was expected to contribute heating the reaction. This was supported by COMSOL simulations of this system (see SI). The inlet cooling water temperature of the coils was kept at 15 °C. An UPT-S2 Ultraflex power supply was used to provide a high current with amplitude (*I*<sub>0</sub>) and frequency *f* to the coils, where *f* is the resonance frequency set by the power supply (by choice of capacitance) and by the coil (by its geometry-dependent inductance). The measurements were made at a low frequency of 68 kHz for the short wide coil and at a high frequency of 189–201 kHz for the three coils with different geometries. The power consumption (*P*<sub>in</sub>) of the power supply was measured by an ABB EQ series Energy meter.

Prior to running steam reforming in the setup, the passivated sample was reduced in 50% H<sub>2</sub> in N<sub>2</sub> while inductively heated to 400 °C. Afterwards, the sample was heated further by induction to the reaction temperature, after which hydrogen, steam, and methane were fed to the reactor.

Methane and hydrogen, grade 3.5 and 5.0, respectively, were fed to the reactor using SLA850 type Brooks digital flow controllers (with an estimated uncertainty on the gas flows of ± 2%). Vaporized demineralized water was provided to the reactor using a Knauer smartline HPLC pump (with an estimated uncertainty of ± 3%), and tubing to the catalytic reactor was heat traced to above 110 °C when running experiments. An Armstrong 11 LD drain trap was used to remove water from the output gas and the dry gas was analysed by gas chromatograph of type GC-TDC/FID in an Agilent 7890B system.

In order to quantify Curie temperature and the hysteresis area of the CoNi/Sm<sub>2</sub>O<sub>3</sub>-Al<sub>2</sub>O<sub>3</sub> sample at elevated temperatures, a portion of the catalyst sample was analysed in a LakeShore 7407 vibrating sample magnetometer (VSM) equipped with a LakeShore 74034 oven option. For this, a boron nitride holder with a screw-on cap was loaded with 35.72 mg of CoNi/Sm<sub>2</sub>O<sub>3</sub>-Al<sub>2</sub>O<sub>3</sub> sample in an argon atmosphere. The VSM measurements were carried out under a volumetric flow of about 150 ml/min of 2.4 mol% H<sub>2</sub> in Ar. Hysteresis measurements of the sample moment versus applied field were obtained for field amplitudes between ± *B*<sub>max</sub>, where *B*<sub>max</sub> ranged from 5 mT to 55 mT in steps of 5 mT, at temperatures from 200 °C to 950 °C in steps of 50 °C. Curie-temperature was determined from measurements of sample moment in an applied field of 10 mT versus decreasing temperature (900–200 °C at 5 °C/min, see SI).

### 3. Modelling

The power losses in the induction-heated reactor system can be modelled as

$$P_{in} = P_{reaction} + P_{coil} + P_{iso} + P_{rest} \quad (3)$$

where *P*<sub>in</sub> is the power delivered to the power supply and equals the total power loss in the system. The power loss *P*<sub>reaction</sub> is the power consumed by the steam reforming reaction (Eqs. (1) and (2)) and the heating of the gas to the required temperature, *P*<sub>coil</sub> is the loss due to resistive heating of the copper coil, *P*<sub>iso</sub> is the energy loss through the insulation, and *P*<sub>rest</sub> is any remaining losses, e.g. in the power supply, cords and components, not studied directly in this article.

The energy transfer efficiency of the system, *η*, is defined as the energy transfer to the gas, *P*<sub>reaction</sub>, relative to the power received by the

system as a whole, *P*<sub>in</sub>, i.e.,

$$\eta = \frac{P_{reaction}}{P_{in}} \quad (4)$$

#### 3.1. Reaction thermodynamics

In order to calculate *P*<sub>reaction</sub> from the experimental data, the conversion of methane was calculated from the carbon balance as

$$X = \frac{y_{CO} + y_{CO_2}}{y_{CO} + y_{CO_2} + y_{CH_4}} \quad (5)$$

where *y*<sub>*i*</sub> is the molar fraction of the *i*'th compound in the dry product gas. The energy supplied to the reaction was taken as the change in enthalpy, given as

$$H = \sum_i y_i \int_{T_{ref}}^T C_p dT \quad (6)$$

where *C*<sub>*p*</sub> is the heat capacity, *T* is the absolute temperature, and *T*<sub>ref</sub> is the reference temperature of the thermodynamical data. Data used for the calculations were taken from Barin [21]. From the change in enthalpy, the power transfer to the gas was calculated as

$$P_{reaction} = H_{out}F_{out} - H_{in}F_{in} \quad (7)$$

where *F* is the molar flow in or out of the catalyst bed.

From the changes in gas composition, the temperature where the given gas would be in equilibrium, *T*<sub>eq</sub>, is defined as

$$Q = K_{SMR}(T_{eq}) \quad (8)$$

where *K*<sub>SMR</sub> is the equilibrium constant for steam methane reforming. The approach to equilibrium in the induction heating setup was found by calculating the reaction quotient as

$$Q = \frac{y_{CO} y_{H_2}^3}{y_{CH_4} y_{H_2O}} p^2 \quad (9)$$

where *y*<sub>*i*</sub> is the molar fraction of the *i*'th gas, and *p* is the measured absolute total pressure.

#### 3.2. Power dissipation

The power dissipated inside the reactor due to hysteresis (*P*<sub>hys</sub>) is partly used to drive the steam methane reforming reaction and partly lost through the insulation. Hence *P*<sub>reaction</sub> can also be derived as the amount of power put into the inductor material (*P*<sub>hys</sub>) minus the power-loss through the insulation (*P*<sub>iso</sub>) as

$$P_{reaction} = P_{hys} - P_{iso} \quad (10)$$

The total input power is then also given as

$$P_{in} = P_{hys} + P_{coil} + P_{rest} \quad (11)$$

The amount of power dissipated by hysteresis heating at temperature *T* of magnetic sample with mass *m*<sub>s</sub> exposed to an alternating magnetic field *B*<sub>app</sub> with amplitude *B*<sub>max</sub> and frequency *f* is

$$P_{hys} = A_{hys}(B_{max}, T) f m_s \quad (12)$$

where *A*<sub>hys</sub>(*B*<sub>max</sub>, *T*) is the area of the hysteresis loop given as:

$$A_{hys}(B_{max}, T) = \oint_{B_{max}} \sigma(B_{app}, T) dB_{app} \quad (13)$$

Here, *σ* is the mass-specific magnetization described by the hysteresis loop at a given temperature *T*. For small *B*<sub>max</sub>, when *σ* is far from saturation at *B*<sub>max</sub>, *A*<sub>hys</sub> is expected to increase proportionally to *B*<sub>max</sub><sup>2</sup> [22]. With increasing temperature, *A*<sub>hys</sub> will generally decrease and be zero above the Curie temperature.

For simplicity it is assumed that the magnetic field, *B*<sub>app</sub>, in a coil of height *h* with *N* windings carrying the time-varying current

$I(t) = I_0 \cos(2\pi ft)$ , is homogeneous and given by the expression for an infinitely long air-coil as

$$B_{\text{app}} = \mu_0 n I(t) \quad (14)$$

where  $n = N/h$  is the winding density. Moreover, the magnetic field amplitude is given in terms of the rms current as  $B_{\text{max}} = \mu_0 n I_0 = \sqrt{2} \mu_0 n I_{\text{rms}}$ .

COMSOL simulations were made to test the validity of this field approximation (see SI). In these, we placed a magnetic material representative for the present sample in each of the three coils and compared the magnetic field strength in the centre of the coil to that obtained using Eq. (14). We found relative centre field strengths of 0.77 for the two short coils and 0.9 for the long coil. Therefore, Eq. (14) overestimates the magnetic field, especially for the two short coils. The COMSOL simulations did not take into account that the sample properties are functions of both magnetic field and temperature, where both properties show a complex dependence on the spatial coordinate in the catalyst material. At this point, we therefore use Eq. (14) in further estimates in the present work and note that this may result in a slight overestimation of the hysteresis heating. A more detailed analysis is left for future work. Finally, the COMSOL simulations showed that the magnetic field outside the coil decreases so rapidly, that it is reasonable to assume that only the amount of sample situated inside the coil is hysteresis heated, *i.e.* in Eq. (12),  $m_s$  is given as:

$$m_s = \pi r_1^2 h_{\text{sc}} \rho_s \quad (15)$$

where  $h_{\text{sc}}$  is the height of the catalyst sample inside the coil.

The temperature variation within the reactor will lead to a spatial distribution of hysteresis losses. In Eqs. (12) and (10), the temperature is assumed to be constant. If the temperature profile of the reactor is known, it is possible to include it in the estimation of  $P_{\text{hys}}$ . However, in our case, we do not know the temperature profile and we therefore make the simplifying assumption that the reactor temperature is given by the average between inlet and outlet gas temperature ( $T_1$ ).

The power loss through the insulation material ( $P_{\text{iso}}$ ) is modelled using Fourier's law of heat conduction in cylindrical coordinates as

$$P_{\text{iso}} = \frac{2\pi h \lambda}{\ln\left(\frac{r_2}{r_1}\right)} (T_1 - T_2) \quad (16)$$

where  $\lambda$  is the thermal conductivity of the insulation,  $h$  is the height of the insulation cylinder,  $r_1$  and  $r_2$  are the inner and outer radii of the cylinder of insulation, respectively, and  $T_1$  and  $T_2$  are the inner and outer temperatures, respectively. As a simplification  $T_1$  was assumed as the average between the inlet temperature and the equilibrium temperature, and  $T_2$  as the cooling water temperature as this is the temperature in the immediate vicinity of the outer surface of the insulation (see Fig. 1).

The power loss in the coil ( $P_{\text{coil}}$ ) is due to Joule heating of the copper tube. The resistive loss in the coil, carrying an alternating current, will be subject to both the skin effect and the proximity effect at the frequencies used in this study (68 kHz and 189–201 kHz). The skin effect is the tendency for the current to concentrate near the surface at high frequencies and hence increase the resistance of the conductor. The characteristic length scale of the penetration depth of an alternating current in a material, the skin depth, is [23]

$$d = \sqrt{\frac{\rho}{\pi f \mu}} \quad (17)$$

where  $\rho$  is the resistivity,  $f$  is the frequency, and  $\mu$  is the permeability. For copper at  $f = 68$  kHz and 189 kHz, the skin depth is  $d = 250$   $\mu\text{m}$  and 150  $\mu\text{m}$ , respectively. The proximity effect is caused by the interaction of one turn in the coil with the changing magnetic field from another neighbouring turn in the coil, whereby additional eddy currents will be induced.

The AC resistance caused by the skin effect and the proximity effect

can be approximated with the following equation, adapted from Nan and Sullivan [24] as

$$R_{\text{coil}} = R_{\text{DC}} \xi \left[ \frac{\sinh(2\xi) + \sin(2\xi)}{\cosh(2\xi) - \cos(2\xi)} \right] \quad (18)$$

here  $R_{\text{DC}} = L\rho/A$  is the direct current resistance of a copper tube of length  $L$  and cross section  $A$ . The proximity factor,  $\xi$ , considers two geometrical aspects, the first is how close the windings are to each other and the second is the ratio of the conductor radius and the skin depth.  $\xi$  is given by

$$\xi = \sqrt{\frac{N\sqrt{\pi}r_0}{h}} \frac{\sqrt{\pi}r_0}{d} \quad (19)$$

where  $r_0$  is the radius of the copper tube,  $h$  is the height of the coil, and  $d$  is the skin depth [24]. As the coils used in this work have close windings and a small penetration depth to tube radius, the proximity factor is larger than 5, this results in the bracketed term in Eq. (18) being very close to 1. Combining with the average resistive power dissipation,  $P = I_{\text{rms}}^2 R_{\text{coil}}$ , we obtain

$$P_{\text{coil}} = I_{\text{rms}}^2 L \frac{\pi r_0}{A} \sqrt{\frac{N\sqrt{\pi}r_0\rho\mu}{h}} \sqrt{f} \quad (20)$$

Combining the expressions for  $P_{\text{reaction}}$  (Eqs. (7) and (10)),  $P_{\text{hys}}$  (Eq. (12)),  $P_{\text{iso}}$  (Eq. (16)) and  $P_{\text{coil}}$  (Eq. (20)), the influences of the different power losses in the reactor setup can be studied.

## 4. Results and discussions

### 4.1. Hysteresis heating

Initially the catalyst's magnetic properties were investigated to verify its applicability for induction-heated steam reforming. The mass-specific magnetization of the catalyst was measured as a function of applied field and temperature in the VSM. These data were used to calculate the hysteresis area as a function of magnetic field and temperature. Fig. 2 shows the hysteresis area ( $A_{\text{hys}}$ ) of the sample as function of magnetic field amplitude ( $B_{\text{max}}$ ) and temperature. The data show an almost quadratic behaviour with  $B_{\text{max}}$  up to about 30 mT. At higher  $B_{\text{max}}$  (up to 60 mT) the area still increases but at a decreasing rate possibly due to saturation effects. The hysteresis area decreases with temperature, from  $\approx 200$  mJ/kg at 200 °C to  $\approx 10$  mJ/kg at 800 °C at  $B_{\text{max}} = 40$  mT. From the VSM data, the Curie temperature was estimated to 877 °C (see inset in Fig. 2) by use of the two-tangent method [25] (see SI). This Curie temperature is in agreement with that expected for a material composition of  $\text{Co}_{50}\text{Ni}_{50}$  ( $\approx 860$  °C) [26].

### 4.2. Steam reforming and energy transfer efficiency

After confirming that the catalyst was susceptible to induction heating up to high temperatures, it was subsequently applied for steam methane reforming reactor tests. The reaction was measured using a dedicated flow setup where the methane conversion ( $X$ ) was determined. Fig. 3 shows an example of such a measurement, where the methane conversion is shown as a function of total input power, for the experiment with the short wide coil insulated with Promasil at a frequency of 68 kHz. At power consumptions between 400 W and 1150 W, the conversion goes from 50% to more than 95%. This power input corresponded to an applied magnetic field ranging from 28–48 mT, as also shown by Fig. 3. In the inset the relation between equilibrium temperature,  $T_{\text{eq}}$ , and conversion,  $X$ , is shown along with the corresponding exit temperature  $T_{\text{out}}$  which spans an interval of 580–740 °C.

The power taken up by the reaction ( $P_{\text{reaction}}$ ) is determined from the gas conversion ( $X$ ) and shown on the right y-axis of Fig. 3. As the energy transfer efficiency is  $\eta = P_{\text{reaction}}/P_{\text{in}}$ , the efficiency can be derived directly from any point in this dataset. Taking the circled point in

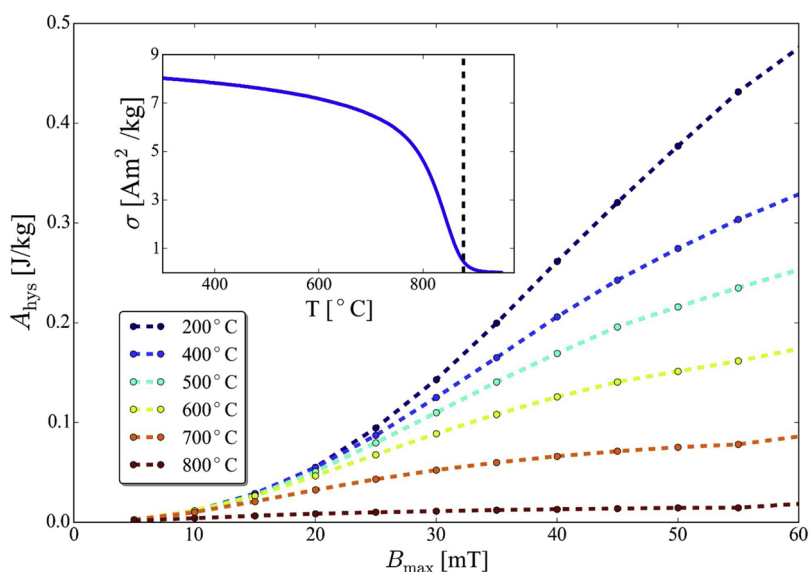


**Fig. 2.** Hysteresis loop area as function of field amplitude for the CoNi/Sm<sub>2</sub>O<sub>3</sub>-Al<sub>2</sub>O<sub>3</sub> sample at 200–800 °C. Dashed lines are guides to the eye. The inset is the mass-specific magnetization vs. temperature for the CoNi/Sm<sub>2</sub>O<sub>3</sub>-Al<sub>2</sub>O<sub>3</sub> sample at 10 mT. Data in the inset was taken during cooling from 950 °C at an absolute ramp rate of 5 °C/min. The vertical line in the inset at 877 °C indicates the Curie temperature. The sample mass in these measurements was 35.7 mg, and all data was measured under a volumetric flow of 150 ml/min of 2.4 mol% H<sub>2</sub> in Ar.

**Fig. 3** as an example, the received reaction power at a total input power of 812 W is 84 W, yielding an energy transfer efficiency of  $\eta = 10\%$ .

Using the approach described above, a range of different configurations of the induction-heated setup was tested and evaluated. An overall comparison of the results from the different configurations is summarised in **Fig. 4**, showing  $\eta$  as function of  $P_{in}$ , in scenarios where the frequency, coil length, coil diameter, and insulation are varied.

Any direct comparison between the experiments shown in **Fig. 4** should be done with care as temperature, gas composition and  $B_{max}$  vary with the input power. One point from each series was therefore selected for comparison. These points were chosen to have a methane conversion close to 90% (in practice it was between 88% and 92%), which corresponds to similar equilibrium temperatures in the range from 691–703 °C. The same average temperature gives similar temperature gradients and the hysteresis loss is then only dependent on the magnetic field. It should be emphasized, that choosing a constant temperature for the calculations means that the magnetic field strength will not be the same between the chosen data points. An overview of the chosen points can be seen in **Table 2**.

#### 4.3. Frequency

In **Fig. 4**, the energy transfer efficiency are shown for the short, wide coil at  $f = 68$  kHz (blue circular points) and  $f = 189$  kHz (red diamond-shaped points). Changing from the low frequency to the high frequency increased the energy transfer efficiency of the system. Specifically at the selected points, for  $f = 68$  kHz in the wide coil,  $P_{in} > 800$  W was required to obtain 90% conversion of methane, resulting in an energy transfer efficiency of 10%. At the higher frequency  $f = 189$  kHz, the same methane conversion required only  $P_{in} \approx 500$  W, consequently giving a higher efficiency of 18%. According to Eq. (12),  $P_{hys}$  is proportional to  $f$ , while Eq. (20) shows that  $P_{coil}$  only increases as  $f^{1/2}$ . This means that the received power increases more than the power losses and hence the energy transfer efficiency should increase with frequency.

Although the experiments indicate that increasing the frequency increases the energy transfer efficiency, it cannot be increased indefinitely. Resistive losses in the electronics (power-supply, transformer) will be a practical barrier for how high the frequency can be

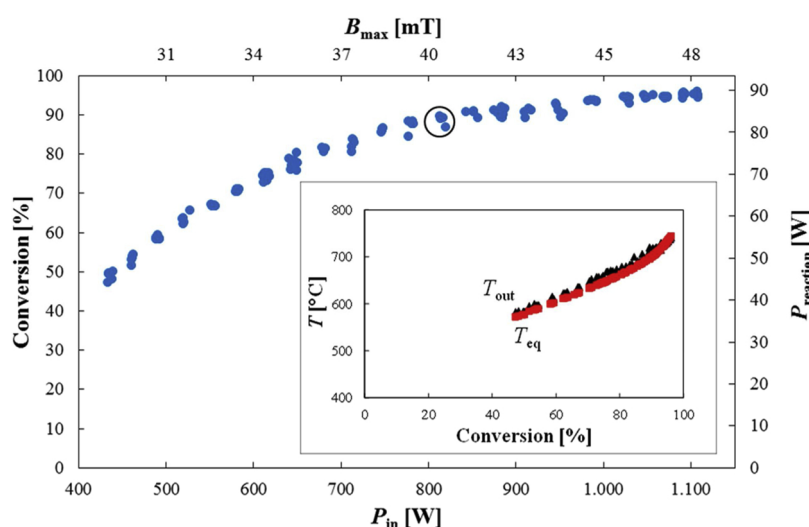


**Fig. 3.** A measurement of methane conversion as a function of input power ( $P_{in}$ ), using the CoNi/Sm<sub>2</sub>O<sub>3</sub>-Al<sub>2</sub>O<sub>3</sub> catalyst, the short wide coil at a frequency of 68 kHz and Promasil insulation. The gas flow was 30 NL/h of CH<sub>4</sub>,  $y_{H_2} = 10.7$  mol%,  $P = 1$  bar, at a steam to carbon ratio of 2, and an inlet temperature of 300 °C. The scale on the magnetic field axis is not linear. The inset shows the equilibrium temperature ( $T_{eq}$ ) and the exit temperature ( $T_{out}$ ) as a function of conversion. On average, the approach to equilibrium in the inset is 10 °C. The circle marks the data point chosen for **Table 2**.



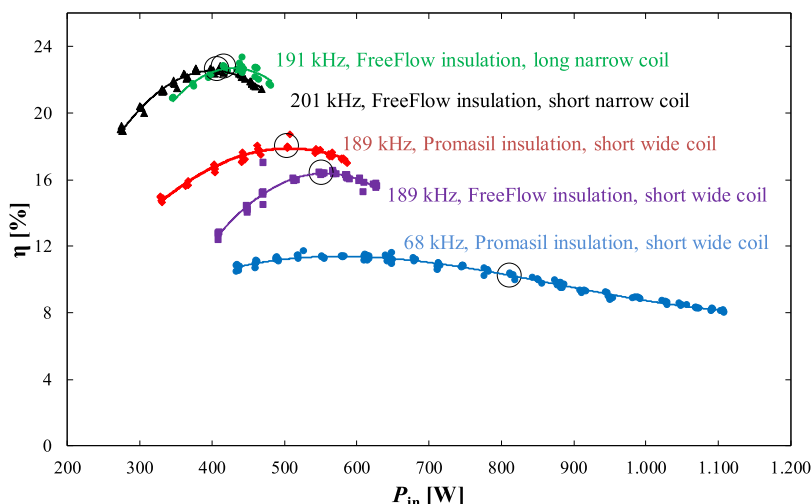


**Fig. 4.** Experimental energy transfer efficiency ( $\eta$ ) as a function of input power ( $P_{in}$ ). All data series are at a flow of 30 NL/h of  $\text{CH}_4$  at a steam to carbon ratio of 2 using the  $\text{CoNi/Sm}_2\text{O}_3\text{-Al}_2\text{O}_3$  catalyst. All lines are guides to the eye. Circles mark points chosen for Table 2.

set. In the case of the UPT-S2 Ultraflex power supply, used in this work, about 200 kHz is the maximum frequency.

#### 4.4. Insulation

Initially in the experimental series, the insulation used for the steam reforming setup was Promasil hard shells. When changing the coil size, FreeFlow insulation was used, as it was significantly easier to work with. Fig. 4 shows the change in efficiency at 189 kHz for the short wide coil, when the insulation is changed from Promasil (red diamond-shaped data points) to FreeFlow (purple square datapoints). As can be seen, FreeFlow leads to a slightly lower efficiency than Promasil (16% vs. 18% efficiency at the selected points). Consequently, the energy transfer efficiency is influenced by the insulation, but the change is minor compared to that by the other variables investigated.

#### 4.5. Coil geometry

##### 4.5.1. Coil radius

From the data in Fig. 4 it can be seen that changing the coil geometry from that of the short wide coil with an inner radius of 20 mm and a height of 75 mm (purple squares) to that of the narrow short coil with a radius of 12.5 mm and a height of 60 mm (black triangles) increases the energy transfer efficiency: The efficiency at 90% conversion (circled points) increased from 16% to 23%, using  $P_{in} = 555$  W and 407 W, respectively. When the radius is reduced, the coil tube length ( $L$ ) is shortened and consequently  $P_{coil}$  decreases (Eq. (20)) and  $\eta$  increases. The Comsol simulations (see SI) showed that the centre-fields were similar in the two short coils, suggesting similar  $P_{hys}$  for the two coils. By the reduction in coil radius, the power loss through the insulation is increased, as reducing the coil radius reduces the amount of insulation in the current layout (see Eq. (16)). However, under the conditions studied in this article, the increase in  $P_{iso}$  is an order of magnitude smaller than the decrease in  $P_{coil}$  when the coil radius is reduced.

**Table 2**

Data for calculating the energy transfer efficiency at the circled data-points in Fig. 4.

Coil	$T_{eq}$ [°C]	$P_{in}$ [W]	$I_{rms}$ [A]	$f$ [kHz]	$B_{max}$ [mT]	$A_{hys}$ [mJ/kg]	$\eta_{exp}$ [%]	$\eta_{calc}$ [%]	$X$ [%]	Insulation
Short, wide	699	812	189	68	40	126	10	5	88	Promasil
Short, wide	691	505	104	189	22	51	18	13	89	Promasil
Short, wide	695	555	108	189	23	51	16	12	89	FreeFlow
Short, narrow	703	407	107	201	22	51	23	30	91	FreeFlow
Long, narrow	691	421	76	191	17	40	23	34	92	FreeFlow

Therefore, decreasing the coil radius is still favourable when optimising the energy transfer efficiency.

The above results suggest that a narrower coil is more optimal in terms of efficiency. If a very thin but efficient layer of insulation could be used, or if insulation could be placed outside the coil, the edge of the coil could be placed close to the tube containing the catalyst material, it is possible that the efficiency could be further increased. If the insulation was to be placed outside the coil, it would probably be necessary to have an un-cooled coil that can handle the heat radiating from the quartz reactor. This concept of placing the insulation outside the coil would present challenges on how well this un-cooled coil would function in a hot environment.

##### 4.5.2. Coil height

The efficiency of two coils with same inner radius of 12.5 mm, but different heights, are compared in Fig. 4. The efficiency of the short narrow coil with a height of 60 mm is shown by the black triangles and the efficiency of the long narrow coil with a height of 135 mm is shown by the green circles. For both coils, the energy transfer efficiencies at 90% conversion (circled points) were around 23%. The short coil achieved this conversion at 410 W, whereas the long coil needed 420 W. Based on the modelling in Section 3, this similarity between the efficiencies may be explained by the scaling of  $P_{hys}$  and  $P_{coil}$  as both scale linearly with height:  $P_{hys}$  is proportional to the sample volume, and  $P_{coil}$  is proportional to the coil length. Additionally, the short coil uses only some of the sample mass whereas the long coil uses all of it.

#### 4.6. Distribution of power losses

Fig. 5 shows the power losses  $P_{reaction}$ ,  $P_{iso}$  and  $P_{coil}$  calculated according to Eqs. (10), (16), and (20) for the selected five points in Fig. 4. The calculated power losses were subtracted from the total experimental power loss ( $P_{in}$ ) to determine  $P_{rest}$  (shown by green in Fig. 5). In all high-frequency experiments,  $P_{rest}$  was  $200 \pm 10$  W, while in the

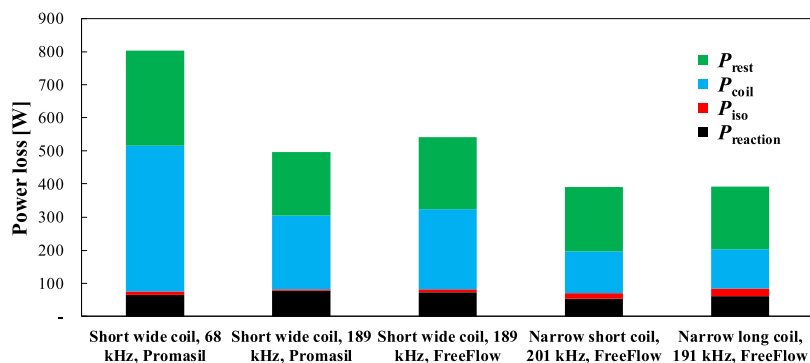


Fig. 5. The estimated power losses in absolute values calculated for the selected points in Table 2 for setups using different frequencies, coil geometries and insulation types.

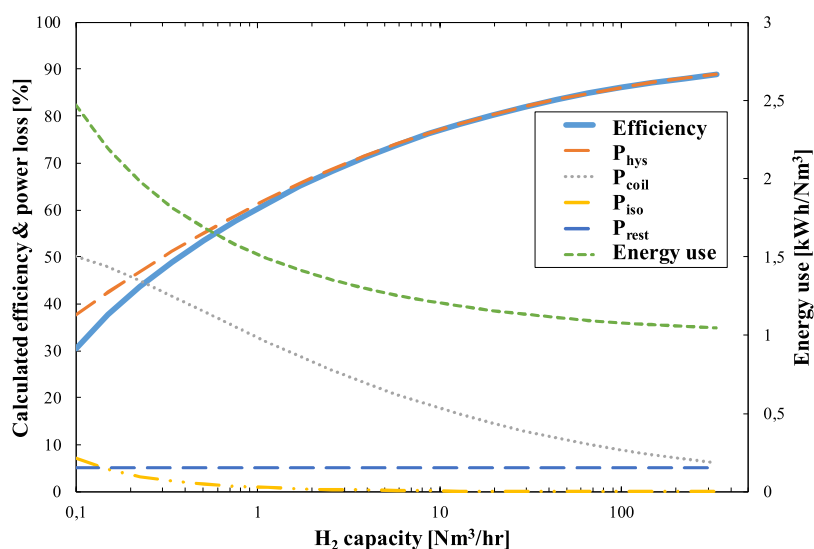


Fig. 6. Calculated energy transfer efficiency and power loss percentages of scaled hydrogen production (left y-axis), as well as energy consumption per normal cubic metre of hydrogen (right y-axis).

low-frequency experiment it was close to 290 W. As  $P_{\text{rest}}$  is approximately constant for fixed frequency, it was concluded to be directly associated with power-losses in electrical components not included in this study, in particular the power-supply. Additionally, the analysis of the data shows that the theoretical framework captures the trends seen in experiments. As the temperature, conversion and flow of methane in the selected data were constant, the power put into driving the reaction and heating the gas should be 84 W. For comparison, Fig. 5 shows that for all set-up configurations  $P_{\text{reaction}}$ , calculated as  $P_{\text{hys}} - P_{\text{iso}}$ , is  $70 \pm 10$  W, which is consistent with this value. Therefore, the model captures the trend of constant  $P_{\text{reaction}}$ , even with the simplifications made in the model.  $P_{\text{coil}}$ , the blue part in Fig. 5, can be lowered through choices in driving frequency and coil geometry, for a constant  $P_{\text{reaction}}$ .

#### 4.7. Extrapolating to larger-scale $H_2$ production

The above sections showed that when changing coil geometry and frequency, it is possible to increase the efficiency by a factor of 2, and that the presented simple theoretical framework provided a consistent description of the experimental observations. On this basis, we have extrapolated the model to larger scale operation to assess the potential performance upon upscaling to an industrially relevant production.

The upscaling is done in such a way that the magnetic field inside the coil is constant. This is achieved by using the same coil current, same winding density, and same ratio between coil radius and height. The upscaling increases the reactor volume linearly with flow, keeping

the gas residence time constant, hence the conversion should be constant when scaling up as well.

As the basis for this extrapolation, parameters from the narrow short coil experiment at 201 kHz were used. The loss in the power supply  $P_{\text{rest}}$  was however assumed to be 5% of the total power loss in each case (instead of  $\approx 20\%$ ), as this is a typical loss in a commercial power-supply in larger systems (see for example [27]).

The resulting efficiencies of these calculations can be seen in Fig. 6, as well as the percentages of  $P_{\text{hys}}$ ,  $P_{\text{iso}}$ , and  $P_{\text{coil}}$ , of the total power loss. The figure indicates, based on the simple theory presented in this article, that the induction-heated system will improve markedly in performance when scaled up. This increase can be attributed to the increasing volume-to-surface area in the system. The hysteresis loss scales with the amount of sample in the system, which is a linear function of the sample volume. The power-loss in the coil, which is the main loss in the system, scales linearly with the coil length (see Eq. (20)), which in turn depends linearly on the surface area of the system. From the figure, it can also be seen that the relative contribution of  $P_{\text{iso}}$  decreases with upscaling, which is also attributed to the decreasing surface area relative to volume.

In Fig. 6, the energy expenditure per  $\text{Nm}^3$   $H_2$  is also plotted. At  $100 \text{ Nm}^3/\text{h}$ , the electric energy expenditure is just around  $1.0 \text{ kWh}/\text{Nm}^3$ . For comparison, the electric energy requirement of an industrial alkaline electrolysis unit in a capacity of  $50\text{--}485 \text{ Nm}^3/\text{h}$  is  $3.8\text{--}4.4 \text{ kWh}/\text{Nm}^3$  [28]. Despite several differences existing between the two technologies, and that the upstream and downstream unit operations of a reformer

have not been included to the reformer, the analysis indicates that induction heating could be competitive to other electrically driven routes to hydrogen production.

It is emphasized that this calculation only focused on the reforming reactor and no efforts was made to make a full process evaluation of a hydrogen plant. This result is based on extrapolation, hence care should be taken when using these numbers directly as errors are extrapolated as well. The trends seen are more trustworthy though.

## 5. Conclusions

We studied the performance increase of induction-heated steam methane reforming introduced by changing the frequency and geometry of the induction coil. Specifically by using a narrower coil with less insulation around the sample and 3-fold higher frequency, we approximately doubled the maximum energy transfer efficiency from 11% to 23%. This increase has been attributed to a higher hysteresis input into the magnetic material by increasing the frequency, and a lower resistive loss in the coil from shortening the copper tube, while maintaining sufficient insulation. In order to explain these general trends in performance, we created a simple theoretical framework to model the hysteresis power loss, the power loss through the insulation, and the resistive power loss in the coil. Using this framework, it was shown that when the induction system was extrapolated to large scale H<sub>2</sub> production, the efficiency of the system is indicated to increase significantly and could be close to 90%. The framework also indicated that when the system is scaled up, it could become commercially competitive with electrolyzers available on the market today.

## Acknowledgments

This work was funded by Innovation Fund Denmark (IFD) under File No. 5160-00004B.

## Appendix A. Supplementary data

Supplementary data associated with this article can be found, in the online version, at <https://doi.org/10.1016/j.cattod.2019.05.005>.

## References

- [1] G. Bercic, J. Levec, Catalytic dehydration of methanol to dimethyl ether. Kinetic investigation and reactor simulation, *Ind. Eng. Chem. Res.* 32 (1993) 2478–2484, <https://doi.org/10.1021/ie00023a006>.
- [2] Z. Anxionnaz, M. Cabassud, C. Gourdon, P. Tochon, Heat exchanger/reactors (HEX reactors): concepts, technologies: state-of-the-art, *Chem. Eng. Process. Process Intensif.* 47 (2008) 2029–2050, <https://doi.org/10.1016/j.ccep.2008.06.012>.
- [3] K. Sundmacher, *Integrated Chemical Processes*, Wiley-VCH Verlag GmbH & Co. KGaA, Weinheim, FRG, 2005, <https://doi.org/10.1002/3527605738>.
- [4] J. Rostrup-Nielsen, L.J. Christiansen, *Concepts in Syngas Manufacture*, Imperial College Press, London, 2011, <https://doi.org/10.1142/p717>.
- [5] B.C.R. Ewan, R.W.K. Allen, A figure of merit assessment of the routes to hydrogen, *Int. J. Hydrogen Energy* (2005), <https://doi.org/10.1016/j.ijhydene.2005.02.003>.
- [6] J.R. Rostrup-Nielsen, J. Sehested, Hydrogen and synthesis gas by steam- and CO\* reforming, *J. Adv. Catal. Sci. Technol.* 47 (2002) 65–139, [https://doi.org/10.1016/S0360-0564\(02\)47006-X](https://doi.org/10.1016/S0360-0564(02)47006-X).
- [7] P.M. Mortensen, I. Dybkjær, Industrial scale experience on steam reforming of CO<sub>2</sub>-rich gas, *Appl. Catal. A Gen.* (2015), <https://doi.org/10.1016/j.apcata.2015.02.022>.
- [8] T.K. Houlding, E.V. Rebrov, Application of alternative energy forms in catalytic reactor engineering, *Green Process. Synth.* (2012), <https://doi.org/10.1515/greens-2011-0502>.
- [9] A. Meffre, B. Mehdaoui, V. Connord, J. Carrey, P.F. Fazzini, S. Lachaize, M. Respaud, B. Chaudret, Complex nano-objects displaying both magnetic and catalytic properties: a proof of concept for magnetically induced heterogeneous catalysis, *Nano Lett.* 15 (2015) 3241–3248, <https://doi.org/10.1021/acs.nanolett.5b00446>.
- [10] P.M. Mortensen, J.S. Engbæk, S.B. Vendelbo, M.F. Hansen, M. Østberg, Direct hysteresis heating of catalytically active Ni-Co nanoparticles as steam reforming catalyst, *Ind. Eng. Chem. Res.* 56 (2017) 14006–14013, <https://doi.org/10.1021/acs.iecr.7b02331>.
- [11] O. Lucia, P. Maussion, E. Dede, J.M. Burdío, Induction heating technology and its applications: past developments, current technology, and future challenges, *IEEE Trans. Ind. Electron.* (2014), <https://doi.org/10.1109/TIE.2013.2281162>.
- [12] L. Lartigue, P. Hugounenq, D. Alloyeau, S.P. Clarck, M. Lévy, J.-C. Bacri, R. Bazzi, D.F. Brougham, C. Wilhelm, F. Gazeau, Cooperative organization in iron oxide multi-core nanoparticles potentiates their efficiency as heating mediators and MRI contrast agents, *ACS Nano* 6 (2012) 10935–10949, <https://doi.org/10.1021/nn304477s>.
- [13] S. Ceylan, C. Friese, C. Lammel, K. Mazac, A. Kirschning, Inductive heating for organic synthesis by using functionalized magnetic nanoparticles inside micro-reactors, *Angew. Chemie - Int. Ed.* (2008), <https://doi.org/10.1002/anie.200801474>.
- [14] S. Chatterjee, V. Degirmenci, F. Aiouache, E.V. Rebrov, Design of a radio frequency heated isothermal micro-trickle bed reactor, *Chem. Eng. J.* (2014), <https://doi.org/10.1016/j.cej.2013.12.059>.
- [15] A. Bordet, L.M. Lacroix, P.F. Fazzini, J. Carrey, K. Soulantica, B. Chaudret, Magnetically induced continuous CO<sub>2</sub> hydrogenation using composite iron carbide nanoparticles of exceptionally high heating power, *Angew. Chemie - Int. Ed.* (2016), <https://doi.org/10.1002/anie.201609477>.
- [16] P.M. Mortensen, J.S. Engbæk, S.B. Vendelbo, M.F. Hansen, M. Østberg, Direct hysteresis heating of catalytically active Ni-Co nanoparticles as steam reforming catalyst, *Ind. Eng. Chem. Res.* (2017), <https://doi.org/10.1021/acs.iecr.7b02331>.
- [17] M.G. Vinum, M.R. Almind, J.S. Engbæk, S.B. Vendelbo, M.F. Hansen, C. Frandsen, J. Bendix, P.M. Mortensen, Dual-Function Cobalt–Nickel Nanoparticles Tailored for High-Temperature Induction-Heated Steam Methane Reforming, *Angew. Chemie* 0 (n.d.), doi:<https://doi.org/10.1002/ange.201804832>.
- [18] J.H. Yi, Development of samarium–cobalt rare earth permanent magnetic materials, *Rare Met. Mater. Eng.* 33 (2014) 633–640, <https://doi.org/10.1007/s12598-014-0405-1>.
- [19] PROMASIL®-1000L - Promat, (n.d.), <https://www.promat-hpi.com/en/products/calcium-silicates/promasil-1000l-products> (Accessed 15 August 2018).
- [20] FREEFLOW® - Promat, (n.d.), <https://www.promat-hpi.com/en/applications/transportation/auto/freeflow-exhausts> (Accessed 15 August 2018).
- [21] I. Barin, *Thermochemical Data of Pure Substances*, VCH, 1989.
- [22] R.E.E. Rosensweig, Heating magnetic fluid with alternating magnetic field, *J. Magn. Mater.* (2002), [https://doi.org/10.1016/S0304-8853\(02\)00706-0](https://doi.org/10.1016/S0304-8853(02)00706-0).
- [23] J. Lammeraner, M. Staffl, *Eddy Currents*, Iliffe Books Ltd., 1966.
- [24] X. Nan, C.R. Sullivan, An improved calculation of proximity-effect loss in high-frequency windings of round conductors, *IEEE 34th Annu. Conf. Power Electron. Spec.* 2003 2 (2003) 853–860, <https://doi.org/10.1109/PESC.2003.1218168>.
- [25] C.S. Grommé, T.L. Wright, D.L. Peck, Magnetic properties and oxidation of iron-titanium oxide minerals in Alae y Makaopuhi lava lakes, Hawaii, *J. Geophys. Res.* 74 (1969) 5277–5293, <https://doi.org/10.1029/JB074i022p05277>.
- [26] R.M. Bozorth, *Ferromagnetism*, (1951), <https://doi.org/10.1109/9780470544624>.
- [27] Sinac PM/PH 50-200 - EFD Induction, (n.d.), [http://www.efd-induction.com/en/Products/Sinac/High/50\\_200\\_PMPH.aspx](http://www.efd-induction.com/en/Products/Sinac/High/50_200_PMPH.aspx) (Accessed 14 September 2018).
- [28] Nel hydrogen, Nel Brochure: The world's most efficient and reliable electrolyser, n. d. [https://nelhydrogen.com/assets/uploads/2017/01/Nel\\_Electrolyser\\_brochure.pdf](https://nelhydrogen.com/assets/uploads/2017/01/Nel_Electrolyser_brochure.pdf) (Accessed 14 September 2018).

# Improving performance of induction-heated steam methane reforming – supporting information

*Mads Radmer Almind, Søren Bastholm Vendelbo, Mikkel Fougt Hansen, Morten Gotthold Vinum, Cathrine Frandsen, Peter Mølgaard Mortensen, Jakob Soland Engbæk*

## Table of Contents

<b>COMSOL simulations:</b> .....	<b>1</b>
<b>Curie-temperature determination:</b> .....	<b>3</b>
<b>References</b> .....	<b>4</b>

## COMSOL simulations

Throughout the paper, we assumed that the applied magnetic field inside the coil is given by the expression for an infinitely long coil,  $B = \mu_0 IN/h$ . This is a simplification compared to a real coil of finite dimensions, where the magnetic field will vary spatially, but also will be affected by the presence of a magnetic material inside the coil. Here, we investigate the validity of this approximation for the three coil geometries without a core material and with a core material representing a typical experimental value for the present system. The relative magnetic permeabilities ( $\mu_r$ ) used in the simulations are given below.

The investigation was carried out using a finite element analysis in Comsol 5.2. The magnetic field was modelled using Comsol's Magnetic and electric field module, solving Amperes law and current conservation. The three different coils were simulated using a 2D axi-symmetric model. The coils were assumed to consist of copper rings with a conductivity of  $5.998 \cdot 10^7$  S/m. The thermal insulation was assumed to have the same electromagnetic properties as air and thereby zero electrical conductivity. The electrical conductivity of the magnetic material was also set to zero, reflecting the low conductivity of the aluminum oxide support and that the magnetic material was in the form of nanoparticles. The boundaries on the side, 25 cm away from the coil, were given by an impedance boundary condition. The amount of energy put into the coil was below 50 mW at full power. The solution was found using the stationary solver in the frequency domain, with a mesh of more than 300000 elements.

### *Coil with air* ( $\mu_r=1$ )

Figure S1 shows the results of the Comsol simulations relative to  $B = \mu_0 IN/h$ . It is observed that the field is strongest in the centre of the coils and is generally lower than that predicted by the simple magnetic field expression. The reduction of the centre magnetic field is about 15% for the



two short coils and 3% for the long coil. It is also noted that the long coil has a significant region with a field close to that in the centre.

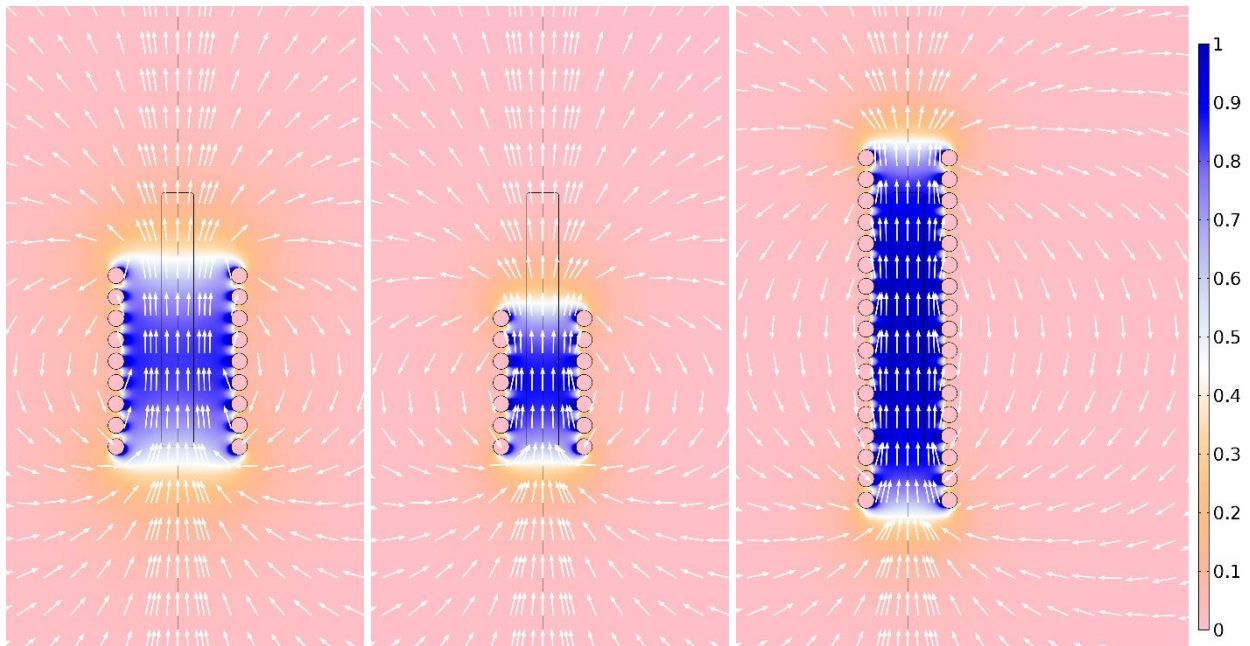


Figure S1: Norm of B-field obtained in finite element calculations relative to the field for an infinitely long air coil,  $B = \mu_0 IN/h$  with no magnetic material inside the coils. The frequency of the applied current was 189 kHz, From left to right, the figure shows the wide coil, the short coil and the long coil. The white arrows indicate a snapshot of the magnetic field direction.

#### Coil with core of magnetic material ( $\mu_r = 3.7$ )

Based on VSM data obtained for  $B_{\max} = 25$  mT at a temperature of 500°C, we estimated the real part of the relative magnetic permeability to  $\mu_r = 3.7$  and repeated the simulation with a core of this material. The results are shown in Figure S2 relative to the field for an infinitely long air coil:  $B = \mu_0 IN/h$ .

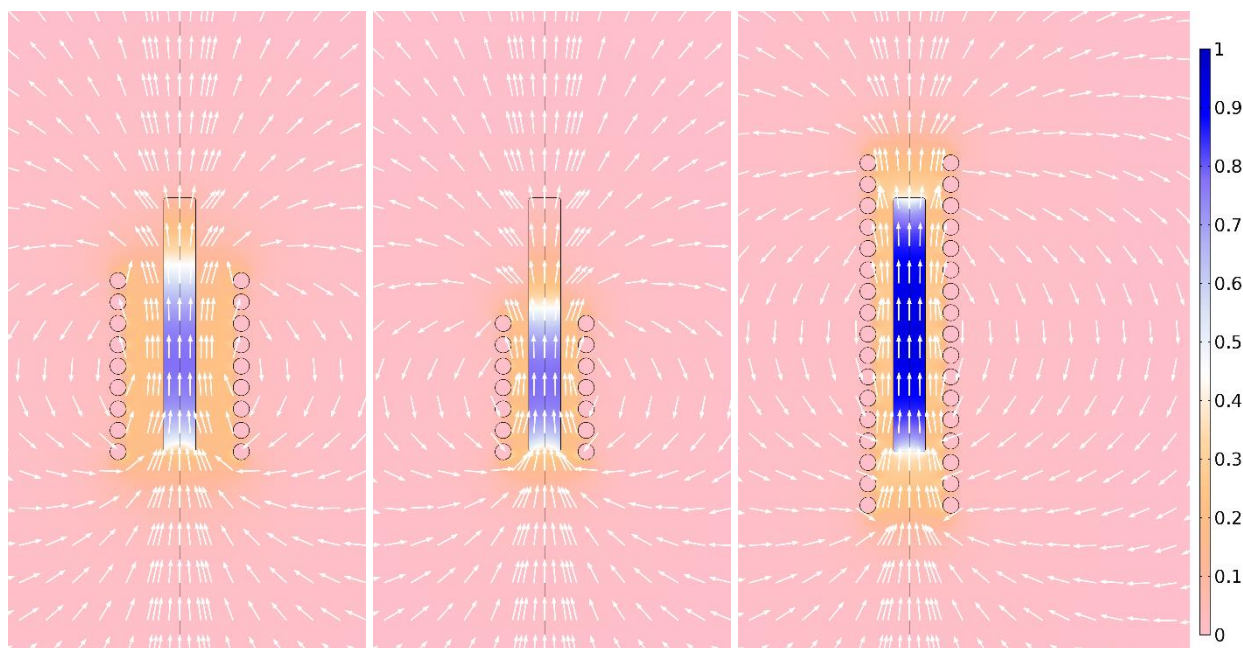


Figure S2: Norm of B-field obtained in finite element calculations relative to the field for an infinitely long air coil,  $B = \mu_r \mu_0 IN/h$  with a magnetic material with a real relative permeability of  $\mu_r = 3.7$ . The frequency of the applied current was 189 kHz. From left to right, the figure shows the wide coil, the short coil and the long coil. The white arrows indicate a snapshot of the magnetic field direction.

The magnetic field intensity is observed to be concentrated in the magnetic material and is, as for the air filled coil, strongest in the centre of the magnetic material. The radial dependence of the field strength is weak and it is observed to decay rapidly near the ends of the coils, i.e., the field is localized to the part of the sample which is inside a coil. The field is most uniform over the magnetic material in the long coil. Comparing to the field for an infinitely long air coil, we find a reduction of the centre magnetic field of about 23 % for the two short coils and 5% for the long coil.

## Curie temperature determination

Curie temperature measurements were made by recording the magnetization of the sample under cooling from 950°C to 200°C at absolute ramp of 5°C/min under a flow of 150 ml/min of 2.4 mol% H<sub>2</sub> in Ar. During this, a data point was recorded every 2 seconds. A lag between the temperature of the sample and the temperature measured by the temperature-sensor in the VSM caused an underestimation of the Curie-temperature of around 10°C, which corresponds to a sample temperature lag of 1-2 minutes at above 700°C. The Curie temperature was determined after exposure of the sample to the mildly reducing atmosphere at 800°C for at least 12 h to ensure stable sample properties.

The Curie temperature was estimated using Grommé's two-tangent method [1]. This method defines the Curie-temperature as the temperature at the intersect between two tangent lines situated before and after the drop in magnetization, respectively (Figure S3).

In our calculations, this was done by fitting the first straight line to the magnetization curve from halfway between the minimum and the zero-point of the second derivative of the magnetization curve to halfway between the zero-point and the maximum in the second derivative of the magnetization

curve (see Figure S3). The second straight line was fitted to the magnetization curve between 930°C and 950°C. The intersection of these lines was found to 877°C. Grommé’s method has a tendency to overestimate the Curie temperature by 10-15°C [2] (estimated on basalt containing magnetite). This means, that the thermal lag from the measurement, and the overestimation in the method will counteract each other, leading to a possible systematic error of up to 10°C in the reported value.

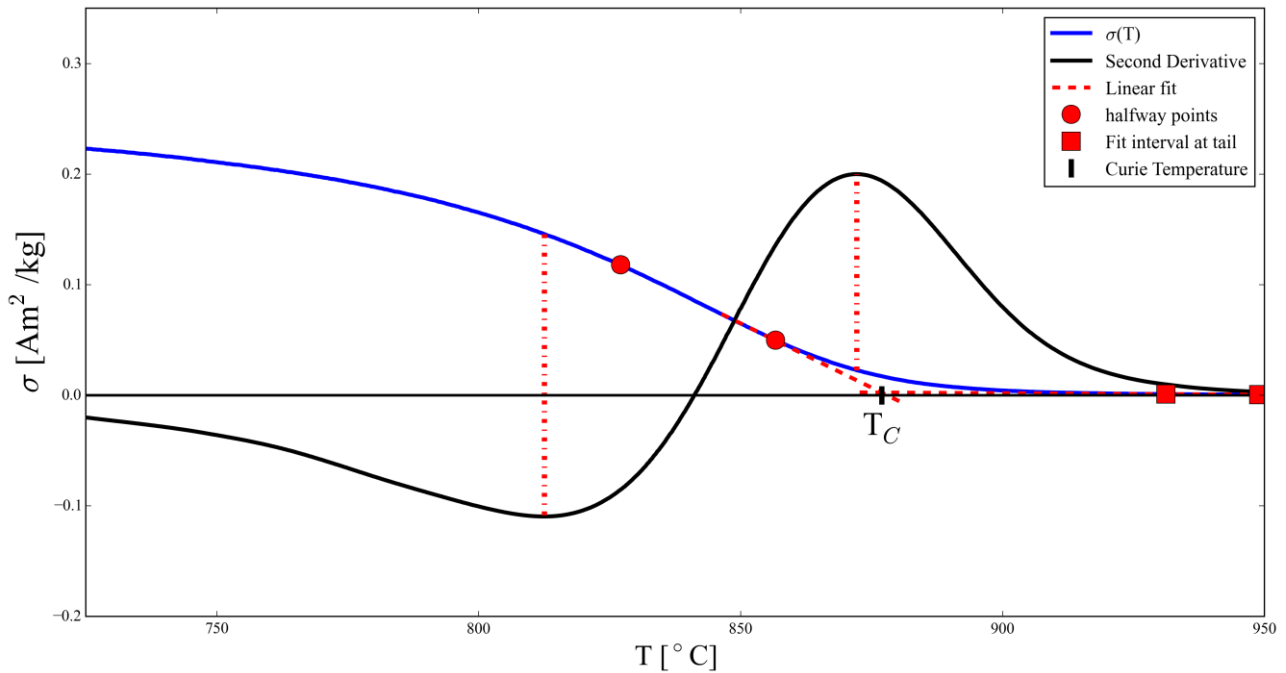


Figure S3: Schematic of two-tangent method for determination of the Curie temperature.

## References

- [1] C.S. Grommé, T.L. Wright, D.L. Peck, Magnetic properties and oxidation of iron-titanium oxide minerals in Alae y Makaopuhi lava lakes, Hawaii, *J. Geophys. Res.* 74 (1969) 5277–5293. doi:10.1029/JB074i022p05277.
- [2] K. Fabian, V.P. Shcherbakov, S.A. McEnroe, Measuring the Curie temperature, *Geochemistry, Geophys. Geosystems.* 14 (2013) 947–961. doi:10.1029/2012GC004440.

### 3.3 Paper III: Tunability of CoNi Nanoparticle Composition for Optimal and Curie-temperature-controlled Induction-heated Catalysis

Following the work done in Paper I and Paper II, we synthesized a range of  $\text{Co}_x\text{Ni}_{(100-x)}/\text{Al}_2\text{O}_3$  with x varying from 10 to 90 mol% in steps of 10 mol%, and made a systematic study of the influence of the CoNi nanoparticle composition on the magnetic and catalytic properties, and how this relates to performance in induction heated SMR.

The study showed that the catalytic properties and magnetic heating properties of the material are inversely correlated. A low Co-content resulted in a large potential for heating at low temperatures, but with a low Curie temperature. The opposite was true for the samples with high Co-contents. Additionally, the Curie temperature put a hard limit on the maximum achievable temperature in the induction heated reactor, with samples reaching a maximum in temperature approx. 30-40 °C under their respective  $T_C$ 's. Increasing the Co content in the sample showed an approximately linear increase in  $T_C$ , and an increase in the magnetic hardness of the material. This increase in magnetic hardness necessitated the use of higher applied magnetic fields in the induction heated reactor, in order to access the larger hysteresis area. The samples with higher Co contents (> 40 mol% Co) were not limited by their  $T_C$ 's, and could reach methane conversions of > 90 %. Tests performed in the induction heated reactor showed a strong qualitative correlation between the magnetic hysteresis measurements and the heating performance during induction heated SMR.

The work laid out in this paper presents the possibility of tuning the maximum operational temperature to avoid overheating of a reaction by tuning Curie temperature of the material. The tunability of the  $\text{Co}_x\text{Ni}_{(100-x)}/\text{Al}_2\text{O}_3$  system also presents the opportunity of optimizing reactor performance by tuning heat transfer and reaction kinetics via the composition of the CoNi particles.

*This paper is currently in preparation*

# Tunability of CoNi Nanoparticle Composition for Optimal and Curie-temperature-controlled Induction-heated Catalysis

Mads R. Almind,<sup>†</sup> Morten G. Vinum,<sup>‡,¶</sup> Sebastian T. Wismann,<sup>‡,†</sup> Mikkel F. Hansen,<sup>§</sup> Søren B. Vendelbo,<sup>||</sup> Jakob S. Engbæk,<sup>||</sup> Peter M. Mortensen,<sup>‡</sup> Ib Chorkendorff,<sup>†</sup> and Cathrine Frandsen<sup>\*,†</sup>

<sup>†</sup>*Department of Physics, Technical University of Denmark, DK-2800 Kgs. Lyngby, Denmark*

<sup>‡</sup>*Haldor Topsøe A/S, DK-2800 Kgs. Lyngby, Denmark*

<sup>¶</sup>*Department of Chemistry, Some company, DK-2100 Copenhagen Denmark*

<sup>§</sup>*Department of Health Technology, Technical University of Denmark, DK-2800 Kgs. Lyngby, Denmark*

<sup>||</sup>*Danish Technological Institute, Gregersensvej 1, DK-2630 Taastrup, Denmark*

E-mail: [\\*frac@fysik.dtu.dk](mailto:*frac@fysik.dtu.dk)

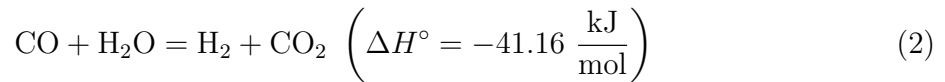
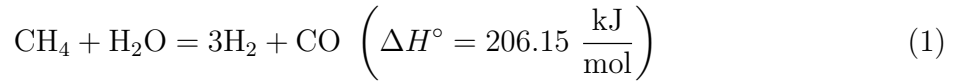
## Abstract

Induction-heating by magnetic hysteresis of nanoparticles inside chemical reactors is an interesting new approach for direct and electrified heating of high-temperature endothermic catalytic reactions. Here, we show how it is possible to tune the induction heating for steam methane reforming, using samples of  $\sim 30$  nm  $\text{Co}_x\text{Ni}_{(100-x)}$  particles on  $\text{Al}_2\text{O}_3$  with well-defined alloy compositions (x varying from 10 to 90, in steps of

10). We find that the heating increases with increasing Ni-content at lower temperatures and smaller induction fields due to Ni being magnetically softer than Co, but the maximum heating temperature increases with Co-content due to the Curie temperature being higher for Co than for Ni. Specifically, the sample Curie temperature increases approximately linearly with Co-content and sets for each alloy a hard limit to the maximum operation temperature in the induction-heated reactor. The compromise between magnetic softness, Curie temperature, and catalytic activity leads to an optimum Co-Ni sample composition at a given operation temperature and induction field amplitude. The hard Curie temperature limit prevents overheating. The magnetic properties obtained on the Co-Ni particles are generally applicable to heating of catalytic reactions. Based on the results, Co-Ni compositions can be chosen in order to tune heat transport and reaction kinetics down through a reactor to optimize reactor performance.

# Introduction

Steam methane reforming (SMR) is a highly endothermic process, in which hydrogen and carbon monoxide are produced by converting methane and steam at temperatures of up to 950 °C.<sup>1</sup> This process, which happens via reactions 1. 2,



Around 75% of the world’s hydrogen is produced from natural gas,<sup>2</sup> primarily through SMR.<sup>2</sup> Most of the hydrogen is used in the production of ammonia for fertilizers.<sup>1</sup> SMR currently accounts for about 3 % of the world’s CO<sub>2</sub> emission.<sup>3,4</sup> In the case of a tubular reformer, the heat and high temperatures needed are achieved through gas burners on the outside of the reactor tube.<sup>1</sup> This results in significant CO<sub>2</sub> emissions but also slows start-up times for the reactor, which is on the order of days.<sup>5</sup> Moreover, external burners to drive endothermic reactions also result in a radial temperature gradient from the hot surface of the reactor tube to the relatively colder center. In industrial applications, heat transfer limitations limit catalyst utilization to around 10% of the available catalytic activity.<sup>1</sup> In conventional heating of steam reforming, this heat transfer from burners to catalyst is the limiting factor.<sup>6</sup> In addition, it is highly energy inefficient, with approximately 50% of the energy from the burners driving the reaction.<sup>1</sup> To combat this, conventional reactors use large heat exchangers to bring the overall efficiency of the reformer to > 90%.<sup>1</sup>

One possible way to tackle simultaneously the heat transfer-challenge and the CO<sub>2</sub> emission from the burners, is to utilize induction heating.<sup>6</sup> Induction heating has the potential to heat locally ”from the inside”, hence supplying heat where it is needed while avoiding large temperature gradients across the reactor tube. At the same time, the heat can be supplied by electricity from renewable sources. In that case, an AC conducting coil, which is wound around susceptor material, produces an alternating magnetic field (”the induction

field”). Energy is then transferred directly to the susceptor inside the reactor, where it can be converted into heat through either magnetic hysteresis or eddy current losses. In case of eddy current losses, a current is induced in a conducting material and this heats the material through resistive losses. This effect is pronounced in larger ( $>$  micrometer) metallic structures. In case of hysteresis heating, the field-reversals of the magnetization in the sample induce an energy loss (hysteresis loss).<sup>7</sup> If the susceptor material consists of magnetic nanoparticles on a non-conductive and non-magnetic support, then the induction heating is due to hysteresis heating of the particles and not due to eddy currents.<sup>7</sup>

Up to now, an often pursued application for induction heating of magnetic nanoparticles has been magnetic hypothermia for cancer treatment.<sup>8–11</sup> Recently, there has also been a rapidly growing interest for utilizing magnetic nanoparticles for induction heating of chemical reactions.<sup>6,12–25</sup> This was pioneered by Kirschnings group, who studied liquid-phase reactions using silica covered iron-oxide core-shell nanoparticle system as heating agent decorated with catalytically active materials.<sup>12</sup> Since then, multiple groups have used induction heating for various reactions. For instance, Bordet et al. utilized iron-carbide nanoparticles for continuous CO<sub>2</sub> hydrogenation,<sup>16</sup> Niether et al. used FeC-Ni core-shell nanoparticles to improve water electrolysis,<sup>17</sup> and Meffre et al.<sup>18</sup> used iron particles for the exothermic Fischer-Tropsch process.<sup>18</sup> In case of high temperature endothermic processes, dry reforming was performed by Varsano et al.,<sup>22</sup> using a compacted disc of Ni<sub>40</sub>Co<sub>60</sub> powder, and Marbaix et al.<sup>23</sup> who used a range of Fe-Co nanoparticle samples on silica-alumina support to tune the heating properties and Curie temperature. Induction-heated SMR was demonstrated using a spinel-supported dual functionality Co-Ni nanoparticle system which works both as catalyst and magnetic susceptor.<sup>5,6,24</sup> These many successful demonstrations of nanoparticles as heating agents for different reactions suggest great promise for novel and sustainable applications but also an increasing need for ways to study and tune induction heating and magnetic properties of magnetic materials.



Here, we present a comprehensive study of the tunability of the magnetic properties of Co-Ni nanoparticles for induction-heating by varying the ratio of cobalt to nickel. We use the magnetic characteristics for Co-Ni particles with a range of well-defined compositions and comparable particle sizes to predict trends and Curie-temperature-control of heating in induction-heated SMR. Based on this, we are able to provide a scheme to estimate the optimum ratio of cobalt to nickel for induction-heating at induction fields of 10-55 mT and temperatures of 200-950 °C.

## Methods

### Synthesis

Samples of  $\text{Co}_x\text{Ni}_{(100-x)}$  nanoparticles (with  $x$  varying from 10 to 90 mol%) on a porous aluminium oxide support were synthesized using the method developed by Vinum et al.<sup>5</sup> Detailed characterization of the dual-function system can also be found in the paper by Vinum et al.. After synthesis, the samples were reduced in pure hydrogen at 850 °C for 4 hours, followed by a passivation at 25°C in 1%  $\text{O}_2$  in  $\text{N}_2$ .<sup>24</sup> An overview of the samples used in this study, along with materials characterisation using the techniques below, can be found in Tab. 1.

### Analyses

Powder x-ray diffraction (XRD) was performed on a PANalytical X'PERT PRO diffractometer using  $\text{Cu K}\alpha$  radiation ( $\lambda = 1.5418 \text{ \AA}$ ). The  $< 125 \mu\text{m}$  grain fraction for each sample was measured between  $5^\circ < 2\Theta < 75^\circ$ , and analysed neglecting lattice strain. The average crystallite size was found via the Scherrer equation.

X-ray fluorescence (XRF) was performed on a Rigaku, Supermini200 WD-XR, using a method based on ISO 12677.

Inductively coupled plasma - optical emission spectrometry (ICP-OES) was performed

on an Agilent 720 ES ICP-OES system, as in Mortensen et al.<sup>6</sup>

Vibrating sample magnetometry (VSM) measurements were performed by use of a LakeShore 7407 VSM. A LakeShore 74034 oven option was used to control the temperature. The samples were loaded in Lakeshore BN cups during measurement. The sample chamber and oven were connected to a volumetric flow of around  $100 \frac{\text{mL}}{\text{min}}$  of 2.4 vol.% H<sub>2</sub> in argon. The hysteresis measurements were performed between  $\pm B_{\text{app}}$ , for values of  $B_{\text{app}}$  of 5 mT to 55 mT in steps of 5 mT, and furthermore for 100 mT, 500 mT and 1500 mT. Temperatures used for these investigations ranged from 200 to 950 °C, in steps of 50 °C. Curie temperature ( $T_C$ ) measurements were performed in a constant field of 10 mT while cooling from 950 to 200 °C at  $5 \frac{^\circ\text{C}}{\text{min}}$ .  $T_C$  was estimated as in Almind et al.,<sup>24</sup> by fitting two straight lines to the magnetization-curve obtained in the  $T_C$  measurements. The first line is fitted from halfway between the minimum to the zero-point in the second derivative of the magnetization-curve to the halfway-point between the maximum and the zero-point in the second derivative of the curve (for a visual representation of this, see the supporting information of Almind et al.<sup>24</sup>). The second line was fitted to the magnetization-curve from 930-950°C. The intersection between these two straight lines is taken as the Curie temperature. In Almind et al.,<sup>24</sup> we estimate a possible systematic error of up to 10 °C in  $T_C$ .

Intrinsic activity measurements were performed in a lab-scale plug flow reactor similar to the one used in Mortensen et al.<sup>6</sup> The reactor was loaded with 20-200 mg sample, in the center of which a thermo pocket was placed to monitor temperature. A grain fraction of 125 – 300  $\mu\text{m}$  was used in all measurements. The intrinsic activity was measured under isothermal conditions at both 450 and 500 °C in a gas flow of  $2 \frac{\text{NL}}{\text{h}}$  CH<sub>4</sub>,  $0.8 \frac{\text{NL}}{\text{h}}$  H<sub>2</sub>,  $6.45 \frac{\text{g}}{\text{h}}$  H<sub>2</sub>O, at 1.2 bar. The dry gas was analyzed by an Agilent 7590 gas chromatograph thermal conductivity detector/flame ionization detector (GC-TCD/FID).

Measurement of methane conversion driven by induction heating was investigated for each sample in a reforming bench scale reactor.<sup>24</sup> Here, approximately 5 g of sample with grain fraction 1-1.3 mm was placed in a quartz tube (with inner diameter of 1.3 cm), and

centered in a water-cooled induction coil (with 17 turns, 13.5 cm tall and 2.5 cm inner diameter). Insulating material from Promasil<sup>26</sup> was placed between the quartz tube and the coil. An AC current (up to approximately 180 A) with a frequency of approx. 195 kHz, was delivered to the coil by an UPT-S2 Ultraflex power supply. An ABB EQ series energy meter measured the power input to the power supply. Gasses were fed to the system using Brooks SLA850 type digital flowmeters which had an estimated uncertainty of  $\pm 2\%$ . The methane and hydrogen gas were of grade 3.5 and 4, respectively. A Knauer Smartline HPLC pump (with an estimated uncertainty of  $\pm 3\%$ ) was used to deliver vaporized demineralized water. When running experiments, the tubing from the Knauer pump to the reactor was traced to  $> 110$  °C. Water was removed from the gas using an Armstrong 11 LD drain tap, and the dry gas was analyzed using an Agilent 7890B system, equipped with a GC-TDC/FID gas chromatograph. Before running an experiment, the passivated Co-Ni sample was reduced in a mixture of 50% H<sub>2</sub> in N<sub>2</sub>, while induction-heated to 400 °C. Afterwards, the sample was heated via induction to the reaction temperature, and H<sub>2</sub>, CH<sub>4</sub>, and steam were introduced.

For both the intrinsic activity measurements and induction-heated reactor studies, the conversion of methane,  $\chi_{\text{CH}_4}$ , was calculated based on the carbon balance as:

$$\chi_{\text{CH}_4} = \frac{y_{\text{CO}} + y_{\text{CO}_2}}{y_{\text{CO}} + y_{\text{CO}_2} + y_{\text{CH}_4}} \quad (3)$$

where the molar fraction of the  $x$ 'th compound in the dry gas is denoted as  $y_x$ .

$\chi_{eq}$ , the equilibrium conversion of methane, in Fig. 5 is calculated via. HSC Chemistry 5.1.

## Results and discussion

### Particle sizes and compositions

Table 1 shows the crystallite sizes,  $D_{\text{Co,Ni}}$ , of the Co-Ni samples together with particle compositions and loadings obtained by XRD, XRF, ICP-OES. The crystallite sizes were found to

be in the narrow range of 25-35 nm for all samples. This is in agreement with the results by Vinum et al.,<sup>5</sup> who synthesized samples of  $\text{Co}_{50}\text{Ni}_{50}/\text{Al}_2\text{O}_3$  by the same synthesis and found particle sizes of ca. 25 nm by XRD and ca. 40 nm by transmission electron microscopy. XRD also shows that the metal loadings (Co+Ni wt%) are similar for all samples ( $33 \pm 2$  wt%) and in agreement with the stoichiometric content of 33 wt%. Correspondingly, XRF and ICP-OES show total Co and Ni loadings of  $31.4 \pm 0.5$  wt% and  $32.7 \pm 0.8$  wt%. Moreover, as seen from Table 1, XRF and ICP-OES confirm the nominal Co-Ni compositions to be correct within 0.5 %.

Table 1: XRD, XRF and ICP-OES analyses on the series of Co-Ni samples. All samples were studied after reactor studies, except for \*, which was a fresh sample.  $\text{Co}_{50}\text{Ni}_{50,\text{i.f.}}$  is an inlet fraction (top layer) of the sample bed in the reactor. Percentages of Co and Ni are atomic% of Co+Ni metal loading.

Sample	XRD		XRF				ICP		
	$D_{\text{Co,Ni}}$ [nm]	Co,Ni [wt%]	Al [wt%]	Co [mol%]	Ni [mol%]	Co+Ni [wt%]	Co [mol%]	Ni [mol%]	Co+Ni [wt%]
$\text{Co}_{20}\text{Ni}_{80}$	28.3	33	30	20	80	31	20	80	33
$\text{Co}_{40}\text{Ni}_{60}$	30.4	34	30	40	60	32	40	60	32
$\text{Co}_{50}\text{Ni}_{50}^*$	27.6	34	30	50	50	32	-	-	-
$\text{Co}_{50}\text{Ni}_{50}$	34.9	33	30	50	50	31	-	-	-
$\text{Co}_{50}\text{Ni}_{50,\text{i.f.}}$	35.3	32	-	-	-	-	-	-	-
$\text{Co}_{60}\text{Ni}_{40}$	26.4	34	30	60	40	31	60	40	33
$\text{Co}_{70}\text{Ni}_{30}$	25.7	34	30	70	30	31	70	30	33

## Curie temperature

Figure 1 shows the mass-specific magnetization,  $\sigma_{\text{R}}$ , of the Co-Ni samples in a static field of 10 mT at temperatures up to 950 °C, normalized to the  $\sigma_{\text{R}}$ -value at 200 °C. From these measurements, the  $T_{\text{C}}$ 's, were determined to 617, 795, 850 and 921 °C for samples  $\text{Co}_{20}\text{Ni}_{80}$ ,  $\text{Co}_{40}\text{Ni}_{60}$ ,  $\text{Co}_{50}\text{Ni}_{50}$ , and  $\text{Co}_{60}\text{Ni}_{40}$ , respectively. From this,  $T_{\text{C}}$  was observed to increase linearly with increasing Co-content in agreement with data in Bozorth<sup>27</sup> (see Fig.1b), which showed an almost linear change in  $T_{\text{C}}$  with composition between Ni ( $T_{\text{C}}=358$  °C<sup>27</sup>) and Co ( $T_{\text{C}}=1121$  °C<sup>27</sup>). For the  $\text{Co}_x\text{Ni}_{(100-x)}/\text{Al}_2\text{O}_3$  samples with  $x \geq 70\%$  Co,  $T_{\text{C}}$  was above the

maximum recorded temperature of 950 °C, and could not be determined. In general, the drop in magnetization close to  $T_C$  was sharp for different samples, with the steepest part of the slopes occurring over a range of approx. 75 °C. This reflects narrow Co-Ni compositions, where the individual nanoparticles have Co-Ni compositions within ca.  $\pm 5\text{wt}\%$  of the nominal compositions of the samples. This is agreement with detailed chemical analyses of individual particles in a similar  $\text{Co}_{50}\text{Ni}_{50}/\text{Al}_2\text{O}_3$  sample.<sup>5</sup>

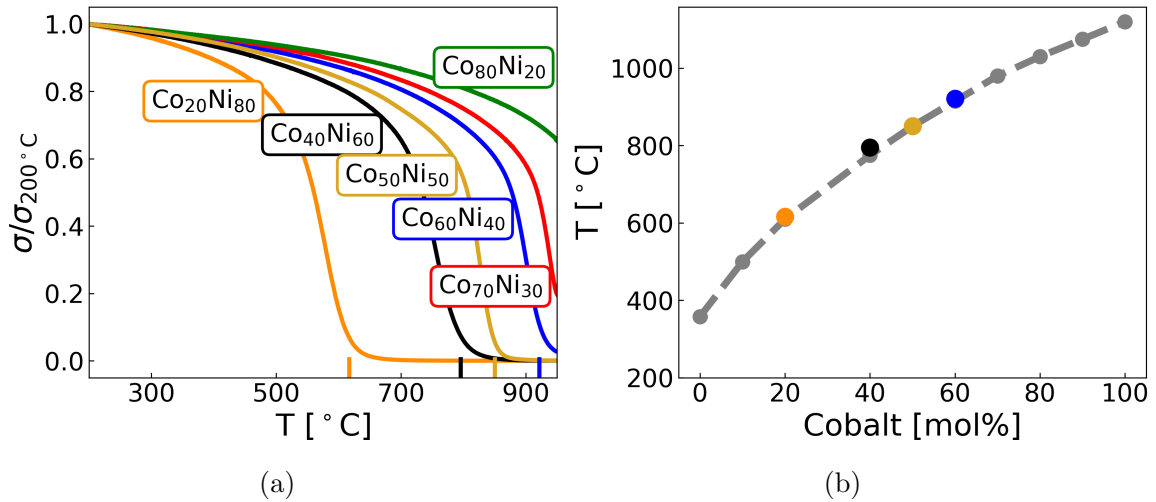


Figure 1: a) Mass-specific magnetization in a field of 10 mT, normalized to the value at 200 °C, as a function of temperature for each sample. The Curie temperatures determined from the curves by Gromme’s two-tangent method are marked on the temperature axis for samples  $\text{Co}_{20}\text{Ni}_{80}$  (617 °C, orange),  $\text{Co}_{40}\text{Ni}_{60}$  (795 °C, black), and  $\text{Co}_{50}\text{Ni}_{50}$  (850 °C, yellow). For sample  $\text{Co}_{60}\text{Ni}_{40}$ , the  $T_C$  of 921 °C (blue) was estimated as from where the tangent of the steepest part of the slope crossed the  $T$ -axis. b) Experimentally obtained values for  $T_C$ , with the same colorscheme as a), along with values from literature (in gray), taken from Bozorth.<sup>27</sup>

## Hysteresis heating

Figure 2a shows the parameters extracted from the hysteresis measurements: the hysteresis area,  $W_h$ , the coercive field,  $\mu_0 H_C$ , and the remnant mass-specific magnetization,  $\sigma_R$ . Specifically, the hysteresis area,  $W_h$ , is the amount of energy dissipated as heat per mass of sample, per field cycle with a given field amplitude,  $B_{\text{app}}$  (maximal applied field in the hysteresis loop), and at temperature,  $T$ :

$$W_h(B_{\text{app}}, T) = \oint_{B_{\text{app}}} \sigma(B, T) dB \quad (4)$$

We found the value of  $W_h(B_{\text{app}}, T)$  by area integration of the hysteresis loops (Fig. 2a) using the trapezoidal rule, giving the values of  $W_h(B_{\text{app}}, T)$  in units of  $\frac{\text{J}}{\text{kg}}$ . As an example, Fig. 2b and 2c shows for  $\text{Co}_{40}\text{Ni}_{60}$  how the hysteresis loop changes with applied field amplitude at constant temperature (550 °C, Fig. 2b) and with temperature at constant field amplitude (55 mT, Fig. 2c). If the hysteresis behaviour is independent of the induction field frequency,  $f$ , then the heat loss per sample mass due to hysteresis, can be found as:

$$P = W_h(B_{\text{app}}, T) * f. \quad (5)$$

The value of  $P$  corresponds to the specific absorption rate (SAR) often reported in induction studies of magnetic nanoparticles<sup>18,19,23</sup> and typically given in units of W/g.

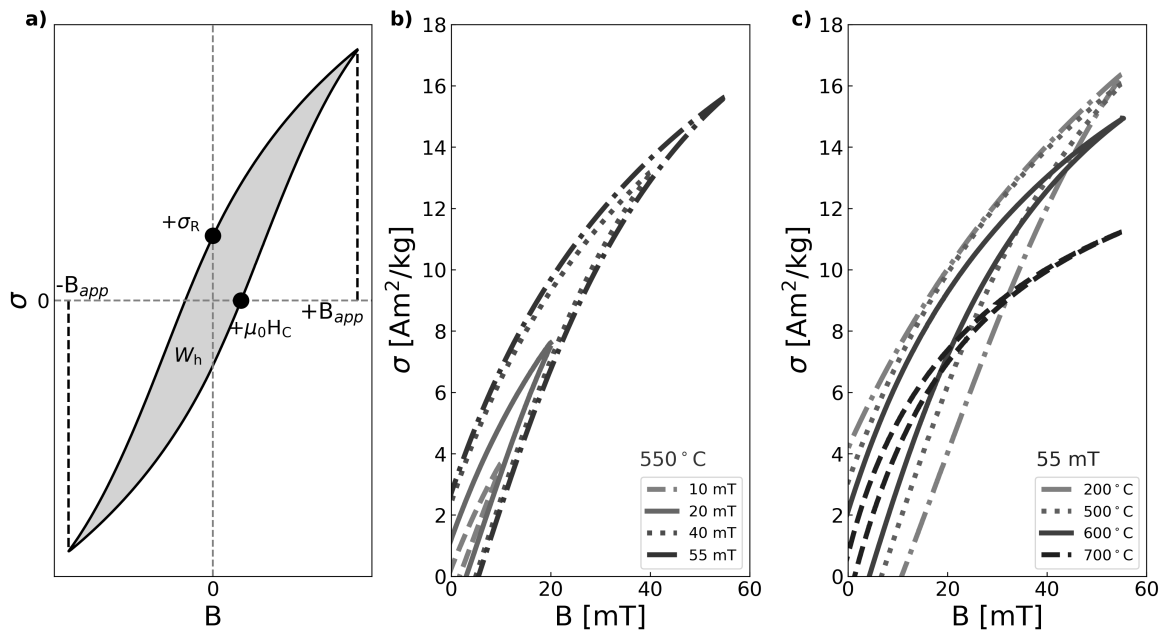


Figure 2: Magnetic hysteresis measurements. a) Sketch of a hysteresis loop with relevant parameters: maximum applied field,  $B_{app}$ , coercive field,  $\mu_0 H_0$ , remnant magnetization,  $\sigma_R$ , and hysteresis area,  $W_h$ . b) Examples of hysteresis loops as a function of  $B_{app}$  for  $\text{Co}_{40}\text{Ni}_{60}$ . c) Examples of hysteresis loops as a function of temperature for  $\text{Co}_{40}\text{Ni}_{60}/\text{Al}_2\text{O}_3$ .

Figure 3 summarizes the values of the parameters  $W_h$ ,  $\mu_0 H_C$ ,  $\sigma_R$  for all the Co-Ni samples as a function of temperature (250 - 950 °C) at field amplitudes of 20 mT, 55 mT and 1500 mT. Here, 1500 mT is the largest field applied in this study and shows the saturation properties of the materials, 55 mT is close to the maximum field amplitude obtainable in our induction-heated reforming setup, and 20 mT is in the middle of the range of field amplitudes typically applied in our induction-heated reforming setup.

From Fig. 3 it can be seen that the sample which has the largest hysteresis area,  $W_h$ , varies with field amplitude and temperature. Hence, there is no single answer to which sample is most suitable for induction heating it depends on available  $B_{app}$  and desired  $T$  and hence on applications.

Specifically we note from Fig. 3 that at a field amplitude  $B_{app}$  of 20 mT and temperatures of around 250 °C,  $W_h$  is larger for the samples with lower Co content, with  $Co_{20}Ni_{80}$  having the largest  $W_h$ . However, upon increasing temperature  $W_h$  decays quickly for the  $Co_{20}Ni_{80}$  sample compared to the more Co-rich samples due to its lower  $T_C$ . For the samples with higher cobalt content,  $W_h$  start from progressively lower values at 20 mT and 250 °C, increases with temperature until it falls off when approaching  $T_C$ . The peak in  $W_h$  for  $B_{app} = 20$  mT is found at progressively higher temperatures for increasing Co-content for samples  $Co_{40}Ni_{60}$ ,  $Co_{50}Ni_{50}$ ,  $Co_{60}Ni_{40}$ , and  $Co_{70}Ni_{30}$ , i.e. at different  $T$ , different compositions provide the maximal value of  $W_h$ .

The increase in  $W_h$  with temperature at a low field amplitude of  $B_{app} = 20$ mT is an effect of the hysteresis loops being minor loops at low temperatures. When the temperature is increased, the coercive field decreases, as can be seen from the change in  $\mu_0 H_C$  with increasing temperature for  $B_{app} = 1500$  mT (Fig. 3). The decrease in  $\mu_0 H_C$  with temperature is a magnetic "softening" of the materials which makes more of the hysteresis loop accessible by the applied field (here 20 mT). The peak in  $W_h$  is not seen for the Co-Ni samples when measured at  $B_{app} = 55$  mT and 1500mT. In these cases, the applied field amplitude is higher



than the coercive field at all temperatures (cf. the coercive field measured at 1500 mT is 25 mT or lower for all samples). However, the fact that the intermediate composition  $\text{Co}_{50}\text{Ni}_{50}$  has the largest  $W_h$  at 55 mT, suggests that the full hysteresis area for the magnetically harder, more Co-rich samples (60-80 mol.%Co), is still not revealed at this field amplitude.

The maximum values in  $W_h$  vs. Co-Ni composition shows a maximum at around 50 mol% Co at 55 mT (black dotted line in Fig. 4). At 55 mT, the  $\text{Co}_{50}\text{Ni}_{50}$  sample shows the largest heating among the different samples at approx. 500-700 °C, cf. Fig. 3. The dissipated energy is around 0.5 J/kg sample at 500 °C. At an AC-field frequency of 200 kHz, this would correspond to an anticipated heat dissipation of ca. 100 W/ $g_{\text{sample}}$  or ca. 300 W/ $g_{\text{CoNi}}$ , cf. Eq. 5.

We note that the samples do not show superparamagnetic behaviour. In case of superparamagnetism, the hysteresis parameters  $W_h$ ,  $\mu_0 H_C$ ,  $\sigma_R$  would become zero above at the so-called blocking temperature,<sup>28</sup> but these three parameters all have distinct values up close to the Curie temperature, cf. Fig. 3. Hence, it is reasonable to assume that the hysteresis behavior is independent of frequency for applications, at least in the range of some hundred kHz.

Based on the VSM results, we predict samples with high nickel content to heat more efficiently at lower temperatures in the reactor than samples with a high cobalt content, but also that the heating of Ni-rich samples are restricted to lower temperatures by their  $T_C$ . Conversely, the high Co-mol% samples are less restricted by their  $T_C$ , but show less heating as the material has a lower hysteresis area for the same field amplitude. In Fig. 5, the  $W_h$ -curve for the sample with the maximum hysteresis area at that temperature has been plotted as a function of temperature for  $B_{\text{app}} = 50, 30, \text{ and } 10$  mT. This shows that there is an optimal Co to Ni ratio for maximal heating, depending on the desired operation temperature of reactor and the magnetic field amplitude of the setup. By extension, this means there should be an optimum Co to Ni ratio to maximize methane conversion while minimizing power input.

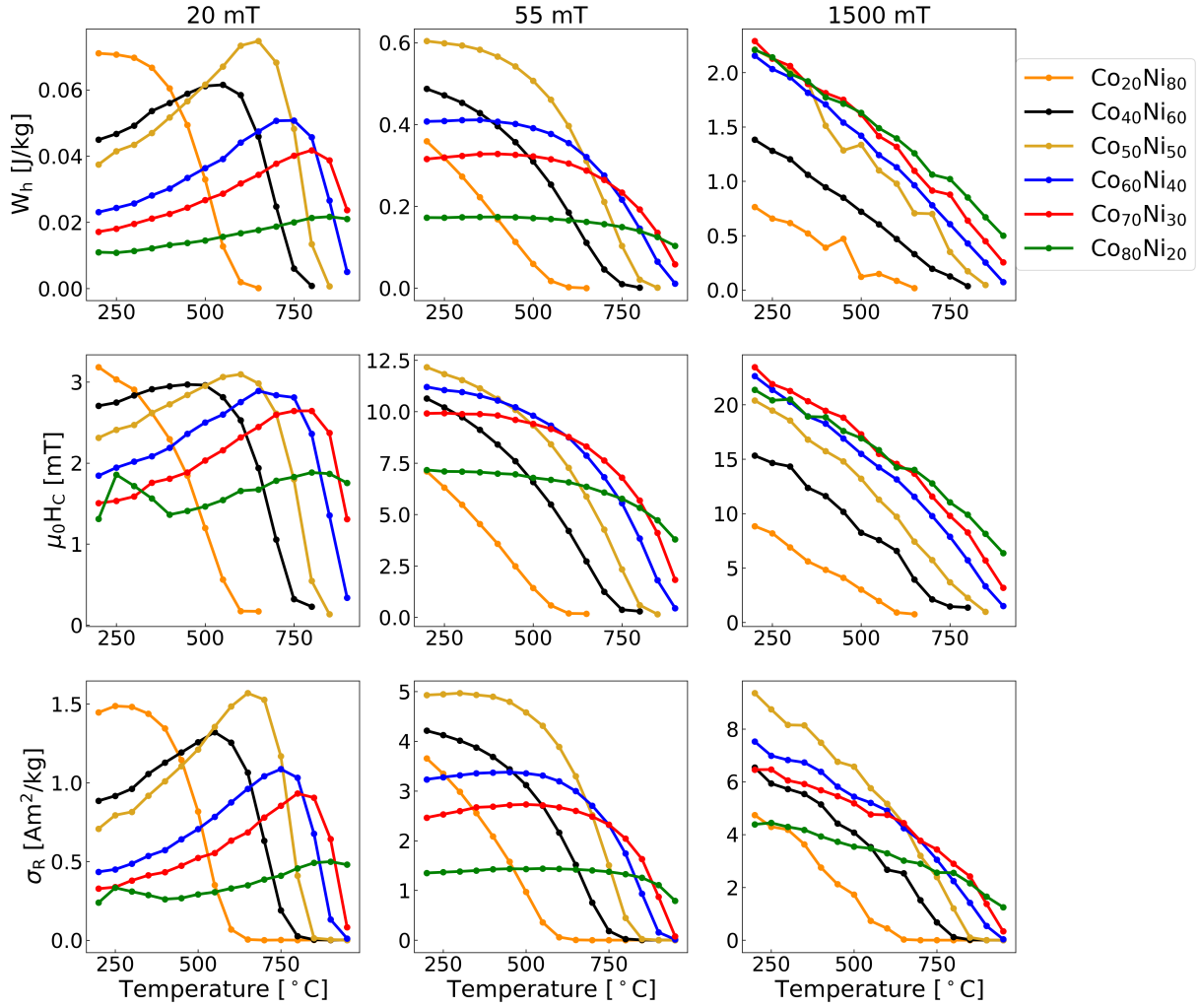


Figure 3: Plots of hysteresis area  $W_h$ , coercive field  $\mu_0 H_C$ , and remanence  $\sigma_R$  as a function of temperature for field amplitudes  $B_{app} = 20, 55,$  and  $1500$  mT.

## Intrinsic activity and optimization

Co-Ni particles may function both as heating agents and as catalysts for induction-heated SMR.<sup>5,6</sup> Due to the dual functionality, the optimal Co-Ni composition will depend both on magnetic properties (described above) and catalytic properties, spanning from Ni, which is a preferred catalysts for steam reforming, to Co, which has very low activity towards steam reforming.<sup>29</sup> Figure 4 shows the intrinsic reaction rate at  $450$  °C and  $500$  °C, the Curie temperatures, and the maximum hysteresis area for each sample at a  $B_{app}$  of  $55$  mT. There is a clear decline in activity towards zero as the cobalt content increases, opposed

by an increasing  $T_C$ . There is an apparent optimum in hysteresis area for  $\text{Co}_{50}\text{Ni}_{50}/\text{Al}_2\text{O}_3$ . From Fig. 4 it can be seen that utilizing these high  $T_C$  nanoparticles for high temperature application comes with a compromise in catalytic activity. This tunability of the magnetic and catalytic properties of  $\text{Co}_x\text{Ni}_{(100-x)}/\text{Al}_2\text{O}_3$  comes as a consequence of cobalt and nickel being fully miscible in all proportions.<sup>27</sup>

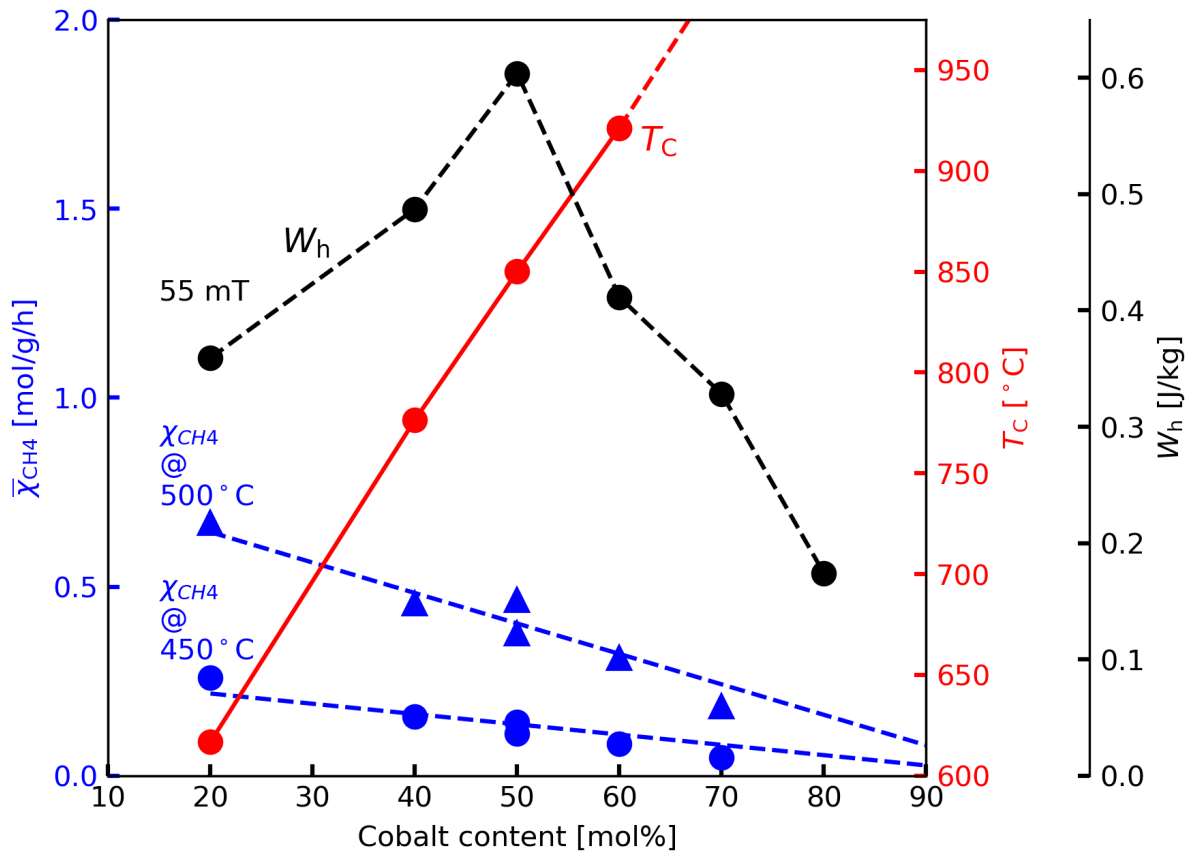


Figure 4: Intrinsic methane conversion obtained from activity measurements (in blue), with dashed lines as guides to the eye, maximal hysteresis area  $W_h$  at  $B_{\text{app}} = 55$  mT (in black) with dashed line connecting points, and Curie temperature (in red) with a solid guide to the eye, all as a function of cobalt-content. The dashed red guide to the eye is the estimated  $T_C$  for samples with  $T_C > 950$  °C

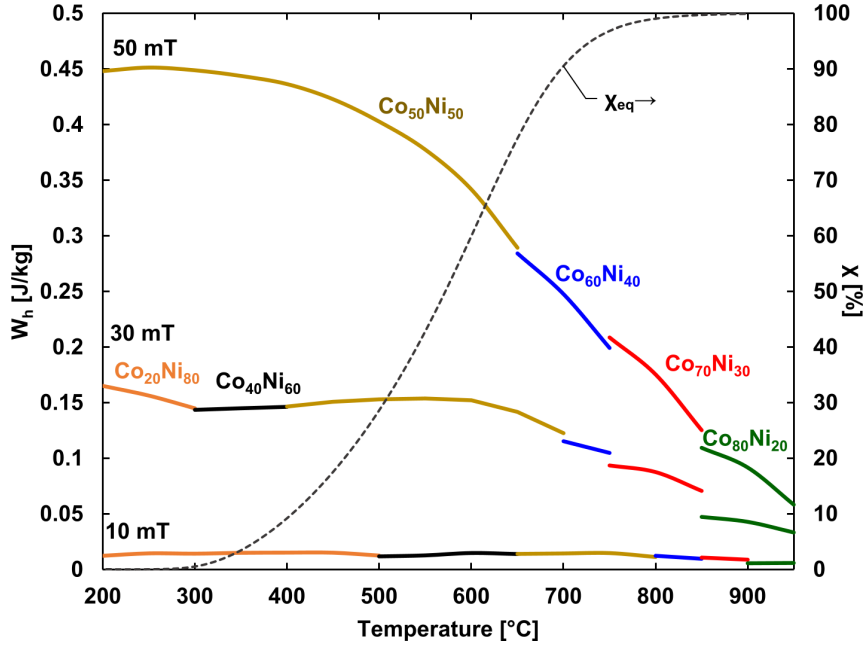


Figure 5: The curve-section with the maximum hysteresis heating  $W_h$  of all the samples in a certain temperature-range plotted as a function of temperature for  $B_{app} = 10, 30,$  and  $50$  mT. The theoretical equilibrium methane conversion,  $X_{eq}$ , as a function of temperature is plotted as a dashed line.

## Induction-heated reforming

We tested the trends seen for  $W_h$  against steam reforming measurements driven by induction heating. Figure 6 shows the temperature obtained by induction-heated SMR for samples  $Co_{20}Ni_{80}$  and  $Co_{40}Ni_{60}$  as a function of field amplitude  $B_{app}$ , for flows of 100, 250 and 500  $\frac{NmL}{min}$   $CH_4$ , at a steam to carbon ratio of 2. The maximum temperature reached in a flow of 100  $\frac{NmL}{min}$   $CH_4$  in Fig. 6 was 588 °C and 757 °C for  $Co_{20}Ni_{80}$  and  $Co_{40}Ni_{60}$ , respectively, which is 29 and 38 °C below the estimated  $T_C$  for the respective samples (dashed lines in Fig. 6). This agrees with a power balance achieved in the system below  $T_C$  between heat dissipated by hysteresis, heat consumed by the SMR reaction, and heat lost to the surroundings through the reactor walls and by the gas flow. The points in Fig. 6 that had the highest temperature for these two samples had an average methane conversion of 57 % for  $Co_{20}Ni_{80}$  and 94 % for  $Co_{40}Ni_{60}$ . Considering the equilibrium conversion (plotted in Fig. 5), temperatures of 600 °C and 750 °C would give conversions of around 60 and 96 %, respectively, which is

similar to the conversions obtained experimentally. The obtained operational temperatures also match the temperatures of 600 °C and 750 °C above which the  $W_h$ -curves in Fig. 3 have almost fully decayed.

These results demonstrate that the SMR operation temperature can be tuned using the composition. This is generally very interesting as a way to avoid overheating in catalytic processes. The maximum operating temperature could only be seen for the  $\text{Co}_{20}\text{Ni}_{80}$  and  $\text{Co}_{40}\text{Ni}_{60}$  samples, as the induction-heated reforming setup was not designed to operate temperatures higher than approx. 870 °C, but similar behavior at higher temperatures is expected below  $T_C$  for the different samples.

Figure 7 shows the methane conversion  $\bar{\chi}_{\text{CH}_4}$  as a function of  $B_{\text{app}}$  for each sample, at a flow of 250  $\frac{\text{NmL}}{\text{min}}$   $\text{CH}_4$ . It can be seen that the  $\text{Co}_{20}\text{Ni}_{80}$  sample responds quickly even to a very low field amplitude, but is also limited to a very low operating temperature and hence low conversion, as a result of the low  $T_C$ . This agrees with what was seen in the VSM results (Fig. 3), where the  $\text{Co}_{20}\text{Ni}_{80}$  sample has a large hysteresis area compared to the other samples at a low field and low temperatures. As the cobalt content increases, the samples can heat to higher temperatures as  $T_C$  increases, which is also reflected in the curves in Fig. 7. Notice, that a higher  $B_{\text{app}}$  is necessary to reach the same conversion when the cobalt content increases. This correlates with the increasing magnetic hardness with increasing Co-content (see Fig. 7). In practice, this could indicate a benefit from tuning the induction-coil to the most optimal  $B_{\text{app}}$  for the sample in question, at the specific temperature needed, thus reducing the power needed to drive the induction field.

In this study, we have run SMR with one Co-Ni composition at a time, but the difference in magnetic and hence induction properties for the different Co-Ni samples could potentially be exploited to make layered reactors in order to further optimize the methane conversion. Specifically, using the most reactive, Ni-rich, samples at the top of the reactor, and shifting

towards the cobalt-rich samples in the bottom where the low intrinsic activity is compensated by the high temperatures, allows for engineering an overall high reaction rate through the entire catalyst bed. As seen from Fig. 5, the optimal layering of material depends on the field amplitude, dictating  $\text{Co}_{50}\text{Ni}_{50}$  being the first layer for  $B_{\text{app}} = 50$  mT, and  $\text{Co}_{20}\text{Ni}_{80}$  being the first layer for  $B_{\text{app}}=30$  and 10 mT.

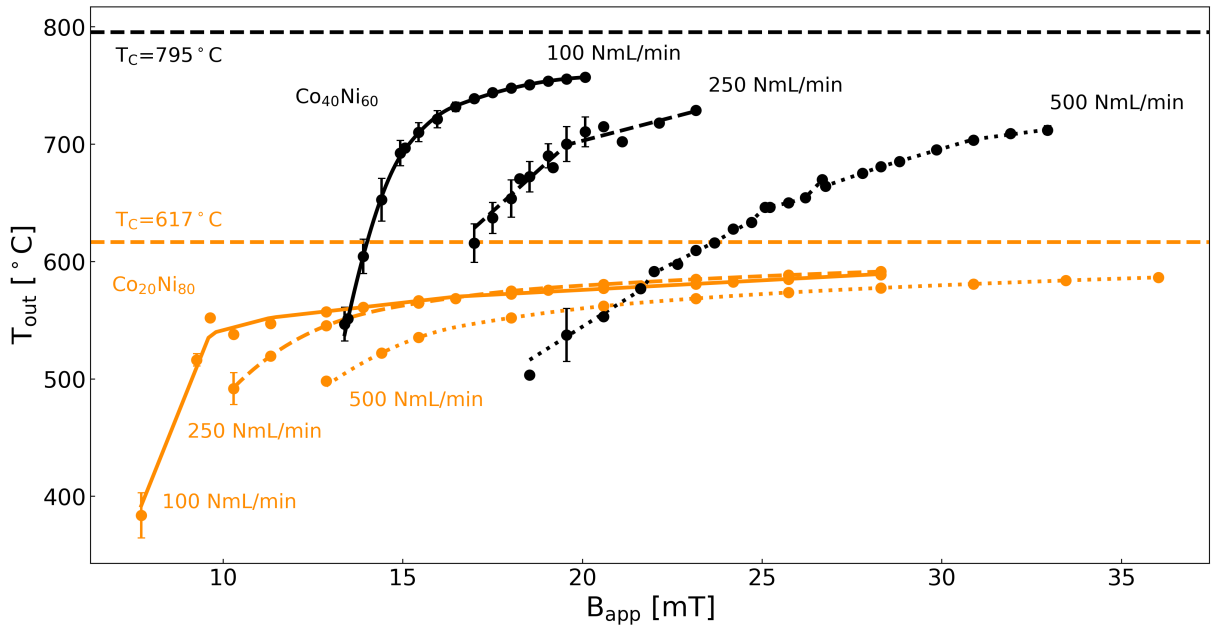
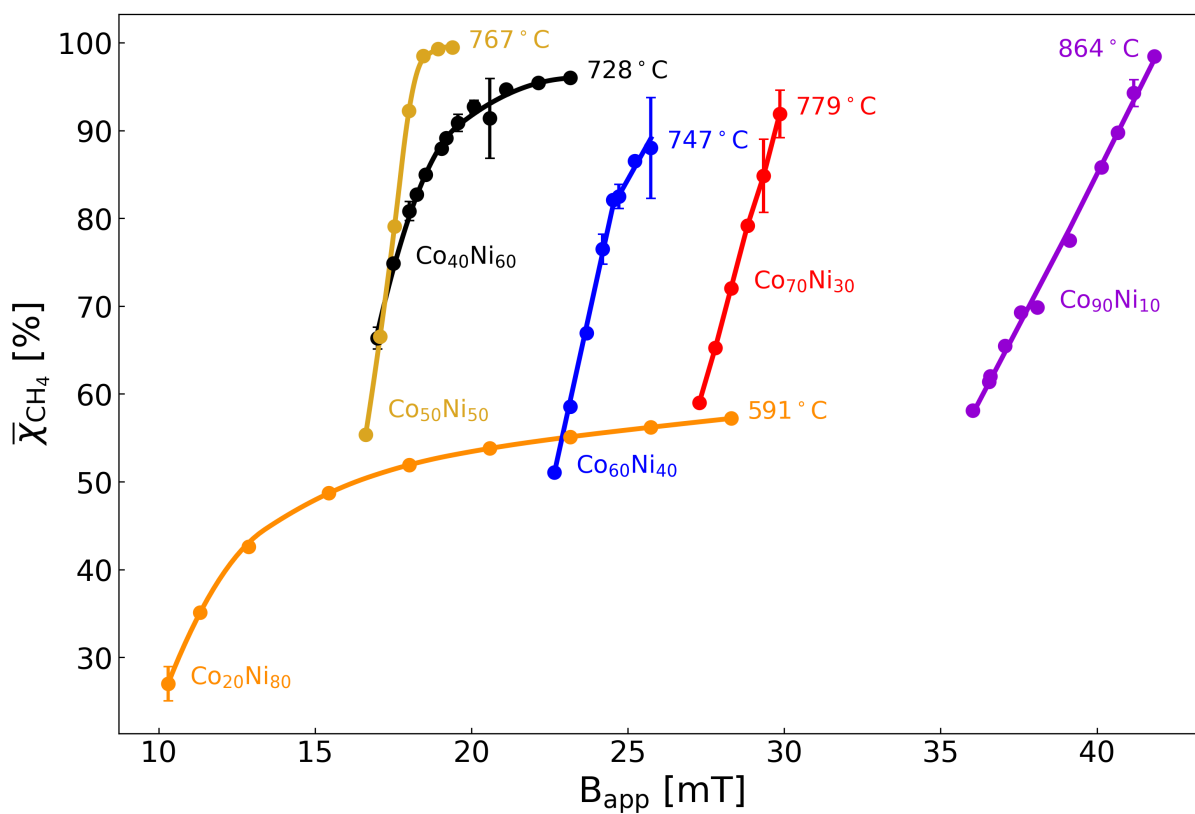


Figure 6: Outlet temperature of steam methane reformer as a function of field amplitude. Orange data are for  $\text{Co}_{20}\text{Ni}_{80}$  and black data for  $\text{Co}_{40}\text{Ni}_{60}$ . Guides to the eye added for ease of viewing:  $100 \frac{\text{NmL}}{\text{min}} \text{CH}_4$  (solid),  $250 \frac{\text{NmL}}{\text{min}} \text{CH}_4$  (dashed), and  $500 \frac{\text{NmL}}{\text{min}} \text{CH}_4$  (dotted). Horizontal dashed lines at  $617^\circ\text{C}$  and  $795^\circ\text{C}$  are the  $T_C$ 's for samples  $\text{Co}_{20}\text{Ni}_{80}$  and  $\text{Co}_{40}\text{Ni}_{60}$ , respectively. Error bars indicate the standard deviation from repeated measurements ( $n \geq 3$ ).



## Conclusions

We have shown for 30 nm Co-Ni particles that the amount of heat delivered to the steam reforming reaction through induction-heating directly relates to the magnetic properties of the Co-Ni material measured by VSM. The magnetic properties can be tuned by changing the Co:Ni ratio. High Ni-content gives rise to high initial hysteresis area and high intrinsic activities, but low Curie temperature. On the other hand, high Co-content gives rise to smaller hysteresis heating and lower intrinsic activities, but higher operation temperatures. The hysteresis heating plotted versus temperature show a peak-feature, when the field amplitude is below the coercive field due to the hysteresis loops being minor loops at low temperatures. The Curie temperature represents a hard upper bound for the operational temperatures available for induction-heated steam reforming, and is freely tunable between cobalt's and nickel's Curie temperatures by changing the Co:Ni ratio. This hard upper bound presents an opportunity to tune the maximum operational temperature in a reactor to avoid overheating, as the material properties auto-regulates the temperature to be below a certain value. This means that there is an optimum temperature-range of operation for a certain Co:Ni-ratio and field amplitudes. This, coupled with the trends seen for the hysteresis areas, could potentially be utilized in a layered-style reactor, with each material being placed in the temperature-zone where their induction-heating is the most optimal, and with induction-coils tuned to these conditions, hence minimizing the required energy needed to heat the reactor.

## Acknowledgement

The work has been funded by Innovation Fund Denmark (Grant number: 5160-00004B).



## References

- (1) Rostrup-Nielsen, J.; Christiansen, L. J. In *Concepts in Syngas Manufacture*; Hutchings, G. J., Ed.; London : Imperial College Press, 2011; Vol. 10.
- (2) IEA, *The Future of Hydrogen*; 2019; <https://www.iea.org/reports/the-future-of-hydrogen>.
- (3) Barreto, L.; Makihira, A.; Riahi, K. The hydrogen economy in the 21st century: a sustainable development scenario. *International Journal of Hydrogen Energy* **2003**, *28*, 267–284.
- (4) Agency, I. E. *CO<sub>2</sub> Capture and Storage: A Key Carbon Abatement Option*; 2008; p 264, <https://doi.org/https://doi.org/10.1787/9789264041417-en>.
- (5) Vinum, M. G.; Almind, M. R.; Engbæk, J. S.; Vendelbo, S. B.; Hansen, M. F.; Frandsen, C.; Bendix, J.; Mortensen, P. M. Dual-Function Cobalt–Nickel Nanoparticles Tailored for High-Temperature Induction-Heated Steam Methane Reforming. *Angewandte Chemie International Edition* **2018**, *57*, 10569–10573.
- (6) Mortensen, P. M.; Engbæk, J. S.; Vendelbo, S. B.; Hansen, M. F.; Østberg, M. Direct Hysteresis Heating of Catalytically Active Ni-Co Nanoparticles as Steam Reforming Catalyst. *Industrial and Engineering Chemistry Research* **2017**,
- (7) Mamiya, H.; Jeyadevan, B. In *Nanomaterials for Magnetic and Optical Hyperthermia Applications*; Fratila, R. M., De La Fuente, J. M., Eds.; Micro and Nano Technologies; Elsevier, 2019; pp 13 – 39.
- (8) Salunkhe, A. B.; Khot, V. M.; Pawar, S. H. Magnetic hyperthermia with magnetic nanoparticles: A status review. *Current Topics in Medicinal Chemistry* **2014**, *14*, 572–594.

- (9) Hervault, A.; Thanh, N. T. K. Magnetic nanoparticle-based therapeutic agents for thermo-chemotherapy treatment of cancer. *Nanoscale* **2014**, *6*, 11553–11573.
- (10) Lartigue, L.; Hugounenq, P.; Alloyeau, D.; Clarke, S. P.; Lévy, M.; Bacri, J.-C.; Bazzi, R.; Brougham, D. F.; Wilhelm, C.; Gazeau, F. Cooperative Organization in Iron Oxide Multi-Core Nanoparticles Potentiates Their Efficiency as Heating Mediators and MRI Contrast Agents. *ACS Nano* **2012**, *6*, 10935–10949.
- (11) Hergt, R.; Dutz, S.; Müller, R.; Zeisberger, M. Magnetic particle hyperthermia: nanoparticle magnetism and materials development for cancer therapy. *Journal of Physics: Condensed Matter* **2006**, *18*, S2919–S2934.
- (12) Ceylan, S.; Friese, C.; Lammel, C.; Mazac, K.; Kirschning, A. Inductive heating for organic synthesis by using functionalized magnetic nanoparticles inside microreactors. *Angewandte Chemie - International Edition* **2008**,
- (13) Chaudhuri, S. R.; Hartwig, J.; Kupracz, L.; Kodanek, T.; Wegner, J.; Kirschning, A. Oxidations of allylic and benzylic alcohols under inductively-heated flow conditions with gold-doped superparamagnetic nanostructured particles as catalyst and oxygen as oxidant. *Advanced Synthesis and Catalysis* **2014**,
- (14) Hartwig, J.; Ceylan, S.; Kupracz, L.; Coutable, L.; Kirschning, A. Heating under high-frequency inductive conditions: Application to the continuous synthesis of the neurolepticum olanzapine (Zyprexa). *Angewandte Chemie - International Edition* **2013**,
- (15) Chatterjee, S.; Degirmenci, V.; Aiouache, F.; Rebrov, E. V. Design of a radio frequency heated isothermal micro-trickle bed reactor. *Chemical Engineering Journal* **2014**,
- (16) Bordet, A.; Lacroix, L. M.; Fazzini, P. F.; Carrey, J.; Soulantica, K.; Chaudret, B. Magnetically Induced Continuous CO<sub>2</sub> Hydrogenation Using Composite Iron Carbide Nanoparticles of Exceptionally High Heating Power. *Angewandte Chemie - International Edition* **2016**,

- (17) Niether, C.; Faure, S.; Bordet, A.; Deseure, J.; Chatenet, M.; Carrey, J.; Chaudret, B.; Rouet, A. Improved water electrolysis using magnetic heating of FeC-Ni core-shell nanoparticles. *Nature Energy* **2018**,
- (18) Meffre, A.; Mehdaoui, B.; Connord, V.; Carrey, J.; Fazzini, P. F.; Lachaize, S.; Respaud, M.; Chaudret, B. Complex Nano-objects Displaying Both Magnetic and Catalytic Properties: A Proof of Concept for Magnetically Induced Heterogeneous Catalysis. *Nano Letters* **2015**, *15*, 3241–3248.
- (19) Asensio, J. M.; Miguel, A. B.; Fazzini, P. F.; van Leeuwen, P. W.; Chaudret, B. Hydrodeoxygenation Using Magnetic Induction: High-Temperature Heterogeneous Catalysis in Solution. *Angewandte Chemie - International Edition* **2019**, *58*, 11306–11310.
- (20) Chen, H.; Lee, J.; Zheng, Y.; Duan, Q. A non-traditional energy transfer process in CWPO heterogeneous reaction for wastewater treatment. *Chemical Engineering Research and Design* **2016**,
- (21) Leclercq, J.; Giraud, F.; Bianchi, D.; Fiaty, K.; Gaillard, F. Novel inductively-heated catalytic system for fast VOCs abatement, application to IPA in air. *Applied Catalysis B: Environmental* **2014**,
- (22) Varsano, F.; Bellusci, M.; La Barbera, A.; Petrecca, M.; Albino, M.; Sangregorio, C. Dry reforming of methane powered by magnetic induction. *International Journal of Hydrogen Energy* **2019**,
- (23) Marbaix, J.; Mille, N.; Lacroix, L. M.; Asensio, J. M.; Fazzini, P. F.; Soulantica, K.; Carrey, J.; Chaudret, B. Tuning the Composition of FeCo Nanoparticle Heating Agents for Magnetically Induced Catalysis. *ACS Applied Nano Materials* **2020**, *3*, 3767–3778.
- (24) Almind, M. R.; Vendelbo, S. B.; Hansen, M. F.; Vinum, M. G.; Frandsen, C.; Mortensen, P. M.; Engbæk, J. S. Improving performance of induction-heated steam methane reforming. *Catalysis Today* **2019**,

- (25) Wang, W.; Tuci, G.; Duong-Viet, C.; Liu, Y.; Rossin, A.; Luconi, L.; Nhut, J. M.; Nguyen-Dinh, L.; Pham-Huu, C.; Giambastiani, G. Induction Heating: An Enabling Technology for the Heat Management in Catalytic Processes. *ACS Catalysis* **2019**,
- (26) PROMASIL®-1000L - Promat. <https://www.promat-hpi.com/en/products/calcium-silicates/promasil-1000l-products>.
- (27) Bozorth, R. M. *Ferromagnetism*; IEEE Press, 1951.
- (28) Bertotti, G. *Hysteresis in Magnetism*; Academic Press, 1998.
- (29) Anderson, J. R.; Boudart, M.; Anderson, J. R. *Catalysis: science and technology, Vol. 5*; Springer, 1984.

## 3.4 Universal Susceptors

In the  $\text{Co}_x\text{Ni}_{(100-x)}/\text{Al}_2\text{O}_3$  system studied in Paper I-III, the catalytic and magnetic properties are intertwined. If the cobalt content increases, the Curie temperature increases, the material gets a higher maximum hysteresis area, and a lower intrinsic activity (as shown in Paper III). Optimizing the magnetic and catalytic properties individually would necessitate a separation of cobalt from nickel. However, if the nickel is separated from the cobalt, the cobalt is no longer stabilized in SMR conditions[56]. Therefore, the cobalt needs to be shielded from the conditions of the reaction somehow, in order to optimize the magnetic heating.

This resulted in our group pursuing a "universal susceptor". In this thesis, a universal susceptor is defined as: "a material that can be heated via an alternating magnetic field under reaction conditions to high temperatures, ( $\geq 200$  °C), while remaining non-reactive, and having the ability to be impregnated, or mixed, with catalyst". Two potential universal susceptors were investigated: treated cobalt-aluminium powder (the "Co- $\text{Al}_2\text{O}_3$  system"), and treated iron-chromium-aluminium powder (the "FeCr- $\text{Al}_2\text{O}_3$  system"). These materials have the ability to create an alumina shell when exposed to the right oxidizing conditions. The idea is that this shell could protect the magnetic material from the harsh conditions in a reactor.

The following two sections summarize the results of the investigations of the Co- $\text{Al}_2\text{O}_3$  system and the FeCr- $\text{Al}_2\text{O}_3$  system as potential universal susceptors. This was a collaborative work, where I was in charge of the magnetic characterisation of the systems. Kimmie K. Moerner prepared and investigated the FeCr- $\text{Al}_2\text{O}_3$  system in her Master's project, and Nikolaj Ø. Langemark prepared and investigated the Co- $\text{Al}_2\text{O}_3$  system in his Master's project. Activity measurements on the Co- $\text{Al}_2\text{O}_3$  system was performed by our partners and Danish Technological institute by Jakob S. Engbæk and Søren B. Vendelbo.

### Cobalt-aluminium

In order to explore the possibility of a universal susceptor, we studied how to preferentially oxidise  $\text{Co}_{79}\text{Al}_{21}$  in order to form a protective shell of alumina around a cobalt core. Via SEM and XRD, it was shown that for particles of around  $5 \mu\text{m}$  this preferential oxidation could yield a cobalt-rich core with a layer of approx.  $0.5 \mu\text{m}$  alumina-shell. However, for particles larger than  $5 \mu\text{m}$ , the particles showed a layer of approx.  $0.4\text{-}0.5 \mu\text{m}$ , where the aluminium had been drawn out of the alloy, with the majority of the particle interior remaining  $\text{Co}_{79}\text{Al}_{21}$ . The sample presented in this section was synthesized by ball-milling commercial  $\text{Co}_{79}\text{Al}_{21}$  (from Goodfellow), after which the powder was heated to  $900$  °C for 10 hours in 5 vol.%  $\text{H}_2$  in Ar, which had passed through a gas bubbler filled with water at  $0$  °C.

VSM was performed on the sample to investigate the hysteresis-heating capabilities of the material, and the results can be seen in Fig. 3.1(a). Here it can be seen how the treatment of the sample more than doubles  $W_h$  below 700 °C in  $B_{app} = 45$  mT, with  $W_h$  showing a maximum of  $0.15 \frac{J}{kg}$  at 700 °C. As the samples approach their  $T_C$  at 855 °C, the difference shrinks, as  $W_h$  approaches zero. The  $T_C$  of 855 °C indicates that the majority of the magnetic material in the sample remains  $Co_{79}Al_{21}$ , with no evidence of the formation of pure Co. In order to draw out more of the aluminium, future studies could focus on ball milling of the powdered alloy in order to get smaller particles ( $\leq 5 \mu m$ ). As seen in Paper IV, it may also be beneficial to reduce the particle size further, down to the nanoscale (the SD size range), to optimize hysteresis heating. Also, the calculations performed in Sec. 1.3 found hysteresis heating to be the dominating heat generating process up until approx.  $8.5 \mu m$ .

The  $Co-Al_2O_3$  sample was mixed with a catalyst of Ni NPs on a  $MgAl_2O_4$  support. The sample could be heated to  $> 600$  °C in a bench scale induction heated SMR reactor using only induction heating. In Fig. 3.1(b) it can be seen how the system could reach approx. 90% conversion or above, for 100, 150, and 200  $\frac{NmL}{min}$  of  $CH_4$ .

These results show a proof-of-concept for how a cobalt-aluminium core-shell system can be synthesized and used as a "universal susceptor" for endothermic reactions when mixed with a catalyst and exposed to an alternating magnetic field. Shown in this study for SMR using a Ni catalyst.

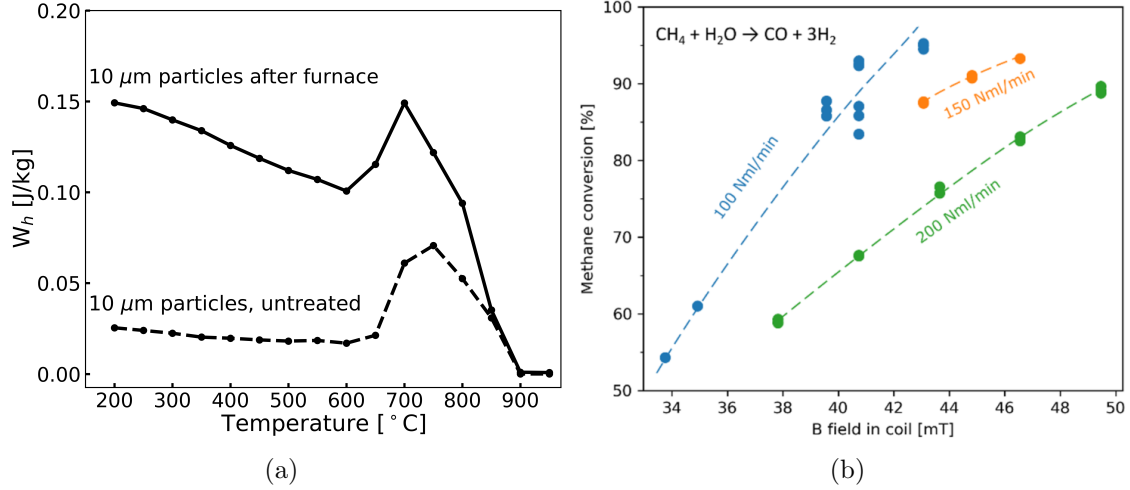


**Figure 3.1:** **a)**  $W_h$  as a function of temperature for the Co- $\text{Al}_2\text{O}_3$  core/shell sample at  $B_{\text{app}} = 45$  mT. **b)** Methane conversion as a function of applied field in the lab-scale hysteresis heated reforming setup of the Co- $\text{Al}_2\text{O}_3$  core/shell system for a hydrogen flow of  $100 \frac{\text{NmL}}{\text{min}}$  (blue),  $150 \frac{\text{NmL}}{\text{min}}$ , and  $200 \frac{\text{NmL}}{\text{min}}$ , with a steam to carbon ratio of 2.

## Iron-chromium-aluminium

$\text{Fe}_{70}\text{Cr}_{25}\text{Al}_5$  was treated in a tube furnace with open ends for 8 hours at 900  $^{\circ}$ C in order to create a protective aluminium-oxide shell. Afterwards, the powder was mixed with  $\text{MgAl}_2\text{O}_4$ -spinel in a ratio of 1:4 FeCrAl to spinel. Finally, this powder was then impregnated with 10 wt.% nickel via incipient wet impregnation (IWI) with  $\text{Ni}(\text{NO}_3)_3$ . The powder impregnated with  $\text{Ni}(\text{NO}_3)_3$  was dried and then calcined at 350  $^{\circ}$ C in air for half an hour. The resulting nickel-oxide nanoparticles were then reduced in the VSM at 850  $^{\circ}$ C for 12 hours in 2.4 vol.%  $\text{H}_2$  in Ar, after 2 hours at 200  $^{\circ}$ C to evaporate any moisture present in the sample.

VSM was used to investigate the magnetic properties of this material, to check that the Ni catalyst particles had not alloyed with the FeCr, and that the hysteresis-properties would be high enough to heat the material to high temperatures ( $> 200$   $^{\circ}$ C). The  $T_C$  curve for the material can be seen in Fig. 3.2(a). Several drops in magnetization are visible in the plot: a clear drop is seen around nickel's Curie temperature at 358  $^{\circ}$ C[23], another drop is seen at 765  $^{\circ}$ C close to  $T_C$  of iron (770  $^{\circ}$ C[23]), as well as at least two drops in between these two. The clear drop in magnetization at the  $T_C$  for nickel indicates that the impregnation was successful with little to no alloying. The sharp drop in magnetization at around 600  $^{\circ}$ C matches the  $\mu_0 H_C$  for a phase of approx.  $\text{Fe}_{75}\text{Cr}_{25}$ [23], whereas the gradual drop between 600

and 750 °C could originate from a range of different compositions of iron-chromium (or iron-chromium-aluminium). The small decay of the signal close to the  $T_C$  of iron could indicate that only small amounts of relatively pure iron was formed during the alumina-forming process.

$W_h$  for this material can be seen for a range of applied fields and temperatures in Fig. 3.2(b). As evident in this figure, the material does exhibit hysteresis, although not as high as, for example, the  $\text{Co}_x\text{Ni}_{(100-x)}/\text{Al}_2\text{O}_3$  system (see Paper I-III). The  $\text{FeCr-Al}_2\text{O}_3$  sample exhibits approx.  $0.006 \frac{\text{J}}{\text{kg}}$  at 500 °C and  $B_{\text{app}} = 55 \text{ mT}$ , at approx. 25 wt.% loading of susceptor material, whereas  $\text{Co}_{50}\text{Ni}_{50}/\text{Al}_2\text{O}_3$  system (see Paper I) exhibited approx.  $0.45 \frac{\text{J}}{\text{kg}}$  under the same conditions, with a loading of 33 wt.%. The  $\text{FeCr-Al}_2\text{O}_3$  sample was still able to be heated inductively, as found via calorimetry. Part of this heating could originate from resistive heating via eddy currents, but further studies are needed in order to answer if this is the case.

This study showed how the  $\text{FeCr-Al}_2\text{O}_3$  system could have the potential to be used as a universal susceptor, although the system is still early in development. A system like this opens up for a broad range of magnetic heating of catalytic reactions using a universal susceptor that is not based on cobalt, which might be preferable in some cases.

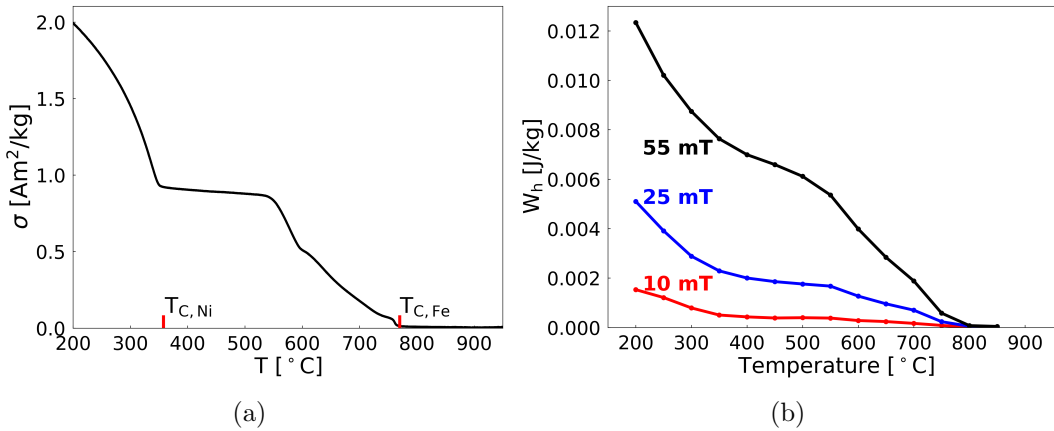


**Figure 3.2:** VSM results from the  $\text{FeCr-Al}_2\text{O}_3$  sample treated in air, mixed with  $\text{MgAl}_2\text{O}_4$ , and impregnated with Ni. **a)** Curie temperature curve for Ni-impregnated  $\text{FeCr-Al}_2\text{O}_3$  on  $\text{MgAl}$ -spinel. **b)**  $W_h$  curve for Ni-impregnated  $\text{FeCr-Al}_2\text{O}_3$  on  $\text{MgAl}_2\text{O}_4$ .



### **3.5 Paper IV: Size-dependent magnetic properties of cobalt nanoparticles for high-temperature applications**

In this paper, we address the role the particle size plays in the energy losses generating the heat for e.g. SMR. To do this, we synthesized samples with cobalt nanoparticle sizes ranging from 19-50 nm, and measured the hysteresis properties of these as a function of applied field (5-1500 mT) and temperature (200-950 °C). The results showed an optimum in  $W_h$ ,  $\sigma_R$ , and  $\mu_0 H_C$ , that depended on the applied field, temperature, and particle size. We found that a particle size distribution centred around 24-31 nm for cobalt had the highest hysteresis area in the broadest range of temperatures and magnetic field amplitudes. This is consistent with the particles being single domain (SD), but not superparamagnetic (SPM), at high temperatures. This is supported by simple estimates of diameters, where SD particles becomes SPM and where they become multidomain (MD).

These studies are of general importance for working with the magnetic properties of cobalt at high temperatures, especially for heating applications, as it gives an approximate size range for maximizing hysteresis heating as a function of applied magnetic field and temperature.

*This paper is currently in preparation*

# Size-dependent magnetic properties of cobalt nanoparticles for high-temperature applications

Mads Radmer Almind, Miriam Varón, Cathrine Frandsen,\* and et al.

*Department of Physics, Technical University of Denmark, 2800 Kgs. Lyngby, Denmark*

E-mail: [\\*frac@fysik.dtu.dk](mailto:*frac@fysik.dtu.dk)

## Abstract

Cobalt has the highest known Curie temperature (1121 °C) and may be used for high-temperature applications such as induction heating of catalytic reactions. However, the high-temperature size-dependent behavior of e.g. power losses in Co particles needs further clarification. To remedy this, we synthesized five samples of polycrystalline cobalt nanoparticles with varying particle sizes (19 nm to 50 nm) on porous support of aluminum-oxide ( $\text{Al}_2\text{O}_3$ ) and studied by vibrating sample magnetometry (VSM) their magnetic hysteresis properties at magnetic field amplitudes ranging from 5 to 1500 mT and temperatures ranging from 200 to 950 °C. From these studies, we find that Co particles with sizes of around 24 nm show the largest hysteresis area ( $W_h$ ) over a large range of fields (from 55 mT and up) and temperatures (200-950 °C). The maximum in hysteresis area shifts towards being for 31 nm particles at a combination of both large field amplitudes and high temperatures (e.g. 500 mT, 800 °C). For a combination of low applied fields and low temperatures (e.g. 45 mT, 200 °C), 19 nm particles show the largest hysteresis area. The maximum in hysteresis measured by VSM is shown to agree with particles being single-domain, but not superparamagnetic at high temperatures.

# Introduction

In all applications of magnetic nanoparticles, it is crucial to understand how the size affects the magnetic properties of the material. This is not trivial, as the magnetic properties are a complex interplay of structure, material, temperature, degree of oxidation, defects, shape, and size distribution. Several groups have, however, studied the effect of particle-size on magnetic hysteresis properties for various materials both experimentally and theoretically. For instance, Kneller and Luborsky<sup>1</sup> showed a dependence of coercivity and remanence on single-domain particle size both experimentally and theoretically on an iron-cobalt system at up to 207 K Lee et al.<sup>2</sup> used a hydrothermal polyol process to synthesize a magnetite multi-grain nanoclusters of well-defined sizes, in a range of 10 to 500 nm, and used this model system to show a maximum in coercivity as a function of particle size at room temperature. Li et al.<sup>3</sup> performed experimental studies on the effect of size for cube-like magnetite nanoparticles in the 10-300 nm range, at 300 K, and also found a maximum in the coercive field as a function of particle size. Through numerical simulations, Bautin et al.<sup>4</sup> estimated a critical size of 32 nm for the magnetic single-domain (SD) to multi-domain (MD) cross-over in polycrystalline cobalt nanoparticles, and quotes a critical size of 45 nm for monocrytalline particles. Several groups, including our own, have been interested in using magnetic susceptor materials in high temperature catalytic applications.<sup>5-11</sup> In these, our group has focused on cobalt-containing alloys.<sup>7,8,10</sup> There has, however, been a lack of research into the optimal size of cobalt nanoparticles at high temperatures for maximizing hysteresis area.

In this study, we have endeavored to experimentally study how the size of cobalt nanoparticles impacts the magnetic properties in fields ranging from 5 to 1500 mT, and temperatures ranging from 200 °C to 950 °C. We investigated the following hysteresis parameters by Vibrating Sample Magnetometry (VSM): the coercive field,  $\mu_0 H_C$ , the mass-specific remnant magnetization,  $\sigma_R$ , and the hysteresis area,  $W_h$ .

## Estimates of critical sizes for hysteresis

The hysteresis area represents the amount of energy lost through various mechanisms in a material, and is found by integration of the hysteresis loop:

$$W_h(B_{\text{app}}, T) = \oint_{B_{\text{app}}} \sigma(B, T) dB \quad (1)$$

where  $W_h$  is the hysteresis-area (in  $\frac{\text{J}}{\text{kg}}$ ),  $B$  is the applied field (in T),  $B_{\text{app}}$  is the field amplitude (in T),  $T$  is the temperature (in °C), and  $\sigma$  is the mass-specific magnetization (in  $\frac{\text{Am}^2}{\text{kg}}$ ). Previous studies have shown that there is a maximum in coercive field and hysteresis area for single-domain particles.<sup>1-4</sup>

If the particles are small enough, they will enter the superparamagnetic (SPM) regime, where the thermal energy can overcome the energy-barrier of the anisotropy energy and flip the magnetization of the nanoparticle. This will happen at some characteristic timescale  $\tau$  that depends both on nanoparticle size and temperature. The magnetization will average to zero if the measuring time,  $t$  (0.3 s in the VSM), is longer than this characteristic timescale. In this case, the hysteresis loop will close such that it has zero coercive field, zero remnant magnetization, and zero hysteresis-area. The relationship between size and blocking temperature,  $T_B$  can be estimated by (here assuming uniaxial anisotropy):

$$T_B = \frac{KV}{k_B \ln(\alpha t / \tau_0)} \quad (2)$$

where  $K = 4.3 \times 10^5 \frac{\text{J}}{\text{m}^3}$  is the anisotropy constant of cobalt at room temperature (RT),<sup>4</sup>  $V$  is the volume of the nanoparticle,  $k_B$  is Boltzmann's constant. The factor  $\alpha$  is usually taken to be around 100,<sup>12</sup> the frequency factor,  $\tau_0$ , is usually taken to be around  $10^{-9}$  s.<sup>12</sup> From Eq. 2, it can be derived that the onset of superparamagnetism will happen below a particle size of ca. 8 nm at RT and of ca. 15 nm at 950 °C, assuming spherical particles and that  $K$  is the same at RT and at 950 °C.

For sufficiently large particles, it will at some point be more energetically favourable to

form magnetic domains rather than remain SD. The critical particle size for the cross over between a SD particle and a two-domain (MD) particle can be estimated for a spherical Co particle with uniaxial anisotropy. We calculate this as the diameter, where the demagnetization energy of a SD particle equals the demagnetization energy of a two-domain particle and the energy of a domain wall through the center of the two-domain particle.<sup>12</sup> The energy contributions are:

$$E_d = \frac{1}{2}\mu_0 V N_d M_S^2 \quad (3)$$

where  $E_d$  is the demagnetization energy,  $\mu_0$  is the vacuum permeability,  $V$  is the volume (assumed to be spherical),  $N_d = \frac{1}{3}$  is the demagnetization-factor for a SD sphere (approximating  $N_d = \frac{1}{6}$  for the two-domain sphere), and  $M_S$  is the saturation magnetization.

$$E_{BW} = \pi\sqrt{AK} \times \text{Area} \quad (4)$$

where  $E_{BW}$  is the domain wall energy,  $A$  is the exchange stiffness,  $K$  is the anisotropy constant of cobalt, and  $\text{Area}$  is the area of the domain wall (assumed to be that of a circle). From this, we find the critical diameter for Co at RT to:

$$d_c = \frac{18\pi\sqrt{AK}}{\mu_0 M_S^2} \quad (5)$$

As can be seen in Eq. 5, this simple calculation of the critical diameter depends on,  $A$ ,  $K$ , and the square of  $M_S$ . Unfortunately, all three parameters depend on temperature,<sup>13–16</sup> and are not well studied at high temperature for fcc cobalt nanoparticles. Myers and Sucksmith<sup>15</sup> found (for a macroscopic cobalt crystal) that the mass specific saturation magnetization went from approx.  $162.5 \frac{\text{Am}^2}{\text{kg}}$  at  $-183 \text{ }^\circ\text{C}$ , to  $161.8 \frac{\text{Am}^2}{\text{kg}}$  at  $20 \text{ }^\circ\text{C}$ ,  $159.1 \frac{\text{Am}^2}{\text{kg}}$  at  $190 \text{ }^\circ\text{C}$ , to  $104.6 \frac{\text{Am}^2}{\text{kg}}$  at  $945 \text{ }^\circ\text{C}$ , with a change from hcp to fcc at  $431 \text{ }^\circ\text{C}$ . The cobalt nanoparticles studied here retain their fcc structure (the high-temperature phase) at room temperature (also seen by Shukla et al.<sup>17</sup>). As the critical diameter in Eq. 5 depends on the square of

the magnetization, the temperature, as well as the phase, could have a large impact on the calculated critical diameter. The anisotropy constant,  $K$ , is also dependent on temperature<sup>14</sup> and particle size,<sup>16</sup> and can vary between  $170 \frac{\text{kJ}}{\text{m}^3}$  to  $230 \frac{\text{kJ}}{\text{m}^3}$  for fcc cobalt nanoparticles<sup>16,18</sup> (although the nanoparticles in these studies were somewhat smaller than the nanoparticles studied here). Likewise, the exchange stiffness,  $A$ , also depends on temperature,<sup>13</sup> and can vary from  $1.3 \times 10^{-11} \frac{\text{J}}{\text{m}}$  and up to  $4.3 \times 10^{-11} \frac{\text{J}}{\text{m}}$ <sup>13</sup> for cobalt, with Moreno et al.<sup>13</sup> calculating a value of  $3.62 \times 10^{-11} \frac{\text{J}}{\text{m}}$  for fcc cobalt. This means that calculations of the critical diameter (via Eq. 5) can vary between 37 nm and 60 nm, using the ranges of parameters listed here (with  $\sigma_s = 161.8 \frac{\text{Am}^2}{\text{kg}}$ ,<sup>15</sup> at 200 °C). The range of 37-60 nm should be an indication of where we would expect to start to see a drop in the coercive field (and by extension, the hysteresis area), as it would start to drop when multiple domains start to form.<sup>1-3</sup> The coercive field should then reach a maximum just before this range of sizes. However, given that the range of sizes that the critical diameter could fall within is quite large, it is evidently challenging to calculate the critical diameter from parameters found in literature. This means, that experimental studies are necessary to investigate the magnetic hysteresis behaviour of cobalt nanoparticles at high temperatures.

## Synthesis

Five samples of Co nanoparticles of different sizes supported on porous 1 mm  $\text{Al}_2\text{O}_3$  spheres were synthesized. These were produced by incipient wetness impregnation (IWI) with cobalt nitrate salt ( $\text{Co}(\text{NO}_3)_2 \cdot 6\text{H}_2\text{O}$ ), followed by drying in air and a heat treatment processes. Two different heat treatments were carried out: 1) heat treatment in one step using 5%  $\text{H}_2$  in argon atmosphere (samples IN-01, IN-02 and IN-05); and 2) two-step heat treatment, first by calcining the samples in air and then reducing the samples in pure hydrogen (samples IN-06 and IN-07). By modifying the metal loading and the heat treatment conditions, different particle sizes were obtained. The preparation details of the five samples are given in Table

1.

Table 1: Sample preparation details.

Heat treatment 1	Sample name	wt.% Co	Drying, Air	Heat treatment, 5% H <sub>2</sub>	
	IN-01	10	12 h, RT	120 °C, 3 h 500 °C 3 h 1000 °C, 3 h	
	IN-02	18	48-72 h, RT	80 °C, 3.5 h 120 °C, 2 h 500 °C 3 h 1000 °C, 5 h	
	IN-05	14	80 °C (until dry)	120 °C, 4 h 500 °C, 3 h 1000 °C, 8 h	
Heat treatm. 2	Sample name	wt.% Co	Drying, Air	Calcination, air	Reduction, pure H <sub>2</sub>
	IN-06	10	2 h, RT 75 °C, 1.5 h	120 °C, 3 h 500 °C, 3 h	1000 °C, 3 h
	IN-07	14	2 h, RT 75 °C, 1.5 h	120 °C, 500 °C, 3 h	1000 °C, 3 h

## Characterisation methods

**Transmission electron microscopy (TEM)** images were acquired using a FEI Tecnai T20 G2 microscope. The samples were prepared for TEM by crushing a small amount of the sample in a mortar and suspending the powder in ethanol, followed by drop casting the suspension on a holey carbon Cu-grid.

**X-ray powder diffraction (XRD)** measurements were obtained on the samples using a PANalytical Empyrean Series 2 diffractometer using Cu-K $\alpha$  radiation with a Bragg-Brentano geometry. Each sample was measured at a  $25^\circ < 2\theta < 85^\circ$  range. The data were smoothed (20 points Savitzky–Golay smoothing) and baseline corrected.

**Vibrating Sample Magnetometry (VSM)** was performed using a LakeShore 7407 VSM equipped with a LakeShore 74034 oven option. A small amount of sample (20-40 mg)

was loaded into a boron-nitride cup in an argon atmosphere. The samples were measured at temperatures up to 950 °C and in magnetic fields up to 1.5 T. All measurements were made while supplying 2.4 vol.% H<sub>2</sub> in Ar to the oven option in the VSM.

## Results and discussion

### Sample characterization

Figure 1 shows TEM images of the five samples of Co nanoparticles on Al<sub>2</sub>O<sub>3</sub> support. For each sample, the size of at least 200 Co particles were measured manually from TEM images using the program ImageJ. In the case of spherical particles, the diameter was measured, for non-spherical nanoparticles the longest direction was measured. The resulting size-distributions (seen in Fig. 1 were fitted with either a log-normal distribution (Samples IN-02, IN-05, IN-06, IN-07) or a normal distribution (Sample IN-01), depending what produced the best fit. The obtained particle sizes are given in Table 2. The particle sizes for the five samples are: approx. 19 nm, 24 nm, 31 nm, 40 nm and 50 nm.



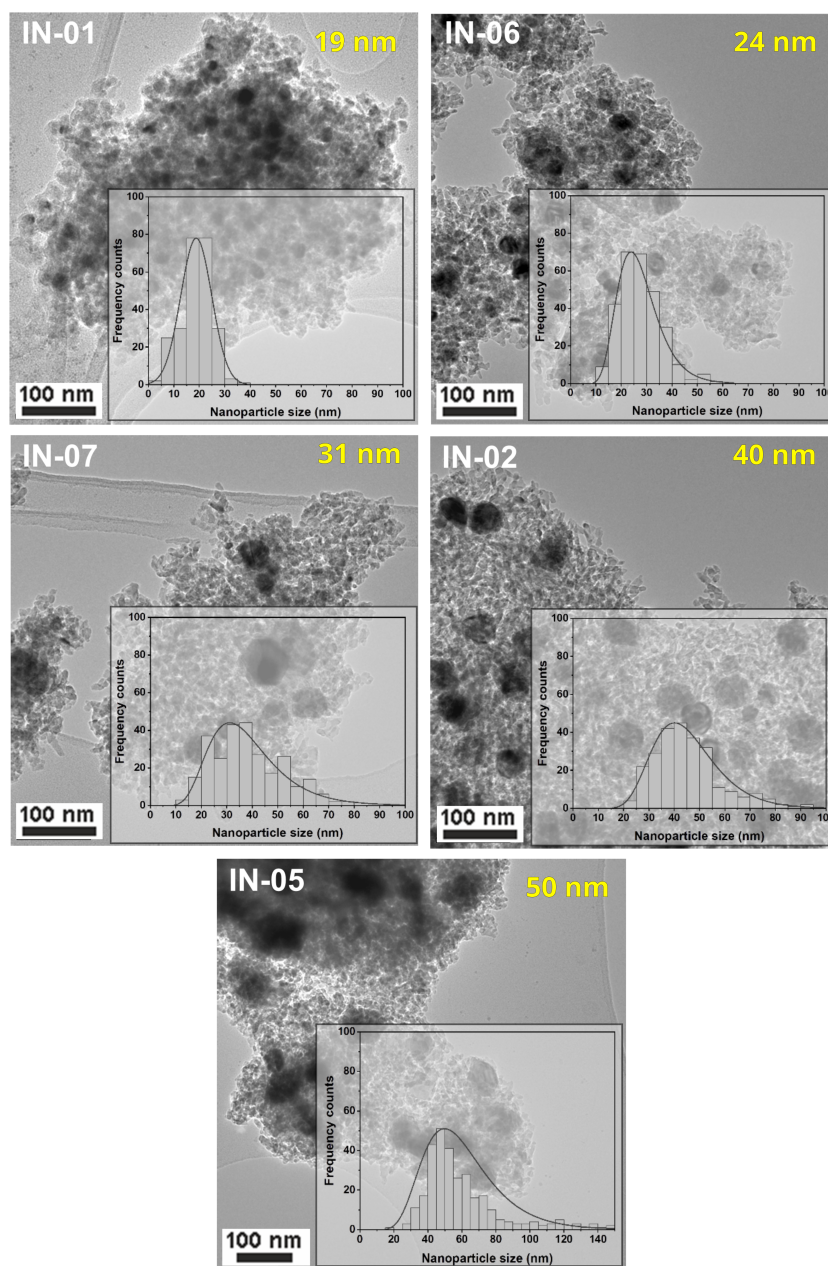


Figure 1: TEM images of samples of Co particles on Al<sub>2</sub>O<sub>3</sub> support. Yellow annotations are the average size (mode) of the particles.

Figure 2 shows XRD data obtained for the five Co samples as well as for a pure Al<sub>2</sub>O<sub>3</sub> support. Rietveld refinement to the data showed a good fit to fcc cobalt nanoparticles on an Al<sub>2</sub>O<sub>3</sub> support, with no signs of significant amounts of other crystalline materials. fcc is the high-temperature structure of cobalt. This implies the transition to fcc cobalt, induced

by the synthesis heat treatment, is irreversible (i.e., the room-temperature hcp phase is not recovered), as also found by Shukla et al.<sup>17</sup> This means that crystalline transitions between fcc and hcp is not expected to show up e.g. in the magnetic measurements. The crystallite size was estimated from the [200] reflection (as the Al signal from the support overlaps with Co at 45°). The sizes are listed in Table 2, and show the same trend in size as the TEM sizes, but generally the crystallite sizes determined from XRD are smaller (ca. 50 %) than the TEM sizes indicating that the particles are polycrystalline.

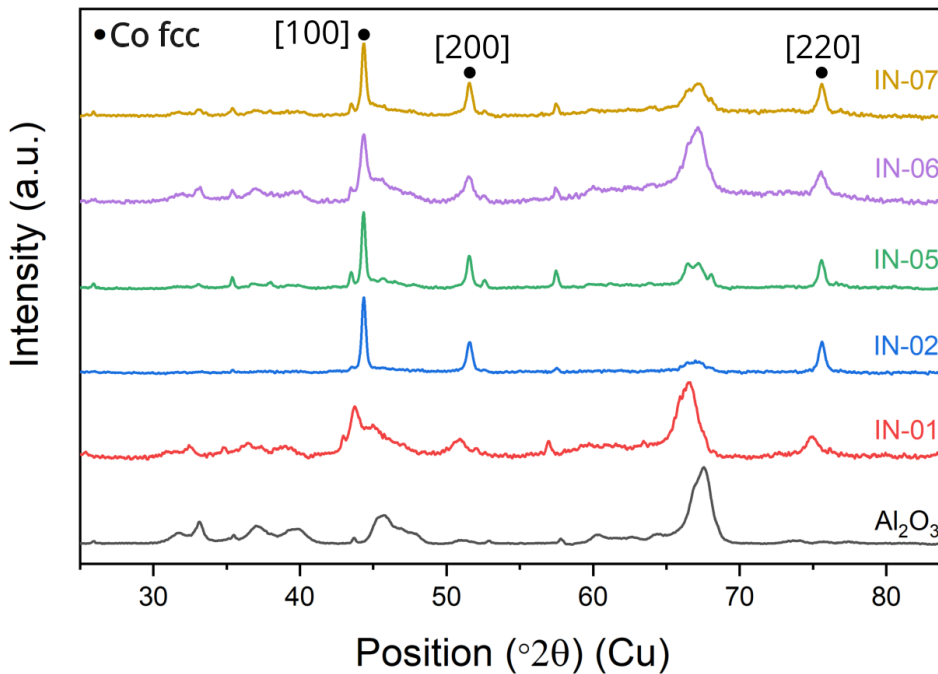


Figure 2: XRD measurements of the Co samples and Al<sub>2</sub>O<sub>3</sub> support. Three cobalt reflections are annotated in the plot.

In order to determine if the samples contained Co only in the form of metallic (reduced) Co, the degree of reduction of Co in the samples we estimated. For this we compared, if there was any reduction in the saturation magnetization of Co in the five samples compared to reference values for Co. The degree of reduction (D.o.R.) of the samples was estimated

by:

$$\text{D.o.R.} = \frac{\sigma_{1500\text{mT},200^\circ\text{C}}^*}{\sigma_{\text{S,ref.}}} \quad (6)$$

where  $\sigma_{1500\text{mT},200^\circ\text{C}}^*$  is the saturation magnetization at  $B_{\text{app}} = 1500 \text{ mT}$ , and  $T = 200 \text{ }^\circ\text{C}$  where the cobalt loading from Tab. 2 has been taken into account, and  $\sigma_{\text{S,ref.}}$  is the reference saturation-magnetization calculated from Myers and Sucksmith's value of  $159.1 \frac{\text{Am}^2}{\text{kg}}$  at  $190 \text{ }^\circ\text{C}$ .<sup>15</sup> The degree of reduction can be seen in Table 2. This, along with the Rietveld refinement, support that the samples, while under investigation in the VSM, consist of metallic cobalt nanoparticles on an alumina substrate, with little to no oxidation, contamination, or alloying of Co.

Table 2: Mode of size-distribution from TEM, estimated crystallite sizes from XRD, cobalt loading in wt.%,  $\sigma$  at  $200 \text{ }^\circ\text{C}$  and  $B_{\text{app}} = 1.5 \text{ T}$ , and degree of reduction, for all samples. Degree of reduction has been abbreviated as D.o.R.. \*IN01 was fitted with a normal distribution, whereas all other samples were fitted with a log-normal distribution.

Sample name	TEM size [nm]	Cryst. size [nm]	Co wt.%	$\sigma$ [ $\frac{\text{Am}^2}{\text{kg}}$ ]	D.o.R. [%]
IN-01*	19	9	10	15.4	97
IN-06	24	12	10	16.3	102
IN-07	31	19	14	22.4	101
IN-02	40	22	18	26.7	93
IN-05	50	24	14	21.4	96

In addition, magnetization curves as a function of temperature were measured to investigate the Curie temperature ( $T_C$ ) or the approach towards it, cf. Fig. 3. The measurements were made under cooling from  $950 \text{ }^\circ\text{C}$  to  $200 \text{ }^\circ\text{C}$  at  $5 \frac{^\circ\text{C}}{\text{min}}$ , with  $B_{\text{app}} = 10 \text{ mT}$ . As cobalt has a  $T_C$  of  $1121 \text{ }^\circ\text{C}$ ,<sup>19</sup> and the VSM oven option is maximally operated at a temperature of  $950 \text{ }^\circ\text{C}$ , we could only observe a partial decrease in magnetization at  $950 \text{ }^\circ\text{C}$ . From the curves in Fig. 3 it can be seen that all samples studied here have a  $T_C$  above  $950 \text{ }^\circ\text{C}$ . This further indicates that the nanoparticles are composed of relatively pure cobalt.

Despite a significant magnetization for all five samples at  $950 \text{ }^\circ\text{C}$ , the smaller particles

show a faster decrease in magnetization with increasing temperature than the samples with larger particle sizes. This is likely to be explained by an approach to the superparamagnetic (SPM) size limit. As the temperature increases, it is possible that the smallest of the particles in the samples may reach their SPM limit, and the magnetization of the sample will drop. Using Eq. 2, the blocking temperature was estimated. A plot of this can be seen in the insert in Fig. 3. This simplified calculation shows that at 950 °C, particles of around 15 nm and below would be superparamagnetic at VSM time scales of 0.3 s. This supports the idea of a fraction of the 19 nm sample could be superparamagnetic at 950 °C, and this could explain the larger decrease in magnetization. It is, however, important to point out, that this calculation is a simple one, and doesn't take the approach to  $T_C$  into account.

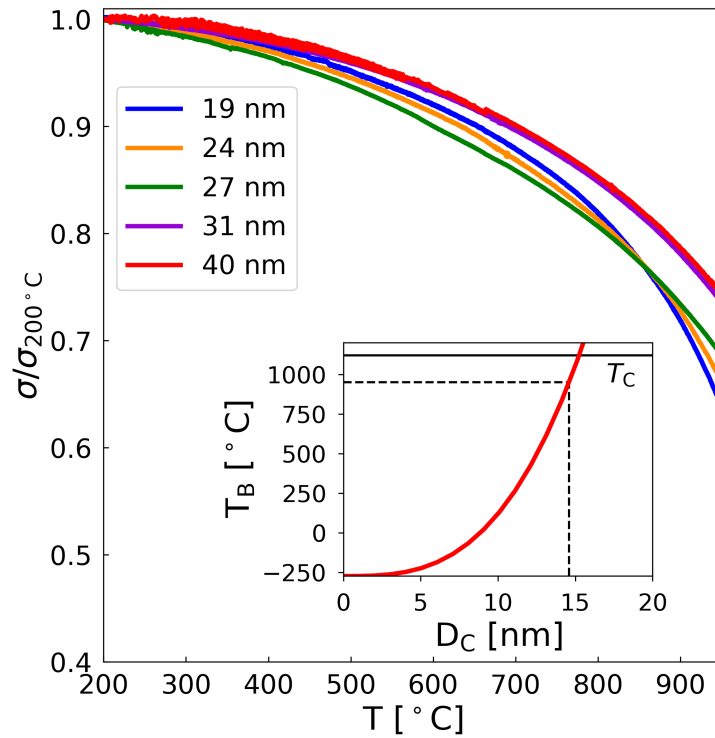


Figure 3: The magnetization  $\sigma$  for all samples as a function of temperature normalized to the value at 200 °C. Insert: Blocking temperature as a function of particle size, calculated using Eq. 2. The horizontal line labeled  $T_C$  on the graph represents cobalt's Curie temperature of 1121°C.<sup>19</sup> Horizontal dashed line in the insert is at 950 °C.

## Hysteresis properties

Hysteresis properties of the five Co samples on alumina support were measured at temperatures from 200 °C to 950 °C, in steps of 50 °C. At each temperature, a series of hysteresis loops were measured using field amplitudes,  $B_{\text{app}}$ 's, ranging from 5 to 1500 mT. In Fig. 4,  $W_h$ ,  $\mu_0 H_C$ , and  $\sigma_R$  can be seen for three representative field amplitudes of 45, 100 and 500 mT, for all five samples. From these measurements, we notice a relative fast decrease  $W_h$ ,  $\mu_0 H_C$ , and  $\sigma_R$  with increasing temperature for the sample with the smallest particle size (19 nm) compared to the samples with larger particle size ( $\geq 31$  nm). Despite being the sample with smallest particle size, the 19 nm sample has relatively large values in  $W_h$ ,  $\mu_0 H_C$ , and  $\sigma_R$  at 200 °C for small field amplitudes ( $< 100$  mT). This fast decrease with temperature could be explained by a similar origin as for the premature drop in magnetization in the  $T_C$  curve, by the approach to the SPM limit. The larger particles ( $\geq 31$  nm) retain, or slightly increase, their  $W_h$  and  $\sigma_R$ , up to higher temperatures than the smallest particles (19 nm) before decreasing. This slight increase (mainly observed at field amplitudes up to 100 mT) could be attributed to a softening of the material (seen as a drop in the coercive field) with temperature, which would lead to a larger hysteresis area at these small field amplitudes with increasing temperature. The 24 nm particles generally show the largest  $W_h$ ,  $\mu_0 H_C$ , and  $\sigma_R$  values.

There is a trend towards saturation values for  $W_h$ ,  $\mu_0 H_C$  and  $\sigma_R$  especially for the larger particles when the applied field increases from 45 mT to 100 and 500 mT. As the field is increased, the 19 nm sample shows a lower increase in hysteresis-area than the larger samples, indicating that these are softer and therefore closer to saturation already at smaller fields. At 500 mT, the samples with the highest hysteresis-areas are the 24 nm sample and the 31 nm sample. The decrease in hysteresis-area for particle-sizes larger than this could be due to a pseudo-single domain to multidomain (MD) structure, as the particle sizes approach the critical diameter (approx. 37-60 nm, found in Eq. 5). We will now go more into detail about how this maximum in  $W_h$  changes as a function of temperature and applied field.

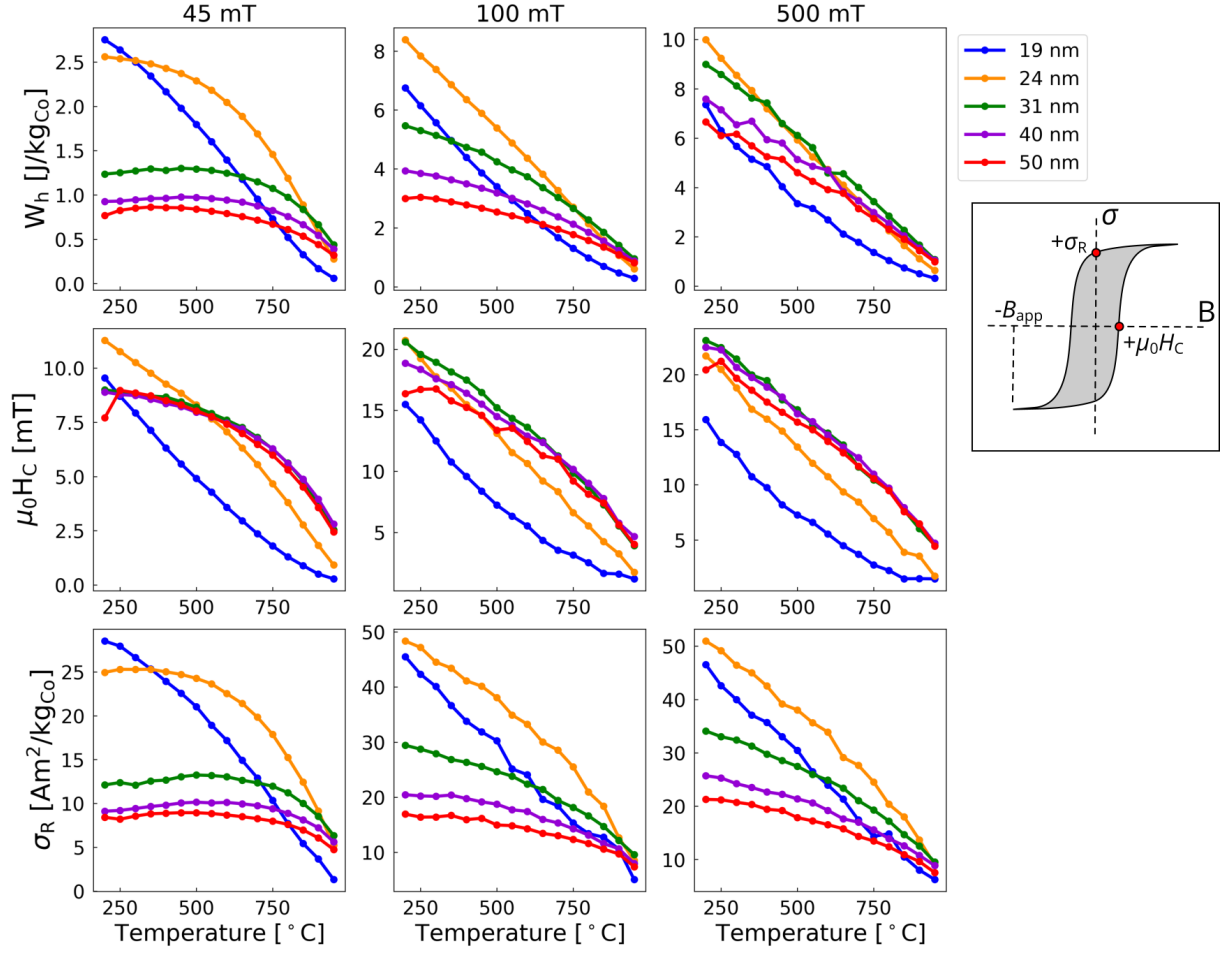


Figure 4: Plots of  $W_h$ ,  $\mu_0 H_C$ , and  $\sigma_R$  obtained from hysteresis loops with field amplitudes of 45 mT, 100 mT and 500 mT at temperatures between 200 and 950 °C. Coloured lines are guides to the eye.  $W_h$  and  $\sigma_R$  have been normalized by the cobalt loading from Tab. 1.

In Fig. 5, the hysteresis-area has been plotted as a function of NP diameter ( $D$ ) for three representative field amplitudes (again 45, 100 and 500 mT), and three representative temperatures (200, 500 and 800 °C). Here it can be seen, that the smallest particles (19 nm) has the largest  $W_h$  at low field amplitudes and temperatures. The particles in the 19 nm samples are most easily magnetized at low field values, and have not yet started to lose their magnetization at 200 °C. However, when the applied field is increased, the 24 nm sample shows the largest  $W_h$ , which matches the effective single domain diameter found by Bautin et al.<sup>4</sup> Moreover, when the temperature is increased, the small particles start losing hysteresis-area, as the thermal energy approaches  $KV$ . This also means that at high field

amplitudes and a high temperature, the maximal  $W_h$  is seen for the 24 nm samples and this shifts to towards slightly larger particle-size (31 nm) at the highest temperatures.

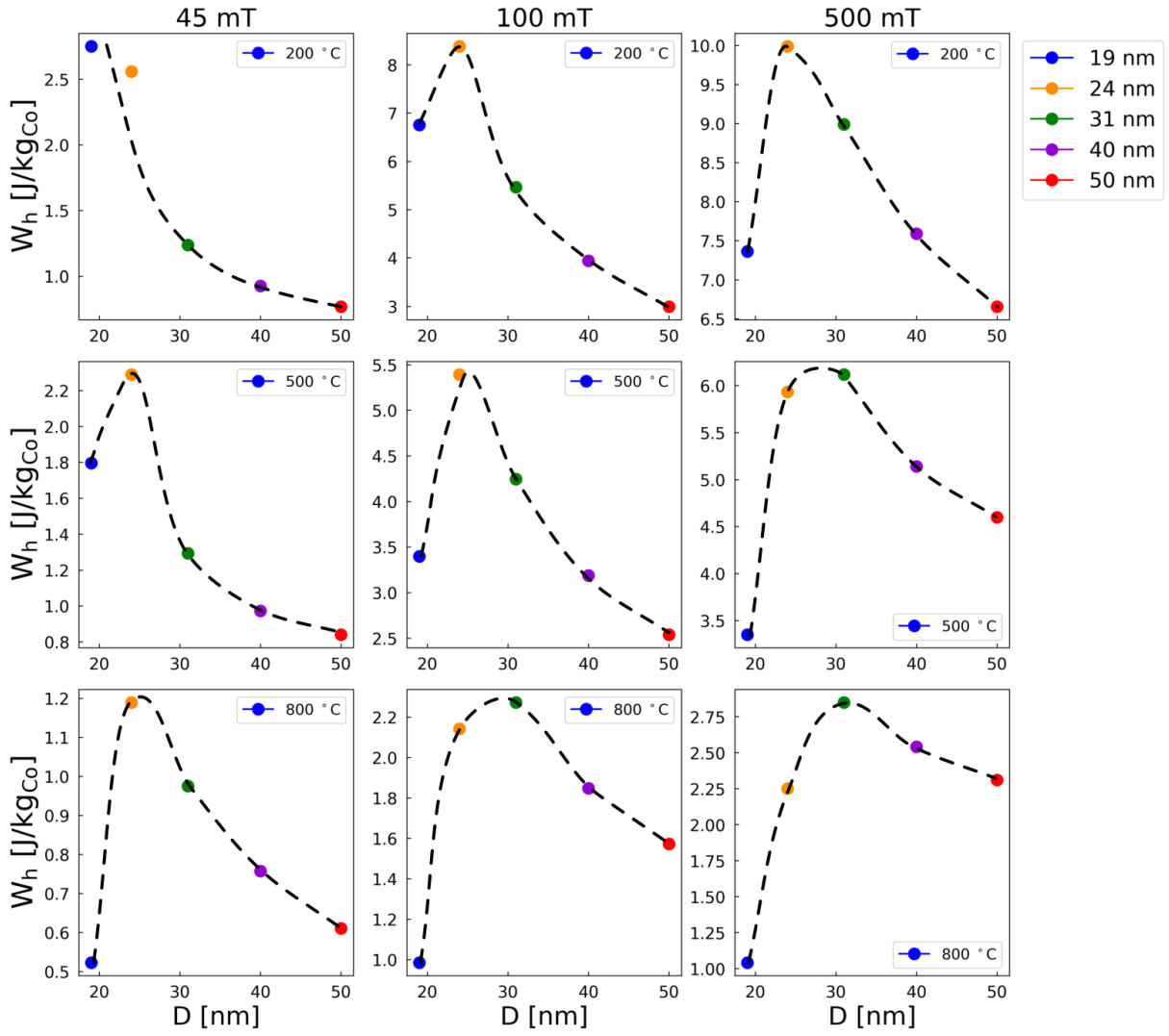


Figure 5: Plot of the hysteresis area, normalized by the cobalt loading, as a function of particle size for applied fields of 45, 100, and 500 mT, at 200, 500, and 800 °C. Black dashed lines are guides to the eye.

## Conclusions

In this paper, we synthesized samples of Co nanoparticles with varying sizes impregnated on porous  $\text{Al}_2\text{O}_3$ -spheres. VSM showed maxima in hysteresis-area, coercive field, and remnant magnetization, which depended on the temperature, magnetic field amplitude, and particle size. The largest hysteresis-area over the broadest range of fields and temperatures was found for the 24 nm sample. At low temperatures and fields, this shifted towards lower particle sizes (19 nm), and at higher temperatures and fields this shifted towards slightly higher particle-sizes (31 nm), but the 24 nm sample was close to the maximum, in all cases. For the samples with small particles, the relatively fast decay of the magnetic properties could be an effect of the smallest particles in that sample becoming superparamagnetic. This is supported by estimates of the blocking temperature as a function of particle size. For larger particles, a switch from a single-domain to a multi-domain magnetic structure could explain the decrease in hysteresis-area. This is supported by a simple calculation of the critical diameter for domain-wall formation. These results could be of use in high temperature magnetic applications of cobalt, as it gives a rough estimate of the particle size most optimal for maximizing hysteresis loss, although the results are of general importance in all applications involving cobalt nanoparticles at elevated temperatures.

## Acknowledgement

This work was funded by Innovation fund Denmark (grant number 5160-00004B).



## References

- (1) KNELLER, E.; LUBORSKY, F. Particle Size Dependence of Coercivity and Remanence of Single-Domain Particles. *Journal of Applied Physics* **1963**, *34*.
- (2) Sung Lee, J.; Myung Cha, J.; Young Yoon, H.; Lee, J.-K.; Keun Kim, Y. Magnetic multi-granule nanoclusters: A model system that exhibits universal size effect of magnetic coercivity. *Scientific Reports* **2015**, *5*.
- (3) Li, Q.; Kartikowati, C. W.; Horie, S.; Ogi, T.; Iwaki, T.; Okuyama, K. Correlation between particle size/domain structure and magnetic properties of highly crystalline Fe<sub>3</sub>O<sub>4</sub> nanoparticles. *Scientific Reports* **2017**, *7*, 9894.
- (4) Bautin, V. A.; Seferyan, A. G.; Nesmeyanov, M. S.; Usov, N. A. Magnetic properties of polycrystalline cobalt nanoparticles. *AIP Advances* **2017**, *7*, 045103.
- (5) Meffre, A.; Mehdaoui, B.; Connord, V.; Carrey, J.; Fazzini, P. F.; Lachaize, S.; Respaud, M.; Chaudret, B. Complex Nano-objects Displaying Both Magnetic and Catalytic Properties: A Proof of Concept for Magnetically Induced Heterogeneous Catalysis. *Nano Letters* **2015**, *15*, 3241–3248.
- (6) Leclercq, J.; Giraud, F.; Bianchi, D.; Fiaty, K.; Gaillard, F. Novel inductively-heated catalytic system for fast VOCs abatement, application to IPA in air. *Applied Catalysis B: Environmental* **2014**,
- (7) Mortensen, P. M.; Engbæk, J. S.; Vendelbo, S. B.; Hansen, M. F.; Østberg, M. Direct Hysteresis Heating of Catalytically Active Ni-Co Nanoparticles as Steam Reforming Catalyst. *Industrial and Engineering Chemistry Research* **2017**,
- (8) Vinum, M. G.; Almind, M. R.; Engbæk, J. S.; Vendelbo, S. B.; Hansen, M. F.; Frandsen, C.; Bendix, J.; Mortensen, P. M. Dual-Function Cobalt–Nickel Nanoparticles Tai-

- lored for High-Temperature Induction-Heated Steam Methane Reforming. *Angewandte Chemie* **0**.
- (9) Varsano, F.; Bellusci, M.; La Barbera, A.; Petrecca, M.; Albino, M.; Sangregorio, C. Dry reforming of methane powered by magnetic induction. *International Journal of Hydrogen Energy* **2019**,
- (10) Almind, M. R.; Vendelbo, S. B.; Hansen, M. F.; Vinum, M. G.; Frandsen, C.; Mortensen, P. M.; Engbæk, J. S. Improving performance of induction-heated steam methane reforming. *Catalysis Today* **2019**,
- (11) Marbaix, J.; Mille, N.; Lacroix, L. M.; Asensio, J. M.; Fazzini, P. F.; Soulantica, K.; Carrey, J.; Chaudret, B. Tuning the Composition of FeCo Nanoparticle Heating Agents for Magnetically Induced Catalysis. *ACS Applied Nano Materials* **2020**, *3*, 3767–3778.
- (12) Blundell, S. *Magnetism in condensed matter*; Oxford University Press, 2001.
- (13) Moreno, R.; Evans, R. F. L.; Khmelevskiy, S.; Muñoz, M. C.; Chantrell, R. W.; Chubykalo-Fesenko, O. Temperature-dependent exchange stiffness and domain wall width in Co. *Physical Review B* **2016**, *94*, 104433.
- (14) Staunton, J. B.; Szunyogh, L.; Buruzs, A.; Gyorffy, B. L.; Ostanin, S.; Udvardi, L. Temperature dependence of magnetic anisotropy: An ab initio approach. *Physical Review B* **2006**, *74*, 144411.
- (15) MYERS, H.; SUCKSMITH, W. THE SPONTANEOUS MAGNETIZATION OF COBALT. *Proceedings of the Royal Society of London Series A-mathematical and Physical Sciences* **1951**, *207*, 427–446.
- (16) Hillenkamp, M.; Oyarzún, S.; Troc, N.; Ramade, J.; Tamion, A.; Tournus, F.; Dupuis, V.; Rodrigues, V. Size effects of the magnetic anisotropy of fcc cobalt nanoparticles embedded in copper. *The European Physical Journal D* **2017**, *71*, 330.

- (17) Shukla, N.; Svedberg, E. B.; Ell, J.; Roy, A. J. Surfactant effects on the shapes of cobalt nanoparticles. *Materials Letters* **2006**, *60*, 1950–1955.
- (18) Jamet, M.; Wernsdorfer, W.; Thirion, C.; Maily, D.; Dupuis, V.; Mélinon, P.; Pérez, A. Magnetic Anisotropy of a Single Cobalt Nanocluster. *Physical Review Letters* **2001**, *86*, 4676–4679.
- (19) Bozorth, R. M. *Ferromagnetism*; IEEE Press, 1951.

### 3.6 Paper V: Retrofittable plug-flow reactor for in situ high-temperature vibrating sample magnetometry

Throughout the project, VSM was used to study the magnetic properties of various susceptor-materials used for heating in induction heated SMR. In our conventional VSM from Lake Shore the sample is situated in a closed boron-nitride cup, in which there is very limited knowledge, or control, of the atmosphere around the sample. Also, conventional VSM has no way of exposing a sample to reducing or oxidizing gas-mixtures relevant to catalysis. Thus, in order to approach in situ conditions, we designed and fabricated a novel retrofittable in situ holder, capable of withstanding the vibration of the VSM, temperatures up to 1000 °C, with the ability to expose the sample to a known gas-mixture chosen by the user, which is not possible in the conventional holder. This system also has the possibility of adding e.g. a mass-spectrometer to analyse the exit-gas.

The paper presented in this section contains a comparison of the retrofittable in situ VSM holder to a conventional high-temperature VSM holder. It showcases the in situ holder's ability to conform to the mass and spatial limitations of the VSM, that it can tolerate the vibrations of the VSM, that is able to be exposed to high temperatures for prolonged periods of time, and that it has the ability to expose a sample to reducing and oxidative gas-mixtures. The current prototype is made of inexpensive materials, and can be readily implemented in conventional type VSM's.

One thing not mentioned in this paper is that we suspect that the 2.4 vol.% H<sub>2</sub> i Ar gas mixture used in the conventional VSM oven option wears down the oven. We have gone through approx. one oven a year during this project, and the manufacturer only recommends using argon. Therefore, the repeated exposure to H<sub>2</sub> (which is reducing to metals, and can also lead to hydrogen embrittlement[57]) could be the cause of the ovens breaking after a year. If this is the case, using the in situ option is the only option available for performing measurements in the VSM using other gasses than Ar, save for purchasing a new oven each year.

The retrofittable in situ holder opens up new possibilities for what is possible to measure on commercially available VSM's. With this holder, samples would be able to be measured in a broad range of gas-mixtures, specified by the user, at high temperatures.

*This paper is currently in preparation*

# Retrofittable plug-flow reactor for in situ high-temperature vibrating sample magnetometry

Mads R. Almind,<sup>†</sup> Jakob S. Engbæk,<sup>‡</sup> Mikkel F. Hansen,<sup>¶</sup> Søren B. Vendelbo,<sup>‡</sup>  
Peter M. Mortensen,<sup>§</sup> Christian D. Damsgaard,<sup>†</sup> Ib Chorkendorff,<sup>†</sup> and Cathrine  
Frandsen<sup>\*,†</sup>

<sup>†</sup>*Department of Physics, Technical University of Denmark, DK-2800 Kgs. Lyngby,  
Denmark*

<sup>‡</sup>*Danish Technological Institute, DK-2630 Taastrup, Denmark*

<sup>¶</sup>*Department of Health Technology, Technical University of Denmark, DK-2800 Kgs.  
Lyngby, Denmark*

<sup>§</sup>*Haldor Topsøe A/S, DK-2800 Kgs. Lyngby, Denmark*

E-mail: [\\*frac@fysik.dtu.dk](mailto:*frac@fysik.dtu.dk)

## Abstract

We developed an in situ sample-holder - akin to a quartz-based plug-flow reactor - for vibrating sample magnetometry (VSM) measurements in gas-controlled environments at ambient pressure and temperatures up to approx. 1000 °C. The holder matches onto a specific type of vibrating sample magnetometer (Lake Shore model 7404-S), but the principles are applicable to other types of VSM. The holder has been tested on powder samples of Co particles on MgAl<sub>2</sub>O<sub>4</sub> support in both reducing and oxidizing atmospheres. The results show control of gas composition and degree of sample reduction/oxidation. In comparison with conventional semi-gas-tight boron nitride

sample cups, the in situ holder shows similar sensitivity but more repeatable measurements while using equivalently small sample amounts. Moreover, the in situ holder uses a closed gas tubing system such that the active gas only passes by the sample and it is not in contact with the VSM and oven parts.

# Introduction

Vibrating sample magnetometry (VSM) is one of the most commonly used techniques to measure hysteresis properties and Curie temperatures of magnetic samples. In practice, the technique typically has a measurement sensitivity of  $10^{-8}$  Am<sup>2</sup>,<sup>12</sup> corresponding to that a sample of 6  $\mu$ g Co with a saturation magnetization of  $162.5 \frac{\text{Am}^2}{\text{kg}}$ <sup>3</sup> at room temperature can be measured to 1 % reproducibility.<sup>2</sup> The wide use of VSM relies on its speed, ease of operation, and flexibility in terms of samples that can be measured. VSM also allows for doing magnetometry at elevated temperatures ( $>75$  °C). Commercial instruments allow for measurements of up to 727 °C<sup>4</sup> or 1000 °C.<sup>5</sup> However, at elevated temperatures the sample may change. For instance, powder samples may, depending on conditions of the sample environment, e.g. oxidize and/or sinter during measurements. In recent years, there has been a rising interest in heating chemical reactions by induction heating<sup>6-12</sup> using magnetic materials at high temperatures. This puts further emphasis on the importance of being able to measure and characterize magnetic samples at relevant conditions at high temperatures.

In order to be able to study catalytic particles in situ by magnetometry, M. Claeys et al. invented an combined chemical reactor and vibrating sample magnetometer<sup>13</sup> for studies during reactions, like the Fischer-Tropsch process,<sup>14-16</sup> in relevant gasses, up to 600+ °C, 50+ bar, and 2 T.<sup>16</sup> This instrument is, however, a custom-built tool for magnetometry at chemical reactor conditions. For many groups, acquiring this sort of instrument is either not financially possible, or is impractical in cases where the group already has a conventional VSM.

Implementing the capability of doing in situ measurements in a conventional VSM at high temperatures comes with several challenges: the holder needs to be non-magnetic, be able to handle the vibration of the VSM while keeping the sample fixed in the holder, and take into account the mass constraints of the vibration head and the spacial constraints of the particular oven option.

Here, we show the proof-of-concept of an in situ VSM holder based on quartz tubes

which, while not of the same height of functionality as the VSM in Claeys' group, can expose a powder sample to a chosen gas-mixture at high temperatures (up to 950-1000 °C), at atmospheric pressure, for extended periods of time, while being inexpensive and easily retrofittable onto any commercially available VSM.

## **Conventional boron nitride sample cups**

For high-temperature measurements (up to 1000 °C), Lake Shore offers commercial boron nitride (BN) sample cups (type 730937) to be used together with their 7400 series VSM and a Lake Shore 74034 oven option. Here the sample material (typically 20-50 mg) is loaded into a BN cup, which is then screwed onto a quartz sample tail, which is connected via a screw to the head drive of the VSM. The gas environment around the BN sample holder is typically Ar, which is recommended by Lake Shore mainly to avoid oxidation of the surrounding oven and of the sample at elevated temperatures. We have also used an Ar gas with 2.4 vol.% H<sub>2</sub> in an attempt to ensure a more reducing sample environment than Ar. The threading in the BN cups does not create a leak-tight seal, and gas might diffuse in and out of the sample holder, as illustrated in Fig. 1. This can be exploited to adjust the sample environment, but the gas flow in and out of the sample is less than optimal. Hence, the gas environment of the sample is subject to large uncertainty during measurement. A concern to us is for instance that water desorption from the particle surfaces can remain in the holder and enhance particle oxidation and sintering with increasing temperature for unspecified time and temperature ranges.

## **The new in situ sample holder**

In order to have a controlled gas environment of samples during high-temperature VSM measurements, we developed an in situ sample holder akin to a plug-flow reactor, which could be used on a standard vibrating sample magnetometer. As a rule of thumb, to achieve



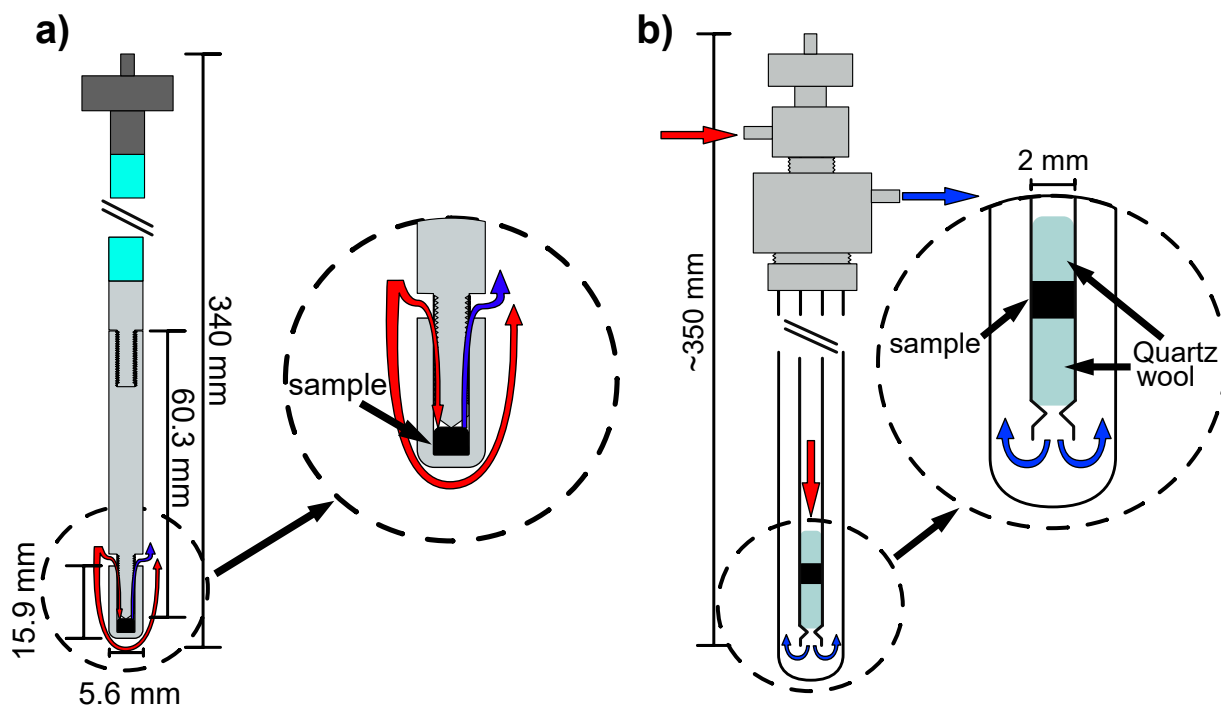


Figure 1: a) Sketch of the conventional boron-nitride sample cup from Lake Shore with an less than optimal degree of gas-diffusion, gas in (red), gas out (blue). b) Sketch of the in situ holder. The sample is loaded into the inner quartz tube and there is a forced gas-flow through the sample, gas in (red), gas out (blue). The outer quartz tubes ensures that the sample gas is separated from the surrounding oven.

plug flow conditions the catalytic particle size must be at least 10 times smaller than the reactor diameter, and at least 50 times smaller than the height of the reactor bed.<sup>17</sup> The support used in this study (PURALOX MG 28<sup>18</sup>) has particle sizes of 30  $\mu\text{m}$ , which is approx. 65 times smaller than the width of the inner quartz tube (2 mm, see Fig. 2), and 100 times smaller than the bed height (approx. 3 mm), which fulfills the rules of thumb for establishing plug flow conditions. Plug flow conditions will ensure that the material in the inner quartz tube will be uniformly exposed to the gas flowing through the quartz tube. In this case the gas will only have to diffuse through the porous support particles to achieve uniform exposure to the gas, while in the conventional BN cup the gas has to diffuse through the threading of the BN cup, and then through the porous support, in order to uniformly expose the sample.

The entire holder is made to match a maximum load of 23 g on the head drive, and to

be able to fit into the 7 mm opening in the Lake Shore 74034 oven option. The principle of the forced gas flow through the sample in the in situ holder is shown in Fig. 1b. The gas is lead through the holder and out without being in contact with the VSM oven or other VSM parts. At the same time the oven is kept in Ar gas as recommended by Lake Shore.

The in situ holder consists of an inner and an outer quartz tube together with an assembly that connects the quartz tubes to the gas system and the VSM head drive. A schematic of the holder can be seen in Fig. 2. The assembly consists of: a top screw, a body, a bottom screw, two plastic spacers, all 3D printed in plastic, and four o-rings. The top screw connects to the VSM head drive via a screw made to fit into the Lake Shore head drive. The whole assembly sits just below the head drive (see Fig. 3b), far from the heating zone of the oven. The lower part of the top screw is hollow, and is equipped with a spout for letting in gas and can be screwed into the body. Two NBR 90 o-rings (inner diameter 3 mm, outer diameter 6 mm) and a plastic spacer fit over the inner quartz tube. These o-rings clamp down on the tube when the top screw is screwed into the body. This is what holds on to the inner quartz tube when the holder vibrates, and also prevents gas from flowing from the head screw and out of the body without flowing through the inner tube. The body is equipped with a spout which functions as gas outlet. The outer quartz tube is held by two NBR 70 o-rings (5 mm inner diameter, 8.5 mm outer diameter) in the same way as the inner quartz tube, when the bottom screw is screwed into the body.

The sample is situated in the inner quartz tube, in a plug-flow reactor style, sandwiched between two layers of Insulfrax quartz wool,<sup>19</sup> cf. Fig. 2. The inner tube is approximately 300 mm long, with an outer diameter of 3 mm, and an inner diameter of 2 mm. Two indents were made approx. 10 mm from the bottom of the inner tube. These are used to anchor the bottom layer of quartz wool that the sample rests on. The inner tube is considered disposable and is loaded with approximately 10 mm<sup>3</sup> (5-10 mg) sample material. The outer tube is approx. 300 mm long with an inner diameter of 4 mm and an outer diameter of 5 mm. The outer tube is closed at the bottom end.

The loading procedure of the inner quartz tube (see Fig. 1b and Fig. 2b and c) was performed under a fume hood. When loading the inner sample tube, a 1.5 mm thick steel rod is used to gently guide the quartz wool down to the indents from the top of the tube. Then, a pipette tip is put into the opening at the top of the tube to act as a funnel for the sample powder. Powder is deposited into the pipette tip, and the quartz tube is gently tapped on the table surface in order for any powder stuck to the side of the quartz tube to trickle down and settle on top of the quartz wool. Afterwards, another layer of quartz wool is put on top of the sample, and the layered structure is gently, but firmly, pressed together, in order for the layered structure not to move from the vibration of the VSM.

When gas is let in through the spout in the top part, it then travels down through the inner quartz tube, where the sample is situated, up through the outer quartz tube, and out through the spout in the body part.

Several tests were made with sample mounted in the inner tube of the in situ holder, while  $10 \frac{\text{mL}}{\text{min}}$  2.4% H<sub>2</sub> in Ar was sent through the tube. Here, it was tested that the hydrogen-argon mixture only exited through the tube, and not through the threading in the body (see Fig. 2), by searching for H<sub>2</sub> leaks with a Testo 316-EX leak detector. In these tests, leaks through the threading were never experienced.

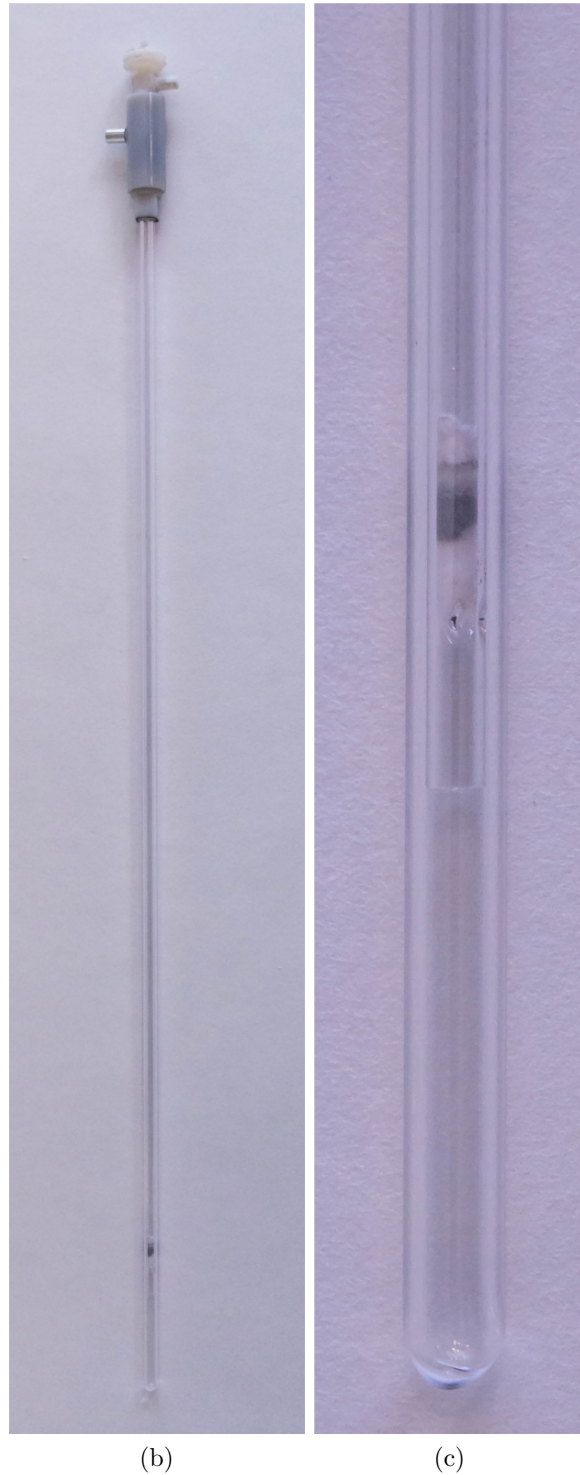
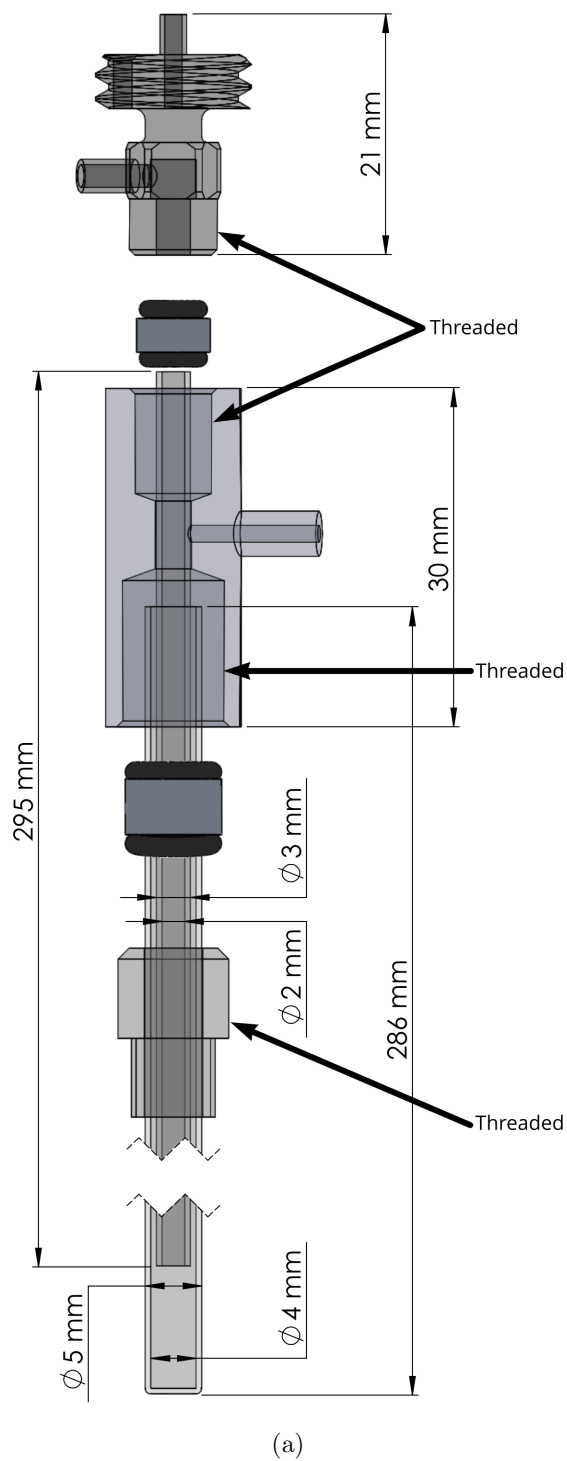


Figure 2: The in situ holder. (a) Technical drawing of the in situ holder consisting of an inner and outer quartz tubes and an assembly for connection to gas system and the head drive. The threading on the top and bottom screws is M8x1. (b) Picture of the fabricated in situ holder. (c) Close-up picture of the concentric quartz tubes with sample (black powder) loaded in the inner quartz tube.

## Gas system

Figure 3a shows a diagram of the gas-system we set up to handle the inlet and outlet gas. The gas tubing outside the VSM is 1/8" stainless steel, and mass flow controllers of type MKS GM50A supply gasses (i.e., hydrogen and argon, in this study). Synthetic air (20 vol.% O<sub>2</sub> in N<sub>2</sub>) was supplied at the variable gas line via a gas flow meter. Pneumatic valves open for the flow of gas, that can either be led through the in situ holder, or through the bypass.

Figure 3b shows a picture of the gas inlet and outlet to in situ holder mounted in the VSM. It is important that the tubes from the gas system to the sprouts on the sample holder are flexible enough that the vibration of the holder is minimally affected. For this we chose tubes of ISO-VERSINIC (a fluoroelastomer) seen as black tubes in Fig. 3b. The ISO-VERSINIC is connected to the 1/8" steel tubing and the spouts of the in situ holder by simply sliding the tubes over the steel tubing and the plastic sprouts. The system might be optimized by more leak-tight solutions. However, no leakage was detected from these tubes, or anywhere else in the system, when searching for leaks with a Testo 316-EX leak detector. Even after several days of running experiments, and multiple exposures of the tip of the sample holder (where the sample is situated, see Fig. 2c) to 950°C, no leaks were detected.

## Instrument preparation

For measurements using BN sample cups, a Lake Shore model 7407 with a Lake Shore 74034 oven option was used. The VSM was calibrated with a nickel sphere calibration sample provided by Lake Shore to a value of 6.92 mAm<sup>2</sup> at an applied magnetic field of 0.5 T.

For in situ measurements, a Lake Shore model 7404-S VSM was calibrated using a Ni calibration sample from Lake Shore. The calibration sample is a nickel sphere with a diameter below 2 mm, that has a moment of 254  $\mu$ Am<sup>2</sup> at an applied magnetic field of 0.5 T. The Ni sphere was mounted in one of the disposable inner tubes in the in situ holder, and saddled in the VSM without the oven mounted. Then, a rotational alignment was made. In this,

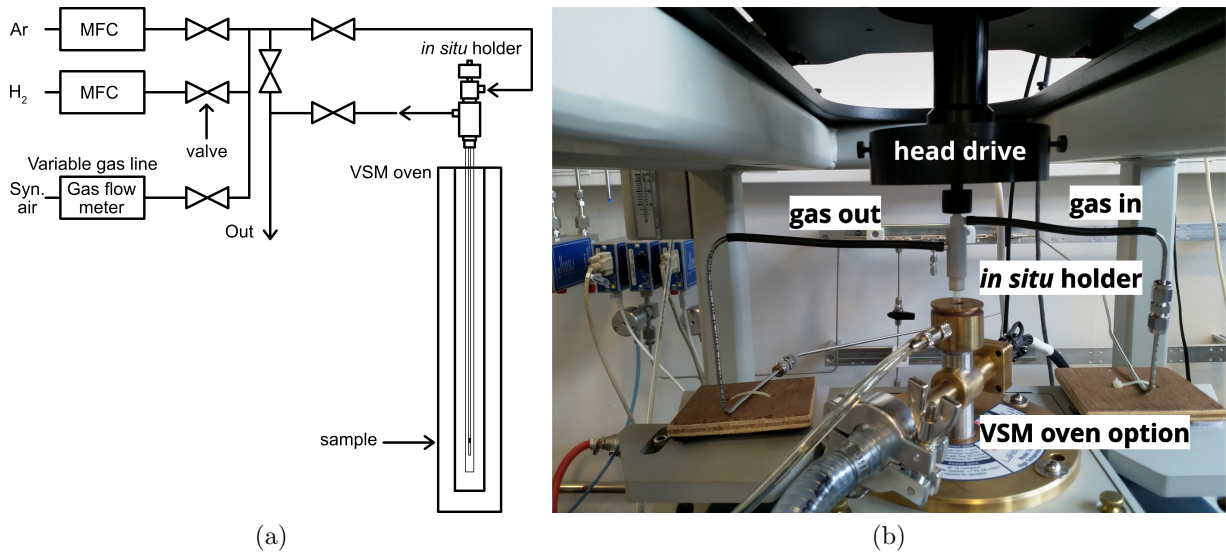


Figure 3: The gas system. (a) Diagram of the system supplying gas to the in situ holder. (b) Picture of the gas supply to the in situ holder mounted underneath the VSM head drive together with the VSM oven.

after saddling at the  $0^\circ$  orientation, the holder was rotated until the maximum deviation in moment was found. This means that the sample was closer to one of the sets of pickup coils. The holder tilt was then adjusted, then the sample was saddled again at the  $0^\circ$  orientation. This procedure was repeated until the holder was straight enough to not be touching the oven wall when mounted in the Lake Shore 74034 oven option. The holder was then removed, the oven mounted, the holder re-mounted, and the oven centered around the holder. The tubes used for gas inlet and outlet were mounted, and a single-point magnetic moment gain calibration was performed. Afterwards, the sample holder was taken out, the oven taken off, and the sample to be measured was mounted in the in situ holder. Another rotational alignment was performed with the holder, and the oven was mounted (and centered around the holder, if needed). The inlet and outlet tubes were connected, and a flow of  $10 \frac{\text{mL}}{\text{min}}$  of 2.4 vol.%  $\text{H}_2$  in Ar was sent through the holder.

The thermal insulation vacuum in the oven option was then pumped down, approx.  $150 \frac{\text{mL}}{\text{min}}$  of Ar connected to the oven option, and the flow through the holder was checked by submerging the tube with the exit gas into water, and seeing that bubbles were rising. Also,

the exit gas was measured with the Testo leak detector, to measure that the hydrogen-argon mixture ran through the holder. Additionally, the area around the in situ assembly was searched for H<sub>2</sub> leaks before starting an experiment. Leaks through the assembly were never experienced. After this, the system was ready to begin measuring.

This procedure, including loading the sample tube, can take anywhere from 2 to 4 hours. From experience, training new users in how to load the holder, prepare the instrument for in situ measurements, and running the experiments, takes up to 1.5 days split over several sessions. These sessions include up to one day for showing and explaining all the steps, and one to two sessions of a couple of hours where the trainee performs all the steps under supervision.

## Sample material

We prepared a material of partially oxidized Co nanoparticles on porous MgAl<sub>2</sub>O<sub>4</sub> spinel support. This material allowed us follow the oxidation and reduction via change of the magnetic moment and thereby test the functionality of the in situ holder. A batch of 2 g of MgAl<sub>2</sub>O<sub>4</sub> with 10 wt.% cobalt was made by incipient wetness impregnation of cobalt-nitride salt (Co(NO<sub>3</sub>)<sub>2</sub>) on PURALOX MG 28 (MgAl<sub>2</sub>O<sub>4</sub>) from Sasol.<sup>18</sup> The impregnated sample was dried at 80°C on a hot plate overnight followed by calcination of the cobalt-nitride salt to cobalt oxide (CoO/Co<sub>3</sub>O<sub>4</sub>) nanoparticles at 450 °C in air for 1 hour. Afterwards, the particles were partially reduced (to Co/CoO/Co<sub>3</sub>O<sub>4</sub>). Metallic Co is ferromagnetic up to 1121 °C, whereas a fully oxidized cobalt sample (CoO/Co<sub>3</sub>O<sub>4</sub>) possesses a close-to-zero magnetic moment. The moment of Co enables magnetic centering of the sample for VSM measurements. The partial reduction was carried out by heating the sample in an atmosphere of 2.4% H<sub>2</sub> in Ar, first to 110 °C for 2 h to remove any moisture in the sample, and then to 850 °C where it was left for 45 min. Afterwards the sample was cooled to room temperature.

Eight powder samples were taken from the batch of partly reduced Co/CoO/Co<sub>3</sub>O<sub>4</sub>



particles on  $\text{MgAl}_2\text{O}_4$  spinel support. Four of the samples were measured on a Lake Shore 7407 model VSM in commercial boron-nitride (BN) cups. The other four samples were measured in the in situ holder on a 7404-S model Lake Shore VSM.<sup>20</sup> All samples were measured vs. temperature in a reducing atmosphere of 2.4 vol.%  $\text{H}_2$  in Ar. One of the in situ samples was subsequently oxidized and then re-reduced in the VSM. The two VSM's are very similar and differences in the measurements presented below are considered a consequence of variations in samples and sample holders and not the different VSMs.

VSM measurements of sample magnetizations rely on sample mass determination. For the BN holders, the empty cups were first measured five times. Then, each cup was filled with approx. 20-50 mg of sample powder, closed, and also weighed five times. The sample mass (listed in Table 1) was determined from the differences of the averages. Weighing was performed on an Ohaus PA224C balance with 0.1 mg precision. Afterwards, the BN sample cup was opened and closed in an Ar atmosphere to replace the air in the sample cup with argon, and then transferred directly to the VSM, spending as little time as possible in air.

The mass-specific saturation magnetization  $\sigma_S$  for the samples in the BN holders at RT at 1.5 T are determined from their magnetic moment measured by VSM divided by their sample mass (cf. Table 1) to  $12.3 \pm 0.4 \frac{\text{Am}^2}{\text{kg}}$ . For pure Co, a  $\sigma_S$  of  $162.5 \frac{\text{Am}^2}{\text{kg}}$  is expected, hence for 10 wt% Co a magnetization of  $12.3 \frac{\text{Am}^2}{\text{kg}}$  shows that the sample as prepared is partly oxidized Co (approx. 24 % of the Co is oxidized).

For the in situ holders, the sample mass is determined in a different way than for the BN samples, as our balance could not accommodate the 300 mm quartz tubes. Specifically, we determined the sample mass in the in situ holders from their magnetic moment at 1.5 T at RT (listed in Table 1) divided by the average mass-specific magnetization of the BN samples at 1.5 T at RT ( $12.3 \frac{\text{Am}^2}{\text{kg}}$ ). The derived sample masses are given in Table 1 (denoted by \*). This method relies on the assumptions that all the samples have the same mass specific magnetization at RT at 1.5 T and that the masses of the samples in the BN cups are well determined. The uncertainty on the sample mass in the in situ holders is estimated



to approx. 3 %.

Table 1: Sample masses for the as-prepared samples together with their sample magnetic moments  $m_{RT,1.5T}$  at RT and 1.5 T, and the mass-specific magnetizations  $\sigma_{RT,1.5T}$  for the samples in BN holders at RT and 1.5 T. The masses for the samples in the in situ holder (marked with \*) have been calculated as  $m_{RT,1.5T}$  divided by the average  $\sigma_{RT,1.5T}$  obtained for the samples in BN cups (12.3 Am<sup>2</sup>/kg, † in the table).

Sample holder	sample mass [mg]	$m_{RT,1.5T}$ [ $\mu\text{Am}^2$ ]	$\sigma_{RT,1.5T}$ [ $\frac{\text{Am}^2}{\text{kg}}$ ]
BN1	22.3	288	12.9
BN2	32.1	393	12.2
BN3	14.1	173	12.3
BN4	16.3	192	11.8
INSITU1	8.8*	109	12.3 <sup>†</sup>
INSITU2	6.0*	74	
INSITU3	10.2*	125	
INSITU4	6.4*	78	

## Results and discussion

Figure 4 shows the magnetization of the partly reduced samples in an applied field of 1 T after they have been heated in a 2.4 vol.% H<sub>2</sub> in Ar gas, first to 200 °C for 2 hours to facilitate evaporation of water moisture in the samples, and then to 850 °C. The measurement of the magnetization shown in Fig. 4 was then carried out over up to 20 hours. As evident, there is significant variation in the measured curves. In principle, the variation between the curves is not very large on an absolute scale, only roughly 5 % at the end of the 20 hours (note the scale of the y-axis). Some of the variation could originate from uncertainty in weighing, saddling, and calibration of the VSM. However, this does not explain the variation in shapes between the in situ samples and the BN samples. The four curves seen in Fig. 4 for the BN samples have very different shapes. Two curves increase in a linear fashion, and then suddenly transition to another linear part with a much lower slope. One curve is almost flat (except for a noisy part), and one does not follow the same trend as the others at

all. The different shapes might be caused by different rates of diffusion in different sample cups, perhaps by how tightly they are screwed together. In case of the BN samples, the magnetization never reached a saturation value, not even after 20 hours. In contrast to this, the curve shapes for the in situ samples in Fig. 4 are consistently similar. They are represented by a fast initial increase in magnetization (= reduction) that flattens out to a plateau as the sample approaches full reduction. This reproducible behavior points to a much more controlled gas environment in the in situ holders.

The blue curve in Fig. 4 is for a sample (INSITU4) that was first reduced as described above, then oxidized in synthetic air (20 vol.% O<sub>2</sub> in N<sub>2</sub>, hence the name INSITU4-oxi), and then re-reduced using the same experimental profile as the others. This treatment could have induced changes in the sample, such as sintering, morphological changes caused by differences in diffusion rates (Kirkendall effect), etc., so it is not surprising that it does not follow the trend of the other in situ samples.

For the measurements of the INSITU samples (Fig. 4) we note fluctuations in  $\sigma$ . Such variations could originate from small mechanical instabilities of the holder, e.g. from the inner quartz tube moving or flexing slightly inside wall of the outer quartz tube. The data obtained after 10 hrs of measurements (Fig. 4) shows a maximal variation of approx.  $0.04 \frac{\text{Am}^2}{\text{kg}}$ , which is equivalent to less than 3 per mille variation in the measurement. This uncertainty is 10 times less than that from weighting the sample. Moreover, these fluctuations correspond to variations in measured magnetic moment of less than approx.  $3 \times 10^{-7} \text{ Am}^2$ , which can then be viewed as the current sensitivity when using the in situ holder with the oven option and a measurement time of 0.3 s per datapoint. This is close to the instrument sensitivity given by the manufacturer (i.e., ca.  $10^{-8} \text{ Am}^2$ , when using the oven option and similar data acquisition times<sup>20</sup>). This shows that the in situ holder performs very well, i.e. that we have succeeded in constructing a stable and durable holder for in situ high-temperature VSM studies. It is possible that the any minor mechanical instabilities in the holder can be fully remediated by e.g. having fixating quartz wool between the inner and

outer quartz tubes or by making the holder assembly in a more rigid material than plastic, e.g. aluminium, but it is not necessarily needed.

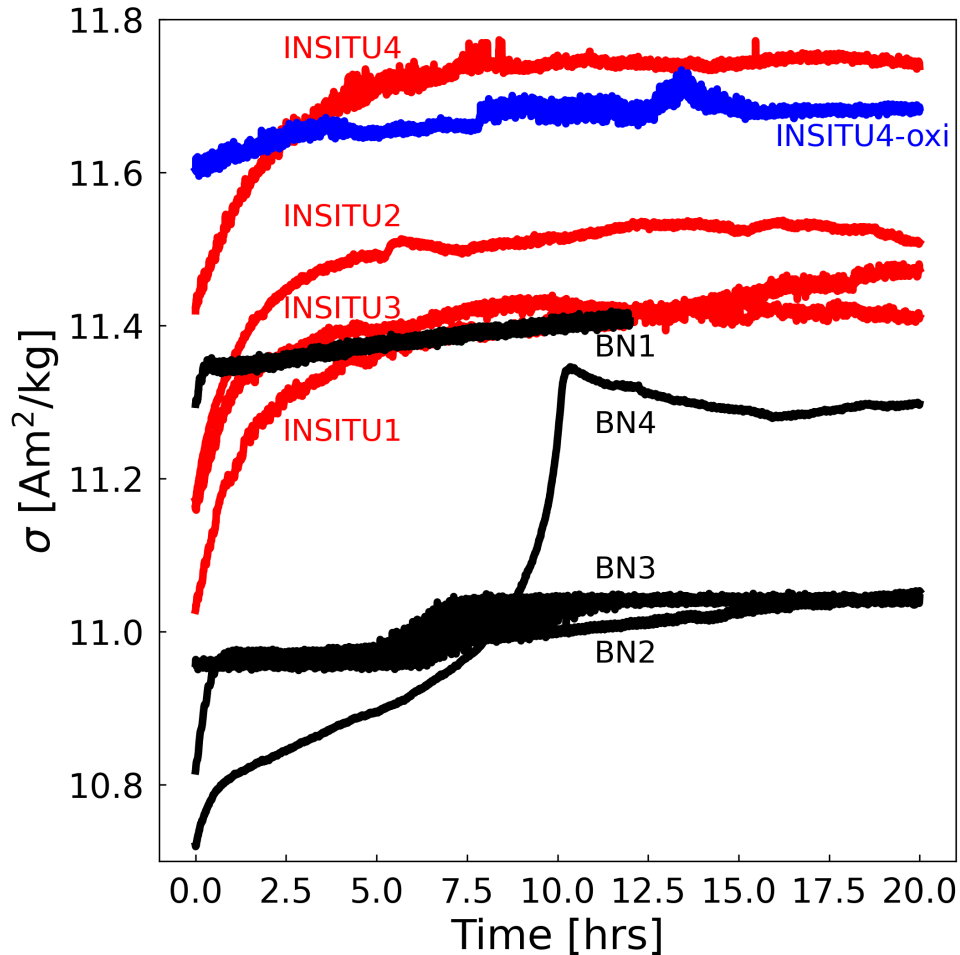


Figure 4: Magnetization curves showing the reduction of samples of  $\text{Co}/\text{CoO}/\text{Co}_3\text{O}_4$  particles on porous  $\text{MgAl}$ -spinel as a function of time. The measurements are taken at  $850^\circ\text{C}$  in an applied magnetic field of 1 T. INSITU samples are coloured red, with the oxidised INSITU sample coloured blue. BN samples are coloured black.

The oxidation of INSITU4-oxi can be seen in Fig. 5. Here, the gas fed to the in situ holder was switched from 2.4 vol.%  $\text{H}_2$  in Ar, to synthetic air (20 vol.%  $\text{O}_2$  in  $\text{N}_2$ ), at room temperature, in an applied magnetic field of 1 T, whereafter the temperature was increased in steps up to  $400^\circ\text{C}$ . From the figure, it is clearly seen, that as the temperature in the VSM oven option is raised,  $\sigma$  drops, as a result of the oxidation of the sample. Full oxidation is reached at  $300^\circ\text{C}$ . Hereafter, only a magnetization of around  $0.3 \frac{\text{Am}^2}{\text{kg}}$  remained. This kind

of investigation is not possible in conventional high temperature VSM using a BN sample cup, as the oven cannot handle exposure to oxidizing atmospheres at elevated temperatures.

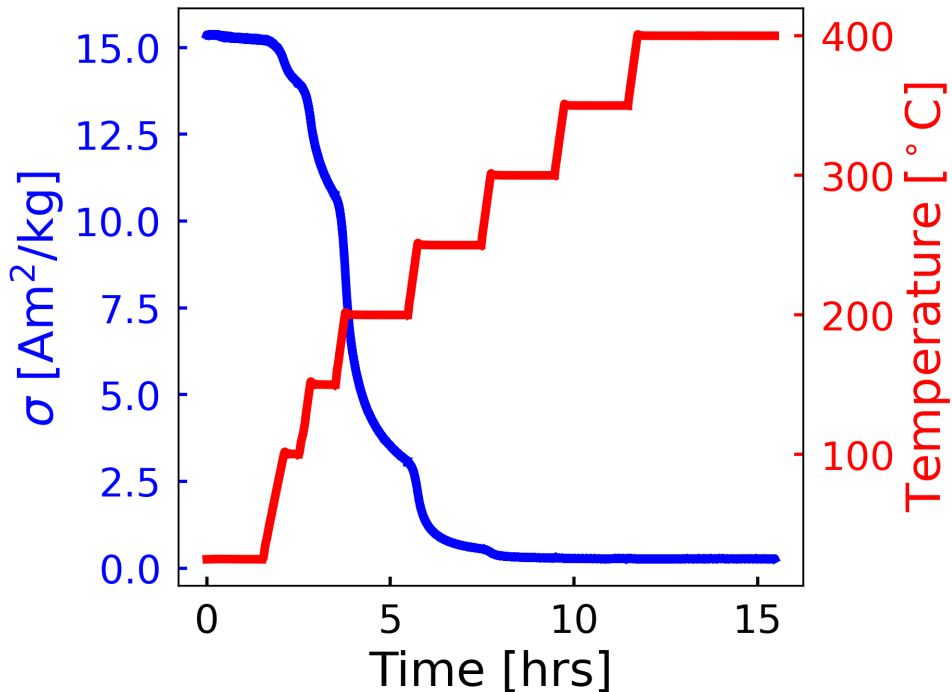


Figure 5: Magnetization  $\sigma$  and temperature as a function of time for a Co nanoparticle sample on porous MgAl-spinel support during oxidation in the in situ VSM holder. In this experiment the sample was exposed to a flow of synthetic air and an applied field of 1 Tesla.

For some of the samples, we also measured their magnetization while ramping from 200 to 850  $^{\circ}\text{C}$  in an applied field of 1 T. This data can be seen in Fig. 6. The sample that had already been oxidized in the in situ holder starts from a close to zero magnetization (around  $0.3 \frac{\text{Am}^2}{\text{kg}}$ , blue curve). The other samples (two in BN holders and two in in situ holders) start at higher magnetization, as these are the samples partially reduced when introduced to the VSM. For all these samples, the reduction starts at around 300  $^{\circ}\text{C}$ . Upon increasing temperature, the magnetization in all five cases rises to a peak, after which the magnetization decays. The decay is caused by the drop in magnetization as temperature approaches the Curie temperature of the samples. Again, the behavior of the similar samples (i.e. those that were partly reduced before the measurement) is almost identical in the in situ holders but

less consistently reproduced in the BN cups probably due to the less optimal gas flow. We also performed measurements at 950 °C (not shown). The in situ system showed stability also at this high temperature. Measurements at 950 °C took approx. 2 hrs and were done twice or more per sample. No changes of the sample holder were observed, neither to the assembly, nor to the inner disposable quartz tubes and the re-used outer quartz tube.

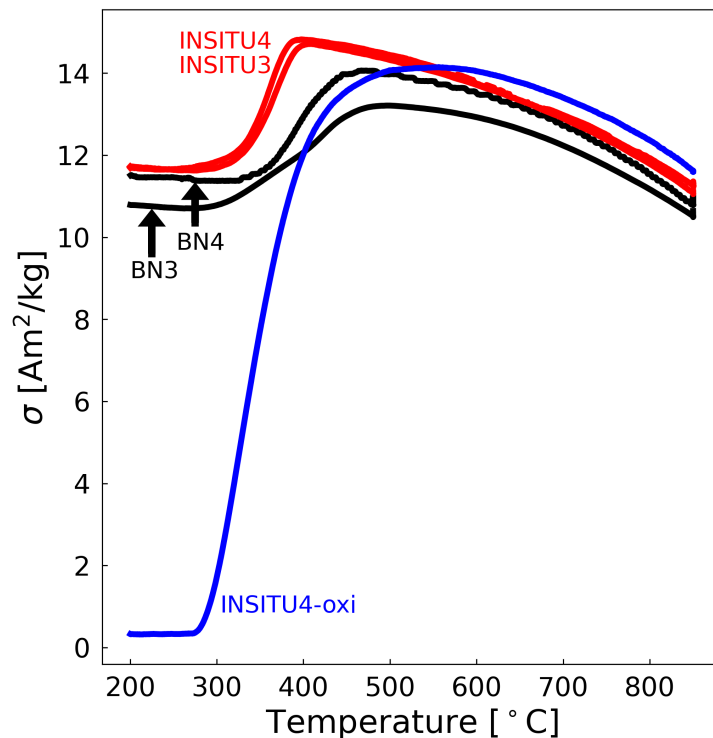


Figure 6: Magnetization  $\sigma$  as a function of temperature while heating to 850 °C, in an atmosphere of 2.4 vol.%  $H_2$  in Ar. The measurements were performed in an applied field of 1 Tesla. Samples measured in the in situ quartz holder are coloured red. Samples measured in a BN cup are coloured black. The blue curve is from the sample that had also been oxidized in the in situ holder prior to this measurement.

The data presented here showed, that the in situ holder can measure just as well as the BN system in these sorts of experiments where a sample is reduced, and the magnetic properties investigated in a weakly reducing atmosphere. Additionally, the in situ also works for studies in an oxidizing atmosphere of synthetic air. As presented in Table 1, the masses of the INSITU samples varied between 6-10 mg. With the loading of 10 % cobalt, this meant that the samples contained about 0.6-1 mg of Co. This is a reduction of magnetic material

of 90-94 % when comparing to the approx. 0.1 g of magnetic material used in the in situ reactor in Claeys's group.<sup>14</sup>

The advantage of this system lies in the freedom to expose the sample to various gas-mixtures, which is not a possibility in the conventional VSM where the gas will interact with the oven. Here, we limited the investigations to a hydrogen-argon mix and synthetic air, but these investigations can be expanded to many different gas mixtures. The gas flow of  $10 \frac{\text{mL}}{\text{min}}$ , and the estimated sample volume of  $10 \text{ mm}^3$ , makes for an exchange of sample volume in gas approximately 17 times per second. If pure  $\text{H}_2$  gas had been chosen instead of  $\text{H}_2$  in Ar, it is likely that the samples in the in situ holders would reduce even faster than what is shown in this paper. The use of pure  $\text{H}_2$  is a possibility only in the in situ holder, as pure hydrogen would be a safety hazard in the open air system used for the BN sample cups. Other advantages of the in situ system include the possibility to analyze the exit gas, and that this system is made of relatively inexpensive materials, that can be easily manufactured. Things yet to be addressed would include an improved estimation of the mass in the quartz tube, and an improvement on the design, allowing for higher-risk gasses to be sent through the system, such as CO.

## Conclusions

In this study, we presented proof-of-concept for an in situ VSM sample holder. The holder can withstand the vibration of the VSM, temperatures of 950°C for prolonged periods of time, at atmospheric pressure, and expose the sample to a gas mixture defined by the user (hydrogen, argon and synthetic air in this study). The results presented here indicate a more controlled reduction of cobalt in the in situ holder than in conventional boron-nitride cups. This is most likely related to a better exposure of the sample to gas. Moreover, with the in situ holder it is possible to do VSM studies in an oxidizing atmosphere at high-temperature, an option not allowed by the conventional VSM setup with BN cups. More measurements are needed to firmly established the advantages of the in situ holder, but the results as of now indicate that this system can perform the same measurements as a conventional system, but has the added features of the user being able to change and control the atmosphere that the sample is exposed to. Future versions of this holder could include a gas-tight holder capable of working with poisonous gasses, adding several more gas-lines, adding an option for introducing water vapour, and a quadropole mass-spectrometer to analyse the exit gas.

## Acknowledgement

This work has been funded by the Innovation Fund Denmark, Grant number: 5160-00004B, and the Villum Center for the Science of Sustainable Fuels and Chemicals (V-SUSTAIN grant 9455).

## References

- (1) Dodrill, B. C. *The Performance of the Model 7400 VSM: Sensitivity*; [https://www.lakeshore.com/docs/default-source/product-downloads/application-notes/the-performance-of-the-model-7400-vsm-sensitivity.pdf?sfvrsn=425ec765\\_{\\_}1](https://www.lakeshore.com/docs/default-source/product-downloads/application-notes/the-performance-of-the-model-7400-vsm-sensitivity.pdf?sfvrsn=425ec765_{_}1), accessed 18/10-2020.
- (2) Graham, C. D. High-sensitivity magnetization measurements. *Journal of Materials Science and Technology* **2000**, *16*, 97–101.
- (3) Myers, H.; Sucksmith, W. The Spontaneous Magnetization of Cobalt. *Proceedings of the Royal Society of London Series A-mathematical and Physical Sciences* **1951**, *207*, 427–446.
- (4) Cryogenic Limited - High Temperature VSM probe. <http://www.cryogenic.co.uk/products/high-temperature-vsm-probe>.
- (5) *Lake Shore 7400-S Series VSM*; [https://www.lakeshore.com/docs/default-source/product-downloads/catalog/vsmcatalog7400-s.pdf?sfvrsn=252b6d1a\\_{\\_}1](https://www.lakeshore.com/docs/default-source/product-downloads/catalog/vsmcatalog7400-s.pdf?sfvrsn=252b6d1a_{_}1), accessed 18/10-2020.
- (6) Ceylan, S.; Friese, C.; Lammel, C.; Mazac, K.; Kirschning, A. Inductive Heating for Organic Synthesis by Using Functionalized Magnetic Nanoparticles Inside Microreactors. *Angewandte Chemie International Edition* **2008**, *47*, 8950–8953.



- (7) Bordet, A.; Lacroix, L.-M.; Fazzini, P.-F.; Carrey, J.; Soulantica, K.; Chaudret, B. Magnetically Induced Continuous CO<sub>2</sub> Hydrogenation Using Composite Iron Carbide Nanoparticles of Exceptionally High Heating Power. *Angewandte Chemie International Edition* **2016**, *55*, 15894–15898.
- (8) Mortensen, P. M.; Engbæk, J. S.; Vendelbo, S. B.; Hansen, M. F.; Østberg, M. Direct Hysteresis Heating of Catalytically Active Ni–Co Nanoparticles as Steam Reforming Catalyst. *Industrial & Engineering Chemistry Research* **2017**, *56*, 14006–14013.
- (9) Vinum, M. G.; Almind, M. R.; Engbæk, J. S.; Vendelbo, S. B.; Hansen, M. F.; Frandsen, C.; Bendix, J.; Mortensen, P. M. Dual-Function Cobalt–Nickel Nanoparticles Tailored for High-Temperature Induction-Heated Steam Methane Reforming. *Angewandte Chemie* **2018**, *130*, 10729–10733.
- (10) Almind, M. R.; Vendelbo, S. B.; Hansen, M. F.; Vinum, M. G.; Frandsen, C.; Mortensen, P. M.; Engbæk, J. S. Improving performance of induction-heated steam methane reforming. *Catalysis Today* **2020**, *342*, 13–20.
- (11) Varsano, F.; Bellusci, M.; La Barbera, A.; Petrecca, M.; Albino, M.; Sangregorio, C. Dry reforming of methane powered by magnetic induction. *International Journal of Hydrogen Energy* **2019**, *44*, 21037–21044.
- (12) Marbaix, J.; Mille, N.; Lacroix, L.-M.; Asensio, J. M.; Fazzini, P.-F.; Soulantica, K.; Carrey, J.; Chaudret, B. Tuning the Composition of FeCo Nanoparticle Heating Agents for Magnetically Induced Catalysis. *ACS Applied Nano Materials* **2020**, *3*, 3767–3778.
- (13) Claeys, M.; van Steen, E.; Visagie, J.; van de Loosdrecht, J. Magnetometer. 2014; Patent no.: US20110204884A1.
- (14) Claeys, M.; Dry, M.; van Steen, E.; du Plessis, E.; van Berge, P.; Saib, A.; Moodley, D. In situ magnetometer study on the formation and stability of cobalt carbide in Fischer–Tropsch synthesis. *Journal of Catalysis* **2014**, *318*, 193–202.

- (15) Fischer, N.; Clapham, B.; Feltes, T.; van Steen, E.; Claeys, M. Size-Dependent Phase Transformation of Catalytically Active Nanoparticles Captured In Situ. *Angewandte Chemie International Edition* **2014**, *53*, 1342–1345.
- (16) Claeys, M.; Dry, M. E.; van Steen, E.; van Berge, P. J.; Booyens, S.; Crous, R.; van Helden, P.; Labuschagne, J.; Moodley, D. J.; Saib, A. M. Impact of Process Conditions on the Sintering Behavior of an Alumina-Supported Cobalt Fischer–Tropsch Catalyst Studied with an in Situ Magnetometer. *ACS Catalysis* **2015**, *5*, 841–852.
- (17) Chorkendorff, I.; Niemantsverdriet, J. *Concepts of modern catalysis and kinetics*, : 2., revised and enlarged edition ed.; Wiley-VCH Verlag: Germany, 2007.
- (18) PURAL MG and PURALOX MG. <https://products.sasol.com/pic/products/home/grades/ZA/5pural-mg-and-puralox-mg/index.html>.
- (19) Home — Unifrax - A Global Specialty Fibers Company. <https://www.unifrax.com/>.
- (20) 7400-S Series VSM. <https://www.lakeshore.com/products/categories/specification/discontinued-products/discontinued-products/7400-s-series-vsm>.

# Chapter 4

## Summary and Perspectives

In this project, we first demonstrated the synthesis of a dual function CoNi/Al<sub>2</sub>O<sub>3</sub> system where the synthesized NPs dispersed on an Al<sub>2</sub>O<sub>3</sub> support acted as both susceptor and catalyst for induction heated SMR (see Paper I). The synthesized CoNi NPs exhibited a high Curie temperature and  $W_h$ , and could heat to high temperatures in a bench scale induction heated SMR reformer, using only induction heating. Testing this system in the induction heated reformer showed that running SMR on the system is not limited by heat transfer, like in a conventional reformer. Instead, the system is limited by reaction kinetics. This is because the NP's are heated locally, inside the reactor, and deliver heat directly to the catalytic sites, which minimizes heat transfer times. The system was stable for >300 hours in reaction conditions, showing no loss of activity or heating ability.

Through the synthesis presented in Paper I, the synthesized material can be modified to contain any active metal needed, which opens up for the use of these types of dopeable and tunable systems for a range of different reactions.

In Paper III, we performed a systematic study of how magnetic properties change when varying the Co content in the dual function CoNi/Al<sub>2</sub>O<sub>3</sub> system, and how this affects heating performance in the induction heated reactor. To do this, we synthesized a range of Co<sub>*x*</sub>Ni<sub>(100-*x*)</sub>/Al<sub>2</sub>O<sub>3</sub>, for  $x = 20, 40, 50, 60, 70, 80, 90$  mol%. Investigations using VSM showed that samples with low cobalt content had a high initial  $W_h$ , but a low  $T_C$ . These samples were able to heat at low  $B_{app}$ 's in the induction heated reactor, but were limited in operational temperatures to 30-40 °C below their respective  $T_C$ 's, matching the decay in the  $W_h$  curves.

When increasing the amount of cobalt in the sample, we found an approximately linear increase in  $T_C$ . Increasing the amount of cobalt also made the material magnetically harder, which was reflected in  $W_h$ , as samples with a higher cobalt content had lower coercive fields at low  $B_{app}$ 's, but higher coercive fields at  $B_{app} = 1500$  mT.

This meant that a higher field was needed when running SMR on the samples with high cobalt contents in the induction heated reformer, in order to access a larger hysteresis area. These samples were, however, not limited by their  $T_C$ , and could reach conversions of  $> 90\%$ .

When looking at the spread of  $W_h$ -curves presented in the data, most of the curves showed a peak in  $W_h$  as a function of temperature. We think, that this peak occurs as an effect of the hysteresis loops being minor loops at low  $B_{app}$ 's. The increased temperature would make the sample less magnetically hard, giving access to larger a hysteresis-area at higher temperatures and low applied fields.

The results obtained in Paper III presents the opportunity to tune the  $T_C$  of the material to prevent overheating in the reactor, as we have shown in the paper that the  $T_C$  puts a hard limit to the operational temperature. Another opportunity presented by the results in this paper, is to layer a reactor with pellets containing different Co:Ni-ratios in order to tune the heating and reaction kinetics down through the reactor, and in that way optimize reactor performance. The results in this paper also show the strong qualitative correlation that exists between the magnetic properties found via VSM, and the heating performance observed in the induction heated reformer.

In Paper II we focused on how to improve the performance of induction heated SMR, by changing the frequency and coil geometry used in the induction heated bench scale reformer. We found that using a narrower coil minimized the resistive power losses in the coil, and increasing the coil frequency from 68 kHz to 201 kHz increased the amount of heat supplied to the reactor. By changing these two parameters, the maximum energy transfer efficiency rose from 11 % to 23 %. We constructed a simple mathematical framework to model the power losses in the system. Using this framework we found that most of the losses occurred in the AC coil, and the surrounding electronics (such as the power-supply). Based on the framework, we made a volumetric scaling of the induction heated reactor to industrially relevant conditions, which indicated an increase in efficiency to  $> 80\%$ . This extrapolation also indicated that the system would be commercially competitive with currently available electrolyzers, when considering only energy requirements.

These results are promising for the development of induction heated catalytic reactions in general, as we through Paper I-III have presented a system that can be tuned to fit a reaction, tuned to optimize heating and reaction kinetics down through the reactor, and indicates a favourable scaling in energy efficiency when scaling to industrial conditions.

In the dual-function  $\text{Co}_x\text{Ni}_{100-x}/\text{Al}_2\text{O}_3$  system studied in Paper I-III, the magnetic and catalytic properties are intertwined. In order to optimize these aspects separately we began our research on universal susceptor systems that should be able to act as susceptors in a wide range of reactions, at high temperatures, while

remaining non-reactive.

Two candidates for universal susceptors were studied in Sec. 3.4: a Co-Al<sub>2</sub>O<sub>3</sub> system, and a FeCr-Al<sub>2</sub>O<sub>3</sub> system. The investigations of the Co-Al<sub>2</sub>O<sub>3</sub> system yielded a  $T_C$  of approx. 850 °C, indicating that not all Al had been withdrawn from the Co<sub>21</sub>Al<sub>79</sub> alloy to form the protective alumina shell.  $W_h$  was approx.  $0.15 \frac{\text{J}}{\text{kg}}$  at  $B_{\text{app}} = 55 \text{ mT}$ . With a metal loading of 33% in some support (comparable to that of the CoNi/Al<sub>2</sub>O<sub>3</sub> system), this would bring  $W_h$  down to approx.  $0.05 \frac{\text{J}}{\text{kg}}$ . This is lower than the approx.  $0.17 \frac{\text{J}}{\text{kg}}$  for Co<sub>50</sub>Ni<sub>50</sub>/Al<sub>2</sub>O<sub>3</sub> at the same applied field and temperature (data taken from the Co<sub>50</sub>Ni<sub>50</sub> sample in Paper III). The system was able to deliver enough heat to drive SMR in the induction heated reactor, reaching  $\geq 90 \%$  conversion for up to  $200 \frac{\text{NmL}}{\text{min}}$ . Future work on this material could include drawing out more aluminium in order to have more pure Co. This could be achieved by e.g. ball milling to smaller particles sizes, or increasing the temperature of the alumina forming step.

The FeCr-Al<sub>2</sub>O<sub>3</sub> system could form a protective alumina shell, but showed multiple magnetic phases. Via the  $T_C$ -curve we could identify phases ranging from a phase matching Fe<sub>75</sub>Cr<sub>25</sub> at 600 °C, to a phase close to that of pure iron at approx. 765 °C (iron, at 770 °C would be within the uncertainty of the  $T_C$  estimation). This system did not have the heating capabilities to drive SMR when put in the induction heated reactor. However, this system would also be more suitable for reactions at temperatures lower than those of SMR. This could for example be propane dehydrogenation (also studied by Marbaix et al.[40]), which typically runs at temperatures from 500 °C to 650 °C[58], and the  $T_C$  of Fe<sub>75</sub>Cr<sub>25</sub> at around 600 °C would make the FeCr-Al<sub>2</sub>O<sub>3</sub> system a good candidate to heat this reaction.

An aspect not addressed in these investigations is the role of heating via eddy currents. As the universal susceptor systems have particle sizes in the  $\mu\text{m}$  range, the simple calculations from Section 1.3 indicate that there could be a significant contribution to heating from both hysteresis losses and eddy current losses. Modelling of the eddy current and hysteresis losses in combination with heating data could help provide a clearer picture of how much each effect contributes to heating. Moreover, calorimetry studies to measure the samples at different frequencies and in relevant gas mixtures could, when compared to VSM-measured hysteresis heating, help in investigating the role of eddy current heating of the universal susceptor systems.

These universal susceptor systems are still early in development, but present an interesting opportunity to make susceptor systems that can heat a multitude of reactions.

The strong qualitative correlation between magnetic properties observed for NP's, and heating performance in the reactor (seen in Paper I-III), presents an opportunity to investigate which particles sizes are optimal for heating in a reactor, based on their  $W_h$  in the VSM. In Paper IV, we investigated the effect of NP size

on cobalt NP's as a function of applied field and temperature. These investigations found an optimum to be around 24-31 nm in diameter for the highest  $W_h$  in the widest array of temperatures and fields. For higher fields and temperatures, this optimum would move slightly towards larger diameters, and the reverse for lower fields and temperatures. For future studies using cobalt NP's in this temperature range, this paper presents an optimum size-range, if maximization of hysteresis loss is desired. Relaxation losses and eddy current losses could also play a role in the induction heating of the susceptor particles. Calorimetry studies at different frequencies and relevant gas atmospheres, could help to elucidate contributions to the heating from relaxation losses and eddy current losses for, respectively, SPM particles ( $\leq 15$  nm, depending on the temperature) and large MD particles ( $\geq 5\mu\text{m}$ ).

In order to study the effect of various gas-mixtures on the magnetic properties of susceptors at high temperatures we fabricated a retrofittable in situ holder for the VSM. This holder can withstand the frequency of the VSM, function at up to 1000 °C, and expose a sample to various gas-mixtures in a closed system in the VSM oven option. We showed the performance of this holder in Paper V, where a reduction, oxidation, an re-reduction of cobalt NP's was shown. These sorts of experiments are not possible in the conventional VSM setup, and this proof-of-concept opens up a wide range of investigations using reducing and oxidative gas-mixtures. The functionality could be expanded upon with the addition of a mass spectrometer to analyse the exit-gas, and a gas-bubbler which can saturate the gas-mixture with water. This last option could be used in future studies of the universal susceptors.

The holder itself is a prototype, and even at this stage of development it considerably increases what is possible to study in the VSM. In future versions, the holder could be made leak-tight, so the use of toxic gasses such as CO could be possible. We have developed concept drawings of this, that could be used for future versions of the in situ holder. Further testing of the holder on various samples could provide valuable data on the stability and capabilities of the holder. One interesting study to be conducted is the utilization of the in situ holder to study when and how the alumina shell forms in the Co- $\text{Al}_2\text{O}_3$  system, which could improve the understanding of how to optimize the synthesis of this universal susceptor. For this, addition of the gas-bubbler mentioned earlier is necessary. This would allow the user to investigate which temperature, time, and gas-mixture is optimal for formation of the protective layer of alumina.

As a last point of discussion we will turn to the goal of this project: "The characterization of magnetic susceptor materials for induction-heated steam methane reforming". Of the systems characterized through this ph.d.-project, the  $\text{Co}_x\text{Ni}_{(100-x)}/\text{Al}_2\text{O}_3$  and Co- $\text{Al}_2\text{O}_3$  systems could deliver the heat necessary to run SMR. This is promising in regards to the overall goal of the project of electrifying SMR. Cur-

rently, resistive heating of SMR is favoured[59], as the challenge of how to scale the induction coil to industrial sizes, and how to implement them in a reactor, has not yet been solved. However, these challenges were outside the scope of the project.

Still, induction heating does have advantages over resistive heating. In resistive heating, presented by Wismann et al.[7, 15], gas diffusion of reactants from the centre of the reactor tube to the washcoat was shown to be the limiting factor. This, and the short contact times of gas to the catalyst washcoat, would make it challenging to use for reactions with slower reaction kinetics that typically use a lot of catalytic material. These could be reactions such as propane dehydrogenation, ammonia cracking, or methanol cracking. For these reactions the typical tubular reactor loaded with catalyst pellets would minimize the bulk diffusion, and the uniform heating made by dispersing susceptor-material through the pellets would make induction heating a likely candidate for electrifying the heating of these processes.

The proof that these magnetic materials can function in the harsh conditions of SMR (Papers I-III, as well as Sec. 3.4) make the challenges of applying these susceptor materials for induction heating of other reactions less daunting. Application of these materials in areas where the current heating method is based on fossil fuels could potentially aid in limiting CO<sub>2</sub> emissions. The magnetic susceptors also have unique properties, such as the Curie temperature, that could be exploited when heating reactions, e.g. utilizing  $T_C$  as a way to avoid overheating. Applying these materials in other reactions is a possible next step, and the studies of NP size for optimal heating, and the in situ holder, should prove useful for any future study of induction heating of these sorts of materials.





# Appendix A

## Appendix

### A.1 Scripts for data-analysis

This section gives an overview of the data-manipulation performed on the VSM data via a couple of Python 3 scripts. The scripts can be seen in the following subsections. The structure of scripts described here is the structure as of the date of writing, but the scripts are subject to change. All hysteresis-data from the VSM is stored in txt-files, as tab-delimited columns specifying  $B_{\text{app}}$ , the magnetic moment, and the temperature. One file, called the "Master-file", details the time each measurement was performed, and what file it was saved to. Fig. A.1 outlines how the scripts takes these files, and outputs the plots seen throughout this thesis.

First, the mass and folders where the data is located are specified manually. Accessing folders is done via the "os"-package[60], and scanning though text-files is done via the "re"-package[61]. By looking through the Master-file, the script finds what temperatures and  $B_{\text{app}}$ 's have been used. Afterwards, the datafiles are loaded into Pandas dataframes (DF)[62], and sorted into runs (see Ch. 2 for the definition of a "run"). These datafiles are treated as described below ( $\star\star$  in Fig. A.1 that references Fig. A.2), put into dataframes, and saved for later access. The shape of the dataframe can be seen in Fig. A.1 at the  $\star$ . The dataframes containing the Curie temperature curves have a slightly different shape, as they only have one  $B_{\text{app}}$ , namely 10 mT. Therefore, these have the same shape as the original datafile, with three columns containing datapoints for time, moment, and temperature. All DF's are saved for easy retrieval for other scripts. From there, the data are plotted via the Matplotlib package[63].

The data-treatment performed on the data ( $\star\star$  in Fig. A.1) has been outlined in Fig. A.2. For the hysteresis-area,  $W_{\text{h}}$ , the hysteresis loop in each datafile is split into two, as seen in the figure. The resulting curves are displaced equal amounts to be in the first and second quadrant, this is done to avoid complications when computing the area under the curve. The area between the curve and the x-axis is

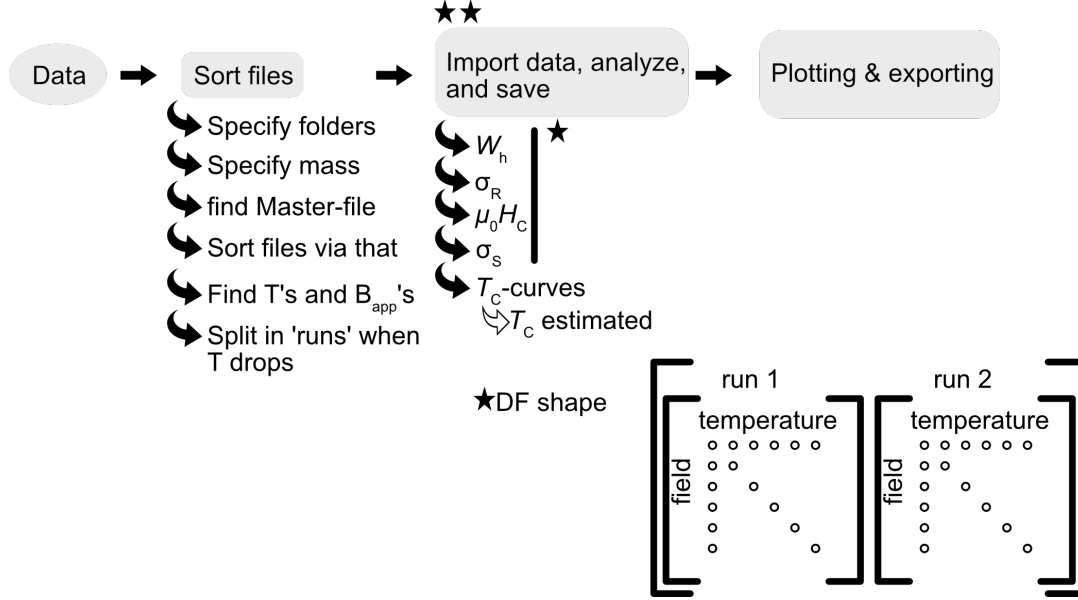


**Figure A.1:** Flowchart of the script used to import, treat, and plot VSM data for all samples seen in this thesis. Circles in  $\star$  represents data-entries, and DF stands for Pandas Dataframe.  $\star\star$  refers to the analysis of the data in Fig. A.2

computed via the Numpy-package's trapz-function[63]. These areas are subtracted from each other to compute  $W_h$ .

$\sigma_R$ ,  $\mu_0 H_C$ , and  $\sigma_S$  were computed in similar ways. For  $\sigma_R$  the datapoints closest to the y-axis were found, subtracted, and averaged:  $\frac{+\sigma_R - (-\sigma_R)}{2}$ . For  $\mu_0 H_C$ , this was done around the values closest to the x-axis instead. For  $\sigma_S$ , the maximum and minimum moments were averaged in the same way as for  $\sigma_R$  and  $\mu_0 H_C$ .

When comparing data across samples, the DF's mentioned above are imported into a new DF, the shape of which can be seen in Fig. A.3, with each dataframe being indexed with the corresponding sample name. If activity-data from the induction-heated reformer (see Paper I-III) is available for the samples, it is imported to dataframes via the Pandas package[62]. Using this, the specific columns of the excel-sheet (as the activity-data is provided in excel) can be imported to a dataframe. Any experimental outliers are deleted, and the data-points are rounded to three decimal-places. Multiple data-points were recorded at each applied field in the induction-heated reformer. These groups of points are averaged, the standard deviation calculated, and written to a dataframe. Plots are then generated from the dataframes via the Matplotlib package[63].

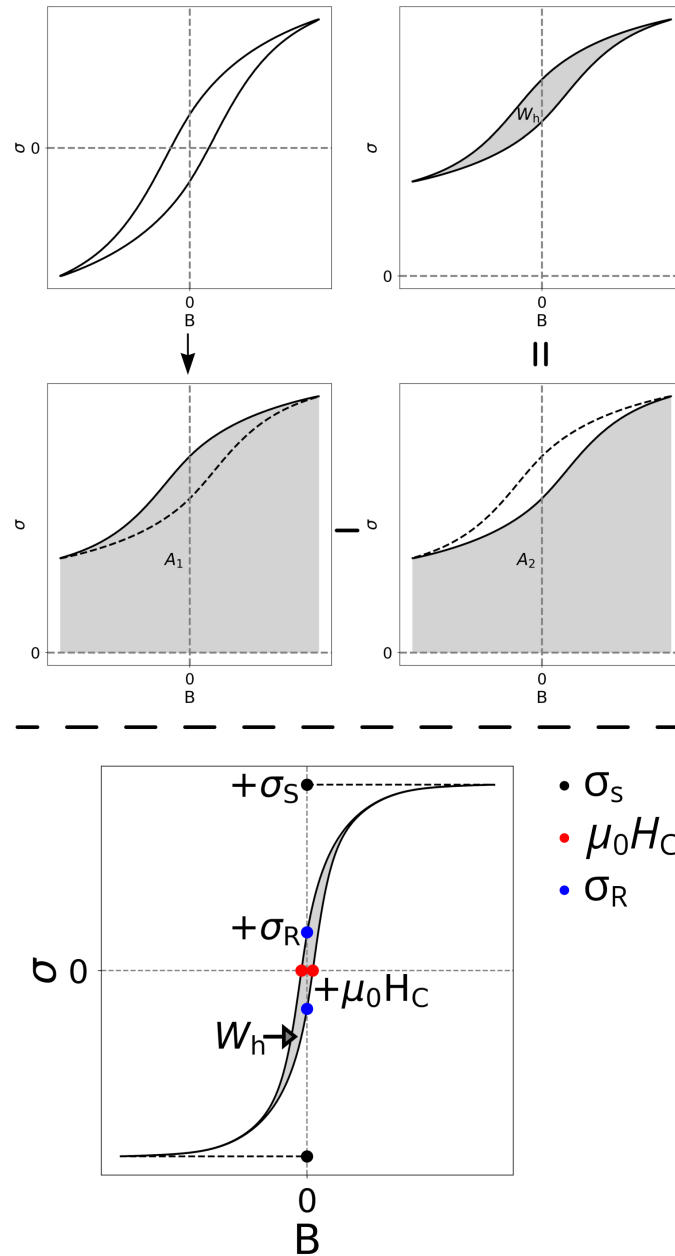


**Figure A.2:** Sketch of the data treatment performed in the script in Fig. A.1 at the  $\star\star$ . Top part: obtaining  $W_h$ , bottom part: points used for obtaining  $\sigma_R$ ,  $\mu_0 H_C$ , and  $\sigma_S$ .

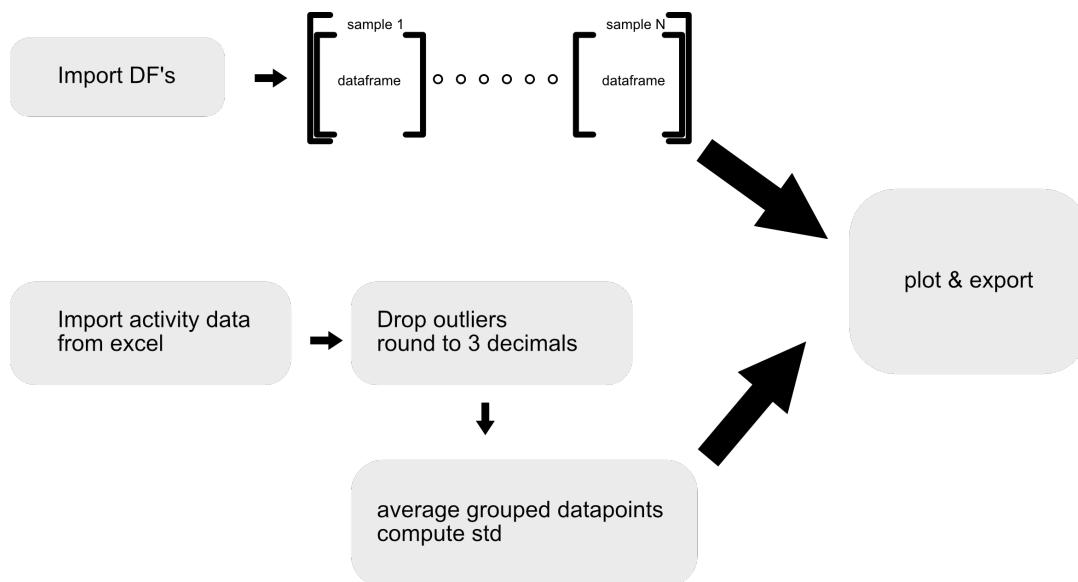


**Figure A.3:** Flowchart of the script used to compare data over a range of sample.

### A.1.1 Example of base script for treating raw data

```
1 # -*- coding: utf-8 -*-
2 """
3 Created on Tue Nov 28 15:26:13 2017
4
5 @author: marad
6 """
7
8 import os
9 os.chdir('C:\\Users\\marad\\Desktop\\INDUCAT_PhD\\VSM\\Cobalt
    stoerrelse investigation\\191018 Co 20 nm on AlOx, 37.9 mg')
10
11 import numpy as np
12 import matplotlib.pyplot as plt
13 import pandas as pd
14 from matplotlib.pyplot import cm #colour-map for plotting
15 from load_defv5 import get_line,get_data,gethys_param,get_tcdata,
    Tc_tangent
16 from def_load_check import Co_load_check
17 import re
18
19 # path to data
20 path = "191018 Co 20 nm on AlOx, 37.933 mg, T-run1 (ProfileData)/"
21
22 """List of all files in folder"""
23
24
25 name_list = os.listdir(path) # Go into the given folder and make
    list of the paths
26 var_path = "191018 Co 20 nm on AlOx, 37.933 mg variables/" #
    variable folder path
27
28
29 # sometimes there can be troubles with the timestamp, therefore we
    will sort the list by the last number in the string
30 full_list = [os.path.join(path,i) for i in name_list]
31 #name_list.sort(key=lambda str: re.sub(".*#", "", str));
32 full_list.sort(key=lambda x: int(''.join(filter(str.isdigit, re.sub
    (".*#", "", x)))))
33 mass = 37.933*10**(-3) # sample weight in grams / should be made
    into function
34 master = full_list[-1]
35 search_string = re.escape("#")
36
37 #
    =====
38 # Automation of getting the experimental profile, fieldstrengths,
```

```

and temperatures
39 #
=====
40 # variables for the lines and values of the temperature levels and
    field levels, respectively
41 lines_T = get_line("Executed RAMP(HTEMP",master)
42 T_list = []
43
44 lines_B = get_line("\hys_c_",master)
45 B_list = []
46
47 with open(master) as datafile:
48     # since it would be annoying to iterate, as well as opening and
        closing, the master file every time, we will save it to a list,
        and delete it later
49     master_list = [line.strip() for line in datafile]
50     # get the temperature/ field values you need from each line in
        lines_T and lines_B
51
52     for i in lines_T:
53         T_list.append(int(re.findall(r'\d+', master_list[i])[0])) #
            the txt file number is the last number r'\d+' finds all WHOLE
            numbers in text
54
55     for i in lines_B:
56         B_list.append(int(re.findall(r'\d+', master_list[i])[0])) #
            field in 0ersted the txt file number is the last number r'\d+'
            finds all WHOLE numbers in text
57
58 # portion the temperature list and field list into runs ASSUMING:
        that a new run is when wither the temperature or the field drops
        /are not ascending anymore
59 T_runs = []
60 B_runs = []
61
62 #for the temperature
63 T_indices = [0]
64 i_start = 0
65 for i in range(1,len(T_list)): #we dont take the first index,
        as that is where the run starts. Otherwise we would get an empty
        data-entry
66 #     if i == 0:
67 #         continue
68
69     if T_list[i] <= T_list[i-1]:
70         T_runs.append(T_list[i_start:i])
71         i_start=i
72         T_indices.append(i)

```

```

73         if i == len(T_list)-1:
74             T_runs.append(T_list[i_start:i+1])
75             T_indices.append(i)
76 #for the field
77     B_indices = [0]
78     i_start = 0
79     for i in range(1,len(B_list)): #we dont take the first index,
80 #         if i == 0:
81 #             continue
82
83         if B_list[i] <= B_list[i-1]:
84             B_runs.append(B_list[i_start:i])
85             i_start=i
86             B_indices.append(i)
87         if i == len(B_list)-1:
88             B_runs.append(B_list[i_start:i+1])
89             B_indices.append(i)
90 ints = np.divide(B_runs[0],10) # fieldstrengths in mT
91
92 #
93 # =====
94 # Get hysteresis data, Coercive fields, Remnant field, and Curie
95 # Temperature(s)
96 # =====
97
98 varlist = os.listdir(var_path)
99 hys_df_list = []
100 Mr_df_list = []
101 Hc_df_list = []
102 list_of_Tcs = []
103 if "hysarea_df0.pkl" in varlist: #check that the hysteresis data
104 #     for the first run is there, otherwise get all the data
105
106
107     for i in range(len(varlist)):
108         if re.search('hysarea_df',varlist[i]):
109             hys_df_list.append(pd.read_pickle(var_path+varlist[i]))
110         if re.search('Mr_df',varlist[i]):
111             Mr_df_list.append(pd.read_pickle(var_path+varlist[i]))
112         if re.search('Hc_df',varlist[i]):
113             Hc_df_list.append(pd.read_pickle(var_path+varlist[i]))
114         if re.search('Tc_df',varlist[i]):
115             list_of_Tcs.append(pd.read_pickle(var_path+varlist[i]))
116     Tc_tangent_method = np.load(var_path+"Tc_tangent_method.npy",
117 allow_pickle=True)

```

```

113
114
115 else:
116     #Get all the data
117     runs_list,places = get_data(master,ints,mass,full_list)
118
119     hys_df_list,Hc_df_list,Mr_df_list,Ms_df_list = gethys_param
120     (runs_list,ints)
121
122     #Get the Tc data
123     Tc_names = ["Measvstime 375 min in 100G"] # first part of
124     the name of the file where the Tc-experiment is saved
125     list_of_Tcs = get_tcdata(master,path,Tc_names,mass,
126     full_list)
127     # Calculate the Tc using the 2nd derivative to make a line,
128     the other line at 930-949 degrees C, use Gromm's tangent
129     method
130     Tc_tangent_method = Tc_tangent(list_of_Tcs,201)
131     np.save(var_path+"Tc_tangent_method",Tc_tangent_method)
132     for i in range(len(hys_df_list)):
133         hys_df_list[i].to_pickle(var_path+"hysarea_df"+str(i)+"
134         .pkl")
135     for i in range(len(Mr_df_list)):
136         Mr_df_list[i].to_pickle(var_path+"Mr_df"+str(i)+".pkl")
137     for i in range(len(Hc_df_list)):
138         Hc_df_list[i].to_pickle(var_path+"Hc_df"+str(i)+".pkl")
139     for i in range(len(list_of_Tcs)):
140         list_of_Tcs[i].to_pickle(var_path+"Tc_df"+str(i)+".pkl"
141         )
142
143 #
144
145 #Create experimental profile
146 #
147
148 B_profile_runs = [None]*len(T_runs) #create list of same dimensions
149 as T_runs, so the plotting is easier
150 #figure out which field-datafiles go into which T-runs by using the
151 indices from earlier
152
153 for i in range(0,len(T_indices)-1):
154     B_profile_indices = []
155     for indice in B_indices: #see what indices in B_indices
156     correspond to the first (50 mT) measurement in the different T-
157     runs

```



```

147 #         if lines_B[B_indices[j]]> lines_T[T_indices[i]] and
        lines_B[B_indices[j]]< lines_T[T_indices[i+1]]:
148 #             if lines_T[T_indices[i]] < lines_B[indice]< lines_T[
        T_indices[i]+1]: #the +1 in lines_T because we want the next
        TEMPERATRUE, not the next time we go to a new run!
149 #                 print lines_T[T_indices[i]], lines_B[indice], lines_T[
        T_indices[i]+1],i,indice
150 #                 B_profile_indices.append(indice)
151
152 # The code snippit above can, unfortunately, only find the FIRST
        indice which is within the temperature run.
153 # this is because we find the linenumbers of the first indice in
        each "run" in field (typically 50 mT), and
154 # the next instance of the "first indice" (50 mT) is in the next
        temperature run. Therefore we will find this next linenumber
155 # for the #first indice" in the following "run" in field, and
        simply take the "B_indice" before that, as this should be the
        last
156 # field in the "field run" we are looking for.
157 # This hopefully explains the anoying "+1" below..
158
159 #         if B_profile_indices: #checks if list is empty
160
161 #             B_profile_indices.append(B_profile_indices[0]+1)
162 #             B_profile_runs[i]=[B_list[B_indices[0]:B_indices[1]]]
163 #             print B_profile_indices
164 #             #would this work if there is only one fieldstrength in the
        run?
165
166 del lines_T, lines_B
167 #%%
168 #
        =====
169 # checking the magnetization vs intrinsic saturation of Co, taking
        loading into account
170 #
        =====
171 # Co_load_check(mass,0.1,runs_list,'IN01-1',0)
172 Co_load_check('IN01-1',18.1,mass,0.1,runs_list,1)
173
174 #%%
175 #
        =====
176
177
178

```

```

179 # FREOM HERE IT IS PLOTTING
180
181
182
183 #
=====
184 #%%
185 #
=====

186 # Plotting the experimental profile
187 #
=====

188 #plt.close("all")
189 fig = plt.figure(figsize = (16,8))
190 ax = plt.gca()
191 ax1 = fig.add_subplot(111)
192
193 #for i in range(len(T_runs)):
194 ax1.step(range(len(T_list)),T_list,"-",color="red",linewidth=3,
         where='post')
195 ax1.set_ylabel("Temperature [ $^{\circ}$ C]",size=22)
196 ax1.tick_params(axis="x",labelsize=18)
197 ax1.tick_params(axis="y",labelsize=18)
198
199 #ax2 = fig.add_subplot(111, sharex=ax1, frameon=False)
200 ax2 = ax1.twinx()
201
202 for i in range(len(B_profile_runs)):
203     if B_profile_runs[i]:
204         for j in range(T_indices[i],T_indices[i]+len(B_profile_runs
205 [i]),1):
206             ax2.plot([j+0.5]*len(B_profile_runs[i][0]),np.divide(
207 B_profile_runs[i][0],10),"o",color="green",linewidth=3)
208 ax2.set_ylabel("B{applied} [mT]",size=22)
209 ax2.tick_params(axis="y",labelsize=18)
210
211 box = ax.get_position()
212 ax.set_position([box.x0, box.y0, box.width*0.94, box.height]) #
213     THIS
214 #plt.xlim(-1,12)
215 #plt.ylim(0,0.1)
216 plt.grid(which='major',color="0.3", linestyle='-', linewidth=0.18,
217 alpha=0.5)
218 plt.grid(which='minor',color="0.3", linestyle=':', linewidth=0.18,
219 alpha=0.5)
220 plt.grid(True)

```

```

216 plt.xlabel("B [mT]",size=22)
217
218
219 plt.legend(ncol= 1, loc='right', fancybox = True, shadow = True,
           bbox_to_anchor = [1.18,0.5], fontsize = 18)
220 plt.title("Experimental profile", size = 25)
221 fig.tight_layout() # otherwise the right y-label is slightly
           clipped
222 plt.savefig("plots/profile.png", format='png', dpi=300)
223
224
225 #%%
226 #
           =====
227 # Plot Wh as a function of field
228 #
           =====
229 plt.close("all")
230
231 #ax = plt.gca()
232
233 for i in range(len(hys_df_list)):
234     fig = plt.figure(figsize = (16,8))
235     color=iter(cm.jet(np.linspace(0,1,len(hys_df_list[i].columns)))
           )
236     for x in hys_df_list[i].columns:
237         c = next(color)
238         plt.plot(hys_df_list[i].index,hys_df_list[i][x],"o",
           linestyle="--",color=c,linewidth=3,label=str(x)+"$^\circ$C") #
           plot the curves
239
240     box = ax.get_position()
241     ax.set_position([box.x0, box.y0, box.width*0.94, box.height])
           #THIS
242     plt.xlim(0,120)
243     plt.ylim(0,1.5)
244     plt.grid(which='major',color="0.3", linestyle='-', linewidth
           =0.18,alpha=0.5)
245     plt.grid(which='minor',color="0.3", linestyle=':', linewidth
           =0.18,alpha=0.5)
246     plt.grid(True)
247     plt.xlabel("B [mT]",size=22)
248     plt.ylabel("W$_h$ [J/kg]",size=22)
249     plt.xticks(fontsize=18)
250     plt.yticks(fontsize=18)
251     plt.legend(ncol= 1, loc='right', fancybox = True, shadow = True
           , bbox_to_anchor = [1.18,0.5], fontsize = 18)

```

```

252     #plt.title("W$_h$(B), Run "+str(run_nr[0]+1), size = 25)
253     plt.savefig("plots/W_h_B_run%.0f.png"%(i+1), format='png', dpi
254               =300)
255     #%%
256     #
257     # Plot Wh as a function of temperature
258     #
259     #plt.close("all")
260
261     for i in range(len(hys_df_list)):
262         fig = plt.figure(figsize = (16,8))
263         ax = plt.gca()
264         color=iter(cm.Dark2(np.linspace(0,1,len(hys_df_list[i].index)))
265                 )
266         #         if i == 1:,
267             c = next(color)
268             plt.plot(hys_df_list[i].columns,hys_df_list[i].iloc[x],"o",
269                     linestyle="-",color=c,linewidth=3,label=str(hys_df_list[i].
270                     index[x])+"mT run "+str(i+1)) # plot the curves
271
272         box = ax.get_position()
273         ax.set_position([box.x0, box.y0, box.width*0.94, box.height])
274         #THIS
275         plt.xlim(150,970)
276         # plt.ylim(0,.5)
277         plt.grid(which='major',color="0.3", linestyle='-', linewidth
278               =0.18,alpha=0.5)
279         plt.grid(which='minor',color="0.3", linestyle=':', linewidth
280               =0.18,alpha=0.5)
281         plt.grid(True)
282         plt.xlabel("Temperature $^{\circ}$C",size=22)
283         plt.ylabel("W$_h$ [J/kg]",size=22)
284         plt.xticks(fontsize=18)
285         plt.yticks(fontsize=18)
286         plt.title("W$_h$(T)", size = 25)
287         plt.legend(ncol= 1, loc='right', fancybox = True, shadow = True
288               , bbox_to_anchor = [1.18,0.5], fontsize = 18)
289         # plt.savefig("plots/W_h_T_run%.0f.png"%(i+1), format='png',
290               dpi=300)
291
292     #%%
293     #

```

```

=====
288 # Plot hysteresis curve for a field strength as a function of
      temperature
289 #
=====

290 plt.close("all")
291 for run in range(len(hys_df_list)):
292     fig = plt.figure(figsize = (16,8))
293     ax = plt.gca()
294     color=iter(cm.Dark2(np.linspace(0,2,len(runs_list[run]))))
295     for i in range(0,len(runs_list[run]),2):
296         for j in [12]:#[len(ints)-3]:
297             c = next(color)
298             plt.plot(runs_list[run][i][j]["Field(mT)"],runs_list[
run][i][j]["Moment(Am2/kg)"],linewidth=2, color = c, label =
str(round(runs_list[run][i][j]["Temperature(C)"][0]))+"\circ$C
") # plot the curve
299         # plt.plot(field_down,moment_down,linewidth=3, color= "blue
") # plot the curve
300     plt.grid(True)
301     plt.xlabel("B [mT]",size=22)
302     plt.ylabel("$\sigma$ [Am2/kg]",size=22)
303     box = ax.get_position()
304     ax.set_position([box.x0, box.y0, box.width*0.94, box.height])
      #THIS
305 #     plt.xlim(-25,25)
306 #     plt.ylim(-10,10)
307     plt.grid(which='major',color="0.3", linestyle='-', linewidth
=0.18,alpha=0.5)
308     plt.grid(which='minor',color="0.3", linestyle=':', linewidth
=0.18,alpha=0.5)
309     plt.xticks(fontsize=18)
310     plt.yticks(fontsize=18)
311     plt.title(str(ints[j])+" mT, Run "+str(run+1), size=22)
312     plt.legend(ncol= 1, loc='right', fancybox = True, shadow = True
, bbox_to_anchor = [1.18,0.5], fontsize = 18)
313     plt.savefig("plots/hysteresis_curves_run_%.0f_%.0f_mT.png"%((
run+1),ints[j]), format='png', dpi=300)
314
315
316
317
318 #%%
319 #
=====

320 # Plot hysteresis curve at a temperature as a function of field

```

```

strength
321 #
=====

322 plt.close("all")
323 for run in [0,1]:
324     # ints=[15000] # field in Gauss
325     fig = plt.figure(figsize = (16,8))
326     ax = plt.gca()
327     color=iter(cm.jet(np.linspace(0,1,len(ints))))
328     for i in [0]:#range(len(runs_list[run])):
329         for j in range(len(ints)):
330             c = next(color)
331             plt.plot(runs_list[run][i][j]["Field(mT)"],runs_list[
run][i][j]["Moment(Am^2/kg)"],linewidth=2, color = c, label =
str(ints[j])+"mT") # plot the curve

332
333     plt.grid(True)
334     plt.xlabel("B [mT]",size=22)
335     plt.ylabel("\sigma$ [Am$^2$/kg]",size=22)
336     box = ax.get_position()
337     ax.set_position([box.x0, box.y0, box.width*0.94, box.height])
#THIS
338 #     plt.xlim(-125,125)
339 #     plt.ylim(-75,75)
340     plt.grid(which='major',color="0.3", linestyle='-', linewidth
=0.18,alpha=0.5)
341     plt.grid(which='minor',color="0.3", linestyle=':', linewidth
=0.18,alpha=0.5)
342     plt.xticks(fontsize=18)
343     plt.yticks(fontsize=18)
344     plt.title(str(T_runs[run][i])+ "$^\circ C, Run "+str(run+1),
size = 22)
345     plt.legend(ncol= 1, loc='right', fancybox = True, shadow = True
, bbox_to_anchor = [1.19,0.5], fontsize = 18)
346 #     plt.savefig("plots/hysteresis_curves_run_%.0f_%.0f_degrees.png
"%(run+1,T_runs[run][i]), format='png', dpi=300)

347
348
349
350
351
352
353 #%%
354 #
=====

355 # Plotting Tc data
356 #

```

```

=====
357 #plt.close("all")
358
359
360 color=iter(cm.Dark2(np.linspace(0,1,len(list_of_Tcs))))
361 fig = plt.figure(figsize = (16,8))
362
363 ax = plt.gca()
364 T_curie = []
365 for i in range(len(list_of_Tcs)):
366     #i = 0
367     c=next(color)
368     # plt.plot(list_of_Tcs[i]["Temperature(C)",savgol_filter(np.
    gradient(savgol_filter(np.gradient(savgol_filter(list_of_Tcs[i]
    ]["Moment(Am^2/kg)",n_smth,3)),n_smth,3)),n_smth,3),linewidth
    =3,color=c,mec=c,label="Run"+str(i+1)) # plot the curve
369     plt.plot(list_of_Tcs[i]["Temperature(C)",list_of_Tcs[i]["
    Moment(Am^2/kg)"],linewidth=3,color=c,mec=c,label="Run"+str(i+1)
    ) # plot the curve
370     # plt.axvline(x=Tc_tangent_method[i], color = c, linestyle='-',
    linewidth = 4, label = "Tangent method - Run "+str(i+1))
371
372
373 #plt.plot(Tc_900C[1][:,2],np.array(Tc_900C[1][:,1])*1e-3/mass_900C,
    linestyle = "--",linewidth=3,color=c,mec=c,label="900C from
    master") # plot the curve - hvor kom massen og 10**-3 fra?
374 box = ax.get_position()
375 ax.set_position([box.x0, box.y0, box.width*0.94, box.height]) #
    THIS
376
377 plt.grid(which='major',color="0.3", linestyle='-', linewidth=0.18,
    alpha=0.5)
378 plt.grid(which='minor',color="0.3", linestyle=':', linewidth=0.18,
    alpha=0.5)
379 plt.xlabel("T [^\circ$C]",size=22)
380 plt.ylabel("$\sigma$ [Am$^2$/kg]",size=22)
381 plt.xticks(fontsize=18)
382 plt.yticks(fontsize=18)
383 plt.xlim(200,950)
384 plt.ylim(0)
385 plt.legend(ncol= 1, loc='best', fancybox = True, shadow = True,
    bbox_to_anchor = [1.,0.5], fontsize = 18)
386 #plt.title("Curie temperature curves, average Curie temperature:
    %.0f "%np.average(T_curie)+t"C", fontsize = 24)
387 plt.title("Curie temperature curves", fontsize = 24)
388 # plt.savefig("plots/Tc.png", format='png',bbox_inches='tight', dpi
    =300)
389

```

```

390 #%%
391 #
=====
392 # Plot Hc as a function of field
393 #
=====

394 plt.close("all")
395
396 ax = plt.gca()
397
398 for i in range(len(Hc_df_list)):
399     fig = plt.figure(figsize = (16,8))
400     color=iter(cm.jet(np.linspace(0,1,len(Hc_df_list[i].columns))))
401     for x in Hc_df_list[i].columns:
402         if i ==1:
403             c= next(color)
404         else:
405             c = next(color)
406         plt.plot(Hc_df_list[i].index,Hc_df_list[i][x],"o",
407                 linestyle="--",color=c,linewidth=3,label=str(x)+" $\circ$ " #
408                 plot the curves
409
410         box = ax.get_position()
411         ax.set_position([box.x0, box.y0, box.width*0.94, box.height])
412         #THIS
413         plt.xlim(0,100)
414         #plt.ylim(0,0.1)
415         plt.grid(which='major',color="0.3", linestyle='-', linewidth
416                 =0.18,alpha=0.5)
417         plt.grid(which='minor',color="0.3", linestyle=':', linewidth
418                 =0.18,alpha=0.5)
419         plt.grid(True)
420         plt.xlabel("B [mT]",size=22)
421         plt.ylabel("Hc [mT]",size=22)
422         plt.xticks(fontsize=18)
423         plt.yticks(fontsize=18)
424         plt.legend(ncol= 1, loc='right', fancybox = True, shadow = True
425                 , bbox_to_anchor = [1,0.5], fontsize = 18)
426         plt.title("Hc(B), Run "+str(i+1), size = 25)
427     # plt.savefig("plots/H_c_B_run%.0f.png"%(i+1), format='png', dpi
428                 =300)
429
430 #%%
431 #
=====
432 # Plot Hc as a function of temperature

```



```

426 #
=====
427 plt.close("all")
428
429 for i in range(len(hys_df_list)):
430     fig = plt.figure(figsize = (16,8))
431     ax = plt.gca()
432     color=iter(cm.Dark2(np.linspace(0,1,len(Hc_df_list[i].index))))
433     for x in range(len(hys_df_list[i].index)):
434         #
435             if i == 1:,
436                 c = next(color)
437                 plt.plot(Hc_df_list[i].columns,Hc_df_list[i].iloc[x],"o",
438                     linestyle="-",color=c,linewidth=3,label=str(hys_df_list[i].index
439 [x])+"mT run "+str(i+1)) # plot the curves
440     box = ax.get_position()
441     ax.set_position([box.x0, box.y0, box.width*0.94, box.height])
442     plt.xlim(150,970)
443     plt.ylim(0,20)
444     plt.grid(which='major',color="0.3", linestyle='-', linewidth
445 =0.18,alpha=0.5)
446     plt.grid(which='minor',color="0.3", linestyle=':', linewidth
447 =0.18,alpha=0.5)
448     plt.grid(True)
449     plt.xlabel("Temperature  $\text{\circ}C$ ",size=22)
450     plt.ylabel("Hc [J/kg]",size=22)
451     plt.xticks(fontsize=18)
452     plt.yticks(fontsize=18)
453     plt.title("Hc(T)", size = 25)
454
455     plt.legend(ncol= 1, loc='right', fancybox = True, shadow = True
456 , bbox_to_anchor = [1.225,0.5], fontsize = 18)
457     plt.savefig("plots/H_c_T_run%.0f.png"%(i+1), format='png', dpi
458 =300)
459     #%%
460 #
=====
461 # Plot Mr as a function of field
462 #
=====
463 plt.close("all")
464
465 #ax = plt.gca()
466
467 for i in range(len(Mr_df_list)):
468     fig = plt.figure(figsize = (16,8))
469     color=iter(cm.jet(np.linspace(0,1,len(Hc_df_list[i].columns))))

```

```

463     for x in Hc_df_list[i].columns:
464         if i ==1:
465             c= next(color)
466         else:
467             c = next(color)
468         plt.plot(Mr_df_list[i].index,Mr_df_list[i][x],"o",
linestyle="--",color=c,linewidth=3,label=str(x)+" $\circ$ C") #
plot the curves
469
470     box = ax.get_position()
471     ax.set_position([box.x0, box.y0, box.width*0.94, box.height])
472     #THIS
473     plt.xlim(0,100)
474     #plt.ylim(0,0.1)
475     plt.grid(which='major',color="0.3", linestyle='-', linewidth
=0.18,alpha=0.5)
476     plt.grid(which='minor',color="0.3", linestyle=':', linewidth
=0.18,alpha=0.5)
477     plt.grid(True)
478     plt.xlabel("B [mT]",size=22)
479     plt.ylabel("Wh [J/kg]",size=22)
480     plt.xticks(fontsize=18)
481     plt.yticks(fontsize=18)
482     plt.legend(ncol= 1, loc='right', fancybox = True, shadow = True
, bbox_to_anchor = [1,0.5], fontsize = 18)
483     plt.title("Mr(B), Run "+str(i+1), size = 25)
484     plt.savefig("plots/M_r_B_run%.0f.png"%(i+1), format='png', dpi
=300)
485 #%%
486 #
=====
487 # Plot Mr as a function of temperature
488 #
=====
489 plt.close("all")
490
491 for i in range(len(hys_df_list)):
492     fig = plt.figure(figsize = (16,8))
493     ax = plt.gca()
494     color=iter(cm.jet(np.linspace(0,1,len(Mr_df_list[i].index))))
495     for x in range(len(hys_df_list[i].index)):
496         #         if i == 1:,
497             c = next(color)
498             plt.plot(Mr_df_list[i].columns,Mr_df_list[i].iloc[x],"o",
linestyle="--",color=c,linewidth=3,label=str(hys_df_list[i].index
[x])+"mT run "+str(i+1)) # plot the curves

```

```

499     box = ax.get_position()
500     ax.set_position([box.x0, box.y0, box.width*0.94, box.height])
501     plt.xlim(150,970)
502     plt.ylim(0,5)
503     plt.grid(which='major',color="0.3", linestyle='-', linewidth
=0.18,alpha=0.5)
504     plt.grid(which='minor',color="0.3", linestyle=':', linewidth
=0.18,alpha=0.5)
505     plt.grid(True)
506     plt.xlabel("Temperature  $\text{\circ C}$ ",size=22)
507     plt.ylabel("Wh [J/kg]",size=22)
508     plt.xticks(fontsize=18)
509     plt.yticks(fontsize=18)
510     plt.title("Mr(T)", size = 25)
511
512     plt.legend(ncol= 1, loc='right', fancybox = True, shadow = True
, bbox_to_anchor = [1.225,0.5], fontsize = 18)
513     plt.savefig("plots/M_r_T_run%.0f.png"%(i+1), format='png', dpi
=300)
514     %%
515
516     #
=====
517     #
518
519     ### WRITING TO CSV
520
521
522     #
=====
523
524
525     %%
526     #
=====
527     # Hysteresis to csv
528     #
=====
529     for i in range(len(hys_df_list)):
530         hys_df_list[i].to_csv("csv_files/hysarea_run%.0.f.csv"%(i+1))
531     %%
532     #
=====
533     # Write Tc Dataframes to CSV

```

```
534 #
-----
535 for i in range(len(list_of_Tcs)):
536     list_of_Tcs[i].to_csv("csv_files/Tc_run"+str(i+1)+".csv", index=
        False)
```

Listing A.1: Base script for raw data analysis

## A.1.2 Example of base script for slicing through data across samples

```
1 """
2 Created on Fri Aug 16 09:50:18 2019
3
4 @author: marad
5 """
6
7 import os
8 import re
9 import numpy as np
10 import matplotlib.pyplot as plt
11 import pandas as pd
12 from matplotlib.pyplot import cm #colour-map for plotting
13 import seaborn as sns
14
15
16 os.chdir('C:\\Users\\marad\\Desktop\\INDUCAT_PhD\\VSM\\Cobalt
    stoerrelse investigation')
17 cwd = os.getcwd()
18 folders = next(os.walk(cwd))[1]
19 # Sort the folders strings by what comes after the V the whole
    thing, (if no V - compare whole string)
20 folders.sort(key=lambda str: re.sub(".*V", "", str));
21
22 # Delete the last entry as it is the plot folder
23 folders = folders[0:-2]
24
25 # as the CoAl-01 100 nm sample does not have a precise mass, it is
    deleted
26 del folders[3]
27 del folders[-1]
28 del folders[-1]
29
30 # sample names are not trivial to import automatically here, so it
    is done manually
31 sample_names = ["1.6um", "2um", "7.5um", "30nm", "16nm", "700nm", "100 nm
    on Al0x", "20 nm on Al0x", "45 nm on Al0x", "40 nm on Al0x", "20 nm
    on Al0x 2", "15-60 nm on Al0x", "30 nm on Al0x"]
```

```

32
33 paths = []
34
35 for i in range(len(folders)):
36     paths.append(folders[i]+"/"+folders[i]+" variables/")
37
38
39 #
40 # =====
41 # Get hysteresis data, Coercive fields, Remnant field, and Curie
42 # Temperature(s)
43 # =====
44
45 Q_dataframe = pd.DataFrame(columns = sample_names)
46 Hc_dataframe = pd.DataFrame(columns = sample_names)
47 Mr_dataframe = pd.DataFrame(columns = sample_names)
48 Tc_dataframe = pd.DataFrame(columns = sample_names) #contains the
49 # data for Tc curves
50 #Tc_list = [] #contains the estimations of Curie-temperature
51 runs_list_dataframe = pd.DataFrame(columns = sample_names)
52
53
54 for j in range(len(paths)):
55     var_path = paths[j]
56     varlist = os.listdir(paths[j])
57
58
59     hys_df_list = []
60     Mr_df_list = []
61     Hc_df_list = []
62     list_of_Tcs = []
63     if "hysarea_df0.pkl" in varlist: #check that the hysteresis
64     # data for the first run is there, otherwise get all the data
65     for i in range(len(varlist)):
66         if re.search('hysarea_df',varlist[i]):
67             hys_df_list.append(pd.read_pickle(var_path+varlist[
68             i]))
69         if re.search('Mr_df',varlist[i]):
70             Mr_df_list.append(pd.read_pickle(var_path+varlist[i]
71             )))
72         if re.search('Hc_df',varlist[i]):
73             Hc_df_list.append(pd.read_pickle(var_path+varlist[i]
74             )))
75         if re.search('Tc_df',varlist[i]):
76             list_of_Tcs.append(pd.read_pickle(var_path+varlist[
77             i]))
78     else:

```

```

70     print("Data missing..")
71
72     Q_dataframe[sample_names[j]]=hys_df_list
73     Hc_dataframe[sample_names[j]]=Hc_df_list
74     Mr_dataframe[sample_names[j]]=Mr_df_list
75     try:
76         Tc_dataframe[sample_names[j]]=list_of_Tcs
77     except ValueError:
78         Tc_dataframe[sample_names[j]]=pd.Series(list_of_Tcs) #
79     WOrkaround, appearantly, the lists are not equal length
80
81     del hys_df_list,Mr_df_list,Hc_df_list,list_of_Tcs, #
82     Tc_tangent_method
83
84     #%%
85     #
86     =====
87
88     # From here on it is plotting and saving
89
90     #%%
91     #
92     =====
93
94     # Plotting Tc's, might need to check up with "Data slicing v03.
95     # py" for finding Tc's directly in this script, but that is for
96     # later
97     #
98     =====
99
100 plt.close("all")
101
102 names_sorted = ['20 nm on AlOx', '20 nm on AlOx 2', '30 nm on AlOx',
103                '40 nm on AlOx', '15-60 nm on AlOx', '45 nm on AlOx', '100 nm on
104                AlOx']
105 sizes_sorted = [18.8,18.8,27.4,38.2,40.1,45.6,60.9]
106
107 color=iter(['b','b','darkorange','k','g','darkviolet','r'])
108 fig = plt.figure(figsize = (8,8))
109
110 ax = plt.gca()
111 T_curie = []
112
113 for i in names_sorted:
114     c=next(color)

```

```

107     for j in Tc_dataframe[i].index:
108         try:
109             #Select dashed linestyle for the first run
110             if j%2 ==0: # % checks for remainder after dividing
111                 continue
112             # style = '--'
113             else:
114                 style = "-"
115             if i == "30nm" or i == "16nm" or i == "700nm": # these
three datasets only have 2 Tc curves
116                 j = 1
117                 # plt.plot(list_of_Tcs[i]["Temperature(C)",
savgol_filter(np.gradient(savgol_filter(np.gradient(
savgol_filter(list_of_Tcs[i]["Moment(Am^2/kg)"],n_smth,3)),
n_smth,3)),n_smth,3),linewidth=3,color=c,mec=c,label="Run"+str(i
+1)) # plot the curve
118 #         plt.plot(Tc_dataframe[i][j]["Temperature(C)",
Tc_dataframe[i][j]["Moment(Am^2/kg)"],linestyle=style,linewidth
=3,color=c,mec=c,label=i+" Run"+str(j+1)) # plot the curve
119             plt.plot(Tc_dataframe[i][j]["Temperature(C)",
Tc_dataframe[i][j]["Moment(Am^2/kg)"/Tc_dataframe[i][j]["Moment
(Am^2/kg)"]][len(Tc_dataframe[i][j]["Moment(Am^2/kg)"])-1],
linestyle=style,linewidth=3,color=c,mec=c,label=str(round(
sizes_sorted[names_sorted.index(i)]))+ ' nm')+" Run"+str(j+1)) #
plot the 'normalized' curve
120             # plt.axhline(y=np.max(Tc_dataframe[i][1]["Moment(Am^2/kg)
"])/2, color = c, linestyle='--', linewidth = 4)#, label = "
Tangent method - Run "+str(i+1))
121         except TypeError:
122             continue
123
124
125
126 box = ax.get_position()
127 ax.set_position([box.x0, box.y0, box.width*0.94, box.height]) #
THIS
128 ax.tick_params(direction='in')
129 plt.grid(which='major',color="0.3", linestyle='-', linewidth=0.18,
alpha=0.5)
130 plt.grid(which='minor',color="0.3", linestyle=':', linewidth=0.18,
alpha=0.5)
131 plt.xlabel("T [^\circ$C]",size=22)
132 plt.ylabel(r"$\sigma/\sigma_{200^\circ \rm C}$ ",size=22)
133 plt.xticks(fontsize=18)
134 plt.yticks(fontsize=18)
135 plt.xlim(200,950)
136 plt.ylim(0)
137
138 # fixing overlap in ticks at origo

```

```

139 plt.rcParams['xtick.major.pad'] = 8
140 plt.rcParams['ytick.major.pad'] = 8
141
142 plt.legend(ncol= 1, loc='best', fancybox = True, fontsize = 18)#,
    bbox_to_anchor = [1,1])
143 #plt.title("Curie temperature curves, average Curie temperature:
    %.0f "%np.average(T_curie)+t+"C", fontsize = 24)
144 # plt.title("Curie temperature curves", fontsize = 24)
145 plt.savefig("plots/Tc_v05.png", format='png',bbox_inches='tight',
    dpi=300)
146 #
147
148 #%%
149
150 #
    =====
151 #Plotting Q(T) for each of the samples
152 #
    =====
153
154 #plt.close("all")
155
156 for i in Q_dataframe.columns:
157     print(i)
158     for j in Q_dataframe[i].index:
159         fig = plt.figure(figsize = (16,8))
160         ax = plt.gca()
161         color=iter(cm.Dark2(np.linspace(0,1,len(Q_dataframe[i][j].
    index))))
162         for x in range(len(Q_dataframe[i][j].index)):
163             #         if i == 1:,
164                 c = next(color)
165                 plt.plot(Q_dataframe[i][j].columns,Q_dataframe[i][j].
    iloc[x], "o", linestyle="-",color=c,linewidth=3,label=str(
    Q_dataframe[i][j].index[x])+"mT run "+str(j+1)) # plot the
    curves
166
167         box = ax.get_position()
168         ax.set_position([box.x0, box.y0, box.width*0.94, box.height
    ])
    #THIS
169         plt.xlim(150,970)
170         # plt.ylim(0,0.05)
171         plt.grid(which='major',color="0.3", linestyle='-',
    linewidth=0.18,alpha=0.5)
172         plt.grid(which='minor',color="0.3", linestyle=':',
    linewidth=0.18,alpha=0.5)
173         plt.grid(True)

```



```

174     plt.xlabel("Temperature  $T$  [C]",size=22)
175     plt.ylabel("Wh [J/kg]",size=22)
176     plt.xticks(fontsize=18)
177     plt.yticks(fontsize=18)
178     plt.title("Wh(T) sample "+i, size = 25)
179     plt.legend(ncol= 1, loc='right', fancybox = True, shadow =
180 #         plt.savefig("plots/W_h_T_"+str(i)+".png",bbox_inches='
181 #             tight', format='png', dpi=300)
182
183 #%%
184
185 #
186 # =====
187 # Plotting Q(T) for a specific field across all samples
188 # =====
189
190 plt.close("all")
191
192 mT = [20,55,100,1500]
193 for x in mT:
194     fig = plt.figure(figsize = (16,8))
195     color=iter(cm.Dark2(np.linspace(0,1,len(Q_dataframe.columns))))
196     for i in sample_names[6:]:#[ '20 nm on AlOx':#, '45 nm on AlOx
197 #         '#100 nm on AlOx', '20 nm on AlOx', '45 nm on AlOx']:#
198 #         # incorporate correction for cobalt in this:
199         if i == '100 nm on AlOx':
200             load_correct =0.14
201             print("done")
202 #         if i == '20 nm on AlOx' or i == '20 nm on AlOx 2' or '15-60
203 #         nm on AlOx':
204             load_correct =0.1
205         if i == '45 nm on AlOx':
206             load_correct =0.18
207         if i == '30 nm on AlOx':
208             load_correct =0.1
209         if i == '40 nm on AlOx':
210             load_correct =0.14
211         if i == '30nm' or i == '30nm':
212             continue
213         else:
214             load_correct = 1 # no correction
215     c = next(color)
216     for j in [1]:#Q_dataframe[i].index:
217         if j%2==0:

```

```

215         style="--" #every equal run (here only the first)
will be dotted
216         else:
217             style = "-"
218             plt.plot(Q_dataframe[i][j].columns, Q_dataframe[i][j].
loc[x]/load_correct, "o", linestyle=style, color=c, linewidth=3,
label=str(i)+" run "+str(j+1)) # plot the curves
219     plt.xlim(150,970)
220 #     plt.ylim(0,0.5)
221     plt.grid(which='major', color="0.3", linestyle='-', linewidth
=0.18, alpha=0.5)
222     plt.grid(which='minor', color="0.3", linestyle=':', linewidth
=0.18, alpha=0.5)
223     plt.grid(True)
224     plt.xlabel("Temperature  $T$  [C]", size=22)
225     plt.ylabel("Wh [J/kg]", size=22)
226     plt.xticks(fontsize=18)
227     plt.yticks(fontsize=18)
228     plt.title("Wh(T), "+str(x)+" mT", size = 25)
229     plt.legend(ncol= 1, loc='right', fancybox = True, shadow = True
, bbox_to_anchor = [1.25,0.5], fontsize = 18)
230 #     plt.savefig("plots/W_h_T_"+str(x)+"_run"+str(j+1)+"
_corrected_v02.png", bbox_inches='tight', format='png', dpi=300)
231 plt.show()
232 #%%
233
234 #
=====

235 # Plotting Hc(T) for a specific field across all samples
236 #
=====

237
238 plt.close("all")
239 mT = [20,55,100,500]
240 for x in mT:
241     fig = plt.figure(figsize = (16,8))
242     color=iter(cm.Dark2(np.linspace(0,1,len(Hc_dataframe.columns)))
)
243     for i in Hc_dataframe.columns:
244         c = next(color)
245         for j in [1]:#Hc_dataframe[i].index:
246             if j%2==0:
247                 style="--" #every equal run (here only the first)
will be dotted
248                 else:
249                     style = "-"
250                 plt.plot(Hc_dataframe[i][j].columns, Hc_dataframe[i][j].

```

```

loc[x], "o", linestyle=style, color=c, linewidth=3, label=str(i)+
run "+str(j+1)) # plot the curves
251 plt.xlim(150,970)
252 plt.ylim(0,25)
253 plt.grid(which='major', color="0.3", linestyle='-', linewidth
=0.18, alpha=0.5)
254 plt.grid(which='minor', color="0.3", linestyle=':', linewidth
=0.18, alpha=0.5)
255 plt.grid(True)
256 plt.xlabel("Temperature  $\text{^\circ C}$ ", size=22)
257 plt.ylabel("Field [mT]", size=22)
258 plt.xticks(fontsize=18)
259 plt.yticks(fontsize=18)
260 plt.title("Hc(T), "+str(x)+" mT", size = 25)
261 plt.legend(ncol= 1, loc='right', fancybox = True, shadow = True
, bbox_to_anchor = [1.18,0.5], fontsize = 18)
262 plt.savefig("plots/H_c_T_"+str(x)+"mT_run"+str(j+1)+"_v01.png",
bbox_inches='tight', format='png', dpi=300)
263 #
264 %%
265
266 #
=====

267 # Plotting Mr(T) for a specific field across all samples
268 #
=====

269
270 plt.close("all")
271 mT = [20,55,100,500]
272 for x in mT:
273     fig = plt.figure(figsize = (16,8))
274     color=iter(cm.Dark2(np.linspace(0,1,len(Mr_dataframe.columns)))
)
275     for i in Mr_dataframe.columns:
276         if i =='100 nm on AlOx':
277             load_correct =0.14
278             print("done")
279         if i =='20 nm on AlOx':
280             load_correct =0.1
281         if i =='45 nm on AlOx':
282             load_correct =0.18
283         else:
284             load_correct = 1 # no correction
285     c = next(color)
286     for j in [0]:# Mr_dataframe[i].index:
287         if j%2==0:
288             style="--" #every equal rune (here only the first)

```

```

will be dotted
289         else:
290             style = "-"
291             plt.plot(Mr_dataframe[i][j].columns, Mr_dataframe[i][j].
loc[x]/load_correct, "o", linestyle=style, color=c, linewidth=3,
label=str(i)+" run "+str(j+1)) # plot the curves
292     plt.xlim(150,970)
293 #     plt.ylim(0,2.5)
294     plt.grid(which='major', color="0.3", linestyle='-', linewidth
=0.18, alpha=0.5)
295     plt.grid(which='minor', color="0.3", linestyle=':', linewidth
=0.18, alpha=0.5)
296     plt.grid(True)
297     plt.xlabel("Temperature  $\text{\circ C}$ ", size=22)
298     plt.ylabel("Moment [Am2/kg]", size=22)
299     plt.xticks(fontsize=18)
300     plt.yticks(fontsize=18)
301     plt.title("Mr(T), "+str(x)+" mT", size = 25)
302     plt.legend(ncol= 1, loc='right', fancybox = True, shadow = True
, bbox_to_anchor = [1.25,0.5], fontsize = 18)
303     plt.savefig("plots/M_r_T"+str(x)+"mT_run"+str(j+1)+"
corrected_v01.png", bbox_inches='tight', format='png', dpi=300)
304 #%%
305 #
=====
306 #     Q vs. size for 20 and 55 mT at 700 deg. C
307 #
=====

308
309 names_sorted = ['20 nm on AlOx', '20 nm on AlOx 2', '30 nm on AlOx',
'40 nm on AlOx', '15-60 nm on AlOx', '45 nm on AlOx', '100 nm on
AlOx']
310 sizes_sorted = [18.8,18.8,27.4,38.2,40.1,45.6,60.9]
311 sizes_err = [6.4,6.4,8.3,13.8,20.2,14.1,28.4]
312
313 sizes = [1.6E-6,2E-6,7.5E-6,30E-9,16E-9,700E-9,100E-9,20E-9,45E
-9,40E-9,20E-9,37.5E-9,30E-9]
314 sizerange_low = np.multiply([0,0,0,0,0,0,60,15,30,30,15,15,20],1E
-9)
315 sizerange_high = np.multiply([0,0,0,0,0,0,150,30,55,60,30,60,40],1E
-9)
316
317 # color=iter(['b','b','darkorange','k','g','darkviolet','r'])
318
319 plt.close("all")
320 mT = [20,30,55,100,500,1500]
321 plot_temp = 200

```

```

322 for x in mT:
323     fig = plt.figure(figsize = (16,8))
324     # color=iter(cm.Dark2(np.linspace(0,1,len(Q_dataframe.columns)))
325     )
326     color=iter(['b','b','darkorange','k','g','darkviolet','r'])
327     for i in names_sorted:#range(len(sizes)):
328         # correction for Co load if it is 100 % Co
329         load_correct = 1
330         c = next(color)
331         col_name = i
332         if col_name == '100 nm on AlOx':
333             load_correct =0.14
334             # print("done")
335         if col_name == '20 nm on AlOx' or i == '20 nm on AlOx 2' or i
336         == '15-60 nm on AlOx':
337             load_correct =0.1
338         if col_name == '45 nm on AlOx':
339             load_correct =0.18
340         if col_name == '30 nm on AlOx':
341             load_correct =0.1
342             # print('works')
343         if col_name == '40 nm on AlOx':
344             load_correct =0.14
345         if col_name == '30nm' or col_name == '30nm':
346             continue
347         for j in [1]:# Mr_dataframe[i].index:
348             if j%2==0:
349                 style="--" #every equal rune (here only the first)
350                 will be dotted
351             else:
352                 style = "-"
353
354                 plt.errorbar(x=sizes_sorted[names_sorted.index(i)],y=
355                 Q_dataframe[col_name][j].loc[x][plot_temp]/load_correct,xerr=
356                 sizes_err[names_sorted.index(i)],fmt="o",color=c,markersize=10,
357                 label=str(sizes_sorted[names_sorted.index(i)]+" nm") # plot the
358                 curves
359 # plt.xlim(0,150E-9)
360 # plt.ylim(0,0.02)
361 plt.ticklabel_format(axis='x', style='sci', scilimits=(0,0))
362 plt.grid(which='major',color="0.3", linestyle='-', linewidth
363 =0.18,alpha=0.5)
364 plt.grid(which='minor',color="0.3", linestyle=':', linewidth
365 =0.18,alpha=0.5)
366 plt.grid(True)
367 plt.xlabel("d [m]",size=22)
368 plt.ylabel(r"W$_{\rm h}$ [J/kg]",size=22)
369 plt.xticks(fontsize=18)
370 plt.yticks(fontsize=18)

```

```

362 plt.title("Q(d), "+str(x)+" mT "+str(plot_temp)+"",  $\text{\textcircled{C}}$ ,
363 size = 25)
364 plt.legend(ncol= 1, loc='upper right', fancybox = True,
365 fontsize = 18)#bbox_to_anchor = [1.1,0.8])
366 # plt.legend(ncol= 1, loc='best', fancybox = True, shadow = True
367 # , fontsize = 18)
368 # plt.savefig("plots/Size_dep_"+str(x)+"mT_"+str(plot_temp)+"deg
369 # "+ "_run"+str(j+1)+"_corrected_v02.png",bbox_inches='tight',
370 # format='png', dpi=300)
371 #del hys_temp
372 #%%
373 #
374 =====
375 # Hc vs. size for 20 and 55 mT at 700 deg. C
376 #
377 =====
378
379 names_sorted = ['20 nm on AlOx', '20 nm on AlOx 2', '30 nm on AlOx',
380 '40 nm on AlOx', '15-60 nm on AlOx', '45 nm on AlOx', '100 nm on
381 AlOx']
382 sizes_sorted = [18.8,18.8,27.4,38.2,40.1,45.6,60.9]
383 plt.close("all")
384 mT = [100]
385 plot_temp = 950
386 for x in mT:
387 fig = plt.figure(figsize = (16,8))
388 color=iter(cm.Dark2(np.linspace(0,1,len(Q_dataframe.columns))))
389 # color=iter(cm.jet(np.linspace(0,1,len(sizes))))
390 for i in names_sorted:# [6,7,8,9,10,11,12]:#range(len(sizes)):
391 # correction for Co load if it is 100 % Co
392 load_correct = 1
393 c = next(color)
394 col_name = i
395 if i == '100 nm on AlOx':
396 load_correct =0.14
397 # print("done")
398 if i == '20 nm on AlOx' or i == '20 nm on AlOx 2' or i == '
399 15-60 nm on AlOx':
400 load_correct =0.1
401 if i == '45 nm on AlOx':
402 load_correct =0.18
403 if i == '30 nm on AlOx':
404 load_correct =0.1
405 if i == '40 nm on AlOx':
406 load_correct =0.14
407 if i == '30nm' or i == '30nm':
408 continue

```

```

399     for j in [1]:# Mr_dataframe[i].index:
400         if j%2==0:
401             style="--" #every equal rune (here only the first)
will be dotted
402         else:
403             style = "-"
404             plt.plot(sizes_sorted[names_sorted.index(i)],
Hc_dataframe[i][j].loc[x][plot_temp]/load_correct,"o", linestyle
=style,color=c,linewidth=3,label=str(sizes_sorted[names_sorted.
index(i)]+" run "+str(j+1)) # plot the curves
405             plt.xlim(0,65)
406             plt.ylim(0)
407             # plt.ticklabel_format(axis='x', style='sci', scilimits=(0,0))
408             plt.grid(which='major',color="0.3", linestyle='-', linewidth
=0.18,alpha=0.5)
409             plt.grid(which='minor',color="0.3", linestyle=':', linewidth
=0.18,alpha=0.5)
410             plt.grid(True)
411             plt.xlabel("d [nm]",size=22)
412             plt.ylabel("H$_C$ [J/kg]",size=22)
413             plt.xticks(fontsize=18)
414             plt.yticks(fontsize=18)
415             plt.title("H$_C$(d), "+str(x)+" mT " + str(plot_temp)+" C",
size = 25)
416             plt.legend(ncol= 1, loc='right', fancybox = True,
bbox_to_anchor = [1.2,0.8], fontsize = 18)
417 # plt.legend(ncol= 1, loc='best', fancybox = True, shadow = True
, fontsize = 18)
418 # plt.savefig("plots/Size_dep_HC_"+str(x)+"mT_"+str(plot_temp)+"
deg+"_run"+str(j+1)+"_corrected_v01.png",bbox_inches='tight',
format='png', dpi=300)
419
420 %%
421 #
=====
422 # Mr vs. size for 20 and 55 mT at 700 deg. C
423 #
=====
424
425 sizes = [1.6E-6,2E-6,7.5E-6,30E-9,16E-9,700E-9,100E-9,20E-9,45E
-9,40E-9,20E-9,37.5E-9,30E-9]
426
427
428 #plt.close("all")
429 mT = [500]
430 plot_temp =950
431 for x in mT:

```

```

432 fig = plt.figure(figsize = (16,8))
433 # color=iter(cm.Dark2(np.linspace(0,1,len(Q_dataframe.columns)))
)
434 color=iter(cm.jet(np.linspace(0,1,len(sizes))))
435 for i in [6,7,8,9,10,11,12]:#range(len(sizes)):
436     # correction for Co load if it is 100 % Co
437     load_correct = 1
438
439     c = next(color)
440     col_name = Mr_dataframe.columns[i]
441     if i == '100 nm on AlOx':
442         load_correct =0.14
443         print("done")
444     if i == '20 nm on AlOx' or i == '20 nm on AlOx 2' or i == '
15-60 nm on AlOx':
445         load_correct =0.1
446     if i == '45 nm on AlOx':
447         load_correct =0.18
448     if i == '30 nm on AlOx':
449         load_correct =0.1
450     if i == '40 nm on AlOx':
451         load_correct =0.14
452     if i == '30nm' or i == '30nm':
453         continue
454     for j in [1]:# Mr_dataframe[i].index:
455         if j%2==0:
456             style="--" #every equal rune (here only the first)
will be dotted
457         else:
458             style = "-"
459             plt.plot(sizes[i],Mr_dataframe[col_name][j].loc[x][
plot_temp]/load_correct,"o", linestyle=style,color=c,linewidth
=3,label=str(sizes[i])+" run "+str(j+1)) # plot the curves
460     plt.xlim(0,150E-9)
461     plt.ylim(0)
462     plt.ticklabel_format(axis='x', style='sci', scilimits=(0,0))
463     plt.grid(which='major',color="0.3", linestyle='-', linewidth
=0.18,alpha=0.5)
464     plt.grid(which='minor',color="0.3", linestyle=':', linewidth
=0.18,alpha=0.5)
465     plt.grid(True)
466     plt.xlabel("d [m]",size=22)
467     plt.ylabel("r M $_{\rm R}$  [J/kg]",size=22)
468     plt.xticks(fontsize=18)
469     plt.yticks(fontsize=18)
470     plt.title("M $_{\rm R}$ (d), "+str(x)+" mT "+str(plot_temp)+" C", size
= 25)
471     plt.legend(ncol= 1, loc='right', fancybox = True, shadow = True
, bbox_to_anchor = [1.25,0.5], fontsize = 18)

```



```
472 # plt.legend(ncol= 1, loc='best', fancybox = True, shadow = True
    , fontsize = 18)
473 # plt.savefig("plots/Size_dep_MR_"+str(x)+"mT_"+str(plot_temp)+"
    deg"+"_run"+str(j+1)+"_corrected_v01.png",bbox_inches='tight',
    format='png', dpi=300)
474
475 #%%
476 #%%
477 #
    =====
478 # Q vs. size raster plot
479 #
    =====
480
481 names_sorted = ['20 nm on AlOx', '20 nm on AlOx 2', '30 nm on AlOx',
    '40 nm on AlOx', '15-60 nm on AlOx', '45 nm on AlOx', '100 nm on
    AlOx']
482 sizes_sorted = [18.8,18.8,27.4,38.2,40.1,45.6,60.9]
483 sizes_err = [6.4,6.4,8.3,13.8,20.2,14.1,28.4]
484
485
486 plt.close('all')
487 nrow = 3
488 ncol = 3
489 fig, axes = plt.subplots(nrow,ncol,figsize = (12,12))
490 mT_plot = [45,100,500]
491 plot_temps = [200,500,800]
492 # samples=[6,7,8,9,10,11,12] # = [0,1,2,6,7,8] #range(len(sizes))
493 #b = mT_plot[0]
494 data_for_eyeguide = []
495 l_style = '-'
496 m_style = 'o'
497 plt_cols = ['b','b','darkorange','k','g','darkviolet','r']
498 for r in range(nrow):
499     plot_temp = plot_temps[r]
500     for c in range(ncol):
501         color=iter(plt_cols)
502         b = mT_plot[c]
503         axes[r,c].tick_params(labelsize=14,direction='in')
504         for i in names_sorted:
505             farve=next(color)
506             # correction for Co load if it is 100 % Co
507             load_correct = 1
508
509             if i == '100 nm on AlOx' or i == '40 nm on AlOx':
510                 load_correct =0.14
511                 # print("correct 100")
```

```

512         if i == '20 nm on AlOx' or i == '20 nm on AlOx 2' or i ==
'30 nm on AlOx' or i == '15-60 nm on AlOx':
513             load_correct = 0.1
514             # print('correct 20s')
515         if i == '45 nm on AlOx':
516             # print('correct 45')
517             load_correct = 0.18
518
519         col_name = i
520         #specify run
521         j = 1
522         axes[r,c].errorbar(x=sizes_sorted[names_sorted.index(i)
],y=Q_dataframe[col_name][j].loc[b][plot_temp]/load_correct,xerr
=sizes_err[names_sorted.index(i)],fmt="o",color=farve,markersize
=10,label=str(round(sizes_sorted[names_sorted.index(i)]))+ " nm")
523         # plot the curves
524         date_for_eyeguide.append(Q_dataframe[col_name][j].loc[b
][plot_temp]/load_correct)
525         if c == 2:
526             axes[r,c].legend([str(plot_temp)+' $\circ$C'], loc
='lower right',fancybox = True, fontsize = 13)
527         else:
528             axes[r,c].legend([str(plot_temp)+' $\circ$C'], loc
='upper right',fancybox = True, fontsize = 13)
529         # legend = plt.legend(handletextpad=-2.0, handlelength
=0)
530         # axes[r,c].annotate(str(plot_temp)+' $\circ$C', xy
=(0.5,0.5))# ,transform = axes[r,c].transAxes,fontsize=18)
531         # axes[r,c].set_ylabel("W$_h$ [J/kg]",size=22)
532         axes[r,c].set_ylim([0,2.5])
533         print("works")
534         if r == 0:
535             axes[r,c].set_title(str(b)+" mT", size = 22)
536
537
538 axes[0,0].set_ylabel(r"W$_h$ [J/kg]",size=25)
539 axes[1,0].set_ylabel(r"W$_h$ [J/kg]",size=25)
540 axes[2,0].set_ylabel(r"W$_h$ [J/kg]",size=25)
541 axes[2,0].set_xlabel("D [nm]",size=22)
542 axes[2,1].set_xlabel("D [nm]",size=22)
543 axes[2,2].set_xlabel("D [nm]",size=22)
544
545 axes[0,2].legend([ str(round(i))+' nm' for i in sizes_sorted],ncol=
1, loc='upper left',bbox_to_anchor=[1.01,1.01], fancybox = True
, fontsize = 18)
546 plt.savefig("plots/D_raster_plot_v02.png",bbox_inches='tight',
format='png', dpi=300)
547 #del hys_temp

```

```
548 #%%
549 #
=====
550 # Raster plot with particle sizes
551 #
=====

552 plt.close("all")
553 #sizes = [1.6E-6,2E-6,7.5E-6,30E-9,16E-9,700E-9,100E-9,20E-9,45E-9]
554 #IN01,IN01,IN06,IN07,IN08,IN02,IN05
555 names_sorted = ['20 nm on AlOx', '20 nm on AlOx 2', '30 nm on AlOx',
    '40 nm on AlOx', '15-60 nm on AlOx', '45 nm on AlOx', '100 nm on
    AlOx']
556 sizes_sorted = [18.8,18.8,27.4,38.2,40.1,45.6,60.9]
557
558 nrow = 3
559 ncol = 3
560 fig, axes = plt.subplots(nrow,ncol,figsize = (12,12))
561 mT_plot = [45,100,500]
562 # samples=[6,7,8,9,10,11,12] # = [0,1,2,6,7,8] #range(len(sizes))
563 #b = mT_plot[0]
564
565 l_style = '-'
566 m_style = 'o'
567 plt_cols = ['b','b','darkorange','k','g','darkviolet','r']
568 for r in range(nrow):
569     for c in range(ncol):
570         axes[r,c].tick_params(direction='in')
571         color=iter(plt_cols)
572         b = mT_plot[c]
573         if r == 0:
574
575             for i in names_sorted:
576                 farve=next(color)
577                 # correction for Co load if it is 100 % Co
578                 load_correct = 1
579
580                 if i == '100 nm on AlOx' or i == '40 nm on AlOx':
581                     load_correct = 0.14
582                     # print("correct 100")
583                 if i == '20 nm on AlOx' or i == '20 nm on AlOx 2' or
i == '30 nm on AlOx' or i == '15-60 nm on AlOx':
584                     load_correct = 0.1
585                     # print('correct 20s')
586                 if i == '45 nm on AlOx':
587                     # print('correct 45')
588                     load_correct = 0.18
589
```

```

590         plot_this = 1/load_correct*Q_dataframe[i][1].loc[b]
591         plot_this.plot(ax = axes[r,c],marker = m_style, ls=
l_style,linewidth = 3,color=farve)
592
593         # axes[r,c].set_ylabel("W$_h$ [J/kg]",size=22)
594         # axes[r,c].set_ylim([0,2.5])
595         # print("works")
596         axes[r,c].set_title(str(b)+" mT", size = 22)
597
598
599
600
601     if r == 1:
602         for i in names_sorted:
603             farve=next(color)
604             Hc_dataframe[i][1].loc[b].plot(ax = axes[r,c],
marker = m_style, ls=l_style,linewidth = 3,color=farve)
605             # axes[r,c].set_ylabel("H$_c$ [mT]",size=22)
606             # axes[r,c].set_ylim([0,26])
607
608     if r == 2:
609         for i in names_sorted:
610             farve=next(color)
611             # correction for Co load if it is 100 % Co
612             load_correct = 1
613
614             if i =='100 nm on AlOx' or i =='40 nm on AlOx':
615                 load_correct =0.14
616                 # print("correct 100")
617             if i =='20 nm on AlOx' or i =='20 nm on AlOx 2' or
i =='30 nm on AlOx' or i =='15-60 nm on AlOx':
618                 load_correct =0.1
619             if i =='45 nm on AlOx':
620                 load_correct =0.18
621             plot_this = 1/load_correct*Mr_dataframe[i][1].loc[b
]
622             plot_this.plot(ax = axes[r,c],marker = m_style, ls=
l_style,linewidth = 3,color=farve)
623
624             axes[r,c].set_xlabel("Temperature $\sim$circ$C",size
=22)
625             axes[r,c].set_label(str(b)+" mT")
626         # axes[r,c].legend()
627         # axes[r,c].set_ylim([0,10])
628         # axes[r,c].yaxis.grid(True, alpha = 0.2)
629         # axes[r,c].xaxis.grid(True,alpha = 0.2)
630         axes[r,c].tick_params(labelsize=18)
631         # plt.yticks(fontsize=18)
632

```

```

633 # label on y axis only on the left
634 axes[2,0].set_ylabel(r"\sigma_{\rm R}$ [Am$^2$/kg]",size=25)
635 axes[1,0].set_ylabel(r"\mu_{\rm O}$H$_{\rm C}$ [mT]",size=25)
636 axes[0,0].set_ylabel(r"W$_{\rm h}$ [J/kg]",size=25)
637
638
639 axes[0,2].legend([ str(i)+' nm' for i in sizes_sorted],ncol= 1, loc
    ='upper left',bbox_to_anchor=[1.01,1.01], fancybox = True,
    fontsize = 18)
640 # plt.savefig("plots/raster plot_v05.png",bbox_inches='tight',
    format='png', dpi=300)
641
642 #%%
643 #
    =====
644 # Calculation of blocking temperature
645 #
    =====
646 def TB(d,t_meas):
647     kB = 1.38064852E-23 #J*K-1
648     alpha = 100
649     tau_0 = 1E-9 # to 1E-12
650     # K = 2.7E5 #J/m^3
651     K = 2.5E5 #J/m^3 from Petit2004
652     V = (4/3)*np.pi*(((d*10**(-9))/2)**3) # assume spherical
653     T_B = K*V/(kB*np.log(alpha*t_meas/tau_0)) - 273.15
654     # T_B = (K*4/3*np.pi*(((d*10**(-9))/2)**3)/(kB*np.log(alpha*
    t_meas/tau_0))
655     return(T_B)
656 #%%
657
658 kB = 1.38064852E-23 #J*K-1
659 alpha = 100
660 tau_0 = 1E-9 # to 1E-12
661 # K = 2.7E5 #J/m^3
662 K = 2.5E5 #J/m^3 from Petit2004
663 # V = (4/3)*np.pi*(((d*10**(-9))/2)**3) # assume spherical
664 X = Symbol('X')
665 r_crit_950 =(((3*(950+273.15)*kB*np.log(alpha*0.3/tau_0))/(4*np.pi*K
    ))**(1/3))*2*10**9
666 # print(TB(10,0.1))
667 #%%
668 plt.close("all")
669 plt_sizes = np.linspace(0,100,100)
670
671 fig = plt.figure(figsize = (16,8))
672 color=iter(cm.Dark2(np.linspace(0,1,len(Hc_dataframe.columns))))

```

```

673 style = "-"
674
675 plt.axhline(y=1121, color = 'k')
676 plt.axhline(y=950, xmin=0, xmax=r_crit_950/20, color = 'k',
677           linestyle='--')
678
679 plt.axvline(x=r_crit_950, ymin=0, ymax=(950+273.15)/(1200+273.15),
680           color = 'k',linestyle='--')
681
682 plt.plot(plt_sizes, TB(plt_sizes, 0.3), linestyle=style, color='r',
683         linewidth=3, label=str(i)+" run "+str(j+1)) # plot the curves'
684
685 plt.xlim(0, 20)
686 plt.ylim(-273.15, 1200)
687 plt.grid(which='major', color="0.3", linestyle='-', linewidth=0.18,
688         alpha=0.5)
689 plt.grid(which='minor', color="0.3", linestyle=':', linewidth=0.18,
690         alpha=0.5)
691 plt.grid(True)
692 plt.xlabel(r"D$_{\rm C}$ [nm]", size=22)
693 plt.ylabel(r'T$_{\rm B}$ [K]$', size=22)
694 plt.xticks(fontsize=18)
695 plt.yticks(fontsize=18)
696 # plt.title("H$_c$(T), "+str(x)+" mT", size = 25)
697 # plt.legend(ncol= 1, loc='right', fancybox = True, shadow = True,
698           bbox_to_anchor = [1.18,0.5], fontsize = 18)
699 # plt.savefig("plots/T_B_v03.png",bbox_inches='tight', format='png
700           ', dpi=300)
701
702 #%%
703 #
704 =====
705
706 # Get mean and variance from lognormal parameters
707 #
708 =====
709
710 import scipy
711 def CDF(x, mu, sigma):
712     cdf = 0.5+0.5*scipy.special.erf((np.log(x)-mu)/(np.sqrt(2)*
713     sigma))
714     return cdf
715
716 INXX_lognorm_size = pd.read_csv("IN-XX_lognorm_size.csv")
717
718 # m = np.exp(INXX_lognorm_size["mu"])
719 # v = np.exp(INXX_lognorm_size["sigma"])
720
721 m = np.exp(INXX_lognorm_size["mu"] - INXX_lognorm_size["sigma"]**2)
722 # v = np.exp(2 * INXX_lognorm_size["mu"] + INXX_lognorm_size["sigma
723     "]]**2) * (np.exp(INXX_lognorm_size["sigma"]**2) - 1)

```

```

709 # v=np.sqrt(np.log(1+(INXX_lognorm_size["sigma"]/INXX_lognorm_size
      ["mu"])**2))
710 v=np.sqrt(np.exp(INXX_lognorm_size["sigma"]**2)-1)*
      INXX_lognorm_size["mu"]
711 # check =
712 # test = pd.concat([INXX_lognorm_size,m])
713 # test = INXX_lognorm_size.join({'mean':m})
714 INXX_lognorm_size['mode'] = m
715 # INXX_lognorm_size['v_geo'] = v
716 print(CDF(INXX_lognorm_size["mode"],INXX_lognorm_size["mu"],
      INXX_lognorm_size["sigma"]))
717 # print(0.5+0.5*scipy.special.erf((np.log(40.129743)-3.77327)/(np.
      sqrt(2)*0.29009)))

```

**Listing A.2:** Example of base script for slicing through data across samples

### A.1.3 Scripts for definitions and functions used in the scripts

```

1 # -*- coding: utf-8 -*-
2 """
3 Created on Thu Dec 14 08:25:18 2017
4
5 @author: marad
6 """
7
8 import re
9 import os
10 import pandas as pd
11 import numpy as np
12
13 def get_line(string, master):
14     """
15     Returns first linenumber containing a specific string.
16     Used e.g. to find start of data with search_string=***DATA***
17     """
18
19     # Convert search string to make sure * is interpreted as \* and
20     # not a wildcard symbol
21     search_string = re.escape(string)
22
23     # Go through datafile line by line
24     lines = []
25     with open(master) as datafile:
26         for linenumber, line in enumerate(datafile):
27
28             # Search for string in the line
29             match = re.findall(search_string, line)
30             if match:
31                 lines.append(linenumber)

```

```

32     #     if not match:
33         #         linewidth = None
34     return lines
35 #%%
36
37 def load_vsm_file(filepath):
38     # Load a full datafile from the VSM
39     # Delimiter of \s+ means any whitespace is delimiter
40     data = pd.read_csv(filepath,
41                        delimiter='\s+',
42                        header=get_header(filepath))
43
44     return data
45
46 #%%
47 #
48 # =====
49 #
50 # Import of data via textrecognition
51 # =====
52
53 def get_data(master, fieldstr, mass, namelist):
54     fieldstr = np.multiply(fieldstr, 10) #go from mT to Oe
55     for elmnt, sym in enumerate(namelist[0]):
56         search_string = re.escape("#")
57         match = re.findall(search_string, sym)
58         if match:
59             l=(elmnt)
60             generated_filename = namelist[0][0:l+1] #+1 because otherwise
61             the l'th element isn't included
62             list_for_length = get_line("hys_c_%i("%fieldstr[0], master)
63             field_sorted_list = np.empty([int(len(list_for_length)/2), 0]).
64             tolist() #half the size because "hys_c_%i(" comes twice in the
65             master file for every time the field is ramped
66
67     temp_places = [] # to check why we have an empty run in the
68     beginning
69     for i in range(len(fieldstr)):
70         # Get all lines in the master file than has the chosen
71         field-strength
72         mT = get_line("hys_c_%i("%fieldstr[i], master)
73         #
74     =====

```



```

70     # TODO : lav lav hentningen af filnavnet automatisk
71     #
=====
72     # Convert search string to make sure * is interpreted as \*
    and not a wildcard symbol
73
74
75     # Go through datafile line by line and save the line that
    states in which file the data is stored
76     data_lines = []
77
78     with open(master) as datafile:
79
80         for linenummer, line in enumerate(datafile):
81
82
83             for j in range(0,len(mT),2):#every second index due
    to the way we look through the file right now
84                 if linenummer == mT[j]+1: # the line we look
    for is one line below the one we find
85                     data_lines.append(line)
86             del linenummer
87
88
89     # Find the file-number in which the data is stored
90     places = []
91     for line in data_lines:
92         places.append(re.findall(r'\d+', line)[-1]) # the txt
    file number is the last number
93
94     temp_places.append(places)
95
96     # loading data
97     # here it is only for the first place in each loop! der
    skal itereres i places
98     for x in range(len(places)):
99         filepath = generated_filename+places[x]+".txt"
100        filename = generated_filename+places[x]+".txt"
101        header_line = get_line("***DATA***",filename)[0]-1
102
103        pd_temp = pd.read_csv(filepath, delimiter='\s+', header
    =header_line, names=("Field(Oe)", "Moment(emu)", "Temperature(C)"
    )
104
105
106
107        # convert to millitesla and ampere meter^2/kg
108        pd_temp["Field(Oe)"]=pd_temp["Field(Oe)"]*10**(-1) #

```

```

convert from Gauss to mT
109     pd_temp.rename(columns={"Field(Oe)": "Field(mT)"},
inplace=True)
110     pd_temp["Moment(emu)"] = pd_temp["Moment(emu)"] / mass #
from emu to emu per gram, which is equal to Am^2/kg
111     pd_temp.rename(columns={"Moment(emu)": "Moment(Am^2/kg)"
}, inplace=True)
112
113     # Delete empty lines from the dataframe as "
skip_empty_lines = True" did not work in the import
114     pd_temp = pd_temp[np.isfinite(pd_temp["Field(mT)"])]
115     field_sorted_list[x].append(pd_temp)
116     del pd_temp, header_line
117
118     # Divide the list of dataframes in to runs and append to
run_list
119     run_indx = []
120
121     # first loop checks where the temperature from the previous
cycle is higher than the current one
122     # e.g. when we go from 950 to 200 deg C in the new run
123     run_tempcheck = 0 # the temperature from the previous loop,
used to check if we have gone down in temperature / e.g. started
a new run
124     for i in range(len(field_sorted_list)):
125         if np.round(field_sorted_list[i][0]["Temperature(C)"][0]) <
np.round(field_sorted_list[i-1][0]["Temperature(C)"][0]):
126             run_indx.append(i)
127         else:
128             run_tempcheck = np.round(field_sorted_list[i][0]["
Temperature(C)"][0])
129     del run_tempcheck
130
131     runs_list = []
132     # The next part splits up the field_sorted_list into runs in
the runs_list
133     for i in range(len(run_indx)):
134         try:
135             runs_list.append(field_sorted_list[run_indx[i]:run_indx
[i+1]])
136         except IndexError:
137             runs_list.append(field_sorted_list[run_indx[i]:len(
field_sorted_list)+1])
138
139     return(runs_list, temp_places)
140     # delete various unneeded variables
141 # del field_sorted_list, data_lines, data_temp
142 #%%
143 #%%

```

```
144 #
    =====
145 # Get all the data from Tc files
146
147 #
    =====
148 def get_tcdata(master, path, Tc_names, mass, full_list):
149     #
    =====
150
151     # Get all the data from Tc files
152     # TODO: lav det meste af dette til separat (generel) funktion
153     #
    =====
154
155     measvtime = []
156     # Get lines where the curie temp is measured
157     for i in range(len(Tc_names)):
158         #measvtimeDown = get_line("MeasVsTimeDown9100s ", master)
159         #measvtimeUp = get_line("MeasVsTimeUp9100s began ", master)
160         measvtime = measvtime + get_line(Tc_names[i], master)
161
162
163     data_lines = []
164     with open(master) as datafile:
165
166         for linenumber, line in enumerate(datafile):
167             for j in range(0, len(measvtime), 2): #every second index
168                 # due to the way we look through the file right now
169                 if linenumber == measvtime[j]+1: # the line we look
170                     for is one line below the one we find
171                         data_lines.append(line)
172
173     del linenumber
174
175     list_of_Tcs = []
176     places = []
177     for line in data_lines:
178         places.append(re.findall(r'\d+', line)[-1]) # the txt file
179         # number is the last number r'\d+' finds all WHOLE numbers in text
180
181     #find the generic filename (everything up to, and counting, the
182     # hashtag)
183     # this is done by searching with regular expressions
184
185     i_start = re.search("/", full_list[0]).start()+1 # find the / in
186     the first entry in the list of of filenames. The +1 is because
```

```

the wau python indexes, so from the index AFTER the / To (
INCLUDING) the #
180 i_end = re.search("#",full_list[0]).start()+1 # find the # in
the first entry in the list of of filenames.
181 gen_filename = full_list[0][i_start:i_end]
182
183
184 #full_list[0][49+1:85+1]
185
186 for x in range(len(places)):
187     filepath = path+gen_filename+places[x]+".txt"
188     filename = gen_filename+places[x]+".txt"
189     header_line = get_line("***DATA***",path+filename)[0]-1
190     pd_temp = pd.read_csv(filepath, delimiter='\\s+', header=
header_line, names=("Field(Oe)", "Moment(emu)", "Temperature(C)", "
Time(sec)"))
191     pd_temp["Moment(emu)"]=pd_temp["Moment(emu)"]/mass # from
emu to emu per gram, which is equal to Am^2/kg
192     pd_temp.rename(columns={"Moment(emu)": "Moment(Am^2/kg)"},
inplace=True)
193     # pd_temp.rename(columns={"Temperature(K)": "Temperature(C)
"},inplace=True) # rename to celsius
194     list_of_Tcs.append(pd_temp)
195     # del pd_temp
196     return(list_of_Tcs)
197     # del pd_temp
198
199 #%%
200 #
=====
201
202
203 # Get Tc from tangent line method using the peaks of the second
derivative
204
205
206 #
=====
207
208 def Tc_tangent(list_of_Tcs,smoothing_window):
209     from scipy.signal import savgol_filter
210     Tc_tangent_method = []
211     for i in range(len(list_of_Tcs)):
212         n_smth = smoothing_window #how many points to smooth the
over in the graph
213         T_grad2 = savgol_filter(np.gradient(savgol_filter(np.
gradient(savgol_filter(list_of_Tcs[i]["Moment(Am^2/kg)"],n_smth

```

```

,3)),n_smth,3)),n_smth,3)
214     T_grad = savgol_filter(np.gradient(savgol_filter(
list_of_Tcs[i]["Moment(Am^2/kg)"],n_smth,3)),n_smth,3)
215     data_M= list_of_Tcs[i]["Moment(Am^2/kg)"]
216     data_T= list_of_Tcs[i]["Temperature(C)"]
217     # The T_scale is only used for scaling the plots
218     # T_scale = [h for h, x in enumerate(data_T) if x>300
and x< 301]
219
220
221     # Temperature interval for finding the mid slope
222     T1 = np.nanargmin(T_grad2) #the "nan" ignores NaN's
223     T2 = np.nanargmax(T_grad2)
224
225     # find mid slope
226     if T1 < T2:
227         p = T1
228         k = T2
229         tag = "Up"
230     else:
231         p = T2
232         k = T1
233         tag = "Down"
234     # Add the start indice where you look for the slope (p) to
where fx. the middle of the slope is
235     mid_slope = np.argmin(np.abs(T_grad2[p:k]))+p
236     max_mom = max(np.abs(T_grad))
237     mid_slope_temp = data_T[mid_slope]
238     mid_slope_mom = data_M[mid_slope]
239
240     if T1 < T2:
241         p = mid_slope-int(round(np.abs(mid_slope-T1)/2))
242         k = mid_slope + int(round(np.abs(T2-mid_slope)/2))
243     else:
244         p = mid_slope-int(round(np.abs(mid_slope-T2)/2))
245         k = mid_slope + int(round(np.abs(T1-mid_slope)/2))
246     x1 = data_T[p:k]
247     y1 = data_M[p:k]
248     lin_fit1 = np.polyfit(x1,y1,1)
249     fit_fn1 = np.poly1d(lin_fit1)
250
251     T5 = [h for h, x in enumerate(data_T) if x> 930 and x< 931]
252     T6 = [h for h, x in enumerate(data_T) if x> 948 and x< 949]
253     # plt.xlim(300,975)
254
255     # fit at fall tail of curve
256     if T5[0] < T6[0]:
257         p = T5[0]
258         k = T6[0]

```

```

259     else:
260         p = T6[0]
261         k = T5[0]
262         x2 = data_T[p:k]
263         y2 = data_M[p:k]
264         lin_fit2 = np.polyfit(x2,y2,1)
265         fit_fn2 = np.poly1d(lin_fit2)
266
267
268
269
270         # solve expressions for x
271         from sympy.solvers import solve
272         from sympy import Symbol
273         x = Symbol('x')
274         Tc_solved = solve(fit_fn1(x)-fit_fn2(x),x)
275         Tc_tangent_method.append(Tc_solved[0])
276     return(Tc_tangent_method)
277 #%%
278 #
279 # =====
280 # Getting hysteresis area, Coercive field and Remanent
281 # magnetization
282 # =====
283
284 def gethys_param(runs_list,ints):#%%
285     hys_df_list = []
286     Hc_df_list = []
287     Mr_df_list = []
288     Ms_df_list = []
289     for run in range(len(runs_list)):
290         # make a dataframe for all the data in the run
291         #run_nr
292         #temps = range(200,1000,50)
293
294         temps = []
295         for i in range(len(runs_list[run])):
296             temps.append(int(round(np.mean(runs_list[run][i][0]["
297 Temperature(C)"])/50)*50)) #the 50's rounds to nearest 50.)
298
299         hysarea_df = pd.DataFrame(index = ints, columns=range(len(
300 temps))) # rename columns as temperatures later
301         Hc_df = pd.DataFrame(index = ints, columns=range(len(temps)
302 )) # rename columns as temperatures later
303         Mr_df = pd.DataFrame(index = ints, columns=range(len(temps)
304 )) # rename columns as temperatures later

```

```

299     Ms_df = pd.DataFrame(index = ints, columns=range(len(temps)
300 )) # rename columns as temperatures later
301     moment_up = []
302
303     field_up = []
304     # for run in run_nr:
305         for i in range(len(runs_list[run])): #Temperatures
306             for j in range(len(runs_list[run][i])): #Fields
307
308                 #Define the field for the upper hysteresis curve
309                 field_minarg = runs_list[run][i][j]["Field(mT)".
310 idxmin() # end-point of the curve in field-column
311                 field_up = runs_list[run][i][j]["Field(mT)"][0:
312 field_minarg+1] # add the 1 to close the graph
313                 #Define the field for the lower hysteresis curve,
314                 # the first point for the field is added to the last point, so the
315                 # curve will be closed
316                 field_down = np.append(big_field[i][np.argmin(
317 big_field[i]):len(big_field[i])],big_field[i][0])
318                 field_down = pd.Series(runs_list[run][i][j]["Field(
319 mT)"][field_minarg:len(runs_list[run][i][j])])
320                 field_down = field_down.append(pd.Series(runs_list[
321 run][i][j]["Field(mT)"][0])) # TODO: fix at det sidste append
322                 element har nÃste index i stedet for nul!
323
324                 #The same for the moments
325                 moment_up = runs_list[run][i][j]["Moment(Am^2/kg)"
326 ][0:field_minarg+1]
327                 moment_down = pd.Series(runs_list[run][i][j]["
328 Moment(Am^2/kg)"][field_minarg:len(runs_list[run][i][j])])
329                 moment_down = moment_down.append(pd.Series(
330 runs_list[run][i][j]["Moment(Am^2/kg)"][0]))# TODO: fix at det
331 sidste append element har nÃste index i stedet for nul!
332
333                 # Hysteresis area
334                 #Use the trapz function to make the intergral, I
335                 # plus the moments with 1000 so all the valus for the hysteresis
336                 # will be positive.
337                 area_up=(abs(np.trapz(moment_up+1000,field_up)))
338                 area_down=(np.trapz(moment_down+1000,field_down))
339                 #The total area will be the intergral of the upper
340                 # cuve minus the intergral of the lower curve.
341
342                 # field index to write to in dataframe:
343                 F_indx = int(round(runs_list[run][i][j]["Field(mT)"
344 ][1]/5))*5
345
346                 if np.isfinite(hysarea_df[i].loc[F_indx]) == False:
347                     #makes sure it doesn't overwrite data

```

```

330         hysarea_df[i].loc[F_idx] = (area_up-area_down)
/1000 # The factor of 1000 converts from mT to Tesla
331     else:
332         print(" something is wrong with i =" +str(i)+ " j
= "+str(j))
333
334     # Remanent field
335     # find the minimum of the absolute value of the upper and
lower part of the hysteresis curve
336     #Temporary variables used to find the point
337     min_indic_field = []
338     field_up_abs = abs(field_up)
339     field_down_abs = abs(field_down)
340     min_indic_field.append(field_up_abs.idxmin())
341     min_indic_field.append(field_down_abs.idxmin())
342     if np.isfinite(Mr_df[i].iloc[j]) == False: #makes
sure it doesn't overwrite data
343         # the moment value Mr where the field crosses
the y-axis (min indices) are found, and the (absolute) average
between the two values are found
344         Mr_df[i].iloc[j] = (np.abs(runs_list[run][i][j
].iloc[min_indic_field[0]]["Moment(Am^2/kg)"])+np.abs(runs_list[
run][i][j].iloc[min_indic_field[1]]["Moment(Am^2/kg)"]))/2 # The
factor of 1000 converts from mT to Tesla
345     else:
346         print(" something is wrong with i =" +str(i)+ " j
= "+str(j))
347
348     # Coercive field
349     # find the minimum of the absolute value of the upper and
lower part of the hysteresis curve
350     #Temporary variables used to find the point
351     min_indic_mom = []
352     moment_up_abs = abs(moment_up)
353     moment_down_abs = abs(moment_down)
354     min_indic_mom.append(moment_up_abs.idxmin())
355     min_indic_mom.append(moment_down_abs.idxmin())
356     if np.isfinite(Hc_df[i].iloc[j]) == False: #makes
sure it doesn't overwrite data
357         # the moment value Mr where the field crosses
the y-axis (min indices) are found, and the (absolute) average
between the two values are found
358         Hc_df[i].iloc[j] = (np.abs(runs_list[run][i][j
].iloc[min_indic_mom[0]]["Field(mT)"])+np.abs(runs_list[run][i][
j].iloc[min_indic_mom[1]]["Field(mT)"]))/2 # The factor of 1000
converts from mT to Tesla
359     else:
360         print(" something is wrong with i =" +str(i)+ " j
= "+str(j))

```



```

361
362     # Saturation magnetisation
363     # find the minimum of the absolute value of the upper and
364     lower part of the hysteresis curve
365         #Temporary variables used to find the point
366         indic_field = []
367         indic_field.append(field_up.idxmax())
368         indic_field.append(field_down.idxmin())
369         if np.isfinite(Ms_df[i].iloc[j]) == False: #makes
370     sure it doesn't overwrite data
371         # the moment value Mr where the field crosses
372     the y-axis (min indices) are found, and the (absolute) average
373     between the two values are found
374         Ms_df[i].iloc[j] = (np.abs(runs_list[run][i][j
375     ].iloc[indic_field[0]]["Moment(Am^2/kg)"])+np.abs(runs_list[run
376     ][i][j].iloc[indic_field[1]]["Moment(Am^2/kg)"]))/2 # The factor
377     of 1000 converts from mT to Tesla
378     else:
379         print(" something is wrong with i =" +str(i)+" j
380     = "+str(j))
381
382     hysarea_df.columns = temps
383     Hc_df.columns = temps
384     Mr_df.columns = temps
385     Ms_df.columns = temps
386     hys_df_list.append(hysarea_df)
387     Hc_df_list.append(Hc_df)
388     Mr_df_list.append(Mr_df)
389     Ms_df_list.append(Ms_df)
390
391     return(hys_df_list,Hc_df_list,Mr_df_list,Ms_df_list)

```

Listing A.3: Base script for raw data analysis

```

1 # -*- coding: utf-8 -*-
2 """
3 Created on Mon Apr 13 16:43:26 2020
4
5 @author: marad
6 """
7 import re
8 import os
9 import pandas as pd
10 import numpy as np
11 def Co_load_check(sample_id,size,mass,loading,runs_list,overwrite):
12     ms = 162.5 #Am^2/kg, from Myers and Sucksmith, 1951: "The
13     Spontaneous Magnetization of Cobalt"
14     # loading = 0.13
15     ms_litt = 162.5*loading*mass*10**(-3)

```

```

15 m_200deg_1500mT =np.mean(runs_list[1][0][-1]["Moment(Am^2/kg)"
16 ][[0,1]])*mass*10**(-3)
17
18 print('Ms-litt.: '+str(ms_litt)+' , Ms_exp: '+str(
19 m_200deg_1500mT)+' , fraction: '+str(m_200deg_1500mT/ms_litt))
20
21 # sample_id = 'IN07'
22 loading_df = pd.DataFrame([[sample_id,size,np.round(mass,5),
23 loading,ms_litt,m_200deg_1500mT]],columns=["sample","size [nm]",
24 "mass [mg]","loading","Ms_litt [Am^2]","Ms_exp [Am^2]"])
25
26 # write the loading check to csv file
27 if 'loading_check.csv' in os.listdir('../'):
28     # overwrite = 1
29     df_temp = pd.read_csv('../loading_check.csv')
30     df_temp=df_temp.sort_values(by = 'size [nm]')
31     if loading_df['sample'][0] in np.array(df_temp['sample']):
32         if overwrite==1:
33             #overwrite csv-entry for that sample
34             for i in range(len(df_temp['sample'])):
35                 if df_temp['sample'][i] == sample_id:
36                     df_temp.iloc[i] = loading_df.iloc[0]
37                     df_temp.to_csv(r'../loading_check.csv',
38 index=False)
39
40             print('Check of loading via saturation
41 magnetization for sample '+sample_id+ " overwritten")
42             # loading_df.to_csv(r'../loading_check.csv',index=
43 False)
44
45             if overwrite == 0:
46                 print('Check of loading via saturation
47 magnetization for sample '+sample_id+' already saved, not
48 overwritten')
49
50             else:
51                 print('Check of loading via saturation magnetization
52 for sample '+sample_id+' has now been added')
53                 df_temp = df_temp.append(loading_df,ignore_index=True)
54                 df_temp=df_temp.sort_values(by = 'size [nm]')
55                 df_temp.to_csv(r'../loading_check.csv',index=False)
56                 # else:
57                 #     df.to_csv('loading_check.csv', mode='a', header=
58 False)
59                 #     #load as dataframe
60                 #     df_temp = pd.read_csv('../loading_check.csv')
61                 #     df_temp.sort_values(by = 'size [nm]')
62
63             else:
64                 print('File didnt exist, has been created and check of
65 loading via saturation magnetization for sample '+sample_id+'

```

```
has been added')
52     loading_df.to_csv(r'../loading_check.csv',index=False)
53     # for i in range(len(list_of_Tcs)):
54         # list_of_Tcs[i].to_csv("../loading/"+path[0:re.search('nm
',path).end()]+ " IN05".csv",index=False)
```

**Listing A.4:** Base script for raw data analysis



# Bibliography

- [1] “Global CO<sub>2</sub> emissions by sector 2018, IEA,” 2018. <https://www.iea.org/data-and-statistics/charts/global-co2-emissions-by-sector-2018>, visited 2020-08-08.
- [2] S. A. Kalogirou, *Solar Energy Engineering: Processes and Systems: Second Edition*. Elsevier Inc., 2014.
- [3] “Lazard levelized cost of energy - version 13,” 2019. <https://www.lazard.com/media/451086/lazards-levelized-cost-of-energy-version-130-vf.pdf>, visited 2020-08-08.
- [4] M. Beaudin, H. Zareipour, A. Schellenberglabe, and W. Rosehart, “Energy storage for mitigating the variability of renewable electricity sources: An updated review,” *Energy for Sustainable Development*, vol. 14, pp. 302–314, 2010.
- [5] A. Raissi and D. Block, “Hydrogen: Automotive fuel of the future,” *IEEE Power and Energy Magazine*, vol. 2, pp. 40–45, 2004.
- [6] “Technology Roadmap - Hydrogen and Fuel Cells,” tech. rep., IEA, Paris, 2015. <https://www.iea.org/reports/technology-roadmap-hydrogen-and-fuel-cells>.
- [7] S. T. Wismann, J. S. Engboek, S. B. Vendelbo, F. B. Bendixen, W. L. Eriksen, K. Aasberg-Petersen, C. Frandsen, I. Chorkendorff, and P. M. Mortensen, “Electrified methane reforming: A compact approach to greener industrial hydrogen production,” *Science*, vol. 364, pp. 756–759, 2019.
- [8] J. Rostrup-Nielsen and L. J. Christiansen, *Concepts in Syngas Manufacture*, vol. 10. London : Imperial College Press, 2011.
- [9] P. M. Mortensen and I. Dybkjær, “Industrial scale experience on steam reforming of CO<sub>2</sub>-rich gas,” *Applied Catalysis A: General*, vol. 495, pp. 141–151, 2015.

- [10] J. R. Rostrup-Nielsen, J. Sehested, and J. K. Nørskov, "Hydrogen and synthesis gas by steam- and CO<sub>2</sub> reforming," in *Advances in Catalysis*, Academic Press, 2002.
- [11] J. R. Rostrup-Nielsen and T. Rostrup-Nielsen, "Large-Scale Hydrogen Production," *CATTECH*, vol. 6, pp. 150–159, 2002.
- [12] P. M. Mortensen, J. S. Engbæk, S. B. Vendelbo, M. F. Hansen, and M. Østberg, "Direct Hysteresis Heating of Catalytically Active Ni-Co Nanoparticles as Steam Reforming Catalyst," *Industrial & Engineering Chemistry Research*, vol. 56, pp. 14006–14013, 2017.
- [13] K. Aasberg-Petersen, J. H. Bak Hansen, T. S. Christensen, I. Dybkjaer, P. S. Christensen, C. Stub Nielsen, S. E. Winter Madsen, and J. R. Rostrup-Nielsen, "Technologies for large-scale gas conversion," *Applied Catalysis A: General*, vol. 221, pp. 379–387, 2001.
- [14] M. G. Vinum, M. R. Almind, J. S. Engbæk, S. B. Vendelbo, M. F. Hansen, C. Frandsen, J. Bendix, and P. M. Mortensen, "Dual-function cobalt-nickel nanoparticles tailored for high-temperature induction-heated steam methane reforming," *Angewandte Chemie*, vol. 57, pp. 10569–10573, 2018.
- [15] S. T. Wismann, J. S. Engbæk, S. B. Vendelbo, W. L. Eriksen, C. Frandsen, P. M. Mortensen, and I. Chorkendorff, "Electrified methane reforming: Understanding the dynamic interplay," *Industrial and Engineering Chemistry Research*, vol. 58, pp. 23380–23388, 2019.
- [16] W. Wang, G. Tuci, C. Duong-Viet, Y. Liu, A. Rossin, L. Luconi, J.-M. Nhut, L. Nguyen-Dinh, C. Pham-Huu, and G. Giambastiani, "Induction Heating: An Enabling Technology for the Heat Management in Catalytic Processes," *ACS Catalysis*, vol. 9, pp. 7921–7935, 2019.
- [17] A. B. Salunkhe, V. M. Khot, and S. H. Pawar, "Magnetic hyperthermia with magnetic nanoparticles: A status review," *Current Topics in Medicinal Chemistry*, vol. 14, pp. 572–594, 2014.
- [18] A. Hervault and N. T. K. Thanh, "Magnetic nanoparticle-based therapeutic agents for thermo-chemotherapy treatment of cancer," *Nanoscale*, vol. 6, pp. 11553–11573, 2014.
- [19] L. Lartigue, P. Hugounenq, D. Alloyeau, S. P. Clarke, M. Lévy, J.-C. Bacri, R. Bazzi, D. F. Brougham, C. Wilhelm, and F. Gazeau, "Cooperative Organization in Iron Oxide Multi-Core Nanoparticles Potentiates Their Efficiency as Heating Mediators and MRI Contrast Agents," *ACS Nano*, vol. 6, pp. 10935–10949, 2012.

- [20] R. Hergt, S. Dutz, R. Müller, and M. Zeisberger, “Magnetic particle hyperthermia: nanoparticle magnetism and materials development for cancer therapy,” *Journal of Physics: Condensed Matter*, vol. 18, pp. S2919–S2934, 2006.
- [21] H. Mamiya and B. Jeyadevan, “Chapter 1 - design criteria of thermal seeds for magnetic fluid hyperthermia - from magnetic physics point of view,” in *Nanomaterials for Magnetic and Optical Hyperthermia Applications* (R. M. Fratila and J. M. De La Fuente, eds.), Micro and Nano Technologies, pp. 13 – 39, Elsevier, 2019.
- [22] F. Fiorillo, *Characterization and Measurement of Magnetic Materials*. Elsevier, 2004.
- [23] R. M. Bozorth, *Ferromagnetism*. IEEE Press, 1951.
- [24] D. Craik, *Magnetism: Principles and Applications*. Wiley, 1995.
- [25] Y. Zhu, L. P. Stubbs, F. Ho, R. Liu, C. P. Ship, J. A. Maguire, and N. S. Hosmane, “Magnetic Nanocomposites: A New Perspective in Catalysis,” *ChemCatChem*, vol. 2, pp. 365–374, 2010.
- [26] Q. Zhang, X. Yang, and J. Guan, “Applications of Magnetic Nanomaterials in Heterogeneous Catalysis,” *ACS Applied Nano Materials*, vol. 2, pp. 4681–4697, 2019.
- [27] J. Leclercq, F. Giraud, D. Bianchi, K. Fiaty, and F. Gaillard, “Novel inductively-heated catalytic system for fast VOCs abatement, application to IPA in air,” *Applied Catalysis B: Environmental*, vol. 146, pp. 131–137, 2014.
- [28] M. Claeys, M. Dry, E. van Steen, E. du Plessis, P. van Berge, A. Saib, and D. Moodley, “In situ magnetometer study on the formation and stability of cobalt carbide in Fischer-Tropsch synthesis,” *Journal of Catalysis*, vol. 318, pp. 193–202, 2014.
- [29] S. Ceylan, C. Friese, C. Lammel, K. Mazac, and A. Kirschning, “Inductive Heating for Organic Synthesis by Using Functionalized Magnetic Nanoparticles Inside Microreactors,” *Angewandte Chemie International Edition*, vol. 47, pp. 8950–8953, 2008.
- [30] J. Wegner, S. Ceylan, C. Friese, and A. Kirschning, “Inductively Heated Oxides Inside Microreactors - Facile Oxidations under Flow Conditions,” *European Journal of Organic Chemistry*, vol. 2010, pp. 4372–4375, 2010.

- [31] S. Ceylan, L. Coutable, J. Wegner, and A. Kirschning, "Inductive Heating with Magnetic Materials inside Flow Reactors," *Chemistry - A European Journal*, vol. 17, pp. 1884–1893, 2011.
- [32] S. Chatterjee, V. Degirmenci, F. Aiouache, and E. V. Rebrov, "Design of a radio frequency heated isothermal micro-trickle bed reactor," *Chemical Engineering Journal*, vol. 243, pp. 225–233, 2014.
- [33] A. Meffre, B. Mehdaoui, V. Connord, J. Carrey, P. F. Fazzini, S. Lachaize, M. Respaud, and B. Chaudret, "Complex Nano-objects Displaying Both Magnetic and Catalytic Properties: A Proof of Concept for Magnetically Induced Heterogeneous Catalysis," *Nano Letters*, vol. 15, pp. 3241–3248, 2015.
- [34] A. Bordet, L.-M. Lacroix, P.-F. Fazzini, J. Carrey, K. Soulantica, and B. Chaudret, "Magnetically Induced Continuous CO<sub>2</sub> Hydrogenation Using Composite Iron Carbide Nanoparticles of Exceptionally High Heating Power," *Angewandte Chemie International Edition*, vol. 55, pp. 15894–15898, 2016.
- [35] S. S. Kale, J. M. Asensio, M. Estrader, M. Werner, A. Bordet, D. Yi, J. Marbaix, P.-F. Fazzini, K. Soulantica, and B. Chaudret, "Iron carbide or iron carbide/-cobalt nanoparticles for magnetically-induced CO<sub>2</sub> hydrogenation over Ni/SiAlOX catalysts," *Catalysis Science and Technology*, vol. 9, pp. 2601–2607, 2019.
- [36] C. Niether, S. Faure, A. Bordet, J. Deseure, M. Chatenet, J. Carrey, B. Chaudret, and A. Rouet, "Improved water electrolysis using magnetic heating of FeC-Ni core-shell nanoparticles," *Nature Energy*, vol. 3, pp. 476–483, 2018.
- [37] J. M. Asensio, A. B. Miguel, P. F. Fazzini, P. W. van Leeuwen, and B. Chaudret, "Hydrodeoxygenation using magnetic induction: High-temperature heterogeneous catalysis in solution," *Angewandte Chemie - International Edition*, vol. 58, pp. 11306–11310, 2019.
- [38] F. Varsano, M. Bellusci, A. La Barbera, M. Petrecca, M. Albino, and C. Sangregorio, "Dry reforming of methane powered by magnetic induction," *International Journal of Hydrogen Energy*, vol. 44, pp. 21037–21044, 2019.
- [39] M. N. Pérez-Camacho, J. Abu-Dahrieh, D. Rooney, and K. Sun, "Biogas reforming using renewable wind energy and induction heating," *Catalysis Today*, vol. 242, pp. 129–138, 2015.
- [40] J. Marbaix, N. Mille, L.-M. Lacroix, J. M. Asensio, P.-F. Fazzini, K. Soulantica, J. Carrey, and B. Chaudret, "Tuning the Composition of FeCo Nanoparticle Heating Agents for Magnetically Induced Catalysis," *ACS Applied Nano Materials*, vol. 3, pp. 3767–3778, 2020.



- [41] M. R. Almind, S. B. Vendelbo, M. F. Hansen, M. G. Vinum, C. Frandsen, P. M. Mortensen, and J. S. Engbæk, “Improving performance of induction-heated steam methane reforming,” *Catalysis Today*, vol. 342, pp. 13–20, 2020.
- [42] “7400 Series VSM.” <https://www.lakeshore.com/products/categories/specification/discontinued-products/discontinued-products/7400-series-vsm>. Visited on: 2020-05-21.
- [43] “7400-S Series VSM.” <https://www.lakeshore.com/products/categories/specification/discontinued-products/discontinued-products/7400-s-series-vsm>. Visited on: 2020-05-21.
- [44] “7400 Series VSM sample kits.” <https://www.lakeshore.com/products/product-detail/7400-s-series-vsm/samplekits>. Visited on: 2020-05-21.
- [45] J. Mallinson, “Magnetometer Coils and Reciprocity,” *Journal of Applied Physics*, vol. 37, pp. 2514–2515, 1966.
- [46] C. D. Graham, “High-sensitivity magnetization measurements,” *Journal of Materials Science and Technology*, vol. 16, pp. 97–101, 2000.
- [47] “Home — Unifrax - A Global Specialty Fibers Company.” <https://www.unifrax.com/>. Visited on: 2020-05-21.
- [48] E. F. Kneller and F. E. Luborsky, “Particle Size Dependence of Coercivity and Remanence of Single-Domain Particles,” *Journal of Applied Physics*, vol. 34, pp. 656–658, 1963.
- [49] J. Sung Lee, J. Myung Cha, H. Young Yoon, J.-K. Lee, and Y. Keun Kim, “Magnetic multi-granule nanoclusters: A model system that exhibits universal size effect of magnetic coercivity,” *Scientific Reports*, vol. 5, p. 12135, 2015.
- [50] Q. Li, C. W. Kartikowati, S. Horie, T. Ogi, T. Iwaki, and K. Okuyama, “Correlation between particle size/domain structure and magnetic properties of highly crystalline Fe<sub>3</sub>O<sub>4</sub> nanoparticles,” *Scientific Reports*, vol. 7, p. 9894, 2017.
- [51] V. A. Bautin, A. G. Seferyan, M. S. Nesmeyanov, and N. A. Usov, “Magnetic properties of polycrystalline cobalt nanoparticles,” *AIP Advances*, vol. 7, p. 045103, 2017.
- [52] D. L. Leslie-Pelecky and R. D. Rieke, “Magnetic properties of nanostructured materials,” *Chemistry of Materials*, vol. 8, pp. 1770–1783, 1996.
- [53] S. Blundell, *Magnetism in condensed matter*. Oxford University Press, 2001.

- [54] C. H. Bartholemew, “Sintering kinetics of supported metals: New perspectives from a unifying gple treatment,” *Applied Catalysis A-general*, vol. 107, pp. 1–57, 1993.
- [55] C. Grommé, T. Wright, and D. Peck, “Magnetic properties and oxidation of iron-titanium oxide minerals in Alae y Makaopuhi lava lakes, Hawaii,” *Journal of Geophysical Research*, vol. 74, pp. 5277–5293, 1969.
- [56] J. R. Anderson and M. Boudart, *Catalysis : Science and Technology*. Springer Berlin Heidelberg, 1984.
- [57] S. P. Lynch, “Hydrogen embrittlement (HE) phenomena and mechanisms,” in *Stress corrosion cracking: Theory and practice* (V. Raja and T. Shoji, eds.), ch. 2, pp. 90–130, Woodhead Publishing, 2011.
- [58] Z.-P. Hu, D. Yang, Z. Wang, and Z.-Y. Yuan, “State-of-the-art catalysts for direct dehydrogenation of propane to propylene,” *Chinese Journal of Catalysis*, vol. 40, pp. 1233–1254, 2019.
- [59] S. Ravn, “Topsoe to build demonstration plant to produce cost-competitive CO2-neutral methanol from biogas and green electricity,” 2019. <https://blog.topsoe.com/topsoe-to-build-demonstration-plant-to-produce-cost-competitive-co2-neutral-methanol-from-biogas-and-green-electricity>, Date accessed: 27/10-2020.
- [60] “os - Miscellaneous operating system interfaces - Python 3.8.3 documentation.” <https://docs.python.org/3/library/os.html>. Visited on: 2020-05-21.
- [61] G. Van Rossum, *The Python Library Reference, release 3.8.2*. Python Software Foundation, 2020.
- [62] W. McKinney *et al.*, “Data structures for statistical computing in python,” in *Proceedings of the 9th Python in Science Conference*, vol. 445, pp. 51–56, Austin, TX, 2010.
- [63] J. D. Hunter, “Matplotlib: A 2d graphics environment,” *Computing in Science Engineering*, vol. 9, pp. 90–95, 2007.